The Pennsylvania State University

The Graduate School

College of Earth and Mineral Sciences

COMPOSITIONAL, MECHANICAL AND HYDROLOGIC CONTROLS ON FAULT SLIP BEHAVIOR

A Dissertation in

Geosciences

by

Matt J. Ikari

Submitted in Partial Fulfillment
of the Requirements
for the Degree of

Doctor of Philosophy

August 2010

The dissertation of Matt J. Ikari was reviewed and approved* by the following:

Chris Marone
Professor of Geosciences
Head of the Graduate Program
Dissertation Co-Advisor
Co-Chair of Committee

Demian M. Saffer
Associate Professor of Geosciences
Dissertation Co-Advisor
Co-Chair of Committee

Eliza Richardson
Assistant Professor of Geosciences

Derek Elsworth
Professor of Energy and Geo-Environmental Engineering

André R. Niemeijer
Research Scientist
Istituto Nazionale di Geofisica e Vulcanologia, Roma, Italy
Special Member

*Signatures are on file in the Graduate School

ABSTRACT

While many aspects of active fault processes have been well characterized, the mechanisms controlling the slip behavior of major faults remain elusive. Fault slip behavior may range from aseismic creep, to intermediate behavior such as slow slip events, to large and destructive earthquakes. Laboratory experiments are an essential component of fault studies, because they allow detailed investigation of processes operating at otherwise inaccessible timescales and locations in the earth. In order to examine the roles of a variety of factors that are likely important in regulating the occurrence or lack of seismic slip, I evaluate the results of numerous laboratory studies of fault behavior, focusing on the effects of fault mineralogy, mechanical effects, and interactions between fluids and faulting processes. More specifically, these experiments are designed to investigate the underlying mechanisms controlling the transition from aseismic slip at shallow levels in the crust to seismic slip at depth, known as the updip limit of the seismogenic zone.

Results of laboratory experiments indicate that mineralogy of fault gouge is a major control on fault behavior. The clay mineral montmorillonite (smectite) has been noted for its potential effect on seismogenesis in subduction zones (as well as all faults in general) due to its ability to take up water in its crystal structure. Dehydration of montmorillonite tends to increase its frictional strength as well as increase its propensity for seismic slip, as documented by a decrease in the frictional velocity dependence parameter a-b. However, the observed decrease in a-b is assisted by both increasing relative quartz percentage and increasing normal stress, implying that the onset of seismic behavior with increasing depth should not be attributed solely to smectite dehydration. Furthermore, clay-rich gouges in general, including those consisting of montmorillonite, illite, and chlorite, are both frictionally weak ($\mu < 0.35$) and velocity-strengthening (frictionally stable, a-$b > 0$) at fluid-saturated conditions and effective normal

stresses up to ~60 MPa. Sheared gouges may also exhibit low fault-perpendicular permeability ($k < 1 \times 10^{-18}$), making them candidates to host high pore pressure. This indicates that faults containing granular, clay-rich gouges are unlikely to show seismic behavior, due their velocity-strengthening nature and stabilizing hydro-mechanical effects resulting from low permeability. Natural, clay-rich fault gouge from the Nankai subduction zone is consistent with these assessments, also showing low friction, low permeability, and velocity-strengthening slip behavior. This behavior is consistent over a variety of faulting systems, including the megasplay fault zone, the frontal thrust system, and the décollement zone. The velocity-dependence of the Nankai samples reveals a frictional stability minima in the range of slip rates that correspond to rates during slow slip events, indicating that these events may be prevalent in the shallow faulting environment.

Friction experiments conducted to high shear strains and using a wide variety of mineralogic compositions as gouge show that weak, phyllosilicate gouges such as most clays and micas tend to be uniformly velocity-strengthening even at high shear strains. By contrast, minerals such as quartz and feldspar tend to become velocity-weakening after a critical amount of shear strain. An intriguing observation is that fault stability may be linked with overall fault strength, in that weak ($\mu < 0.5$) gouges are velocity-strengthening, while strong gouges ($\mu \geq 0.5$), even those composed of phyllosilicates, may be both velocity-strengthening and velocity-weakening.

In comparing the frictional behavior of granular gouge and lithified fault rock as an analogue for cataclastic fault rocks at seismogenic depths, the lithification of fault rock is found to have a significant strengthening effect, however in phyllosilicate-rich rocks pre-existing foliation provides a weakening mechanism that offsets the strengthening due to lithification. This weakening depends on the intensity of foliation such that strongly foliated rocks, such as books of mica sheets, are significantly weaker than granular mica gouges. Very thick fault zones can exhibit a reduction in measured apparent friction, the magnitude of which may be related to the orientation of through-going R1 shears and internal structural complexity. Consistent velocity-strengthening behavior is observed for both lithified and granular phyllosilicate-rich samples despite the observation of slip localization features in microstructural analysis, suggesting that as an isolated parameter advanced lithification state of fault rock is also inadequate for allowing seismic slip nucleation.

Collectively, the results of the experiments in this study have several important implications for fault slip behavior. Granular, unconsolidated phyllosilicate-rich gouges, such as those that are common at shallow depths in both subduction zones and strike-slip faults, will tend to be aseismic, a condition that may be related to their overall weakness. The transition from aseismic to seismic slip at the updip limit of the seismogenic zone should be driven by changes in pressure and temperature, due to the overall ambient conditions as well as inducing changes in the character of the fault material itself. These may include compositional changes and mechanical effects of the lithification process, such as consolidation and cementation. However, when tested as isolated variables, the dehydration of smectite, conversion of smectite to illite, and lithification of fault gouge were found to be insufficient in allowing unstable slip behavior. It is possible that these processes may still play a role but must be combined with other conditions such as high shear strain, localized deformation, and an increased proportion of intrinsically strong minerals in order to drive seismogenic behavior.

TABLE OF CONTENTS

LIST OF FIGURES

LIST OF TABLES

ACKNOWLEDGEMENTS

I would like to thank my advisors Chris Marone and Demian Saffer for their extraordinary guidance, knowledge, and patience in helping me produce this dissertation. I also thank all members of my committee for their advice and help as well. Thanks also to all members of the Penn State Rock Mechanics Lab, past and present, for all their help and support. Funding for this dissertation was provided by NSF grants to Marone and Saffer.

Chapter 1

INTRODUCTION AND BACKGROUND

The slip behavior of faults is a fundamental process that operates in a wide variety of settings and at all scales in the earth. Frictional slip on faults is the mechanism for one of the most destructive natural disasters in existence, large earthquakes in the brittle crust. Earthquakes along subduction megathrusts are particularly hazardous because of the potential for large magnitude earthquakes, in addition to the risk of tsunami generation. In subduction zone settings as well as in major crustal faults, a reasonably well-defined seismogenic zone has been identified [*Sibson*, 1986; *Marone and Scholz*, 1988; *Hyndman et al.,* 1997; *Scholz,* 1998]. While the transition from seismic to aseismic slip at the lower boundary of the seismogenic zone is inferred to be controlled by the onset of quartz plasticity at 300-350˚C [*Sibson*, 1984; *Hyndman et al.*, 1997; *Blanpied et al.,* 1998], the processes and controlling factors that govern the upper transition from aseismic to seismic behavior are poorly understood. Furthermore, both stable (aseismic) and unstable (seismic) slip can be observed even within the depth limits of the seismogenic zone. This is evidenced by the global variability subduction zone seismicity, and in large continental faults such as the San Andreas, in which portions of the same fault exhibit creep while other portions host large earthquakes [e.g. *Irwin and Barnes,* 1975; *Bakun et al*., 2005]. Understanding the frictional properties of fault gouge is crucial to understanding the generation and nature of earthquakes as well as the strength of crustal faults. This work presents the results and interpretations of laboratory experiments, the goals of which are as follows:

1. Determine the strength and stability of both natural and synthetic fault gouges at a wide range of stresses, slip velocities, and shear strain.

2. Evaluate the effect of fault gouge mineralogy, especially the type and quantity of phyllosilicate minerals on the strength and stability of fault gouge.
3. Quantify the evolution of permeability, porosity, and potential overpressure development of sediments during shear, and their effect on frictional properties.
4. Compare the results of synthetic fault gouges with those obtained using natural fault gouge from the Nankai subduction zone, offshore Japan.
5. Examine the effect of fault rock lithification state on fault strength and frictional stability.
6. Synthesize experimental results to help identify the mechanisms explaining the transition from aseismic to seismic behavior in major fault zones.

This dissertation is presented as a series of manuscripts. This introductory chapter provides background information and provides an overview that connects the subsequent chapters. Chapters 2, 3, 4, 5, 6, and 7 present results and interpretations of laboratory experiments and are either published or are pending publication in peer-reviewed journals.

Although the research presented in this dissertation may be applied to active faults in all settings, much of it focuses on fault behavior along subduction megathrusts. The shallow portions of subduction zones (<40 km depth) are characterized by an aseismic portion and a deeper, seismogenic portion capable of generating large and destructive earthquakes [*Hyndman et. al*, 1997]. The transition from aseismic to seismic faulting occurs at ~5-15 km depth, and the mechanism by which this transition occurs is the subject of much debate [*Shimamoto*, 1985; *Hyndman et al.*, 1997; *Moore et al.*, 2007; *Marone and Saffer,* 2007]. Several ideas have been introduced to explain this transition and identify the dominant controlling factors (Figure 1). These include the smectite-to-illite clay mineral reaction [*Hyndman et. al*, 1997], consolidation and lithification [*Marone and Saffer*, 2007], and diagenetic to low-grade metamorphic processes [*Moore and Saffer*, 2001]. *Marone and Saffer* [2007] and *Moore and Saffer* [2001] argue that the transition from stable to unstable fault behavior is the result of fault sediments reaching a critical lithification stage due to compaction and consolidation [*Marone and Scholz*, 1988; *Byrne et. al*, 1988]. Within unconsolidated sediment, shear is distributed within the gouge layer, resulting in stable sliding. In contrast, lithified fault rock may exhibit localized shear which is associated with unstable sliding [*Marone et. al*, 1992; *Scruggs and Tullis*, 1998]. Additionally, the overlying rock must also have reached a sufficient consolidation and lithification state in order to support a significant stress drop associated with large earthquakes, as accretionary prism sediments are very weak [*Byrne et. al*, 1988; *Scholz*, 1998]. In addition to the smectite-illite transition, the 100-150°C temperature regime also corresponds to several diagenetic to low-grade metamorphic processes that contribute to consolidation and cementation [*Moore and Saffer*, 2001].

As stated above, one of the proposed controlling mechanisms responsible for the onset of seismic fault behavior in subduction zones has previously thought to be the transformation of detrital smectite to illite [*Hyndman et. al,* 1997]. Montmorillonite (a type of smectite) has been targeted as a potential source of fault weakness because of its unusually weak frictional behavior [*Vrolijk*, 1990]. It has been suggested that the source of this weakness is the result of interstitial water within the clay structure [*Bird*, 1984; *Morrow et al.,* 2000]. Water content of smectites is expected to decrease with depth due to increasing temperatures [*Bird*, 1984] and at temperatures of ~60-150°C smectite transforms to illite [*Pytte and Reynolds*, 1989]. The observation that the onset of subduction zone seismicity coincides with this temperature combined with friction experiments showing that the clay mineral illite is frictionally stronger than smectite [*Morrow et al.,* 1992] have lead to the hypothesis that the updip limit of seismicity in subduction zones may be controlled by dehydration of smectite and its eventual transformation to illite. Recent experimental results, however, indicate that while illite may be stronger than smectite, illite does not exhibit the unstable sliding behavior that would allow for seismogenesis [*Saffer and Marone*, 2003; *Kopf and Brown,* 2003; *Brown et al.,* 2003]. In Chapter 2 of this dissertation, I present the results of experiments in which the frictional behavior of montmorillonite-rich fault gouges is measured as a function of hydration state (amount of bound water retained in the clay crystals) as well as a function of bulk clay percentage.

While smectite clays have been given special attention because of their potential role as a source of fluids and ions in fault zones, all the major clay minerals may be common components in fault zones of all settings [*Vrolijk and van der Pluijm*, 1999; *Underwood*, 2007]. This emphasizes the need for detailed frictional characterization of all major clay minerals relevant to major fault zones. In Chapter 3, I report results of frictional strength, frictional stability, and post-shear fault-normal permeability measurements for gouges composed of montmorillonite, illite, and chlorite. These experiments were conducted saturated, with controlled pore fluid pressure, and at effective normal stresses relevant to the updip limit of the seismogenic zone in convergent margins. Based on previous research, common mechanical characteristics of clay minerals include low friction and low permeability [e.g. *Morrow et al.,* 1984; *Brown et al.,* 2003; *Faulkner and Rutter,* 2003], however studies of the frictional stability of clays and clay gouges are less common. Furthermore, low permeability may greatly influence fault behavior by enhancing hydro-mechanical processes. In long-term steady state pore pressure models developed by *Saffer and Bekins* [1998, 2006] it is low pore pressure values near hydrostatic levels that enhance fault instability, thus declining pore fluid pressures have been associated with the updip limit of seismicity [*Moore and Saffer*, 2001]. This is based on stability models developed by *Scholz* [1998], in which given an unstably sliding fault material, the degree of instability will increase with higher effective stress (lower pore pressure). High pore pressures near lithostatic values are often thought to be related to extremely weak faults in the case of creeping strike-slip faults [*Byerlee*, 1990; *Rice*, 1992; *Blanpied et al.,* 1992] and also to earthquake triggering [*Sleep and Blanpied*, 1992; *Beeler et al.,* 2000] although these effects are thought to be due to episodic transiently high pore pressure. Transiently high pore pressures manifested in low permeability gouges are also thought to enhance fault stability through mechanisms such as thermal pressurization or shear-enhanced compaction [e.g. *Segall and Rice*, 2006].

The above studies were conducted using either synthetic mixtures or naturally occurring clay-rich sediments not obtained from fault zones as analogues for fault gouge. To augment these studies, I conducted friction and permeability measurements on natural fault gouge obtained from a major thrust splay fault within the Nankai accretionary complex during IODP Expedition 316. Splay faults are of particular interest because models using tsunami and seismic waveform inversions have shown that they may have participated in seismic slip during historical great earthquakes in the Nankai area [*Cummins and Kaneda*, 2000; *Tanioka and Satake*, 2001; *Kikuchi et al.,* 2003] and may also be the loci of slow slip events [*Ito and Obara,* 2006]. The results of these experiments are reported on Chapters 4 and 5 and were conducted under saturated, controlled fluid pressure conditions similar to those reported on in Chapter 3. One of the main conclusions drawn in Chapters 2, 3, 4, and 5 is that granular, clay-rich fault gouges are both frictionally weak and frictionally stable under a wide range of conditions. Additionally clay-rich gouges exhibit consistently low permeability, which enhances stable slip behavior due to transient pore pressure effects. Because of the abundance of clay minerals typically found in major fault zones, the question of which factors can cause an initially stable fault material to become seismogenic becomes an outstanding problem. In Chapters 6 and 7, I return to investigation of fault gouge analogues in order to investigate a wide range of fault compositions to explicitly test effects of shear strain and lithification state on the frictional behavior of phyllosilicate-rich fault materials, and to compare them with those of phyllosilicate-poor composition.

While some authors have suggested that fault weakness may be linked with aseismic (stable) sliding [e.g. *Ruff and Kanamori*, 1983; *Tichelaar and Ruff*, 1993], theoretical treatment of fault friction indicates that fault stability depends solely on second-order effects rather than overall friction levels [e.g. *Tullis*, 1988; *Scholz*, 2002]. At the moment, there is a lack of definitive evidence supporting either viewpoint. In Chapter 6, I present results of a suite of experiments measuring the frictional strength and stability for a wide range of gouge compositions and over large amounts of accumulated shear strain, which has been previously shown to have a significant impact on fault stability [*Beeler et al.,* 1996; *Mair and Marone*, 1999]. This study allows comparison of friction data between phyllosilicate-rich gouge and phyllosilicate-poor gouge, and also between gouges that exhibit stable slip behavior and those whose slip may be unstable. Using the results of this data set, I will show that frictionally weak gouges, such as those containing a large proportion of clay minerals, also tend to exhibit stable slip behavior. This assertion is further supported by the results presented in Chapter 7, in which I show that the lithification process by itself cannot drive unstable behavior in fault rock composed of weak, phyllosilicate minerals.

The overarching goal of this research is to move closer to understanding why some fault sections have the propensity for large magnitude earthquakes and why some do not. This study focuses on specifically on the shallow areas in subduction zones because this striking difference in behavior (i.e., transition from stable creep to seismogenic slip) occurs in adjacent portions of the same geologic system, but the conclusions drawn may ideally be applicable to any major area of faulting. As discussed above, much work has been done to develop hypotheses regarding the factors that may have the most influence in causing this phenomenon. The experimental results presented in this dissertation provide extensive documentation of the frictional strength, frictional stability, and permeability of a wide variety of fault gouge compositions under a wide variety of conditions. Interpretation of these results shows that the potential for seismic slip on major faults is controlled by a complex interplay of mineralogy, hydrologic character, and mechanical state of the fault gouge.

Chapter 2

EFFECT OF HYDRATION STATE ON THE FRICTIONAL PROPERTIES OF MONTMORILLONITE-BASED FAULT GOUGE

Abstract

We report on laboratory experiments examining the effect of hydration state on the frictional properties of simulated clay and quartz fault gouge. We tested four mixtures of Ca-montmorillonite and quartz (100%, 70%, 50%, and 30% montmorillonite) at four hydration states: dry (<4.50 wt% water), 1 water interlayer equivalent (4.5-8.7 wt% water), 2 layer (8.7-16.0 wt% water) and 3 layer (>16.0 wt% water). We controlled the hydration state using either oven drying (for <13wt% H_2O) or saline solutions (to achieve >13 wt% H_2O under conditions of controlled RH). For each clay/quartz mixture and hydration state, we measured frictional properties over a range of normal stresses (5-100 MPa), and sliding velocities (1-300 μm/s). We observe a systematic decrease in the coefficient of friction (μ) with increasing water content, normal stress, and clay content. Values of μ for 50/50 mixtures range from 0.57-0.64 dry and decrease to 0.21-0.55 for the most hydrated cases (wet). For layers of 100% montmorillonite, μ ranges from 0.41-0.62 dry and 0.03-0.29 wet. As water content is increased from 0-20.0 wt%, the friction rate parameter *a-b* becomes increasingly positive. Variation in *a-b* values decreases dramatically as normal stress increases. If our experimental results can be applied to natural fault gouge, the combination of stress state, hydration state, and quartz content that facilitates unstable fault behavior implies that the onset of shallow seismicity in subduction zones is more complicated than a simple transition from smectite to illite.

Introduction

Understanding the frictional properties of fault gouge is crucial to understanding the generation and nature of earthquakes as well as the strength of crustal faults. For subduction zone faults, which form within fine-grained marine sediments, the expanding clay smectite is of particular interest because (1) it is common in the protolith [*Vrolijk and van der Pluijm*, 1999], (2) can exhibit exceptionally low friction [*Logan and Rauenzahn,* 1987; *Saffer et al*., 2001], and (3) has been suggested as a candidate source of fault weakness [*Vrolijk*, 1990; *Morrow et al.,* 2000]. Water content of smectites is expected to decrease with depth due to increasing temperatures [*Bird*, 1984] and at temperatures of 100-150°C smectite transforms to illite [*Pytte and Reynolds*, 1989]. It has been observed that the onset of subduction zone seismicity coincides with this temperature range [*Hyndman*, 1997]. The clay mineral illite is frictionally stronger than smectite [*Morrow et al.,* 1992]; as such it has been proposed that the updip limit of seismicity in subduction zones is controlled by the transformation of smectite to illite within the downgoing sediments [*Hyndman et. al.,* 1997]. This theory has been called into question recently by studies indicating that while illite may be stronger than smectite, under sliding conditions illite does not exhibit the unstable sliding behavior that would allow for seismogenesis [*Saffer and Marone*, 2003; *Kopf and Brown,* 2003; *Brown et al.,* 2003]. Although this indicates that the factors controlling the updip limit of seismicity may be more complicated than previously believed, water content may still be a major factor influencing the frictional behavior of subducting clays. Here, we investigate the conditions that affect the strength of clay dominated gouge, focusing on the mineral montmorillonite (a type of smectite) and quantifying the role of hydration state in strength and frictional behavior.

Montmorillonite has been targeted as a potential source of fault weakness because of its unusually weak frictional behavior [*Vrolijk*, 1990]. It has been suggested that this weakness is the result of interstitial water within the clay structure [*Bird*, 1984; *Morrow et al.,* 2000]. We examined the effect of water on the frictional behavior of laboratory simulated clay gouge by controlling its water content and performing experiments in which we vary the normal stress, shearing velocity, and the relative proportion of clay and quartz. Hydration state has been indirectly studied in previous work by controlling the ambient humidity on sealed layers consisting of 100% quartz [*Frye and Marone,* 2002], as well as some smectite-quartz mixtures at room conditions [*Saffer and Marone,* 2003; *Hong and Marone,* 2005]. The velocity dependent frictional behavior of the quartz layers was found to change from strengthening to weakening with increasing relative humidity (RH). The overall frictional strength was unaffected by humidity [*Frye and Marone,* 2002]. Quartz, however, has a low capacity for water retention so it is possible that the effect of water content is more pronounced in a layer either completely or partially composed of an expanding clay.

Experimental Methods

Water Content

The aim of this study is to examine the effect of hydration state on frictional properties; therefore careful control of water content in the samples is essential. In previous experiments with layers consisting of 100% quartz, hydration state has been inferred by using a layer equilibrated with a controlled RH [*Frye and Marone,* 2002]. When montmorillonite reaches equilibrium with the surrounding air, the water content in the clay depends on the ambient temperature and RH [Bird, 1984]. Following *Bird* [1984], we describe hydration state based on the number of water interlayers. These interlayer water molecules are bound to the silicate layers and the exchangeable cation, Ca^{2+}, in arrangements parallel to the silicate sheet (Figure 2-1). A 1 layer arrangement includes 3-4 water molecules surrounding a cation, while a 2 layer arrangement consists of 6 octahedrally-bound water molecules [*Colten-Bradley,* 1987]. For clays in which water molecules are in excess of the 2 layer arrangement (estimating a maximum of 8 water molecules per cation) the water is oriented randomly, similar to bulk water. We refer to this as a “3 layer” configuration. “Dry” samples are considered those containing less than 3 water molecules per cation. At room conditions (~45% RH and 25°C) montmorillonite contains water in a 2-layer configuration [*Bird*, 1984].

Based on a simple calculation using a molar mass of 757 g/mol for Ca-montmorillonite and 18 g/mol for water, we find that dry layers contain <4.5 wt% water, a 1 layer arrangement contains 6.7-8.7 wt% water; a 2 layer arrangement contains 10.6-16.0 wt% water, and a 3 layer arrangement contains >16.0 wt% water (Figure 1). Samples may have intermediate water content; gouge that contains 9.2 wt% water, for example, may consist of clay particles with 1 and 2 water layers. To control the water content of our samples, we constructed time-dependent drying curves by dehydrating samples from room conditions via oven drying at 105°C and recording the weight loss (Figure 2-2). The water content, or wt% water, varies smoothly and predictably with time in response to heating. These data are highly reproducible and show that most of water is driven off within the first 4 hours; although there is some variability between mixtures, any hydration state below ~13 wt% water can be attained. When no further weight reduction in the weight of clay sample was observed with continued heating, we designated this as the 0 wt% reference point in the drying curves. We verify that all bound water was driven off via oven drying by drying clay samples at elevated temperatures (~260°C) and noting negligible further weight loss. Additionally, we performed Fourier-Transform Infrared Spectroscopy (FTIR) on samples of oven-dried and room condition montmorillonite exposed to dry gas (nitrogen) for 210 minutes, results of which are consistent with a “dry” sample that is no more than ~1 wt% water and a room condition sample with ~13 wt% water. To reach water contents above that of a sample equilibrated with room humidity, we hydrated samples in a sealed environment containing a supersaturated Na_2CO_3 solution.

Using the methods described above, we preconditioned simulated gouge material to a desired hydration state prior to each experiment (Table 2-1). During the experiments, the RH of the air surrounding the sample was controlled in a sealed environment to prevent any changes in water content. In addition, we verified that the hydration state at the end of each experiment was unchanged from the initial condition by oven drying the gouge immediately following the experiment.

Friction Measurements

We conducted experiments in a biaxial testing apparatus to measure frictional behavior under controlled normal stress and sliding velocity. Two layers of sample fault gouge were sheared within a three-piece steel block assembly in a double-direct shear configuration (Figure 2-3). Gouge layers were constructed in a leveling jig to be a uniform area (5 x 5 cm) and thickness (4-5 mm), which compacted to 2-3 mm under load. This three-block unit was then loaded into the testing apparatus and a normal force was applied prior to shear (Figure 2-3). The frictional contact surfaces were grooved to ensure that shearing occured within the layer and not at the layer-block interface. The contact area was maintained at 5 cm by 5 cm.

We ran a suite of experiments at normal stresses ranging from 5-100 MPa for a series of gouge compositions (ranging from 0% to 70% quartz by weight) and for a range of controlled hydration states (Table 2-1). Mean grain size of Ca-MM was 60 μm with 80% of the grain diameters between 3 and 142 μm, determined by using laser obscuration in a Malvern Mastersizer. Mean grain size of quartz sand was 110 μm; grain sizes fit a Gaussian distribution with 99% of the grain diameters between 53 and 212 μm.

Measurements of initial porosity were made by dividing the void volume (total volume minus sediment volume) by the total volume of the sample following *Marion et al.* [1992]. Total volume was the contact area times the initial layer thickness; sediment volume was the mass of gouge material divided by the sample density. Sample density varied between 2.35 g/cm^3 and 2.78 g/cm^3 depending on the clay percentage and water content of the clay portion [*Lambe and Whitman*, 1969]. The initial porosity of samples (on the benchtop, under a load of ~6 kPa) composed of 30% montmorillonite was 50% for “dry” samples and 46% for “3 layer” samples. Porosity of 100% montmorillonite was 61% for “dry” samples and 58% for “3 layer” samples. Initial porosity values for samples with 2 water interlayers are 44%, 48%, 51%, and 54% in samples composed of 30%, 50%, 70%, and 100% montmorillonite, respectively. The values we report are similar to porosity values obtained by *Marion et al.* [1992] at atmospheric conditions.

Gouge layers were sheared at constant velocity for the first 10 mm of fault slip to develop a steady-state fabric and minimize any effect of net displacement. Three sets of velocity step sequences were then initiated, each at a given normal stress (Table 2-1, Figure 2-4). Each velocity step sequence consisted of incrementally increasing the sliding velocity from 1 μm/s to 300 μm/s and then back down to 10 μm/s. The duration of each velocity step was the time necessary to displace a distance of 400 microns. Steady state sliding was usually achieved after ~1.5 mm of displacement in each sequence. We measured overall shear strength of fault gouge (τ) and coefficient of sliding friction (μ) after 10 mm of displacement after application of each normal stress for consistency (Figure 2-4). The coefficient of sliding friction μ was calculated as: $\tau = \mu\sigma_n + c$, where σ_n is the applied normal stress (Handin, 1969; Byerlee, 1978) and the intercept c is the cohesion (typically zero for our experimental gouge).

Results

Frictional Strength

The shear strength (and coefficient of friction) of the gouge is strongly dependent on its water content (Figures 2-5, 2-6). This effect is more pronounced with increased normal stress and with higher clay content (Figure 2-5). The failure envelope exhibits rollover at 25-40 MPa; this is more dramatic with increased clay and increased water content (Figure 2-5). The steady state coefficient of sliding friction decreases systematically with increasing water content, normal stress, and clay content (Figure 2-6, 2-7). For example, at 40 MPa, μ ranges from 0.49-0.62 dry, while 3 layer samples range from 0.09-0.48 for all mixtures. With water content held constant, increased normal stress also reduces the coefficient of friction for all mixtures; for example, in the 1 layer samples μ decreases from 0.52-0.64 at 5 MPa to 0.23-0.56 at 100 MPa. Note that the reduction in μ is more pronounced in layers with higher clay percentage; in comparing mixtures containing 30% and 100% montmorillonite over all normal stresses and hydration states, both mixtures have similar maximum values (0.62 for 100%, 0.63 for 30%) but μ in 100% montmorillonite decreases to 0.03 at high normal stress and water content while the minimum value of μ for 30% montmorillonite layers under the same conditions is 0.42. This is consistent with previous findings in which increased clay percentage causes a decrease in coefficient of friction [*Logan and Rauenzahn,* 1987].

Velocity Dependence

We classify frictional velocity dependence using the parameter *a-b*; defined as:

$(a - b) = \dfrac{\Delta \mu_{ss}}{\ln(V / V_o)}$, where $\Delta\mu_{ss}$ is the change in steady state sliding friction, and V_o and V are the sliding velocities at initial and new steady state friction respectively [*e.g. Marone,* 1998], (Figure 2-8). Positive *a-b* values indicate velocity-strengthening behavior, whereas negative a-b values indicate velocity-weakening behavior. Velocity-weakening is a prerequisite for stick-slip behavior which is associated with earthquake nucleation [*Scholz*, 2002].

Results of the velocity stepping tests indicate that the majority of the gouge samples exhibit velocity-strengthening behavior. For all mixtures, we observe a large variance in *a-b* for low normal stress and variance decreases with increased normal stress. Dry samples, as opposed to samples with at least 1 layer of bound water, maintain some velocity-weakening behavior throughout the entire normal stress regime (whereas the hydrated samples do not) and are less velocity-strengthening in general (Figure 2-9). At 5 MPa, both hydrated and dry samples have similarly large ranges of *a-b* (-0.0042 to 0.0123 for hydrated samples, -0.0037 to 0.0140 for dry samples), whereas at 100 MPa, the *a-b* values in hydrated layers range from 0.0005 to 0.0049 and in dry layers values range from -0.0008 to 0.0020.

In hydrated samples, the lowest values of *a-b* are associated with low sliding velocity (1-3 μm/s); these change from velocity-weakening to velocity-strengthening with increased normal stress, which is consistent with previous data [*Saffer et al.,* 2001] (Figure 2-10). The more positive *a-b* values are associated with samples sliding at high velocity (100-300 μm/s); these tend to decrease with increased normal stress. The same trend can be identified in dry samples but is less clearly defined than in the hydrated samples. Generally, at a given normal stress, higher sliding velocity yields more positive *a-b* values (Figure 2-11).

With increased sliding velocity, two additional trends can be identified. First, samples with higher clay percentage are generally more velocity strengthening regardless of water content (Figure 2-12). Second, within the trend in *a-b* for each individual gouge mixture, higher water content slightly increases *a-b* values. In the most hydrated samples, those containing 30% montmorillonite are comparable only to the lowest *a-b* values exhibited by 100% montmorillonite regardless of normal stress and sliding velocity (Figure 2-12). In dry samples, *a-b* values are comparable, but it is noteworthy that mixtures containing 30% montmorillonite show velocity weakening behavior for all normal stresses.

Na-Montmorillonite

We performed 6 experiments with 100% Na-montmorillonite in order to determine whether frictional behavior is cation-specific. These experiments yielded data for dry (0.5 wt% water), 1 layer (5.5, 5.6 wt% water), and 2 layer (12.1, 13.0 wt% water) samples over the same range of normal stresses and sliding velocities as the Ca-montmorillonite experiments (Table 2-1). Room condition Na-montmorillonite samples were 1 layer and hydrated samples were 2 layer, lower states of hydration than Ca-montmorillonite at the same conditions. This is expected because the lower charge of Na^{+} doubles the negative charge of the clay structure, allowing approximately half the amount of water to remain in the interlayer [*Eberl et al.,* 1993]. Sliding friction values for Na-montmorillonite are 0.55 to 0.45 for dry samples, 0.35 to 0.22 for 1 layer samples, and 0.28 to 0.04 for 2 layer samples. Compared to Ca-montmorillonite, values of μ for dry samples are slightly lower (~0.05 lower), and 1 layer and 2 layer values are significantly lower (~0.1 to 0.15 lower for all normal stresses). However, the trend of lower friction values with both increasing water content and increasing normal stress remains the same as for Ca-montmorillonite. Observations of frictional velocity dependence for Na-montmorillonite are also consistent with those for Ca-montmorillonite.

Discussion

Comparison to Previous Data

The trends in μ we observe are in very good agreement with previous work conducted on montmorillonite gouge. For 2 layer 100% montmorillonite, μ decreases from 0.35 to 0.12 as normal stress is increased from 5 to 100 MPa, and for 2 layer samples containing 50% montmorillonite, μ decreases from 0.59 to 0.27 over the same normal stress range. This is comparable to the results of *Saffer and Marone* [2003] in which μ decreased from ~0.32 to ~0.10 and from ~0.57 to ~0.21 in layers of 100% and 50% montmorillonite, respectively under the same normal stress range. The large decrease in μ from 0.60 under dry conditions to 0.03 in 3 layer 100% montmorillonite at 25 MPa is similar to the decrease observed by *Morrow et al.* [1992] when comparing dry and saturated montmorillonite gouge. At 40 and 70 MPa, values of μ for 3 layer 30%, 70%, and 100% montmorillonite samples are similar to values reported by *Logan and Rauenzahn* [1987] at 50 and 70 MPa confining pressure for 25%, 75%, and 100% montmorillonite samples. We also observe systematically higher values of μ in samples with higher quartz content; this was also observed by *Logan and Rauenzahn* [1987] and *Kopf and Brown* [2003] who document a strong correlation between increasing μ and decreasing clay content (increasing quartz content).

The systematic increase in μ with increasing quartz content may also be related to the strength of grain-to-grain contacts between minerals [*Logan and Rauenzahn*, 1987]. We observe that gouge samples with higher quartz content have lower initial porosity values than samples with high clay content. However, when subjected to normal stress prior to shearing, the high quartz samples tend to have higher porosities. We infer that once a normal load has been applied, the major mineralogic constituent in the gouge supports the majority of the load; i.e., in gouge with high quartz content, quartz grains will likely impinge on other quartz grains, and in gouge with high clay content the clay minerals will likely impinge on each other [*Marion et al.*, 1992]. Thus, the shear strength of the gouge will be controlled by the strength of the minerals in contact with each other, rather than the initial porosity. Quartz strength is independent of humidity, with $\mu =$ ~0.6-0.65 [*Mair and Marone*, 1999; *Frye and Marone*, 2002], whereas we observe that montmorillonite strength is highly variable and is inversely related to water content.

Although the trend of weakening with increasing water content in montmorillonite is clear, the mechanism by which this weakening occurs is not. A variety of mechanisms have been suggested for water-assisted weakening of fault gouge. Expulsion of interlayer water from a bound state within the crystal structure to pore space due to mechanical pressure may reduce friction by increasing the pore pressure, thereby reducing the effective normal stress [*e.g. Colten-Bradley,* 1987; *Fitts and Brown,* 1999]. In a compaction experiment in which 2 layer 100% montmorillonite was subjected to load steps of 5, 15, 25, 40, 70, and 100 MPa for a duration of 15 minutes without shearing, porosity was reduced from 59% under zero normal load to 7% at 100 MPa. This indicates that porosity reduction due to compaction and shear could potentially have brought the porosity to extremely low values. Because we performed experiments on undersaturated sediments, expulsion of bound water from the clay structure may not significantly affect the sample porosity, as bound water expulsion into pore space is approximately compensated by pore volume increase due to collapse of the clay mineral structure once the water is expelled. Nevertheless, the porosity may have been reduced enough that transient pore pressure buildup may have occurred.

Another potential explanation is that interlayer water may support the applied normal stress within the clay structure itself, thereby allowing slip at low effective stress between the octahedral layers [*Bird*, 1984]. At the moment, however, there is little evidence that this particular mechanism occurs. In contrast to experiments on undersaturated sediments, several previous studies report on friction experiments with sediments saturated with deionized water [*Moore and Lockner,* 2004; *Moore and Lockner,* 2007] or brine having seawater composition [*Brown et al.,* 2003; *Kopf and Brown,* 2003]. Some of these studies suggest that low friction values represent the strength necessary to shear through films of water molecules bonded to mineral surfaces in proportion to that mineral's interlayer charge [*Moore and Lockner,* 2004; *Moore and Lockner,* 2007]. Although the composition of the pore fluid may increase the strength montmorillonite gouge, this increase is very small (0.02 increase in μ in the presence of a 1 molar brine) [*Lockner et al.,* 2006]. It may be possible that these surface effects due to saturation, and effective stress changes caused by increased pore pressure, combine to cause unusually weak gouge. More experimentation is necessary to determine the exact mechanism of gouge weakening.

Our observed trends in *a-b* are also in close agreement with previous studies. Most of the previous studies have been conducted on samples sheared to very limited displacements and without precise control on sample normal stress, which tends to result in biased results for friction velocity dependence [*e.g. Dieterich,* 1981; *Beeler et al.,* 1996]. However, we compare to those values for completeness. *Morrow et al.* [1992] report an *a-b* value of 0.0005 for 100% montmorillonite at 100 MPa, consistent with our data. *Logan and Rauenzahn* [1987] report that 100% quartz is velocity weakening, while all other clay mixtures in their study were velocity strengthening. Because their samples were not oven-dried, this observation is most comparable to our reported *a-b* values for partially hydrated samples. *Logan and Rauenzahn,* [1987] as well as *Saffer et al.* [2001] also observed unstable sliding at very low velocity. We also observe this behavior; however, at higher sliding velocities and higher normal stress this behavior vanishes in all but the dry samples, which is consistent with previous observations of velocity strengthening behavior in non-dry mixtures containing montmorillonite [*Logan and Rauenzahn,* 1987; *Saffer et al.,* 2001]. The similarity of these observations lead to two important points. First, the presence of (non-dry) montmorillonite causes fault gouge to be weak; progressive increase in relative quartz percentage causes the gouge to strengthen. Second, other than some unstable behavior at very low sliding velocity and very low normal stress, montmorillonite gouge slides stably even in very low proportions (30%), whereas quartz exhibits unstable sliding.

Application to Natural Systems

We have shown the systematics of the frictional behavior of montmorillonite-quartz gouges over a wide range of conditions, including water content, applied normal stress, clay content, and sliding velocity. Realistically, however, the range of these conditions in natural faults is much narrower. For example, subduction zones do not consist of 100% Ca-montmorillonite, nor does clay retain 20 wt% water to depths at which pressures are 100 MPa. To apply our experimental results to subduction zone conditions, we must consider a subset of our experiments that are consistent with in-situ fault gouge compositions and hydration states.

We may estimate the conditions of hydration and bulk clay content with depth. For real faults we assume an effective vertical component of normal stress increase of 8 MPa/km and a temperature gradient of 20-25°C/km. Water content decreases with increasing depth; with effective stresses as low as ~1.3 MPa, smectite may not contain more than 2 layers of water [*Fitts and Brown,* 1999]. Due to increasing temperature and normal stress, interlayer water content reduces to 1 layer at 67-81°C and the remaining layer is expelled at 172-192°C [*Colten-Bradley,* 1987]. This corresponds to clay containing 1 layer of water at ~3-8 km, and at depths greater than 8-km, only “dry” clay may exist. Although abundant fluid and overpressures may exist within fault zones, the thermally driven expulsion of interlayer water should result in “dry” montmorillonite, with fluid in pore spaces rather than in the clay interlayers [Colten-Bradley, 1987].

Smectite content in gouge can be large [*Vrolijk and van der Pluijm,* 1999]; at many subduction zones, for example, the percentage of smectite in the bulk sediment can be greater than 50% [*Underwood,* 2007]. Above 150°C (and below 300°C), significant quartz precipitation may occur via pressure solution and recrystallization downdip, increasing the relative percentage of quartz [*Moore and Saffer,* 2001; *Moore et al.,* 2006]. In applying our data to natural faults, we assume an initial gouge composition of 70% montmorillonite which changes gradually to 30% montmorillonite with depth. Given that quartz is velocity-weakening in this pressure and temperature window [*Blanpied et al.,* 1998; *Mair and Marone,* 1999] we expect the gouge to become more velocity-weakening as the relative percentage of quartz to stably sliding clay (which by this depth has most likely been transformed to illite) increases with depth.

In a simplified analysis merging our data with estimated in-situ subduction zone conditions and progressive changes in gouge compositions, we see a clear velocity-weakening trend and crossover into negative *a-b* values between 5 and 9 km depth, consistent with both the updip limit of seismicity and the smectite-illite transition (Figure 2-13). The data are shown here without regard for sliding velocity; however recall from Figure 2-11 that high sliding velocities tend to accentuate the trend towards velocity weakening. This result suggests that although the updip limit of seismicity may coincide with the smectite-illite transition temperature, this transition alone may not be sufficient to cause fault gouge to become seismogenic. Instead, it appears that the onset of seismic behavior is more complicated and requires a combination of conditions that include, but may not be limited to, quartz content, clay dehydration, sliding velocity, and stress state. More experimentation is necessary to conclusively determine the relative importance of these and other factors.

Conclusions

Water content of montmorillonite has a profound effect on the frictional strength and constitutive properties of fault gouge. With increasing water content, the overall frictional strength of gouge becomes much lower and, in the cases of very high water and clay content, gouge exhibits rollover in the frictional failure envelope (i.e., above a given normal stress, shear strength increases only slightly). Increasing water content also leads to velocity strengthening behavior. In applying our results to the geologic conditions in subduction zones, we note that decreasing water content, increasing quartz content, and increasing normal stress may combine to cause a transition to velocity-weakening behavior at depths consistent with the onset of subduction zone seismicity. The smectite-illite transition by itself does not appear to be sufficient to explain the onset of subduction zone seismicity.

Figures

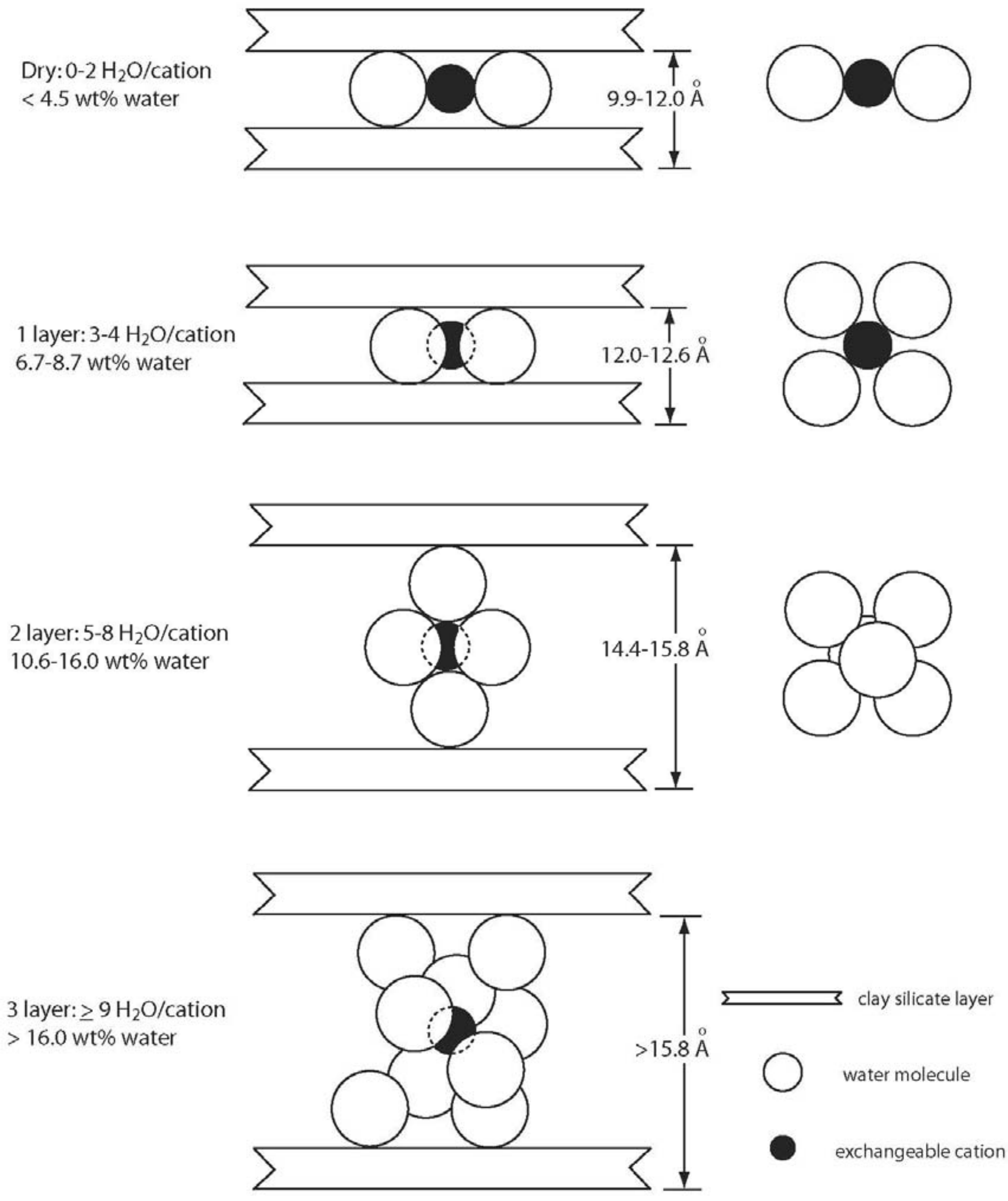

Figure 2-1. Structure of interlayer water in Ca-montmorillonite and corresponding wt%. Dry layers contain fewer than 2 water molecules per cation. 2 layer arrangements are octahedral with 6 water molecules per cation. Above 2 layers, the water takes on a random arrangement. Note that intermediate stress states may exist where more than one layer arrangement may be present. Modified from Colten-Bradley, 1987.

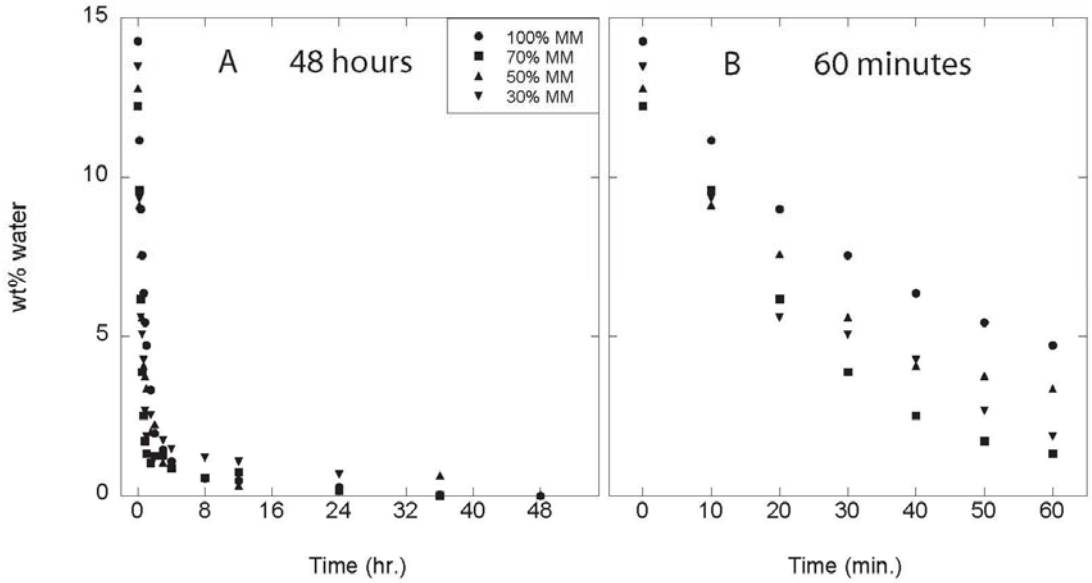

Figure 2- 2. Experimentally derived time-dependent drying curve for all Ca-montmorillonite/quartz mixtures at 105°C for A: 48 hours, and B: 60 minutes.

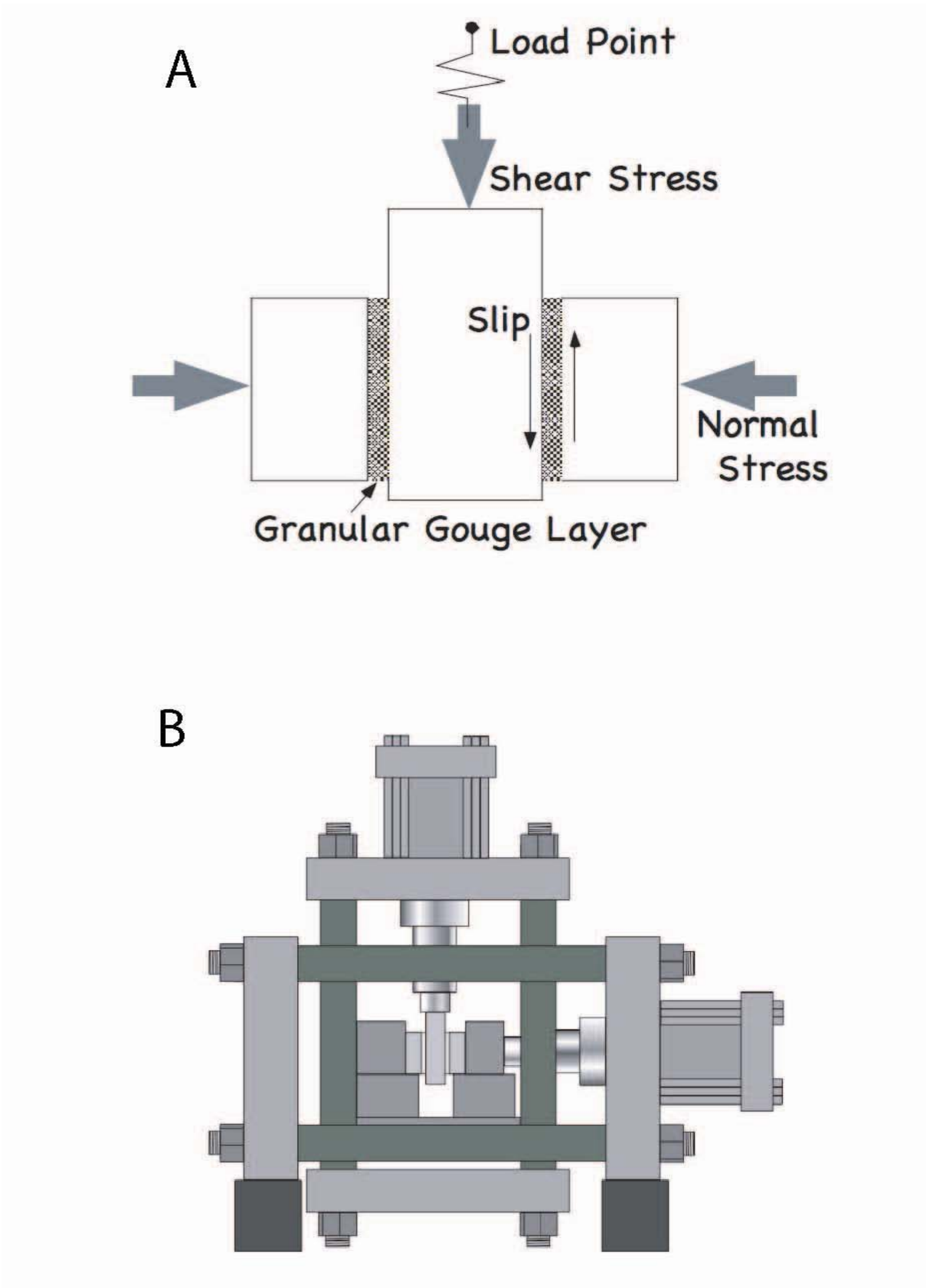

Figure 2-3. Setup of biaxial stress experiments. Samples are loaded in between grooved sliding blocks (A). Sliding blocks are then loaded in biaxial stressing apparatus (B).

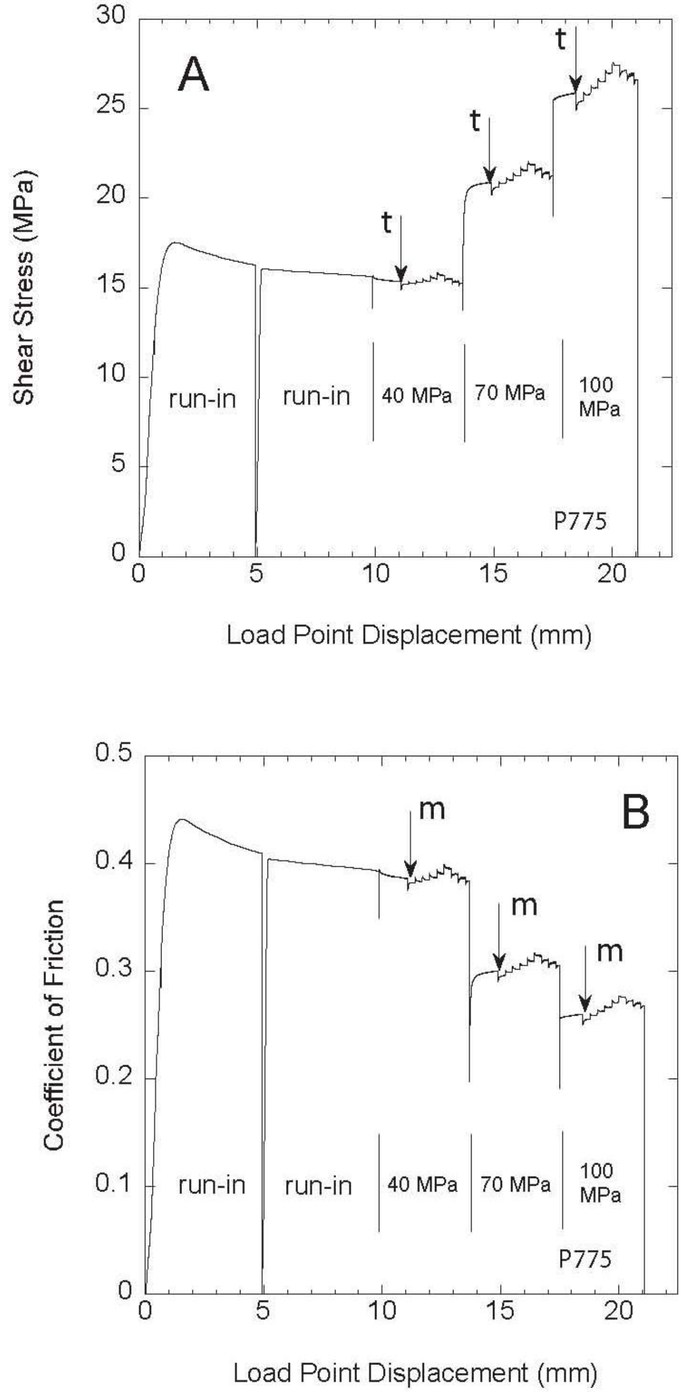

Figure 2-4. Example of a typical experiment: shear stress (A) and coefficient of friction (B) are plotted against load point displacement, which is equal to the displacement during sample shearing. The shear strength value τ and the coefficient of friction μ are taken after 1.6 mm of displacement during each velocity step sequence.

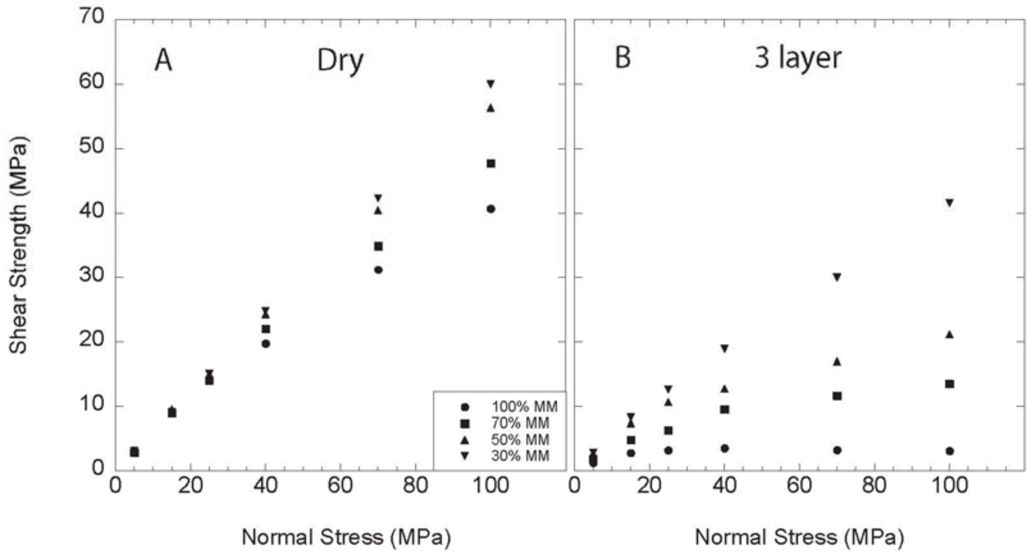

Figure 2-5. Shear strength with increasing normal stress for all mixtures, comparing A: the most dry samples and B: the most hydrated 3 layer samples. MM=Ca-montmorillonite.

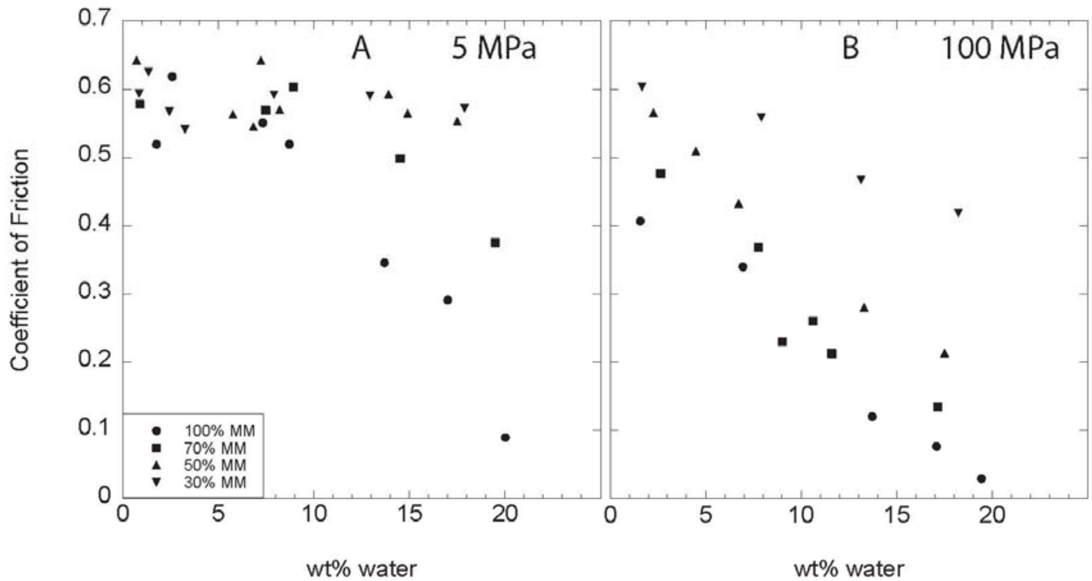

Figure 2-6. Coefficient of friction plotted against increasing water content at normal stresses of A: 5 MPa and B: 100 MPa.

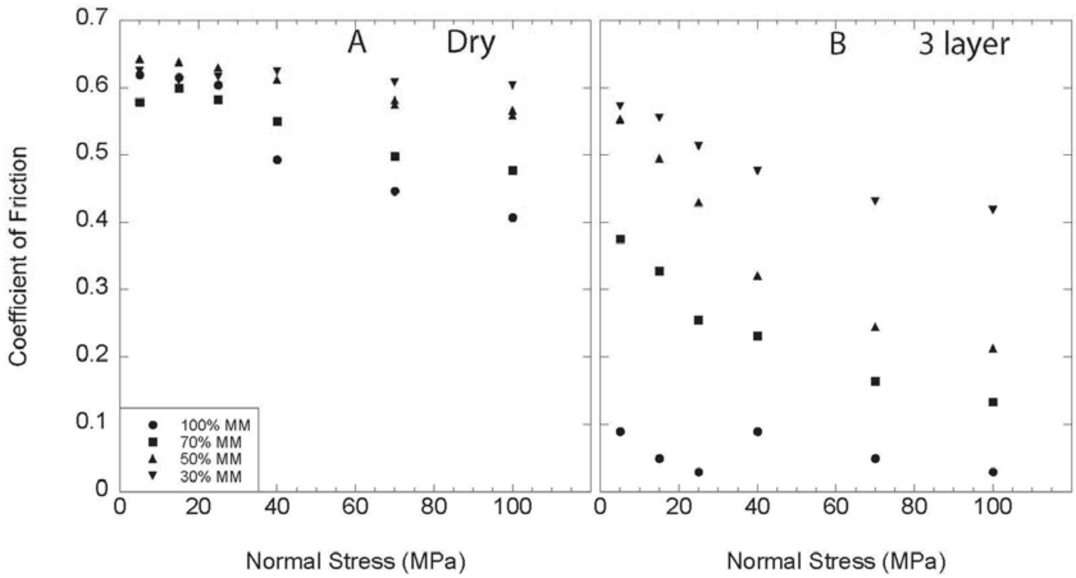

Figure 2-7. Coefficient of friction plotted against increasing normal stress, showing all mixtures and comparing A: the driest samples with B: the most hydrated 3 layer samples.

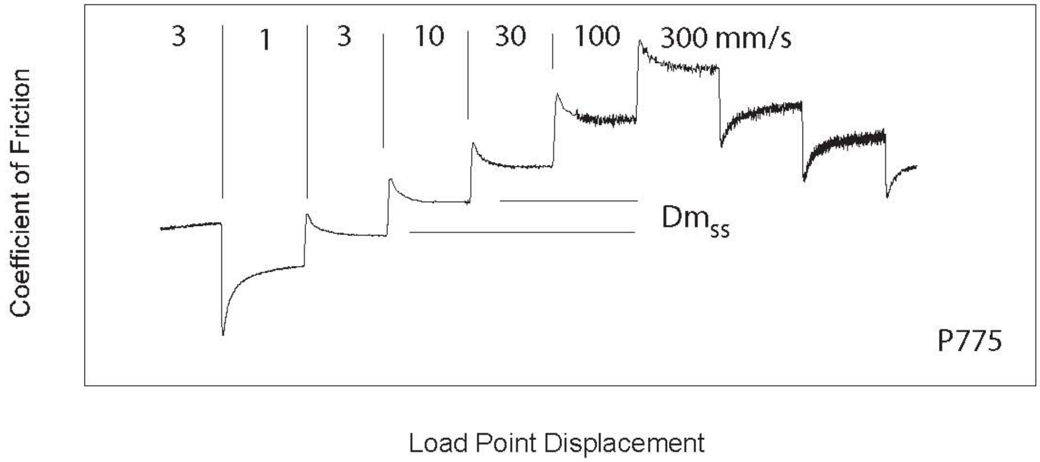

Figure 2-8. An example of a velocity step sequence and the change in steady state sliding friction used to determine the parameter a-b. Sliding velocity is instantaneously increased, and a-b is calculated using the value of $\Delta\mu_{ss}$ as a result of the increase.

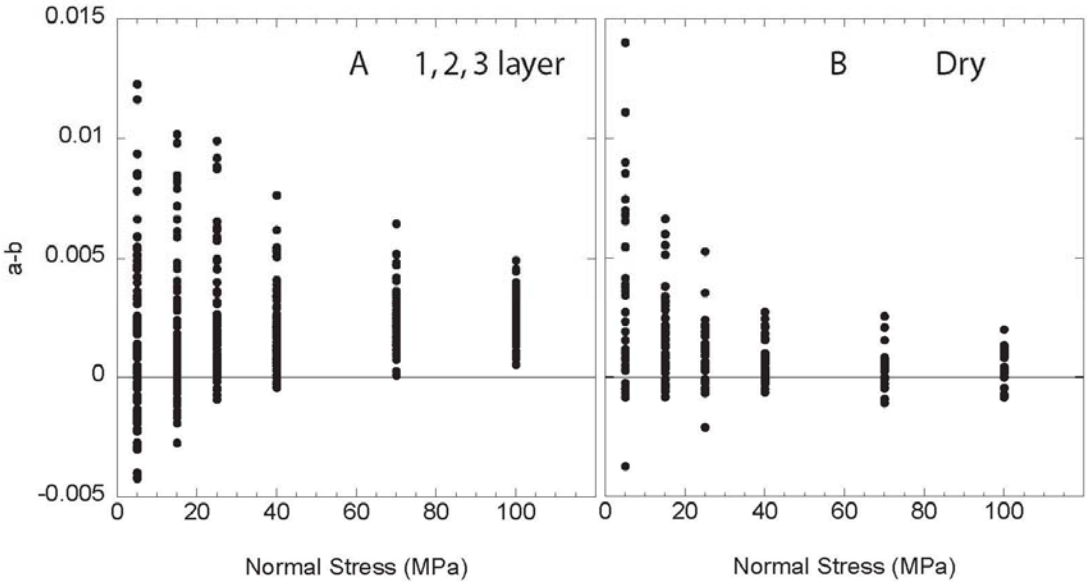

Figure 2-9. a-b values for all mixtures with increasing applied normal stress for A: 1, 2, and 3 layer samples (>4.5 wt% water) and B: dry samples (<4.5 wt% water).

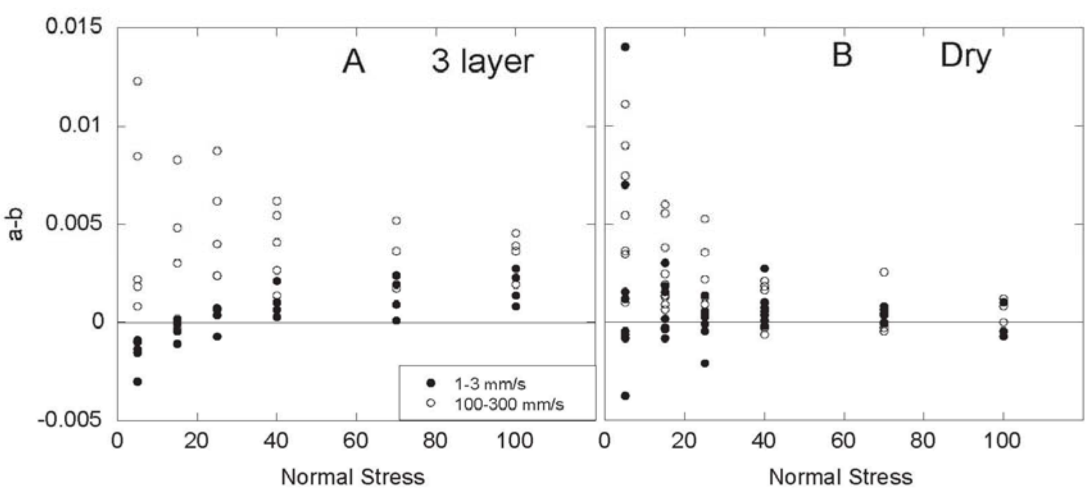

Figure 2-10. a-b for all mixtures with increasing normal stress comparing high and low sliding velocities for A: 3 layer and B: dry samples.

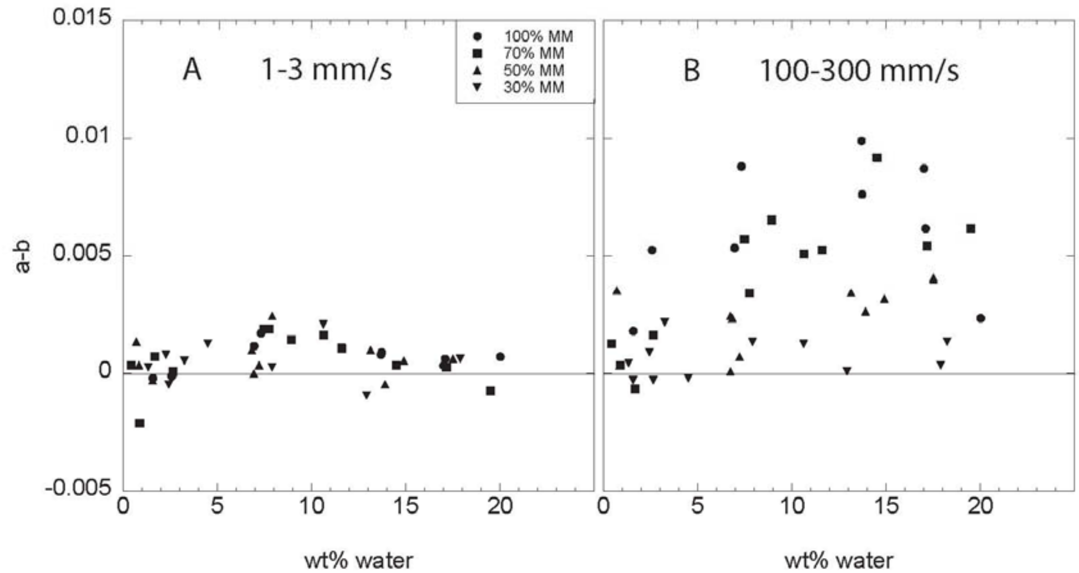

Figure 2-11. a-b plotted against increasing water content for all mixtures at a normal stress of 25 MPa comparing A: sliding velocity increase from 1-3 μm/s and B: sliding velocity increase from 100-300 μm/s.

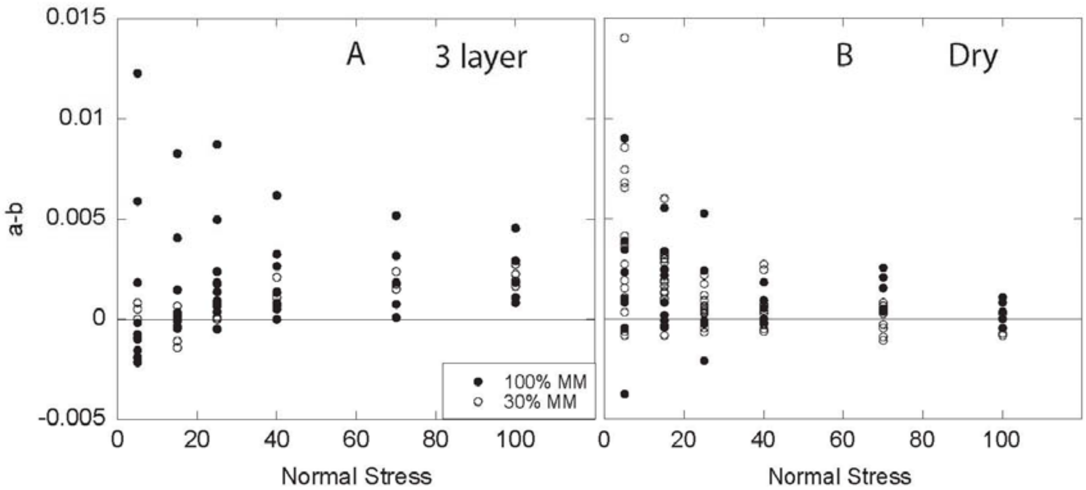

Figure 2-12. a-b values with increasing normal stress comparing high clay percentage (100% MM) and low clay percentage (30% MM) for A: 3 layer and B: dry samples.

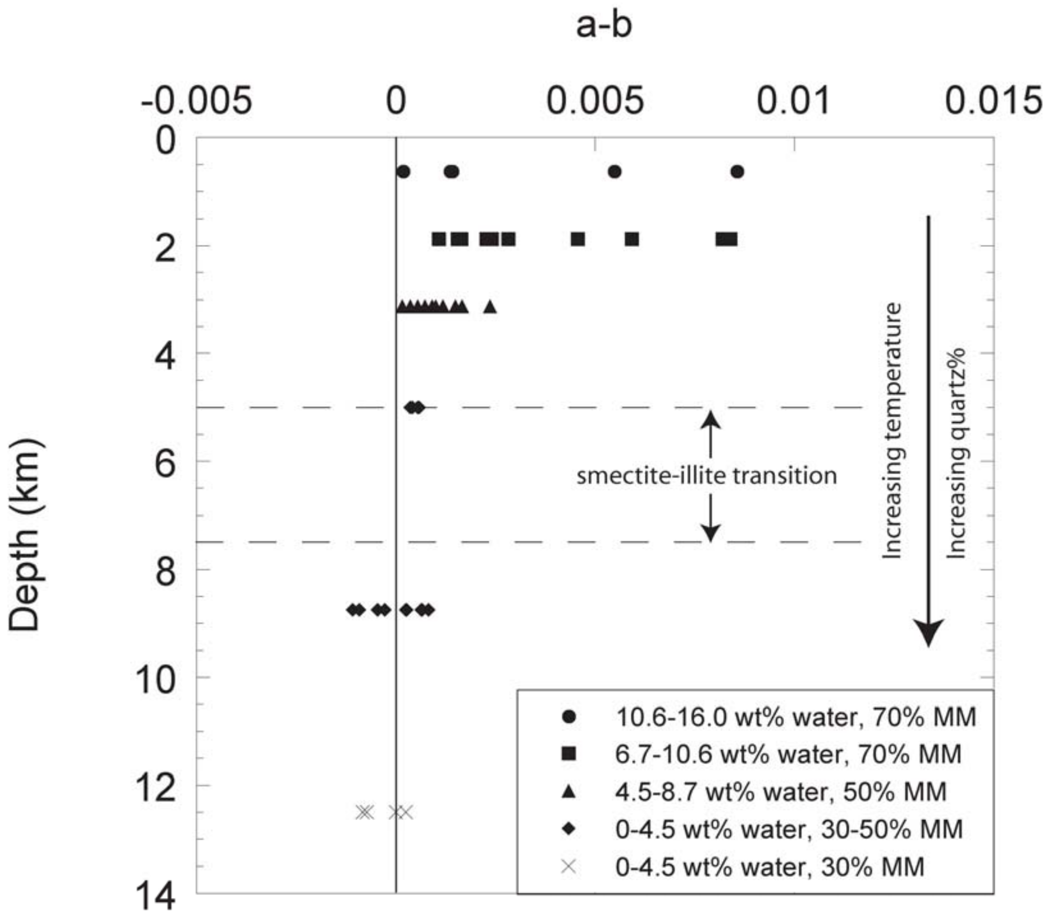

Figure 2-13. a-b values at conditions that may be expected at given depths in a subduction zone. Assumed effective pressure gradient is 8 MPa/km and assumed temperature gradient is 20-25°C/km.

Tables

Experiment	% Montmorillonite	σ_n (MPa)	Layer Thickness Under Load (μm)	Wt% Water	Water Arrangement
p1019	70	15,25,40	3865	0.4	dry
p699	50	5,15,24	3005	0.7	dry
p696	30	5,15,40	3420	0.8	dry
p706	70	5,15,24	3735	0.9	dry
p787	30	5,15,26	3225	1.3	dry
p709	100	40,70,100	2610	1.6	dry
p788	30	40,70,99	2945	1.7	dry
p1018	100	5,15	4215	1.7	dry
p790	50	40,70,99	3290	2.3	dry
p736	30	5,15,24	3505	2.4	dry
p695	30	40,70	2840	2.5	dry
p701	70	40,70,100	3100	2.6	dry
p711	100	5,15,24	3640	2.6	dry
p735	30	5,15,24	-	3.3	dry
p740	50	40,70,100	3285	4.5	1 layer
p733	50	6,15	2380	5.8	1 layer
p748	50	40,70,100	3155	6.7	1 layer
p747	50	5,15,25	2990	6.8	1 layer
p738	100	40,70,100	2510	6.9	1 layer
p784	50	5,15,24	3105	7.2	1 layer
p723	100	5,15,24	3825	7.3	1 layer
p730	70	5,15,24	3960	7.5	1 layer
p749	70	40,70,100	3045	7.7	1 layer
p751	30	5,15,24	3385	7.9	1 layer
p752	30	40,70,100	2625	7.9	1 layer
p1012	50	5,15,26	4220	8.2	1 layer
p1011	100	5,15	3450	8.7	1 layer
p783	70	5,15,25	3750	8.9	2 layer
p846	70	40,70,99	3070	9.0	2 layer
p775	70	40,70,99	3040	10.6	2 layer
p782	70	40,70,99	2945	11.6	2 layer
p1037	50	40, 70, 99	3310	11.8	2 layer
p1007	100 (<45 μm)	5,15,25	3405	12.6	2 layer
p780	30	5,15,25	3340	12.9	2 layer
p781	30	40,70,100	2765	13.1	2 layer
p1008	100 (<45 μm)	40,70,99	2290	13.3	2 layer
p776	100	5,15,24	3310	13.7	2 layer
p774	100	40,70,100	2620	13.7	2 layer
p777	50	5,15,25	3045	13.9	2 layer
p759	70	5,15,24	3860	14.5	2 layer
p734	50	5,15,24	3200	14.9	2 layer
p807	100	5,15,24	3410	17.0	3 layer

Experiment	% Montmorillonite	σ_n (MPa)	Layer Thickness Under Load (μm)	Wt% Water	Water Arrangement
p806	100	40,70,100	2485	17.1	3 layer
p805	70	41,71,101	2605	17.2	3 layer
p808	50	5,15,25	3780	17.5	3 layer
p809	50	40,70,99	2975	17.5	3 layer
p815	30	5,15,25	3290	17.9	3 layer
p816	30	40,70,99	2555	18.2	3 layer
p849	100	40,70,99	2155	19.4	3 layer
p814	70	5,15,25	3410	19.5	3 layer
p858	100	5,15,25	3130	20.0	3 layer
p859	100 (Na) (3 μm)	5,15,25	3290	0.5	dry
p861	100 (Na) (3 μm)	40,70,100	2530	0.5	dry
p857	100 (Na) (3 μm)	5,15,25	3575	5.5	1 layer
p850	100 (Na) (3 μm)	40,70,99	1950	5.6	1 layer
p886	100 (Na) (3 μm)	40,70,99	2165	12.1	2 layer
p874	100 (Na) (3 μm)	4,14,24	2930	13.0	2 layer

Table 2-1. Experiment Parameters. Clay is Ca-montmorillonite unless specified as Na. Mean grain size is 60 mm unless specified. Layer thickness under load taken at the lowest normal stress in experiment.

Chapter 3

FRICTIONAL AND HYDROLOGIC PROPERTIES OF CLAY-RICH FAULT GOUGE

Abstract

The slip behavior of major faults depends largely on the frictional and hydrologic properties of fault gouge. We report on laboratory experiments designed to measure the strength, friction constitutive properties, and permeability of a suite of saturated clay-rich fault gouges, including: a 50-50% mixture of montmorillonite-quartz, powdered illite shale, and powdered chlorite schist. Friction measurements indicate that clay-rich gouges are consistently weak, with steady-state coefficient of sliding friction < 0.35. The montmorillonite gouge (μ = 0.19-0.23) is consistently weaker than the illite and chlorite gouges (μ = 0.27-0.32). At effective normal stresses from 12 to 59 MPa, all gouges show velocity-strengthening frictional behavior in the sliding velocity range 0.5-300 μm/s. We suggest that the velocity-strengthening behavior we observe is related to saturation of real contact area, as documented by the friction parameter *b*, and is an inherent characteristic of non-cohesive, unlithified clay-rich gouge. Permeability normal to the gouge layer measured before, during, and after shear ranges from $8.3\text{x}10^{-21}$ m^2 to $3.6\text{x}10^{-16}$ m^2; permeability decreases dramatically with shearing, and to a lesser extent with increasing effective normal stress. The chlorite gouge is consistently more permeable than the montmorillonite and illite gouge, and maintains a higher permeability after shearing. Permeability reduction via shear is pronounced at shear strains < ~5, and is smaller at higher strain, suggesting that shear induced permeability reduction is linked to fabric development early in the deformation history. Our results imply that the potential for development of excess pore pressure in low permeability fault gouge depends on both clay mineralogy and shear strain.

Introduction

Clay minerals are abundant in mature fault zones, including both subduction megathrusts and continental transform faults like the San Andreas Fault, and their properties are considered a major control on macroscopic fault behavior in the brittle crust [*Vrolijk and van der Pluijm*, 1999; *Underwood*, 2007; *Numelin et al.,* 2007; *Ikari et al.,* 2007]. For example, the presence of weak clay minerals is hypothesized as one mechanism to explain the overall mechanical weakness of major plate boundary faults [e.g., *Wu et al.,* 1975; *Deng and Underwood*, 2001]. Increasing pressure and temperature with depth alter clay minerals via mineral transformation, dehydration, and mechanical consolidation, and the accompanying changes in fault zone lithification state and/or clay mineralogy have been proposed as an explanation for the upper transition from aseismic to seismic fault slip [*Marone and Scholz,* 1988; *Hyndman et al.,* 1997; *Moore and Saffer,* 2001; *Saffer and Marone*, 2003]. Fault strength and stability may also be affected by changes in effective normal stress and slip rate [e.g., *Scholz*, 1998]. In this respect, the hydrologic properties of clay-rich gouge have a significant effect on fault behavior, because low permeability gouges may act as a barrier to fluid flow, allowing the development of high pore pressures (and thus reduced effective stress) within the fault zone. In this study, we report on frictional and hydrologic properties of clay-rich fault gouge determined from confined biaxial shear experiments carried out within a newly constructed pressure vessel under true-triaxial conditions. We investigate the effects of clay mineralogy, fluid flow, sliding velocity, and effective normal stress.

Many previous studies have focused on characterizing the frictional behavior of clay-rich gouge, primarily to investigate basic frictional strength [*Wang and Mao,* 1979; *Logan and Rauenzahn,* 1987; *Morrow et al.,* 1992, 2000; *Saffer and Marone*, 2003; *Kopf and Brown,* 2003; *Bourlange et al.,* 2004; *Moore and Lockner,* 2004; *Ikari et al.,* 2007]. These studies have shown that clay contents as low as 15-20% significantly affect the strength of faults [*Shimamoto and Logan*, 1981] and that fault gouges dominated by clay minerals, especially montmorillonite, illite and chlorite, are frictionally weak (coefficient of friction μ: $0.03 < \mu < 0.50$) under a variety of conditions (normal stress, water content, and clay content). Less common are studies involving large strains that report detailed measurements of the transient and steady-state frictional response to perturbations in loading velocity or strain rate. Such measurements of rate- and state-friction are necessary to understand the stability of frictional sliding. Systematic study of frictional constitutive properties, particularly under conditions relevant to faulting in the upper seismogenic crust, is also needed to parameterize models of rupture nucleation and propagation, including those aiming to explain thermal pressurization and slow slip events [e.g., *Liu and Rice*, 2005; *Rice*, 2006, *Segall and Rice*, 2006; *Rubin*, 2008]. Previous experiments have shown that montmorillonite and illite-rich gouges are velocity-strengthening for both sub-saturated [*Saffer and Marone,* 2003; *Ikari et al.,* 2007] and saturated conditions [*Logan and Rauenzahn*, 1987; *Morrow et al.,* 1992; *Brown et al.,* 2003], but have been conducted over a limited suite of experimental conditions, and the friction constitutive properties have not been comprehensively or systematically investigated.

Fault gouge permeability is also an important parameter affecting fault mechanics, because low fault-normal permeability can facilitate the development of high pore fluid pressures from regional hydrologic processes, fault zone compaction, or thermal pressurization [*Hubbert and Rubey*, 1959; *Rice*, 1992; *Sleep and Blanpied*, 1992; *Wibberley and Shimamoto,* 2005; *Faulkner and Rutter,* 2001; *Noda and Shimamoto*, 2005; *Segall and Rice,* 2006; *Bizzarri and Cocco*, 2006a,b], leading to substantially reduced fault strength. For example, in subduction zones, low effective stress in the décollement as a result of high pore pressure is a likely control on the structure of accretionary prisms [*Davis et al*., 1983; *Byrne and Fisher,* 1990; *Le Pichon et al.,* 1993] and possibly the updip limit of seismicity [*Moore and Saffer,* 2001; *Wang and Hu*, 2006]. High pore pressures have also been offered as an explanation for the apparent anomalous weakness of the San Andreas Fault [*Byerlee*, 1990; *Hickman*, 1991; *Rice*, 1992], and recent results from the SAFOD borehole suggest that the fault acts as a barrier to regional scale fluid flow [e.g., *Wiersburg and Erzinger,* 2007, 2008]. Previous laboratory experiments have revealed that sediments composed of at least 50% clay minerals have very low permeabilities ($\leq 10^{-18}$ m^2). These include unsheared [*Kwon et al.,* 2004; *Yang and Aplin*, 2007], naturally sheared [*Faulkner and Rutter,* 2000, 2003], and both naturally sheared and laboratory sheared samples [*Morrow et al.,* 1984; *Zhang et al.,* 1999; *Zhang and Cox,* 2000; *Takahashi et al.,* 2007; *Crawford et al.,* 2008].

Although many studies have assessed frictional strength and stability of fault gouge, detailed and systematic investigations of frictional constitutive behavior under conditions relevant to seismogenic faulting in the upper crust are rare. Most existing studies consider only a limited range of experimental conditions (shear strain, effective normal stress, gouge composition, saturation, or sliding velocity). Furthermore, it remains a challenge to compare results from different experimental configurations (e.g. ring shear in which samples are small and slip velocity may vary across the sample; triaxial shear where the geometry is complex, cocking may occur, jacket stretching is an issue, and shear offset is limited; and direct shear where fluid access and stress conditions can be complex). In this paper we combine measurements of shear strength, frictional stability, and permeability for both sheared and unsheared clay-rich gouges under a wide range of effective normal stresses, shear strains, and sliding velocities. We obtain friction and permeability data simultaneously from in-situ measurements and explore coupled evolution of permeability and frictional behavior as a function of shear strain.

Experimental Methods

We test three clay-rich fault gouges, each containing a significant proportion of a different major clay mineral. Naturally occurring chlorite schist and illite shale are used as chlorite- and illite-rich gouges, respectively. Our montmorillonite-rich gouge is a synthetic 50-50 wt% mixture of commercially obtained Ca-montmorillonite (Ca-MM) and silt-sized quartz. The chlorite schist and illite shale were powdered in a disk mill and sieved to < 106 μm grain size. For the illite shale, X-ray diffraction (XRD) analysis shows that the bulk powder is primarily composed of illite (59%), quartz (23%), kaolinite/dickite (9%), and plagioclase (4%), with the modal percentages of individual clay minerals determined by XRD analysis of clay separates [*Saffer and Marone,* 2003]. The chlorite schist is composed of chlorite (46%), plagioclase (35%), quartz (12%), and illite (6%). Mean grain size of the Ca-MM is 60 μm with 80% of the grain diameters between 3 and 142 μm, determined by laser obscuration in a Malvern Mastersizer [e.g. *Ikari et al.,* 2007]. Scanning electron microscope (SEM) images of the materials we studied indicate that the montmorillonite/quartz mixture and illite shale have a similar grain size and grain size distribution, whereas the chlorite schist has a larger average grain size and a smaller proportion of small grains (Fig. 3-1A-C). Based on the SEM imaging, the large fragments in the chlorite gouge appear to be aggregates of smaller clay grains (Fig. 3-1D-F). Kaolinite gouge is not included in this study, but an extensive study of the strength and permeability of kaolinite-rich gouge was performed by *Crawford et al.* [2008].

A total of 15 experiments were conducted using a pressure vessel within a servo-controlled biaxial testing apparatus under true-triaxial conditions (Figure 3-2), [*Samuelson et al.,* 2006, 2007]. The pressure vessel is designed to accept a three-block double-direct shear assembly, which is sealed with rubber jackets and subjected to confining pressure (P_c). Two layers of sample fault gouge are sheared between roughened, steel forcing blocks. Sample gouge layers are constructed in a leveling jig to a uniform initial thickness of 4 mm (for 12-25 MPa effective normal stress) or 5 mm (for 42-59 MPa effective normal stress), which compacts to ~1.5-2.5 mm after shear under applied normal stress. Sample contact area is 30.78 cm^2 (for 12-25 MPa effective normal stress) or 32.94 cm^2 (for 42-59 MPa effective normal stress).

Normal stress on the gouge layer is applied by a combination of the confining pressure P_c and a piston that enters the vessel through a dynamic seal (Fig. 3-2B-C). The applied load and P_c are independently controlled via a fast-acting hydraulic servo mechanism. The gouge layers are sheared by driving the center block with a vertical piston and hydraulic ram. Normal and shear loads are measured to a precision of +/- 0.1 kN. Confining fluid is food-grade heat transfer oil (XCELTHERM 600, Radco Industries) and pore fluid is deionized water in order to minimize the effects of water chemistry changes due to buffering from interaction with the gouge [e.g, *Faulkner and Rutter,* 2000]. Effective normal stress is held constant and shear is imposed by controlling the vertical load point displacement external to the pressure vessel. Displacement at both the vertical and horizontal load points is measured to a precision of +/- 0.02 μm. True shear displacement and sliding velocity at the layer boundaries are calculated after accounting for apparatus stiffness [see *Ikari et al.*, 2007] and compression of the rubber jackets. The effect of seal friction on the pistons that enter the pressure vessel contributes less than 1.5% of the measured shear stress values.

Pore fluid access is via NPT fittings in the pressure vessel and forcing blocks, and flexible tubing allows displacement parallel and normal to the gouge layers (Figure 3-2). The inner diameter of the tubing is 1.75 mm. Each forcing block has internal conduits and distribution channels that supply pore fluid to sintered stainless steel frits in contact with the layers, which provide even distribution of fluid over the entire area of the layer. Filter paper between the sample and the frits on the downstream end prevents the frit permeability from being reduced by clogging with fine particles. The system is capable of maintaining two independent pore pressures. We refer to the fluid pressure of the center block and the center block side of each layer as Pp_a, and the side blocks as Pp_b. For the experiments described in this paper, fluid flow is directed normal to the layers and to the shear direction. Each of the three pressures, P_c, Pp_a, and Pp_b are independently servo-controlled and can operate in pressure or flow (displacement) control. All three pressures are measured or controlled to +/- 7 kPa, and fluid volume is measured or controlled to +/- 1.6×10^{-10} m^3. In the case of the pore pressure, displacement control is used to apply either a constant flow rate or closed boundary condition, and pressure control is used to apply a constant pressure boundary condition.

Each of our experiments consists of three stages, which yield both frictional and hydrologic data. Initially, we saturated all samples at low normal stress (< 15 MPa hydrostatic pressure) prior to applying the target effective normal stress to ensure that the layers were uniformly saturated. Stage 1 consists of measuring the layer-perpendicular permeability prior to shearing by applying a constant fluid pressure gradient (0.5–6 MPa) across the sample and conducting a steady state flow-through test. Stage 2 consists of shearing at a constant pore pressure of 5 MPa (Figure 3A). During shear, a velocity-stepping test is conducted to measure frictional constitutive properties. In Stage 3, after termination of shearing, a pore pressure gradient is again imposed in order to measure post-shear permeability in the same manner as Stage 1. Shear stress is not removed during the permeability measurement, but relaxes to a residual value under a condition of zero shear displacement rate, in a similar manner to that observed in conventional slide-hold-slide friction tests (inset, Figure 3-3B). In addition, we conducted trial experiments in which the fluid pressure gradient was applied during shear. These dynamic permeability measurements yield very similar results to those we obtained during Stage 3; however for consistency between experiments and to minimize the affect of shear during the flow measurements, we report only permeability values under the quasi-static conditions (as in Stages 1 and 3).

We also conducted three experiments in which permeability was measured as a function of shear displacement (Figure 3-3B). These experiments were conducted once for each gouge composition at an effective stress of 32 MPa. In these experiments, shearing was paused and permeability was measured at load point displacements of ~3, 5, 7, and 12 mm in addition to the pre- and post- shear measurements using the same flow-through technique described above. Similar to the post-shear permeability measurements described above (Stage 2), shear stress relaxes via creep during the permeability measurements. Table 1 lists the experimental parameters for all experiments in this study.

Friction Measurements

During shear (Stage 2), pore pressure at the upstream end of the sample (Pp_a) was held constant at 5 MPa, while at the downstream end (controlled by Pp_b) a no-flow condition was imposed in order to document any overpressure generated during shear and evaluate our control of Pp in the layer. The samples were sheared at a constant velocity of 5 or 11 μm/s until steady state shear strength was achieved (Figure 3A). The velocity was then increased step-wise from 0.5-300 μm/s in velocity-stepping tests [e.g. *Marone*, 1998] (Figure 3-4). Shear displacement during each velocity step was 400 or 800 μm. Maximum shear displacement for these layers was 36 mm; shearing was typically terminated at displacements of ~20 mm. Due to differences in initial layer thickness and total displacement, maximum shear strain ranged between 4 and 48. In some experiments, we observed a slight increase in pore pressure (as measured in Pp_b) as a result of shearing in the low permeability samples. These pore pressure transients represent a maximum of 3% of the total effective stress, and are typically << 1%.

The steady-state shear stress τ was measured prior to the initiation of the velocity-stepping test. The coefficient of sliding friction μ was then calculated as:

$$\tau = \mu\sigma_n' + c \tag{1}$$

[*Handin*, 1969; *Byerlee*, 1978] where *c* is cohesion, and the effective normal stress σ_n' is the difference between the applied normal stress σ_n and the pore fluid pressure:

$$\sigma_n' = \sigma_n - Pp \tag{2}$$

The pore pressure *Pp* is taken as the average of the pore pressure at the drained and undrained boundaries. Maximum error in effective normal stress due to the differing boundary conditions described above is < 1.3%. The cohesion *c* is assumed to be negligible for the unconsolidated gouge used in our experiments.

We quantify frictional stability using the friction rate parameter *a-b*; defined as:

$$a - b = \frac{\Delta\mu_{ss}}{\ln\left(V / V_o \right)} \tag{3}$$

where $\Delta\mu_{ss}$ is the change in the steady state coefficient of friction upon an instantaneous change in sliding velocity from V_o to *V* [e.g. *Marone*, 1998]. Positive *a-b* values indicate velocity-strengthening behavior, whereas negative *a-b* values indicate velocity-weakening behavior. Velocity-weakening is a prerequisite for stick-slip behavior which is associated with earthquake nucleation [*Dieterich and Kilgore,* 1996; *Marone*, 1998; *Scholz*, 2002]. Equation (3) represents the steady-state form of *Dieterich's* [1979, 1981] constitutive law describing rate- and state-dependent frictional behavior:

$$\mu = \mu_o + a\ln\left(\frac{V}{V_o}\right) + b\ln\left(\frac{V_o\Theta}{D_c}\right) \tag{4}$$

$$\frac{d\Theta}{dt} = 1 - \frac{V\Theta}{D_c} \tag{5}$$

where *a* and *b* are empirically derived constants (unitless), Θ is the state variable (units of time), and D_c is the critical slip distance. The state variable is inferred to be the average lifetime of contact points that control friction, and the critical slip distance is the displacement over which those contacts are renewed. Under steady state sliding conditions, the average time that a contact exists is constant, reducing the left side of Equation (5) to zero, and substitution of the state variable at steady state Θ_{ss} into (4) yields Equation (3).

To obtain the values of the constitutive parameters *a, b,* and D_c, we model the velocity-step data following *Saffer and Marone* [2003]. The interaction of the sample with its elastic surroundings is incorporated according to the equation:

$$\frac{d\mu}{dt} = K(V_{lp} - V) \tag{6}$$

where K is the stiffness of the fault surroundings (in this case the testing apparatus and sample blocks) normalized by normal stress ($K = \sim 3\text{x}10^{-3}\ \mu\text{m}^{-1}$ at 25 MPa normal stress), V_{lp} is the load point velocity, and V is the true slip velocity. We then solve Equations (5) and (6) simultaneously, with Equation (1) as a constraint, using a fifth-order Runge-Kutta method. The constitutive parameters are then obtained as solutions to a non-linear inverse problem using an iterative least-squares method [*Reinen and Weeks*, 1993; *Blanpied et al.,* 1998; *Saffer and Marone*, 2003] (Figure 3-5).

The pore pressure in Equation (2) used to calculate the shear stress is an average of the pore pressure at the drained (Pp_a) and undrained (Pp_b) ends of the sample. The measurement of pore pressure at the undrained sample boundary also provides a method for quantifying the potential effects of pore pressure transients on our reported values of frictional strength (μ) and constitutive parameters (*a-b, a,* and *b).* To quantify the uncertainty associated with this effect, we report upper and lower bounds on all frictional properties, computed using the pore pressure at the drained boundary and at the undrained boundary of the layer as minima and maxima on *Pp* in Equation (2). The error is extremely small; data and model inversions for friction calculated using average pore pressure (reported in the results section and Table 3-2), pore pressure at the undrained boundary, and pore pressure at the drained boundary are all within 3.5% (Figure 3-5). The example shown in Figure 3-5 is from the velocity step that had largest variation between pore pressure boundary conditions in any of our experiments. This indicates that our constitutive modeling results are insensitive to transient pore pressure effects caused by differing sample boundary conditions, unless rapid changes in pore pressure within the gouge layer are not accurately tracked by the measurement of Pp_b due to the finite volume and compliance of the "downstream" fluid reservoir that causes a dampening and delay of the signal at the measurement point. We discuss this possibility in detail below.

Permeability Measurements

In each individual flow-through permeability test (Stages 1 and 3), we imposed a constant fluid pressure normal to the layer, and calculated permeability from the resulting flow rate across the sample after reaching steady state, (Figure 6) according to Darcy's law:

$$Q = \frac{kA}{\eta}\frac{dPp}{dx} \tag{7}$$

where Q is the volumetric flow rate (m^3 s^{-1}), k is the sample permeability (m^2), A is the cross-sectional area of the sample (m^2), η is the viscosity of water (Pa-s), dPp is the imposed fluid pressure difference across the sample, and dx is the layer thickness. We calculate permeability, k, using η = 1.12x10^{-3} Pa-s and A = 0.005 m^2 (this is the area of the permeable frit, which is slightly smaller than the area of the forcing blocks). Two volumetric flow rates are measured, one from the sample inlet (Pp_a) and one from the sample outlet (Pp_b), (Figure 10a). We define Q as the average flow rate and consider the system to be at steady-state only when $Q_a = Q_b$ to within < 5%.

Results

Frictional Strength

We measured overall shear strength of the fault gouge (τ) and coefficient of sliding friction (μ) after attaining a residual, or steady state, shear strength (Figure 3-3). The stress-strain curves typically exhibit a peak shear stress and rollover to a residual value at shear strains of ≤ 5. Montmorillonite gouges show a prominent stress peak and decay, whereas chlorite and illite gouges show a gradual rollover without a strong peak. All gouge strength and coefficient of friction values are low (Figure 3-7), with $\mu < 0.35$. Chlorite and illite gouge are nearly identical in strength, with μ ranging from 0.27 to 0.32. However, montmorillonite gouge is significantly weaker than illite and chlorite gouge, with $\mu = 0.19$-0.23. There is no clear dependence of μ on effective normal stress (Figure 3-7).

Frictional Constitutive Properties

All three of the gouges exhibit velocity-strengthening frictional behavior (Figure 3-8; Table 3-2). Values of a-b for illite gouge range from ~0.003 to 0.010; a-b ranges from ~0.001 to 0.006 for montmorillonite gouge and ~0.003 to 0.010 for chlorite gouge (Figure 3-8). We find that a-b is independent of effective normal stress in all cases, but exhibits a positive dependence on sliding velocity with values increasing by ~0.002 per order of magnitude increase in upstep velocity for all three gouges (Figures 3-8, 3-9). In all cases, we find that $a > b$ (Figures 3-10, 3-11; Table 3-2). Values of a cluster between 0.010 and 0.001 and are generally insensitive to effective normal stress. Values of a for montmorillonite gouge are generally lower (most are < 0.005) than those for illite and chlorite gouges. As is the case for (a-b), values of a for all three gouge types exhibit a positive dependence on sliding velocity (Figure 3-11). In contrast, values of b exhibit varying amounts of scatter for each gouge type, and most values cluster near 0 (Figure 3-10). These values are generally independent of normal stress and sliding velocity, but with some exceptions the most negative values of b are associated with low effective normal stress and high sliding velocity. The velocity dependence of a-b results from positive rate dependence of a and a negative or neutral rate dependence of b (Figures 3-9, 3-11). The critical slip distance D_c exhibits substantial scatter but is generally on the order of 10s of microns, and is insensitive to both effective normal stress and sliding velocity (Table 3-2). It should be noted that for values of b approaching 0, D_c is undefined and thus uncertainty is large.

Dilation

We measured dilation of the gouge layer in response to step increases in sliding velocity, and report it using the parameter α:

$$\alpha = \frac{\Delta h}{\ln\left(V / V_o \right)} \tag{9}$$

where Δh is the change in layer thickness in response to a velocity change from V to Vo [*Marone and Kilgore,* 1993]. Dilatancy of fault gouge has important implications for the evolution of macroscopic fault frictional properties because: (1) it may cause strengthening by depressurization of pore fluid [*Segall and Rice*, 1995; *Samuelson et al.,* 2007], (2) it tends to counteract thermal pressurization, and (3) it may enhance shear localization [*Marone and Kilgore,* 1993]. Furthermore, changes in dilatancy rate have been linked to velocity-strengthening behavior [*Marone et al.,* 1990]. We observe consistently positive values of α for all experimental conditions in this study (0.2-1.9 μm) (Figure 3-12). No discernible trend in α is observed with sliding velocity.

Permeability

The chlorite gouge exhibits the highest permeability over the entire range of effective normal stresses, both before and after shearing, with permeability ranging from $1.4x10^{-17}$ m^2 to $3.6x10^{-16}$ m^2 before shear, and $7.9x10^{-19}$ m^2 to $6.0x10^{-17}$ m^2 after shear (shear strains of 7-23). Montmorillonite and illite gouge permeabilities are lower than that of chlorite, however before shearing montmorillonite permeability is similar to that of chlorite and illite permeability is significantly lower. After shear, both montmorillonite and illite gouges are significantly less permeable than the chlorite gouge (Figure 3-13); the permeability of the montmorillonite gouge ranges from $1.1x10^{-17}$ m^2 to $2.6x10^{-16}$ m^2 before shear, and decreases to $1.7x10^{-20}$ m^2 to $2.5x10^{-19}$ m^2 after shear. For illite gouge, permeability ranges from $7.5x10^{-20}$ m^2 to $5.0x10^{-17}$ m^2 before shear, and decreases to $8.3x10^{-21}$ m^2 to $4.4x10^{-19}$ m^2 after shear. For the montmorillonite and chlorite gouges (both before and after shear), increased effective normal stress reduces permeability only up to ~35 MPa, above which *k* is independent of effective normal stress. In contrast, permeability of illite gouge decreases, with some scatter, over the entire range of effective normal stress.

As expected, pre-shear permeability is consistently higher than post-shear permeability. However, the effect of shear on permeability differs between gouges (Figure 3-14). Shear induced permeability reduction is greatest early in the strain history for all three materials, dropping rapidly up to shear strains of ~5 before approaching a steady value at higher strains. However, the montmorillonite permeability decreases by a factor of ~1000, whereas the permeability of illite gouge is only reduced by a factor of ~10 and chlorite gouge by a factor of ~20.

Discussion

Comparison to Previous Data

Our results are consistent with existing friction and hydrologic data, but are more comprehensive and systematic than previous studies. Our steady-state friction values for illite shale and montmorillonite-quartz (μ = 0.27-0.32 and μ = 0.19-0.23, respectively) are significantly lower than previously reported values obtained from experiments run under understaturated conditions (μ = 0.50-0.60 and μ = 0.27-0.50, respectively), [*Saffer and Marone,* 2003; *Ikari et al.,* 2007]. This is consistent with results from our previous work [*Ikari et al.,* 2007] and with other data [*Morrow et al.*, 2000; *Moore and Lockner*, 2004] showing that water-saturation of phyllosilicate minerals reduces frictional strength by as much as 60%.

For chlorite gouge, our observed friction values of μ = 0.27-0.32 are similar to a reported value of μ = ~0.38 for saturated, powdered chlorite schist at 100 MPa effective normal stress [*Moore and Lockner* 2004], especially after accounting for jacketing and apparatus effects that tend to cause strain hardening in the triaxial geometry. *Logan and Rauenzahn* [1987] reported a friction value of ~0.30 for a saturated 50-50% montmorillonite-quartz mixture, similar to our upper value of 0.23 for gouge of the same composition. For pure montmorillonite gouge, the values reported by *Morrow et al.* [1992] (0.18 to 0.29) are significantly higher than values of 0.03-0.16 reported for pure montmorillonite by other authors [*Logan and Rauenzahn,* 1987; *Kopf and Brown,* 2003; *Ikari et al.,* 2007]. Part of this discrepancy is likely related to differences in testing apparatus. *Morrow et al.* [1992] obtained friction coefficients of ~0.38 to 0.48 for a powdered illite shale and ~0.18 to 0.29 for pure montmorillonite. The high end of their range is likely due to considerable strain hardening, as noted above, however the lower end of their range is similar to our results. We note that our friction values for 50-50% montmorillonite-quartz mixtures are comparable to those of *Morrow et al.* [1992] (0.18 to 0.29) for pure montmorillonite gouge.

Brown et al. [2003] and *Kopf and Brown* [2003] report results from seawater-saturated friction experiments performed on both mineral standards and natural clay-rich samples from the Nankai (SW Japan) and Barbados subduction thrusts. Their reported friction values for pure chlorite, illite, and smectite gouges are lower than ours; one likely explanation for this difference is that their gouges were monomineralic, whereas our samples contained ~50 wt% quartz [*Logan and Rauenzahn,* 1987; *Saffer and Marone,* 2003; *Ikari et al.,* 2007]. Moreover, the work by *Kopf and Brown* [2003] indicates a negligible dependence of friction on effective normal stress for chlorite and illite, and significantly lower strength of smectite, both of which are highly consistent with our results. *Kopf and Brown* [2003] report friction values in the range of $\mu = 0.10\text{-}0.30$ for natural samples from Nankai and Barbados, and *Brown et al.* [2003] report similarly low friction values ($\mu = 0.17\text{-}0.27$) for samples from Nankai with comparable clay contents to our samples. This suggests that our sample gouges can be considered suitable analogs to those from natural fault zones.

Our observation of strong velocity-strengthening behavior for these three gouges also agrees with results from a small number of existing studies of rate-dependent frictional behavior of clay-rich gouges. *Saffer and Marone* [2003] and *Ikari et al.* [2007] found that undersaturated montmorillonite gouges can range from highly velocity-strengthening to slightly velocity-weakening. *Ikari et al.* [2007] further showed that increased hydration state of montmorillonite tends to inhibit frictional instability, which is consistent with the strong velocity-strengthening of the saturated montmorillonite-quartz gouge that we report here. *Logan and Rauenzahn* [1987] also report (*a-b)* values of 0.0010 to 0.0100 for gouges containing 25% to 75% montmorillonite. Although they did not report (*a-b)* values, *Brown et al.* [2003] observed velocity-strengthening behavior in their smectite, illite, and chlorite gouges. *Morrow et al.* [1992] and *Saffer and*

Marone [2003] both report consistent velocity-strengthening for illite shale. *Morrow et al.* report an *(a-b)* of ~0.0050 for a velocity increase from 0.01 to 1 μm/s, which is comparable to our observed values for a 1 to 3 μm/s velocity step. *Saffer and Marone* [2003] report *(a-b)* values of ~0.0010 to 0.0040, lower than our reported values (0.0037 to 0.0096); however, the gouges in this study were saturated while those in *Saffer and Marone* [2003] were not.

It is likely that the higher *a-b* values in this study are the result of fully saturated clays and combined clay-granular behavior. However, it is also possible that transient pore pressure reduction due to gouge dilation may contribute to velocity strengthening, based on our consistent observation of dilation with velocity step increases. Dilation values of 0.2-1.9 μm are consistent with previous measurements of dilation in granular fault gouge at shear strains > ~5 [*Marone and Kilgore*, 1993]. Although we cannot rule out transient reductions in pore pressure within the layers locally at the microscale, we believe these effects are small because of our data demonstrating negligible changes in the (undrained) downstream pore pressure Pp_b (e.g., Figure 3-5).

Our permeability measurements are also compatible with previous measurements for clay-rich sediments and sheared gouges. For a 50-50% montmorillonite-quartz mixture, *Takahashi et al.* [2007] report a pre-shear permeability of 2.9×10^{-19} m^2, and post-shear permeability of 2.7×10^{-21} m^2 at an effective normal stress of 75 MPa and a shear strain of ~3. At a slightly lower effective normal stress of 58 MPa, we observe very similar values of 9.3×10^{-18} m^2 pre-shear, and 1.7×10^{-20} m^2 at a shear strain of 4.0. *Faulkner and Rutter* [2003] reported permeabilities for intact gouge from the Carboneras fault, which contained illite and chlorite, but no smectite. At room temperature and an effective stress range of 25-75 MPa, they observe permeabilities of ~6×10^{-21} to 8×10^{-20} m^2, which are similar to values we report for illite shale at effective normal stresses of 25-58 MPa. *Faulkner and Rutter* [2003] also observed a trend of decreasing permeability with increasing effective stress. *Kwon et al.* [2004] observed very low permeability in intact illite shale at effective stresses ranging from 2-10.5 MPa ($2x10^{-20}$ m^2 to $3x10^{-22}$ m^2). These values are similar to values we observe in powdered illite shale at high effective normal stress ($5.8x10^{-20}$ m^2); we attribute the higher permeability we observe at lower effective normal stress to the non-cohesive nature of our samples.

Morrow et al. [1984] report permeabilities for granular samples of pure montmorillonite, pure illite, and a chlorite-rich fault rock. The highest permeability values they report are ~$7x10^{-21}$ m^2 for montmorillonite gouge, ~$6x10^{-20}$ m^2 for illite gouge, and ~$3x10^{-19}$ m^2 for chlorite gouge in triaxial compression with confining pressures of 5 to 10 MPa. These values are significantly lower than the permeability we observe, however we attribute this to the purity of the montmorillonite and illite samples in their experiments. *Morrow et al.* [1984] also observed permeability reduction as a result of shear, in general agreement with our observations. However, the magnitude of permeability reduction was significantly smaller for illite (~0.5 orders of magnitude) and montmorillonite (~0.2 orders of magnitude) than in our experiments, which may be the result of lower strains (≤ 10) in their experiments compared to ours.

Mechanisms of Observed Hydromechanical Behavior

The observed frictional behavior for all the gouges in this study indicates that under the conditions we investigated, faults with these clay compositions are frictionally weak and are not candidates for seismic nucleation. The fact that clay minerals are common in major active fault zones, combined with the observation that clay minerals generally slide stably at normal stress conditions relevant to typical depths of earthquake nucleation, suggests that factors other than clay composition are likely to control the updip limit of the seismogenic zone. The consistent velocity-strengthening nature of clay-rich fault gouges may be attributed to the characteristic velocity-strengthening behavior of granular, non-cohesive gouge [e.g., *Marone and Scholz*, 1988]. This behavior may be accentuated by dilation-driven transient depressurization of pore fluid with increased sliding velocity, which would increase the effective normal stress.

The purely frictional component of gouge behavior may be analyzed within the context of nominally room-dry experimental work by detailed examination of individual frictional constitutive parameters *a* and *b*. The contribution of transient pore fluid depressurization to the velocity-strengthening behavior of fault gouge is only manifested in fluid-saturated gouge; under these conditions in clay-rich gouge, decoupling of pure frictional effects from poroelastic effects is not straightforward, because water likely affects both the surface properties of clays (and thus frictional behavior of grain contacts) and also mediates transient changes in shear strength via its effects on effective normal stress [e.g., *Moore and Lockner*, 2004; *Samuelson et al*., 2006, 2007]. However, because both frictional and poroelastic mechanisms act to enhance velocity-strengthening, detailed quantification of their relative contributions is probably less important than characterizing their combined net effect on macroscopic fault behavior. However, it is important to note that transient pore fluid effects are highly dependent on gouge permeability, which implies that gouge permeability may have a significant impact on frictional stability [e.g., *Segall and Rice*, 1995; *Samuelson et al*., 2006, 2007].

Frictional Behavior

The values of the friction constitutive parameter *a* we observe are similar to those observed by *Saffer and Marone* [2003] and *Ikari et al*. [2007] for undersaturated montmorillonite-rich and illite-rich gouges. Thus, the higher *a-b* values observed in this study are attributable to lower values of *b*. Previous studies have interpreted the physical significance of *b* to be a measure of frictional strength change due to evolution of contact surfaces [*Dieterich*, 1979, 1981; *Scholz*, 2002]. At low velocities, values of *b* approaching 0 are consistent with the idea of "contact saturation" in which mineral surfaces are in complete contact, and therefore the real area of contact does not evolve when the velocity is perturbed [*Saffer and Marone*, 2003]. This is most likely to occur in phyllosilicates because of (1) their characteristic platy structure, (2) their high grain compressibility, and (3) the increased tendency of phyllosilicate gouges to readily compact and align, especially when saturated with fluid.

Negative values of b, or in some cases b_2 where a second state variable is required, have been reported previously for gabbro at room temperature [*Marone and Cox*, 1994] and for granular quartz and granite at elevated temperature [*Karner et al.,* 1997; *Blanpied et al.,* 1998]. Values of b approaching 0 have been observed in frictional studies involving other weak minerals such as serpentine [*Reinen et al.,* 1991] and talc [*Moore and Lockner,* 2008]. Additionally, *Chester and Higgs* [1992] found that a value of $b = 0$ provided the best fit for modeling data from high temperature ultrafine quartz experiments in which dissolution-precipitation mechanisms are active. Microstructural observations from the *Chester and Higgs* [1992] experiments indicated almost a complete loss of porosity, suggesting contact saturation.

Contact saturation would also lead to normal stress-independent shear strength, as observed by *Saffer and Marone* [2003], who noted a coincidence of b values near zero, and the onset of decreasing pressure-dependence of shear strength at effective normal stresses > ~40 MPa. Our results are consistent with this hypothesis, in that we observe both low dependence of shear stress on effective normal stress, and b values near zero throughout the range of effective normal stress we investigated. The occurrence of low normal stress-dependent shear strength (or, alternatively, rollover in friction envelope) at low effective normal stress in our study is similar to that observed by *Saffer and Marone* [2003] and *Ikari et al.,* [2007]. At high velocities, occurrence of $b = 0$ and the negative rate dependence of b may occur because contact lifetime is sufficiently small that any time-dependent strengthening effects are negligible.

Our constitutive modeling also indicates some negative values of *b,* which are more difficult to interpret (Figure 3-5). The fact that values of both *a* and D_c for velocity steps with negative *b* are similar to those with a positive *b* seems to validate the existence of significantly negative values of *b*. However, if we interpret a value of $b = 0$ to signify saturation of contact area, then negative values of *b* (evolution to a higher shear strength) cannot be associated with a further increase in contact area. In fact, our observation of dilatancy during velocity steps would seem to indicate the opposite. We propose two possible explanations that may cause the observation of negative values of *b*, one a pure mechanical effect, the second requiring operation of pore fluid. The first (mechanical) explanation is that during a velocity increase, shear stress may transiently increase due to a dilatant mechanism unrelated to porosity. This might be accomplished by macroscopic gouge layer deformation via the formation of small-scale "kink" structures [*Mares and Kronenberg,* 1993]. In this case, the aggregate expansion from either kink formation or crystal deformation would thus be observable as dilation of the gouge layer, and would occur over the characteristic displacement D_c. We caution that this mechanism for a negative *b*, while plausible, is highly speculative. The second explanation for negative *b* requires transient changes in pore fluid pressure, which we explore in the next section.

Effects of Transient Pore Pressure on Friction

In fluid saturated fault gouge, transient changes in pore fluid pressure may have a significant effect on friction if the layer is unable to efficiently drain. This is likely in sheared, clay-rich fault gouge in which the permeability is extremely low [e.g., *Segall and Rice*, 1995]. Immediately following a velocity step, we consistently observe positive dilation, indicating an increase in pore volume. This should result in a local reduction of pore fluid pressure, which would in turn cause a local increase in effective normal stress. Normal stress-stepping experiments [*Linker and Dieterich*, 1992; *Richardson and Marone*, 1999; *Boettcher and Marone*, 2004; *Hong and Marone,* 2005] have shown that the shape of the frictional response to a normal stress step is described by a linear increase, followed by a positive logarithmic decay to a steady-state value. Qualitatively this is the same as our observed frictional response to a velocity step when b is negative (e.g. Figure 3-5).

Transient decreases in pore pressure will be observable as an increase in shear stress if pore fluid is unable to diffuse into the layer over the duration of the velocity steps, which range from 2.67 - 800 s in our study. The time necessary for fluid pressure to re-equilibrate after a perturbation can be estimated from a characteristic diffusion time t:

$$t = \frac{h^2 S}{2\kappa} \tag{10}$$

Where h is the layer thickness, and (κ/S) is the hydraulic diffusivity (m^2/s), where κ is hydraulic conductivity (m/s) and S is specific storage (m^{-1}). Specific storage is given by: $S = \gamma_w(\beta_p + \varphi\beta_w)$, where γ_w is the specific weight of water (N/m^3), β_p is the compressibility of the porous matrix (m^2/N), β_w is the compressibility of water (m^2/N), and φ is fractional porosity. In Equation (10), we use the full layer thickness, which represents the maximum distance between a potential location of pore fluid perturbation and the controlling reservoir. Assuming that water is much less compressible than the clay gouge and that the porosity is low, the term $\varphi\beta_w$ can be neglected. Substituting into Equation (10) and rewriting κ in terms of intrinsic permeability and fluid viscosity yields an expression for the characteristic diffusion time:

$$t = \frac{h^2 \beta_p \eta}{2k} \tag{11}$$

Assuming that the compressibility of our gouge layers falls within the range of plastic clay (2.1x10^{-6} m^2/N) and medium hard clay (6.9x10^{-8} m^2/N) [*Domenico and Mifflin,* 1965], the calculated characteristic diffusion times of most of our gouge layers is longer than the duration of the longest velocity step (800 s), especially for gouges with permeability less than $1x10^{-18}$ m^2 (montmorillonite, illite). However, our observation of minimal excess pore pressure development downstream (Pp_b) suggest that this is a small effect if present at all, likely because the actively dilating zone within the gouge layer is very thin, such that the pathlength for fluid pressure diffusion in Equation (11) is considerably smaller than our assumed value of *h*. Nevertheless, we cannot rule out the possibility that transient depressurization of pore fluid may contribute to the observed velocity-strengthening behavior.

Although transient pore pressure reduction may contribute to the observed velocity-strengthening behavior, we emphasize that it is unlikely to act as the sole cause of low to negative values of *b*. For instance, high permeability gouge such as chlorite at 12 MPa effective normal stress has a calculated characteristic diffusion time of 0.2–5.6 s. This is sufficient time for any pore pressure deficit to be replenished at all except possibly the highest slip velocity, however *b* is negative over the entire velocity range. Additionally, in extremely low permeability gouge such as montmorillonite, at effective normal stresses of > 25 MPa, positive values of *b* are still observed despite the fact that equilibration times determined from Equation (11) are considerably longer than the duration of the velocity step. These observations indicate that the strongly positive rate dependence of clay-rich gouge is primarily a result of inherent frictional characteristics of the gouge, and that transient fluid depressurization probably plays a secondary role. Based on our data, we cannot definitively determine the relative importance of these processes, but because the two effects are complementary rather than competing, we consider their combined net effect on shear strength (as measured in our experiments) to be the most relevant to macroscopic fault behavior. If transient depressurization of pore fluid is in fact a significant contributor to velocity-strengthening behavior, then gouge permeability likely plays an important role in fault stability. We anticipate that its effect will be amplified if the pore pressure is high relative to the effective normal stress.

Permeability and Pore Pressure

The low permeability observed in clay-rich fault gouge, especially in montmorillonite- and illite- rich gouge, is not surprising, nor is the reduction in permeability as a result of shearing and increased effective stress [e.g., *Arch and Maltman*, 1990; *Crawford et al.*, 2008]. We note that most of the permeability reduction during shearing occurs at low shear strains for all three gouge materials (≤ 5), (Figure 3-14). This permeability decrease occurs over the same range of shear strains as the attainment of residual friction, which is consistent with the idea that fabric development is the underlying cause of both observations [*Haines et al.,* 2009].

Numerical modeling studies have shown that overpressures within fault zones can be generated by either (1) a source of fluids at the root of the fault, combined with sufficient permeability anisotropy (3-5 orders of magnitude) such that the fault acts as a fluid conduit parallel to the structure and barrier normal to it [e.g., *Rice,* 1992], or (2) a source of fluid internal to the fault, combined with low overall permeability [e.g., *Sleep and Blanpied*, 1992; *Miller et al.*, 1996]. Some experimental results show that in sheared phyllosilicate gouges, permeability is reduced both normal and parallel to the fault plane, which can cause permeability anisotropy of up to 3 orders of magnitude [*Faulkner and Rutter,* 1998] but usually lower than 2 orders of magnitude [*Brown and Moore,* 1993; *Dewhurst et al*., 1996; *Zhang et al*., 1999, 2001]. However, high pore pressures may still be generated and maintained if overall permeability is sufficiently low. Based on our experimental results, the potential magnitude of pore pressure developed by these mechanisms is likely to depend on gouge mineralogy.

The hydrologic properties of our chlorite gouge are also intriguing in their difference from montmorillonite and illite gouges. Not only does the chlorite gouge exhibit consistently higher permeability than the montmorillonite and illite gouges under all of our experimental conditions, but shearing does not reduce the chlorite gouge permeability as much as in the other gouges. This most likely results from the larger average grain size of the chlorite gouge; this result may still be relevant to natural faults, because chlorite is formed at higher pressure and temperature conditions than montmorillonite and illite, and thus detrital chlorite may be more likely to remain as larger aggregates within natural shear zones.

Application to Natural Fault Zones

Based on our experimental results, we suggest a conceptual model for the effects of permeability and frictional constitutive properties on macroscopic fault behavior, using subduction thrusts as an example (Figure 3-15). We illustrate the difference between a low permeability gouge dominated by smectite or illite, and a high permeability gouge dominated by minerals such as chlorite or quartz or kaolinite, which have similar strength and permeability to chlorite [*Crawford et al*., 2008]. Both net shear strain and the vertical overburden stress σ_v are expected to increase downdip along the thrust plane. Due to the similar permeability and frictional velocity-dependence of montmorillonite and illite gouges, the smectite-illite transition is not expected to significantly affect permeability or sliding stability [e.g., *Saffer and Marone*, 2003; *Brown et al*., 2003]. Montmorillonite or illite gouges, however, have sufficiently low permeability that elevated pore pressures are likely and would significantly lower the effective normal stress and shear strength. This may potentially explain both the low inferred shear stresses along strike-slip faults (such as the San Andreas) [e.g. *Hickman*, 1991] and subduction thrusts [*Wang and He*, 1999].

In contrast, based on the modest permeability reduction at shear strains of above ~10, our results indicate that chlorite- or quartz-rich gouges could maintain their high permeability to significant depth. This would limit their potential to develop high pore pressures, leading to higher effective normal stress, which in turn increases the tendency for unstable slip [e.g. *Scholz,* 1998]. Lower overall pore pressure may also reduce potential velocity-strengthening from dilatancy-driven transient pore pressure reduction. Moreover, lower overall pore pressure would facilitate consolidation and lithification of gouge, processes hypothesized to govern the upper aseismic-seismic transition (the "updip limit") [*Marone and Scholz,* 1988; *Moore and Saffer,* 2001; *Marone and Saffer,* 2007; *Moore et al.,* 2007]. This suggests that the upper transition from aseismic slip to the seismogenic zone should occur shallower along a high-permeability décollement than along a low-permeability one [e.g., *Saffer and Bekins*, 2006] (Figure 3-15).

Our experimental results indicate that non-cohesive, unlithified sediment may be inherently velocity-strengthening, because the frictional contact saturation thought to cause extremely low (or negative) values of b is predominant in unlithified gouge at low temperature. Thus, we argue that increasing normal stress and total accumulated shear strain in the fault slip direction alone are insufficient to cause fault instability, and that the transition to seismic slip may require processes such as gouge lithification via consolidation, cementation, mineral diagenesis, and dissolution-precipitation reactions [*Marone and Scholz,* 1988; *Moore and Saffer,* 2001; *Marone and Saffer,* 2007; *Moore et al.,* 2007]. These processes become increasingly active at higher temperatures, and thus are expected to have a larger effect with increasing depth. Support for this hypothesis comes from numerous rock mechanics studies showing that velocity-weakening behavior (large values of b, exceeding a) is observed in intact, initially bare rock-on-rock granite experiments [e.g. *Dieterich*, 1979, *Tullis and Weeks*, 1986]. Velocity-weakening behavior has also been observed in granular fault gouge in which shear localization has occurred, causing the gouge behavior to be similar to that in rock-on-rock experiments [*Beeler et al.,* 1996; *Scruggs and Tullis,* 1998; *Niemeijer and Spiers,* 2005]. In localized shear of lithified or semi-lithified rock, individual grains are prevented from arranging to a state of maximum contact area, resulting in values of $b > a$ and thus leading to velocity-weakening.

Because the constitutive parameter a is always positive, values of $b \leq 0$ guarantee velocity-strengthening behavior. Modeling of the temporal distribution of aseismic creep events, such as earthquake afterslip, using spring-slider models typically requires velocity-strengthening friction [e.g. *Marone et al.,* 1991]. *Perfettini and Avouac* [2004] modeled postseismic slip following the 1999 Chi-Chi earthquake in Taiwan using a rate-dependent model only, which is essentially a rate- and state-dependent model in which $b = 0$. Additionally, *Savage and Langbein* [2008] recently modeled postseismic relaxation following the 2004 Parkfield, California earthquake. They found that afterslip was satisfactorily modeled using both rate-only and rate- and state-dependent friction but that the rate- and state-dependent models required b to be negative. Our finding that the constitutive parameter b is in fact ≤ 0 over a relevant range of effective normal stress and slip velocities provides the first direct laboratory constraint for realistic fault zone materials that supports these models, especially when considering faults with abundant clay minerals.

Conclusions

We performed laboratory experiments on water saturated clay-rich fault gouges containing montmorillonite, illite, and chlorite at effective normal stresses up to 59 MPa. Our results indicate that these clay-rich gouges are consistently weak, with a coefficient of friction of < 0.35. Montmorillonite gouge is consistently the weakest gouge, with $\mu = 0.19$-0.23. All of the gouges we investigated are velocity-strengthening (stably sliding) over the range of conditions we explored. The velocity-strengthening behavior we observe may be characteristic of non-cohesive, unlithified phyllosilicate gouge material caused by low values of the friction constitutive parameter b.

Permeability measurements of clay-rich gouge indicate that shearing significantly reduces cross-fault permeability. Montmorillonite and illite gouges are consistently the least permeable, whereas chlorite gouge is the most permeable and also maintains a higher permeability after shearing. This characteristic may be significant in that the presence or formation of chlorite may allow drainage, thus reducing pore pressure and allowing increased effective stress in the fault zone. Because high pore pressure hinders processes such as consolidation and cementation, low pore pressure and high effective stress may increase the likelihood for seismic nucleation if fault instability is indeed linked to cohesive strengthening and lithification.

Figures

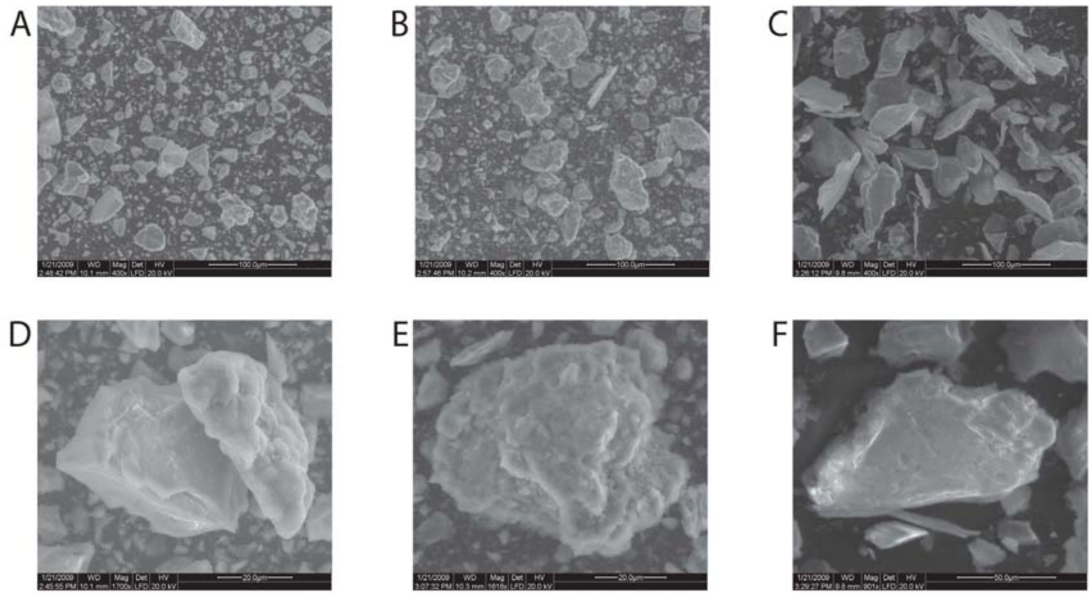

Figure 3-1: SEM images of the bulk starting material used as gouge at 400x magnification: A. montmorillonite/quartz, B. illite shale, C. chlorite schist. D shows a close up view of an individual quartz grain (left) and montmorillonite aggregate (right). E and F show aggregates of illite and chlorite, respectively.

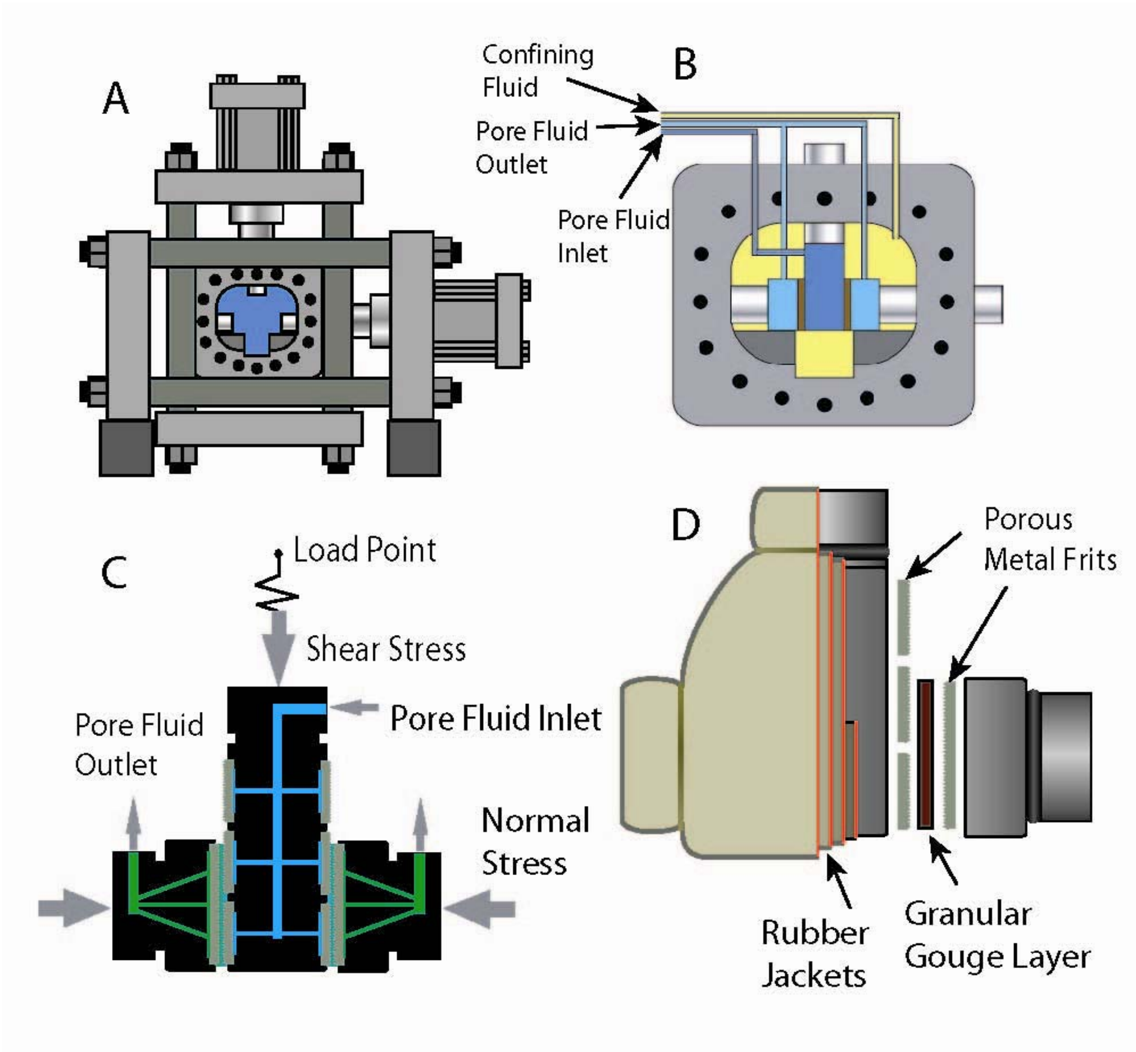

Figure 3-2: A. Biaxial stressing apparatus with pressure vessel. B. Three-block assembly inside pressure vessel showing fluid lines. C. Internal plumbing structure of three-block sample assembly showing pore fluid inlet and outlets. D. Three-block sample assembly showing sample gouge layer, porous metal frits, and rubber jackets.

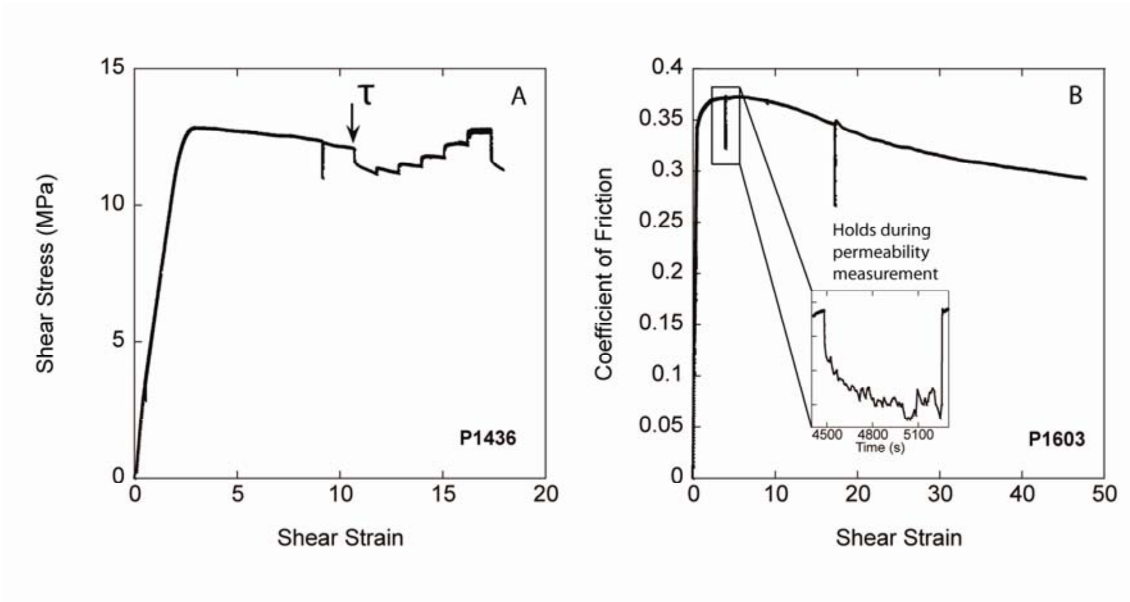

Figure 3-3: A. Example of a typical friction experiment. τ indicates displacement at which the residual shear strength value is taken; this value is also used to calculate the coefficient of friction μ. B. Example of a typical experiment measuring permeability as a function of shear strain. During a permeability measurement, shearing is stopped and friction relaxes (inset).

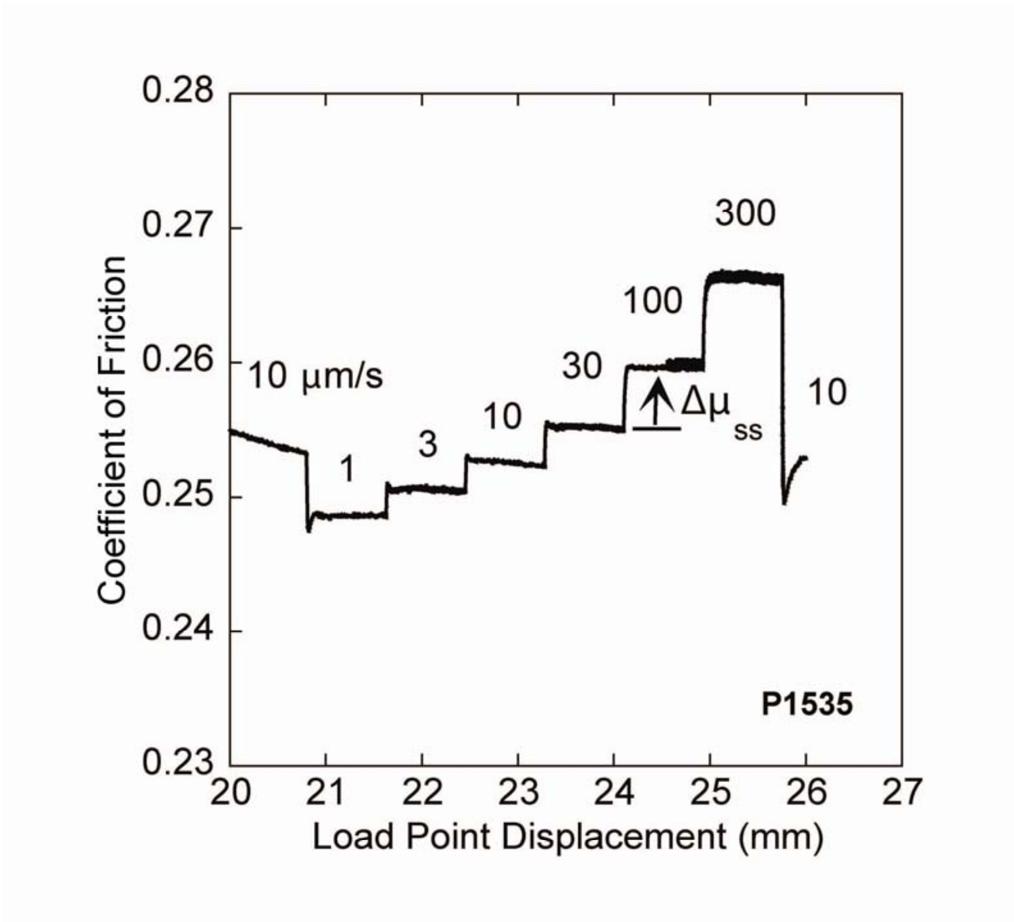

Figure 3-4: Example of a velocity-stepping test. Load point velocity is increased in discrete steps; resulting measured change in steady-state friction is used to calculate the rate and state parameters *a. b, a-b, and Dc*. Constant, long-term friction trends are removed.

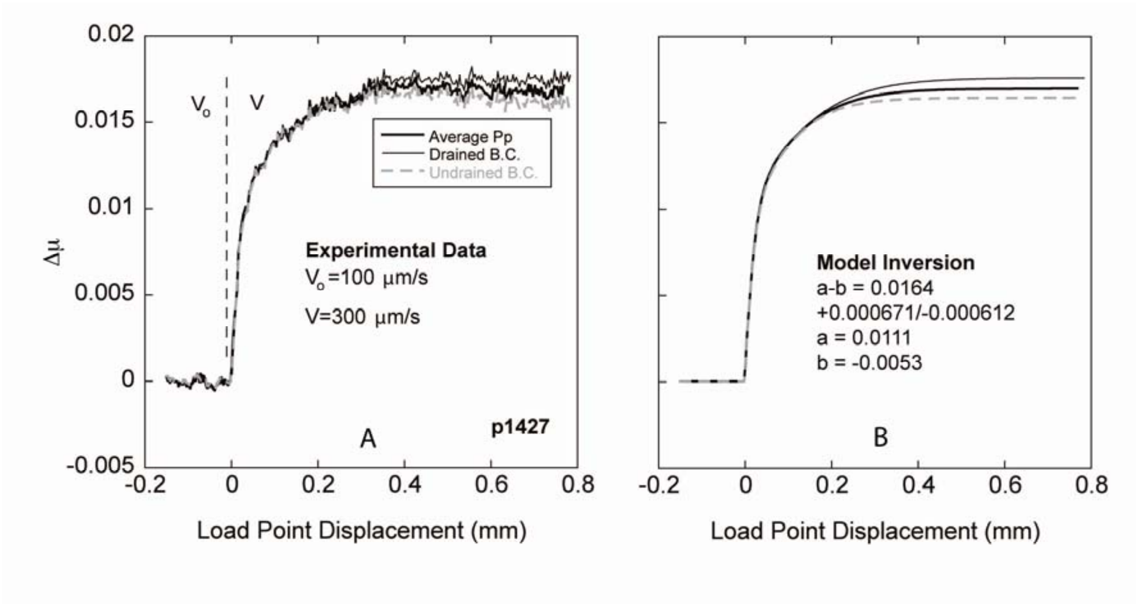

Figure 3-5: A. Example of experimental data from an individual velocity-step. B. Model inversion of the velocity step in A. Three curves are shown for both the experimental data and model, with friction calculated using average pore pressure, pore pressure at the (controlled *Pp*) drained boundary, and pore pressure measured at the undrained boundary. Differences between the curves represent the maximum variation due to different boundary conditions.

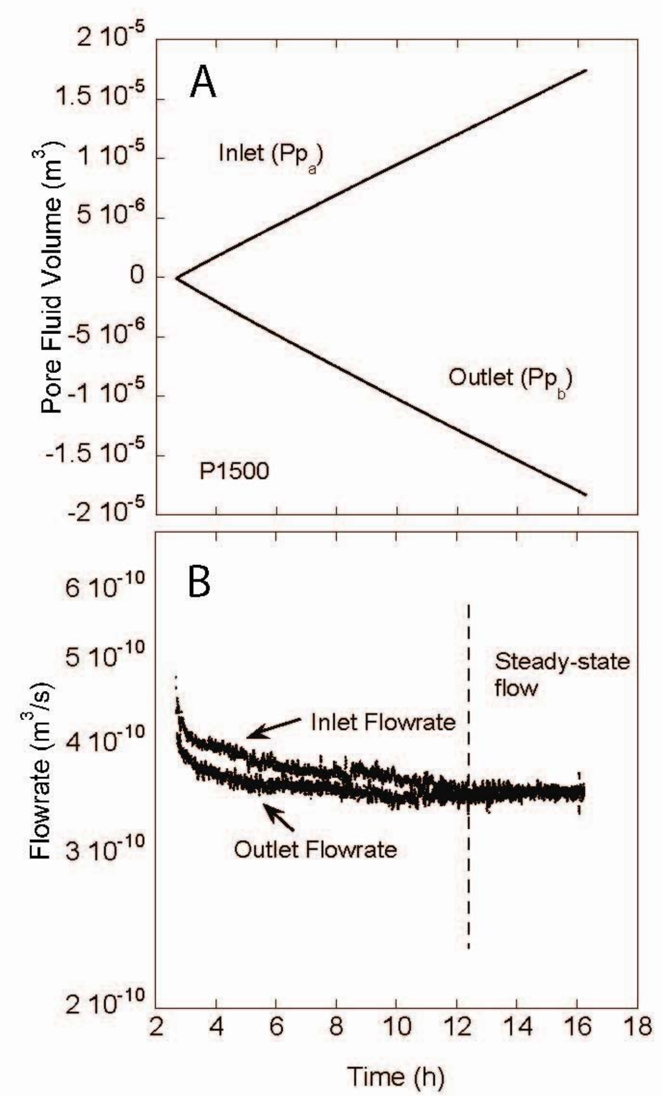

Figure 3-6: Example of a typical permeability experiment. A. Displacement of pore fluid into (inlet) and out of (outlet) sample layer vs. time. B. Volumetric flowrate of into and out of sample layer with time. Permeability is measured when steady-state flow is achieved.

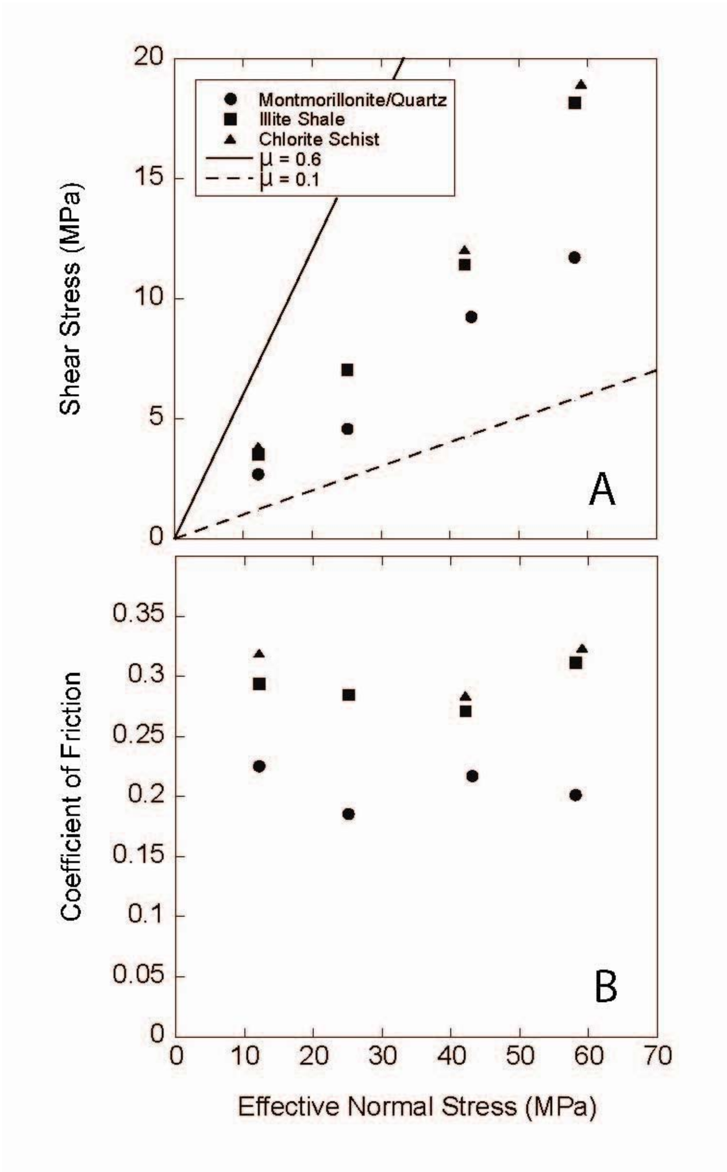

Figure 3-7: A. Residual shear stress vs. effective normal stress in a Coulomb-Mohr diagram. Friction envelopes for $\mu = 0.6$ and $\mu = 0.1$ are shown for reference. B. Coefficient of friction vs. effective normal stress.

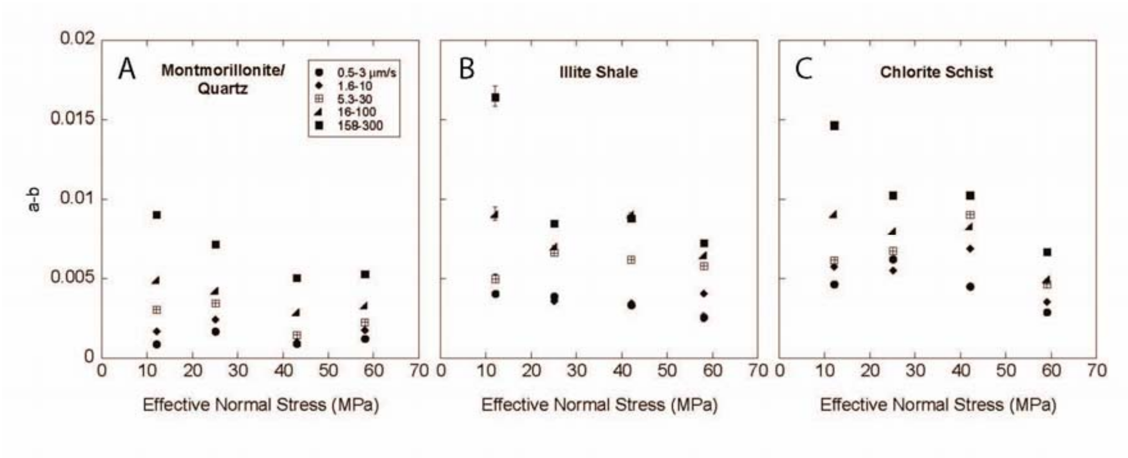

Figure 3-8: *a-b* vs. effective normal stress for A. montmorillonite-rich gouge, B. illite-rich gouge, and C. chlorite-rich gouge. Uncertainty in individual friction parameters due to small pore pressure transients in the layer as described in the text (c.f. Figure 4) are shown by error bars, which are smaller than the symbols in most cases.

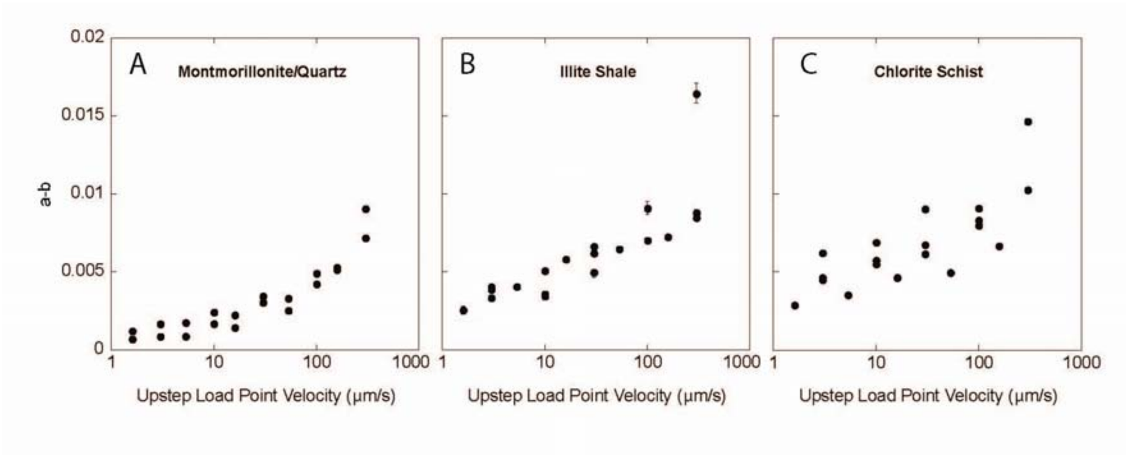

Figure 3-9: *a-b* vs. upstep load point velocity for A. montmorillonite-rich gouge, B. illite-rich gouge, and C. chlorite-rich gouge. Error bars are determined as described for Figure 8.

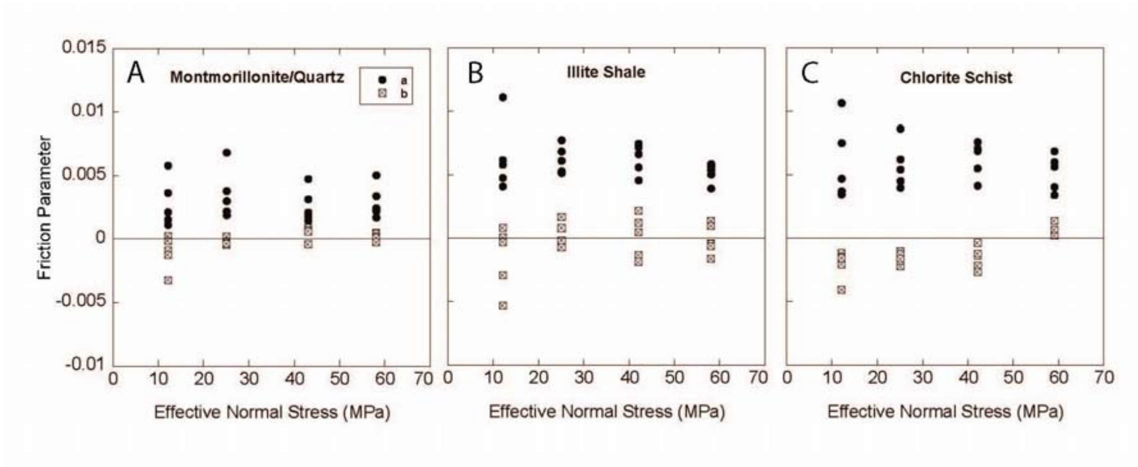

Figure 3-10: Constitutive parameters *a* and *b* vs. effective normal stress for A. montmorillonite-rich gouge, B. illite-rich gouge, and C. chlorite-rich gouge. Error bars are determined as described for Figure 7.

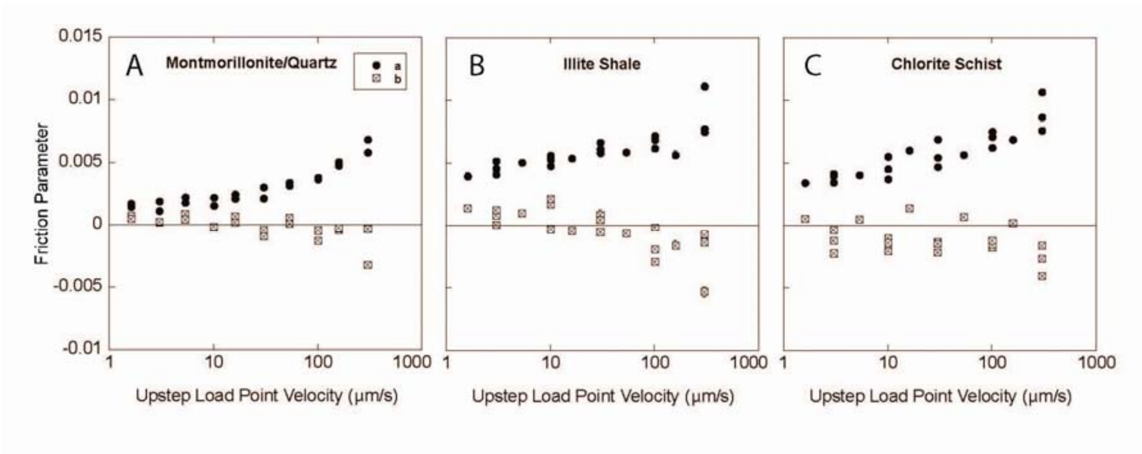

Figure 3-11: Constitutive parameters *a* and *b* vs. shear velocity for A montmorillonite-rich gouge, B. illite-rich gouge, and C. chlorite-rich gouge. Error bars are determined as described for Figure 7.

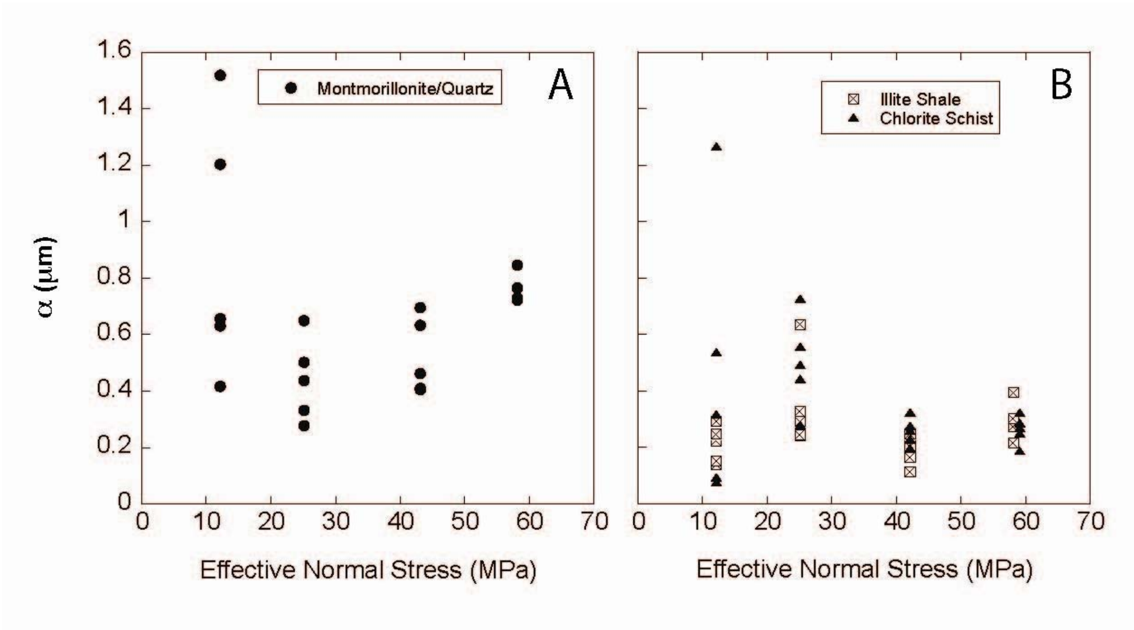

Figure 3-12: Dilatancy parameter α vs. effective normal stress for A. montmorillonite-rich gouge, and B. illite- and chlorite- rich gouge.

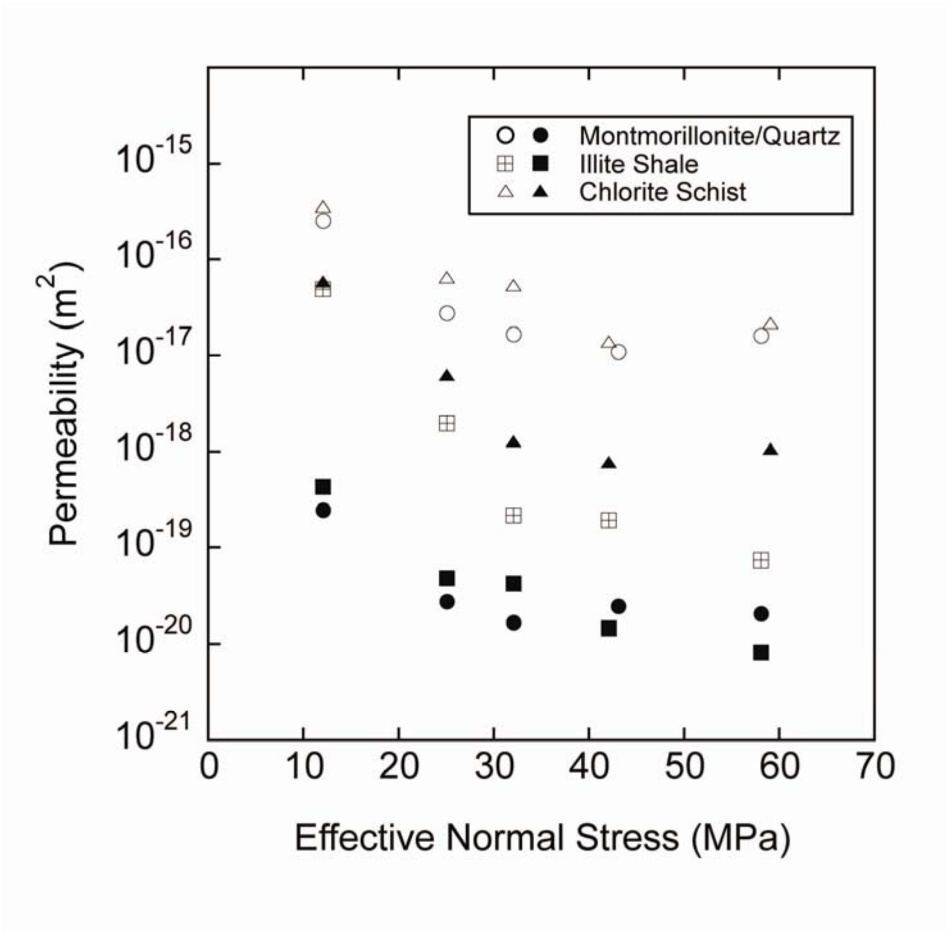

Figure 3-13: Permeability vs. effective normal stress for all three clay gouges. Open symbols indicate pre-shear permeability, solid symbols indicate post-shear permeability.

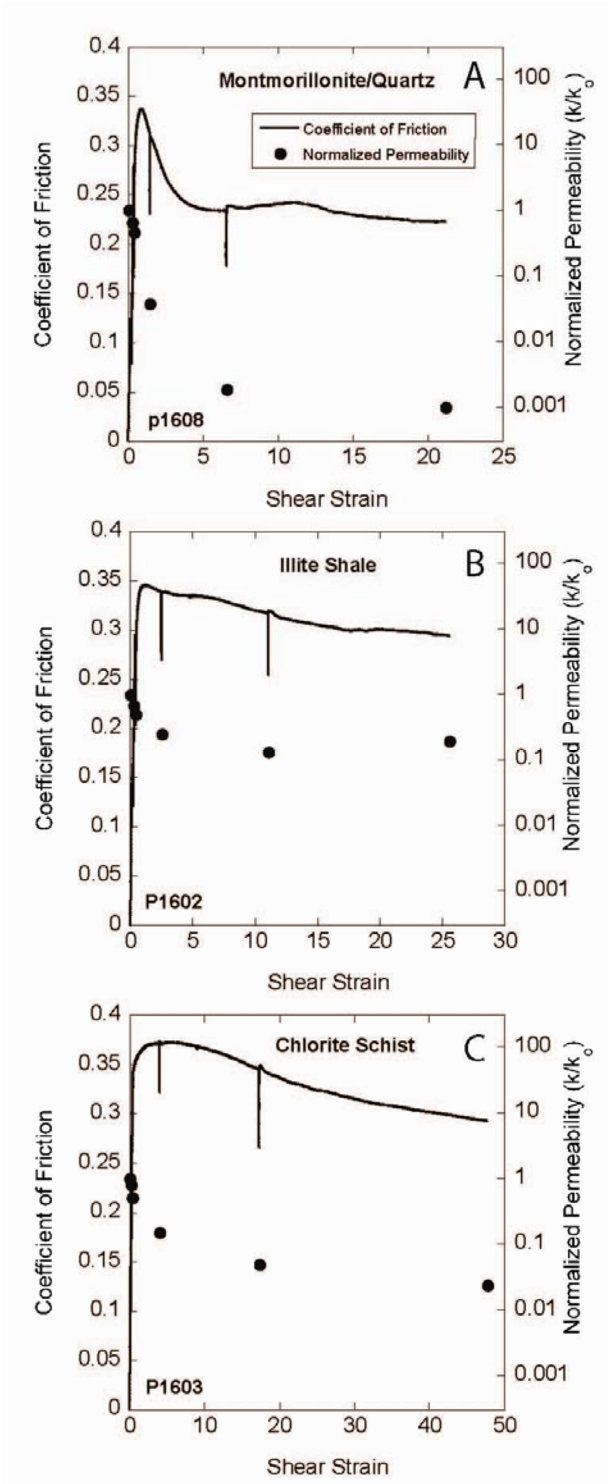

Figure 3-14: Normalized permeability and coefficient of friction as a function of shear strain for A. montmorillonite-rich, B. illite-rich, and C. chlorite-rich gouges. Permeability values are normalized to the pre-shear permeability value k_o.

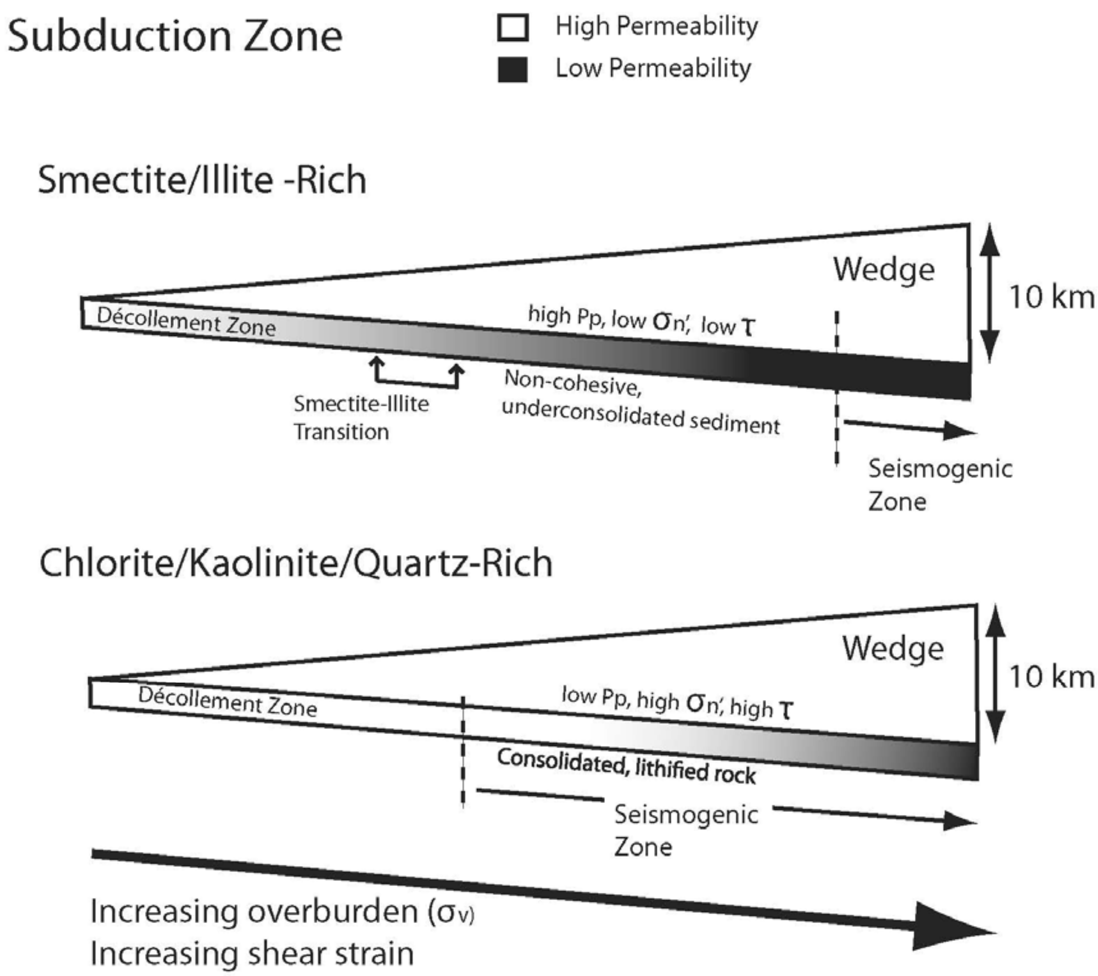

Figure 3-15: Model illustrating the possible geologic effects of low permeability and high permeability sediments in subduction zone megathrusts. For both wedges, the aseismic zone is associated with unlithified sediments and high pore pressure, low effective normal stress, and low shear stress in the décollement, while the seismogenic zone is associated with lithified fault rock, low pore pressure, high effective normal stress, and high shear stress. Basal dip angle is assumed to be 5°, overburden stress gradient is assumed to be ~20 MPa/km.

Tables

Experiment	Gouge	σ_n' (MPa)	Pc (MPa)	Pp (MPa)*	Sliding velocity (μm/s)	Layer thickness under load (μm)	Maximum Shear Strain
p1421	Montmorillonite/Quartz	12	6	5	1,3,10,30,100,300	2085	8.9
p1418	Montmorillonite/Quartz	25	12	5	1,3,10,30,100,300	2115	8.9
p1500	Montmorillonite/Quartz	43	20	5	0.5, 1.6, 5.3, 16, 53, 158	2065	5.2
p1535	Montmorillonite/Quartz	58	28	5	0.5, 1.6, 5.3, 16, 53, 158	2785	4.0
p1427	Illite Shale	12	6	5	1,3,10,30,100,300	1310	10.3
p1426	Illite Shale	25	12	5	1,3,10,30,100,300	1620	11.2
p1437	Illite Shale	42	20	5	1,3,10,30,100,300	1510	16.5
p1521	Illite Shale	58	28	5	0.5, 1.6, 5.3, 16, 53, 158	1515	8.3
p1423	Chlorite Schist	12	6	5	1,3,10,30,100,300	905	22.8
p1422	Chlorite Schist	25	12	5	1,3,10,30,100,300	1540	13.4
p1436	Chlorite Schist	42	20	5	1,3,10,30,100,300	1340	17.9
p1534	Chlorite Schist	59	28	5	0.5, 1.6, 5.3, 16, 53, 158	1730	6.5
p1608	Montmorillonite/Quartz	32	12	5	11	1755	21.2
p1602	Illite Shale	32	12	5	11	1685	25.6
p1603	Chlorite Schist	32	12	5	11	1180	47.8

Table 3-1: Experiment parameters. *Pore pressure during shear, controlled by Ppa.

Experiment	Gouge	σ_n' (MPa)	V_o (μm/s)	V (μm/s)	*a*	*b*	*a-b*	D_c (μm)	*a* SD	*b* SD	D_c SD
p1421	Montmorillonite/Quartz	12	1	3	0.0012	0.0003	0.0009	14.2	0.00005	0.00005	4.13
p1418	Montmorillonite/Quartz	25	1	3	0.0019	0.0003	0.0017	10.8	0.00004	0.00004	2.03
p1500	Montmorillonite/Quartz	43	0.5	1.6	0.0015	0.0008	0.0007	5.9	0.00003	0.00003	0.25
p1535	Montmorillonite/Quartz	58	0.5	1.6	0.0018	0.0005	0.0012	8.2	0.00002	0.00002	0.32
p1421	Montmorillonite/Quartz	12	3	10	0.0016	-0.0001	0.0017	25.9	0.00005	0.00005	25.82
p1418	Montmorillonite/Quartz	25	3	10	0.0022	-0.0002	0.0024	117.2	0.00002	0.00002	27.40
p1500	Montmorillonite/Quartz	43	1.6	5.3	0.0018	0.0009	0.0009	5.4	0.00004	0.00004	0.30
p1535	Montmorillonite/Quartz	58	1.6	5.3	0.0023	0.0005	0.0018	4.7	0.00004	0.00004	0.48
p1421	Montmorillonite/Quartz	12	10	30	0.0022	-0.0009	0.0031	78.3	0.00008	0.00006	9.17
p1418	Montmorillonite/Quartz	25	10	30	0.0031	-0.0004	0.0035	87.3	0.00006	0.00005	28.14
p1500	Montmorillonite/Quartz	43	5.3	16	0.0022	0.0007	0.0014	10.0	0.00002	0.00002	0.34
p1535	Montmorillonite/Quartz	58	5.3	16	0.0025	0.0002	0.0023	7.0	0.00004	0.00003	1.28
p1421	Montmorillonite/Quartz	12	30	100	0.0037	-0.0012	0.0049	88.6	0.00022	0.00020	23.86
p1418	Montmorillonite/Quartz	25	30	100	0.0039	-0.0004	0.0042	38.4	0.00011	0.00010	24.95
p1500	Montmorillonite/Quartz	43	16	53	0.0032	0.0006	0.0025	19.6	0.00004	0.00003	1.56
p1535	Montmorillonite/Quartz	58	16	53	0.0034	0.0001	0.0033	30.0	0.00002	0.00002	10.27
p1421	Montmorillonite/Quartz	12	100	300	0.0059	-0.0032	0.0091	102.6	0.00020	0.00018	10.14
p1418	Montmorillonite/Quartz	25	100	300	0.0069	-0.0003	0.0072	78.5	0.00018	0.00017	104.76
p1500	Montmorillonite/Quartz	43	53	158	0.0048	-0.0004	0.0052	33.3	0.00002	0.00002	3.10
p1535	Montmorillonite/Quartz	58	53	158	0.0051	-0.0002	0.0053	37.0	0.00003	0.00002	7.08
p1427	Illite Shale	12	1	3	0.0041	0.0002	0.0039	52.8	0.00004	0.00004	47.05
p1426	Illite Shale	25	1	3	0.0052	0.0008	0.0044	14.8	0.00006	0.00005	1.21
p1437	Illite Shale	42	1	3	0.0046	0.0013	0.0034	44.4	0.00002	0.00002	0.89
p1521	Illite Shale	58	0.5	1.6	0.0040	0.0014	0.0026	45.1	0.00004	0.00003	1.53
p1427	Illite Shale	12	3	10	0.0048	-0.0003	0.0051	79.4	0.00004	0.00004	34.05
p1426	Illite Shale	25	3	10	0.0053	0.0017	0.0036	92.3	0.00003	0.00002	2.22
p1437	Illite Shale	42	3	10	0.0057	0.0022	0.0035	99.9	0.00002	0.00002	1.35
p1521	Illite Shale	58	1.6	5.3	0.0051	0.0010	0.0041	52.2	0.00003	0.00003	3.16
p1427	Illite Shale	12	10	30	0.0059	0.0009	0.0050	2297.1	0.00007	0.00024	702.78
p1426	Illite Shale	25	10	30	0.0062	-0.0005	0.0066	91.9	0.00005	0.00004	11.20
p1437	Illite Shale	42	10	30	0.0163	0.0098	0.0066	1.5	0.00001	0.00001	0.07
p1521	Illite Shale	58	5.3	16	0.0054	-0.0004	0.0058	246.3	0.00001	0.00007	85.44
p1427	Illite Shale	12	30	100	0.0062	-0.0029	0.0091	17.7	0.00087	0.00086	7.71
p1426	Illite Shale	25	30	100	0.0069	-0.0001	0.0070	23.6	0.00003	0.00024	192.74
p1437	Illite Shale	42	30	100	0.0072	-0.0019	0.0091	105.5	0.00005	0.00004	3.92
p1521	Illite Shale	58	16	53	0.0059	-0.0006	0.0065	32.1	0.00003	0.00002	2.10
p1427	Illite Shale	12	100	300	0.0095	-0.0066	0.0161	84.9	0.00035	0.00032	6.57
p1426	Illite Shale	25	100	300	0.0078	-0.0007	0.0085	539.5	0.00011	0.00244	48736.14
p1437	Illite Shale	42	100	300	0.0075	-0.0013	0.0088	1053.4	0.00007	0.00331	20520.65
p1521	Illite Shale	58	53	158	0.0057	-0.0016	0.0073	33.2	0.00004	0.00004	1.16

Experiment	Gouge	σ_n' (MPa)	V_o (μm/s)	V (μm/s)	*a*	*b*	*a-b*	D_c (μm)	*a* SD	*b* SD	D_c SD
p1423	Chlorite Schist	12	1	3	0.0062	-0.0076	0.0138	123.4	0.00006	0.00004	1.66
p1422	Chlorite Schist	25	1	3	0.0040	-0.0022	0.0062	53.6	0.00003	0.00002	0.87
p1436	Chlorite Schist	42	1	3	0.0042	-0.0003	0.0045	30.5	0.00003	0.00002	2.93
p1534	Chlorite Schist	59	0.5	1.6	0.0035	0.0006	0.0029	8.9	0.00003	0.00003	0.49
p1423	Chlorite Schist	12	3	10	0.0077	-0.0122	0.0198	182.4	0.00007	0.00007	2.73
p1422	Chlorite Schist	25	3	10	0.0046	-0.0010	0.0055	37.7	0.00008	0.00008	4.65
p1436	Chlorite Schist	42	3	10	0.0056	-0.0014	0.0069	43.9	0.00003	0.00003	1.38
p1534	Chlorite Schist	59	1.6	5.3	0.0041	0.0005	0.0035	5.8	0.00010	0.00010	1.42
p1423	Chlorite Schist	12	10	30	0.0047	-0.0014	0.0062	9.0	0.00026	0.00025	2.15
p1422	Chlorite Schist	25	10	30	0.0055	-0.0013	0.0067	31.1	0.00008	0.00007	2.34
p1436	Chlorite Schist	42	10	30	0.0069	-0.0021	0.0091	106.3	0.00002	0.00002	1.66
p1534	Chlorite Schist	59	5.3	16	0.0061	0.0014	0.0047	1.6	0.00027	0.00027	0.34
p1423	Chlorite Schist	12	30	100	0.0076	-0.0015	0.0091	29.9	0.00020	0.00019	5.40
p1422	Chlorite Schist	25	30	100	0.0063	-0.0017	0.0080	46.2	0.00015	0.00015	5.51
p1436	Chlorite Schist	42	30	100	0.0071	-0.0012	0.0083	34.6	0.00007	0.00007	2.76
p1534	Chlorite Schist	59	16	53	0.0057	0.0007	0.0050	11.0	0.00006	0.00005	1.06
p1423	Chlorite Schist	12	100	300	0.0107	-0.0040	0.0147	56.0	0.00036	0.00034	7.15
p1422	Chlorite Schist	25	100	300	0.0087	-0.0016	0.0103	57.8	0.00019	0.00018	10.28
p1436	Chlorite Schist	42	100	300	0.0076	-0.0026	0.0103	67.8	0.00015	0.00014	5.51
p1534	Chlorite Schist	59	53	158	0.0069	0.0002	0.0067	3.1	0.00033	0.00033	9.67

Table 3-2: Constitutive parameters for least squares fit of the Dieterich Law.

Chapter 4

FRICTIONAL AND HYDROLOGIC PROPERTIES OF A MAJOR SPLAY FAULT SYSTEM, NANKAI SUBUDCTION ZONE

Abstract

We report on laboratory experiments examining the frictional and hydrologic properties of fault gouge and wall rock along a borehole transect that crosses a major out-of-sequence thrust splay fault within the Nankai accretionary complex. At 25 MPa effective normal stress, the fault zone material is frictionally weak (μ<0.44) and exhibits low permeability after shearing (k<5.5x10-20 m2). Fault zone samples are weaker and less permeable than the surrounding wall rocks, consistent with their slightly higher clay abundance. All samples exhibit velocity-strengthening frictional behavior over most of the experimental conditions we explored, consistent with aseismic slip at shallow depths. The fault and wall rock both exhibit prominent minima in the friction rate parameter (a-b) for sliding velocities of 1-10 μm/s (~0.1-1.0 m/day), comparable to rates for slow slip events. This suggests that the frictional properties of fault zone material play a central role in governing the mode of slip on subduction megathrusts.

Introduction

At subduction zones, sediments on the incoming oceanic plate are commonly underthrust beneath a forearc wedge and, at accretionary margins, the upper part of the sedimentary section is off-scraped forming an accretionary prism [*Scholl et al.,* 1980; *Underwood*, 2007]. As a result, the plate boundary fault localizes within the sedimentary package, often within clay-rich strata [*Deng and Underwood*, 2001; *Moore et al.*, 2001]. Within the accretionary prism, major out-of-sequence thrust (OOST) faults may splay off of the plate boundary, as in the Nankai subduction zone offshore Japan [*Park et al.,* 2002; *Moore et al.,* 2007] (Figure 4-1). At the Nankai margin, the extent of coseismic rupture for the 1944 Tonankai (M_w=8.1) earthquake determined by tsunami and seismic waveform inversions (Figure 4-1b) suggests that significant coseismic slip occurred along a major splay fault, termed the "megasplay" [*Sagiya and Thatcher,* 1999; *Park et al.,* 2000; *Tanioka and Satake,* 2001; *Kikuchi et al.,* 2003]. This inference is consistent with theoretical studies that suggest rupture is likely to branch along such structures [*Kame et al.,* 2003]. Interpretations of recent seismic reflection data indicate that the megasplay is tectonically active [*Park et al.,* 2002; *Moore et al.,* 2007] and thus appears to also accommodate long term plate motion. Furthermore, recent work suggests that slow slip may occur along splay faults, both as very low frequency earthquakes [*Ito and Obara,* 2006] and in the form of postseismic relaxation [*Sagiya and Thatcher*, 1999].

The frictional properties of fault rocks are a key control on fault shear strength, as well as rupture propagation and the nature of slip. The mode of fault slip, ranging from aseismic to slow events, tremor and earthquakes, has been correlated with the response of friction to slip velocity perturbations in laboratory experiments [e.g. *Marone*, 1998; *Scholz*, 2002]. Fault slip behavior is also closely related to fault-normal permeability. If permeability is sufficiently low, it can facilitate transient changes in strength via shear-enhanced compaction, thermal pressurization by frictional heating, or depressurization induced by dilatancy [e.g. *Segall and Rice*, 2006]. Previous work on analogs of natural fault gouge has shown that gouge mineralogy, and specifically the presence of clays, is a primary control on shear strength, frictional stability, and permeability [e.g. *Morrow et al.,* 1992; *Saffer and Marone,* 2003; *Crawford et al.,* 2008; *Ikari et al.,* 2009]. Here, we report the results of shearing and permeability experiments conducted at conditions approximating those in-situ, on material retrieved from the Nankai megasplay fault during Integrated Ocean Drilling Program (IODP) Expedition 316.

Geologic Setting: Nankai Accretionary Complex

The Nankai accretionary complex off the coast of SW Japan is formed by subduction of the Philippine Sea plate beneath the Eurasian plate (Figure 4-1). As noted above, a major feature of the accretionary complex is an out-of-sequence splay fault bounding the seaward edge of the Kumano forearc basin, which branches from the main décollement ~50-55 km landward of the deformation front and terminates near the seafloor ~25 km from the deformation front [*Moore et al.*, 2007, 2009] (Figure 4-1).

We obtained a suite of samples collected during IODP Expedition 316, part of the Nankai Trough Seismogenic Zone Experiment (NanTroSEIZE) [*Kimura et al.,* 2008]. These samples were retrieved from Site C0004 along a depth transect spanning the megasplay fault system, from 119-439 mbsf (meters below sea floor) (Figures 4-1, 4-2). The hanging wall (lithologic Unit II, Figure 4-2) is mostly composed of upper to middle Pliocene hemipelagic mudstones, and extends from 78–258 mbsf. The main fault zone of the megasplay (lithologic Unit III) is a fault-bounded package between 258 and 308 mbsf defined by biostratigraphic age reversals [*Kimura et al.,* 2008; *Expedition 316 Scientists,* 2009]. It is composed of fractured and brecciated mid-Pliocene hemipelagic muds with minor interbedded volcanic ash. The footwall (lithologic Unit IV) is overridden slope apron sediment, consisting of lower Pleistocene fine-grained hemipelagic claystones with some sand turbidite layers [*Kimura et al.,* 2008; *Expedition 316 Scientists,* 2009]. Total clay mineral content generally ranges between ~40%-70% within our study interval, plagioclase content ranges from ~10%-40%, and minor calcite is present throughout the section. The highest clay contents (and lowest plagioclase contents) occur within the fault zone (Figure 4-2) [*Expedition 316 Scientists*, 2009]. We conducted experiments on one sample from the hanging wall, four from the fault zone, and two from the footwall (Figure 4-2).

Experimental Methods

We conducted experiments using a true-triaxial testing machine with servo-hydraulic control. Friction and permeability normal to the shear direction were measured under saturated and controlled pore pressure conditions in the double-direct shear geometry, in which two layers of gouge are sheared between two side forcing blocks and a central block, and fluids are introduced via porous frits at the sample faces (for a detailed description of the experimental configuration, see *Ikari et al.,* [2009]). The hanging wall sample and one footwall sample were tested as intact wafers trimmed from whole-round cores and sheared in a direction parallel to bedding (Figure 2). The four samples from the fault zone and a second sample from the footwall were obtained as brecciated mudstone. These samples were dried at ~40°C, disaggregated by hand, and sieved to a grain size of <106 μm to remove any remaining large mudstone aggregates, and to limit the effects of grain size and comminution of these aggregates on friction at low shear strains (<~5). Upon saturation and application of normal stress (prior to shearing), layer thickness of the disaggregated gouge was ~1.5 mm. The fragile nature of the intact wafers required the use of thicker samples (2.5 to 4 mm prior to shearing).

In each experiment, shear was implemented as a displacement rate boundary condition (11 μm/s) at the gouge layer boundary. Effective normal stress was maintained at 25 MPa, and includes the combined effects of confining pressure (P_c), externally applied normal load, and pore pressure (P_p). During shear, P_c was held constant at 6 MPa, pore pressure at the upstream face of the sample (Pp_a) was held constant at 5 MPa, and that at the downstream sample face of each layer (Pp_b) was set to a no-flow (undrained) condition in order to monitor pore pressure [e.g., *Ikari et al.*, 2009]. In order to simulate in-situ conditions, we used 3.5 wt% NaCl brine as pore fluid. After attainment of steady-state shear stress (typically at shear strain of ~5), we measured friction constitutive properties using velocity-step tests that consisted of a factor of 3 jump in velocity in the range 0.03-100 μm/s. After shearing, a constant pore pressure gradient was applied across the layer perpendicular to the shear direction, and the resulting steady-state flow rate was used to calculate the permeability (k) by Darcy's law.

We measure the steady-state shear stress (τ) prior to the initiation of velocity steps. The coefficient of sliding friction μ is calculated by:

$$\tau = \mu\sigma_n' + c \tag{1}$$

where c is cohesion (assumed to be negligible), and σ_n' is the effective normal stress, computed using the average of the pore pressures at the drained and undrained boundaries. We quantify frictional stability using the friction rate parameter (a-b):

$$a - b = \frac{\Delta\mu_{ss}}{\ln\left(V/V_o\right)} \tag{3}$$

where $\Delta\mu_{ss}$ is the change in the steady-state coefficient of friction for a change in sliding velocity from V_o to V [e.g. *Marone*, 1998]. Positive values of (a-b) indicate velocity-strengthening behavior, whereas negative values indicate velocity-weakening, a necessary (though not sufficient) condition for stick-slip behavior associated with earthquake nucleation [*Scholz*, 2002].

We determined values of the friction rate parameter (*a-b*) and other constitutive parameters using an inverse modeling technique with an iterative least-squares method, using *Dieterich's* [1979] constitutive law for friction coupled with an expression describing machine stiffness [*Reinen and Weeks*, 1993; *Saffer and Marone*, 2003; *Ikari et al.,* 2009].

Results

All of the samples we tested are frictionally weak, with a coefficient of friction $\mu<0.5$. The weakest samples are from within the fault zone ($0.37\leq\mu\leq0.44$), and these have significantly lower strength than the surrounding wall rocks ($0.41\leq\mu\leq0.47$) (Figure 4-3A). Post-shear permeability (k) for all of the samples is $\leq7.0\times10^{-19}$ m^2 (Figure 4-3B). Samples from within the fault zone are uniformly less permeable ($2.2\times10^{-20}<k<5.5\times10^{-20}$ m^2) than the surrounding wall rocks ($1.5\times10^{-19}<k<7.0\times10^{-19}$ m^2). The low overall values of friction and permeability are consistent with previous experimental studies of saturated clay-rich gouges [e.g. *Crawford et al*., 2008; *Ikari et al.,* 2009].

In contrast to the frictional strength and permeability values, the frictional velocity dependence (*a-b*) is similar for the fault zone and wall rocks. With one exception (sample C0004D-42R-3, 335.42 mbsf), (*a-b*) is uniformly positive, ranging from 0.0004–0.0069 (Figure 4-3C, D). For all of our samples, the lowest values of (*a-b*), including the one observation of velocity-weakening, occur at slip velocities of 1-10 μm/s. In comparing the intact footwall sample with the disaggregated and remolded footwall sample, we find that their frictional strength, velocity-dependence, and permeability are similar (Figure 4-3).

Implications for Fault Slip and Hydrologic Behavior

Although the samples we tested are lithologically similar to first-order (described as hemipelagic mudstones), material from within the fault zone is consistently weaker than the wall rocks. Samples from within the fault zone also exhibit both lower permeability than the wall rock samples, and low absolute values of permeability. These observations are consistent with slightly higher clay content in the fault zone (~55% vs. ~40%), especially in comparison to the footwall [*Deng and Underwood*, 2001]. Low permeability may facilitate both high ambient pore pressures within the fault zone and transient strength changes during slip. The similarity of frictional strength and permeability for intact wafers and disaggregated gouge suggests that for these relatively shallow samples, lithification and fabric are poorly developed and/or have little effect on mechanical and hydrologic properties.

Frictional velocity dependence is almost always positive and does not vary significantly between samples or as a function of position across the fault zone (Figure4- 3C, D). This is consistent with several recent studies showing that clay-rich gouges are generally velocity-strengthening [e.g., *Morrow et al.,* 1992; *Saffer and Marone*, 2003; *Ikari et al.*, 2009]. The slight differences in mineralogy between the fault zone and wall rocks that appear to influence frictional strength and permeability do not affect the frictional stability, consistent with previous work showing that (*a-b*) is less sensitive to changes in clay mineral content than is frictional strength [*Ikari et al.,* 2007].

The overall velocity-strengthening behavior of the fault zone indicates that seismic slip will not nucleate along the megasplay at these shallow depths, and if coseismic slip propagates from a nucleation zone deeper on the fault, it would need to overcome the stabilizing properties of the shallow fault zone for rupture to reach the seafloor. Due to low permeability, this effect would be magnified by dilation-induced depressurization in low-permeability gouge, which would lead to strengthening and further stabilize slip [e.g., *Segall and Rice*, 2006]. Although coseismic slip may not reach the seabed, other types of transient slip phenomena may propagate along faults with near velocity-neutral frictional behavior [*Rubin*, 2008]. Our work indicates that seismic slip on deeper parts of the megasplay may ultimately reach the seafloor in the form of postseismic relaxation (earthquake afterslip) [*Marone et al.,* 1991; *Perfettini and Ampuero*, 2008], slow slip events, or low frequency earthquakes [e.g., *Ito and Obara*, 2006]. This is consistent with recent studies documenting reverse faulting focal mechanisms for very low frequency earthquakes in the accretionary wedge that likely initiated on out-of-sequence thrusts [*Ito and Obara,* 2006]. Postseismic relaxation has been documented in the region of great Nankai earthquakes [*Thatcher*, 1984] and much of it likely occurs along splay faults [*Ito and Obara*, 2006].

Notably, the lowest values of (*a-b*) in our experiments occur for sliding velocities of 1-10 μm/s (~0.1-1 m/day) (Figure 3D). This is slightly higher than the observed velocities for slow slip events at the Nankai margin and earthquake afterslip in northeast Japan, reported at 1.1-4.3x10^{-8} m/s (0.011-0.043 μm/s) [*Ide et al.,* 2007], but approximately matches the range of estimated slip velocity of 1.5-5.0x10^{-7} m/s (0.15-0.5 μm/s) for slow earthquakes on the San Andreas Fault in California [*Linde et al.,* 1996; *Ide et al.,* 2007]. Based on our experimental data, the frictional stability of the fault zone should increase at slip velocities >~10 μm/s, which is a condition that favors slow slip by arresting nucleation of a dynamic rupture [*Rubin*, 2008].

Conclusions

Shear strength and permeability in the megasplay are low throughout the depth range examined in this study, consistent with its clay-rich lithology. Friction coefficient and permeability of the fault zone are both lower than that of the hanging wall and footwall, which may be related to slightly higher clay content in the fault zone. All samples exhibit stable frictional behavior, also consistent with clay-rich lithology, but (*a-b*) values are relatively insensitive to these mineralogical variations. The velocity-strengthening behavior of the fault zone suggests that seismic rupture is unlikely to reach the seafloor. However, velocity-strengthening friction and the observed consistent minima in (*a-b*) at sliding velocities of 1-10 μm/s are favorable for earthquake afterslip and interseismic slow slip events, which may be common at shallow depths along the megasplay.

Figures

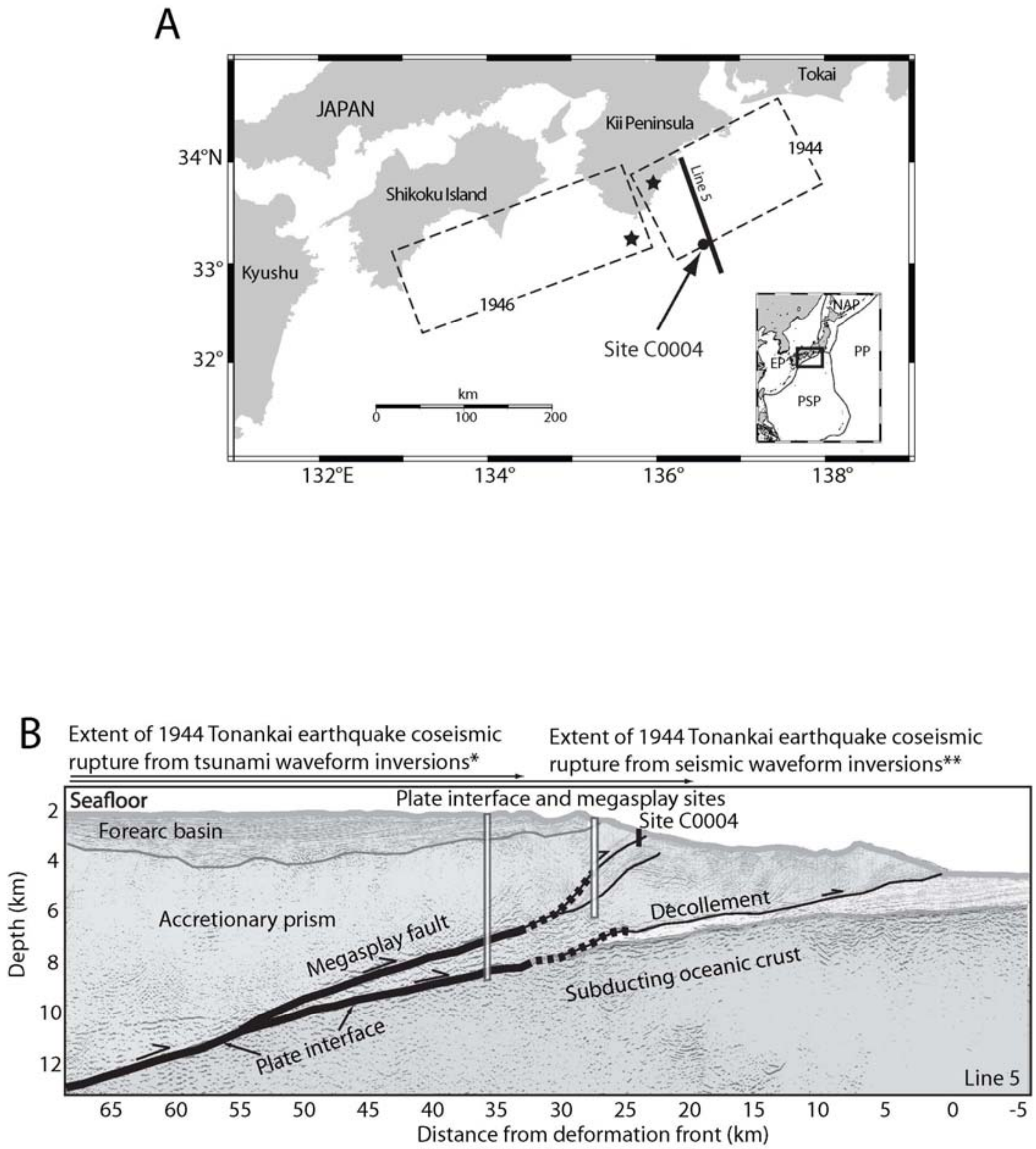

Figure 4-1: A. Map of the Nankai area showing location of drill site C0004, as well as the rupture areas (dashed boxes) and epicenters (stars) of the 1944 Tonankai and 1946 Nankaido earthquakes (modified from *Kimura et al.,* [2008]). B. Profile of the megasplay along Line 5 in Figure 1A, showing drill site C0004, approximate location of our samples, and planned deeper drillsites.. Also shown are estimates of the updip extent of coseismic slip inferred for the 1944 Tonankai earthquake [**Tanioka and Satake*, 2001; ***Kikuchi et al.,* 2003], (modified from *Kimura et al.,* [2008]). The zone of coseismic slip is shown by heavy lines; dashed lines denote uncertainty based on difference between the two inversions.

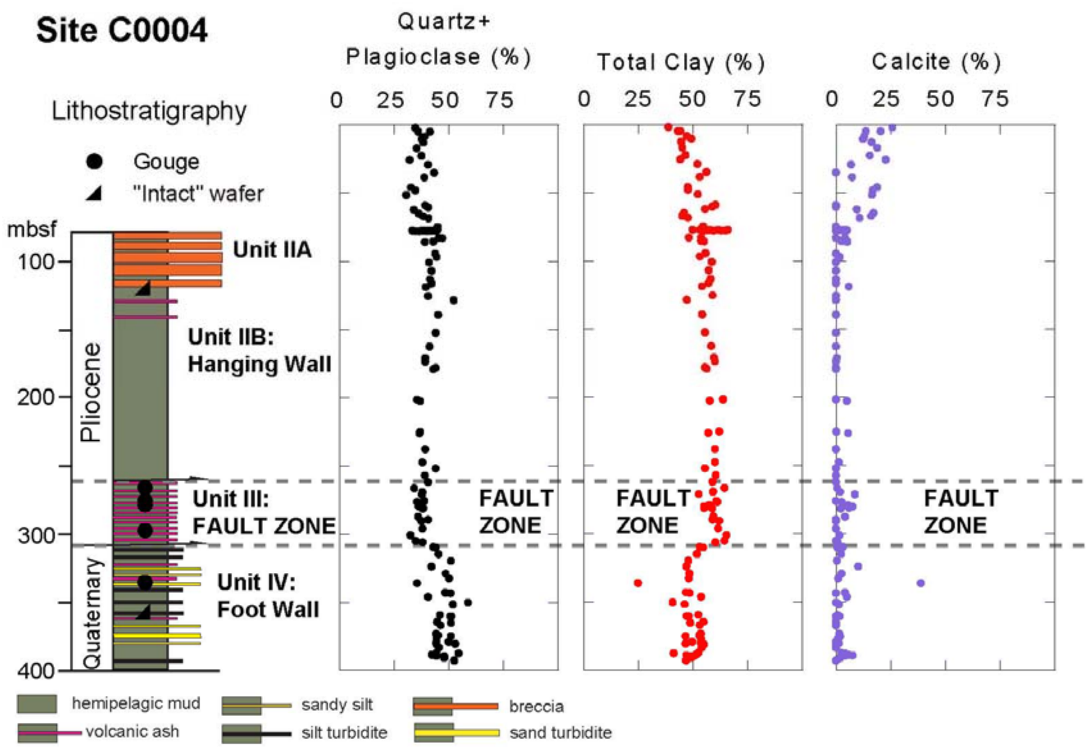

Figure 4-2: Summary of sample locations and lithostratigraphy (Left column), and mineralogy data (Right columns) at site C0004. The lithostratigraphy is modified from M.B. Underwood (unpub. data). Symbols show experimental sample locations superimposed on the column at the appropriate depth. We studied samples: C0004-15X-2, 27R-1, 29R-2, 30R-1, 34R-1, 42R-3, 47R-2, and 42R-3.

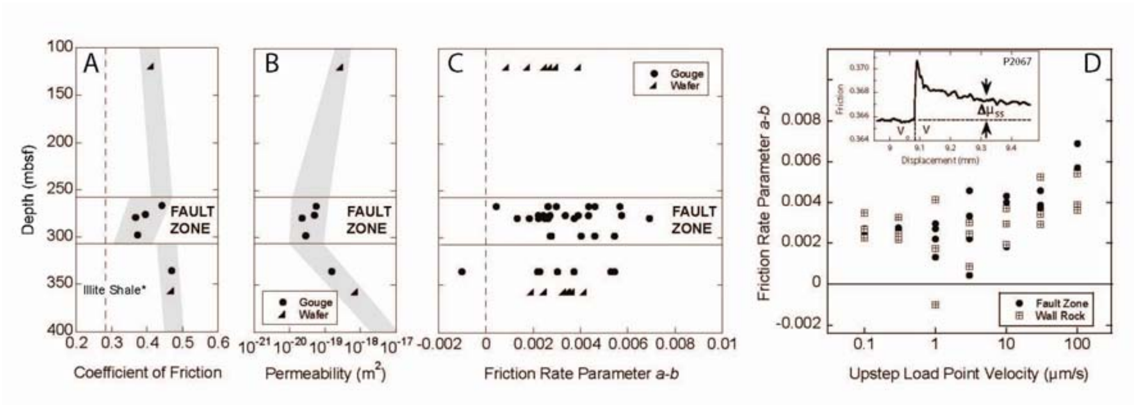

Figure 4-3: A. Coefficient of friction μ as a function of depth. A reference line is shown for illite shale (μ=0.285) under similar experimental conditions [**Ikari et al.,* 2009]; an envelope illustrating the range of the measurements is shown by gray shading. B. Permeability k as a function of depth. C. Friction rate parameter (*a-b)* as a function of depth. D. (*a-b)* as a function of up-step load point velocity. Inset shows data from a representative velocity step test from 0.1-0.3 µm/s (Sample C0004D-30R-1, experiment p2067), indicating velocity-strengthening frictional behavior.

Chapter 5

SLIP BEHAVIOR OF FAULT SYSTEMS IN THE NANKAI CONVERGENT MARGIN

Abstract

At the Nankai convergent margin, the subduction process produces an accretionary complex that hosts a variety of distinct fault systems. We compare the frictional slip behavior of the megasplay, frontal thrust, and décollement by conducting laboratory experiments on fault gouge and wall rock sampled during IODP Expedition 316 and ODP Leg 190. We observe predominantly low friction ($\mu \leq 0.46$), consistent with the clay-rich nature of the samples. Samples from the décollement zone (Site 1174) are consistently weaker than those from the megasplay area (Site C0004) and the frontal thrust system (Site C0007) with $\mu \leq 0.28$. Fault zone material from the megasplay is significantly weaker than the surrounding wall rocks, a pattern not observed in the frontal thrust and décollement. All samples exhibit primarily velocity-strengthening frictional behavior over most of the experimental conditions we explored, consistent with aseismic slip at shallow depths. Slip stability does not vary between fault zones and wall rock at the three settings; however, a previously observed minimum in the friction rate parameter *a-b* at sliding velocities of ~1-3 µm/s (~0.1-0.3 m/d) for the megasplay is also observed for both the frontal thrust and décollement. The similarity of these slip rates to those of slow slip events suggests that shallow aseismic slip transients can be explained by rate- and state-dependent constitutive laws for friction. Our experimental results show that subtle differences exist between the three fault settings, however low friction, generally velocity-strengthening

behavior, and reduced frictional stability in a discrete range of slip rates are consistent observations in these shallow, clay-dominant materials.

Introduction

The development of accretionary prisms at convergent margins, such as the Nankai region offshore Japan (Figure 5-1), results in a complex structure that involves folding and faulting [*Scholl et al.,* 1980; *Moore et al.,* 2009]. A consequence of this is that faults developed within the accreted material are commonly clay-rich as they are derived from pelagic and hemipelagic sediments [*Underwood*, 2007]. This includes the décollement [*Deng and Underwood*, 2001; *Moore et al.*, 2001] and major out-of-sequence thrust (OOST) faults that splay off of the plate boundary [*Park et al.,* 2002; *Moore et al.,* 2007]. The Nankai subduction zone has historically hosted numerous large magnitude earthquakes including the 1944 Tonankai (M_w = 8.1) and 1946 Nankaido (M_w = 8.3) events [*Ando*, 1975; *Sagiya and Thatcher*, 1999]. While coseismic slip in great subduction earthquakes is usually assumed to be confined to the décollement, the extent of coseismic rupture for the both the 1944 and 1946 earthquakes determined by tsunami and seismic waveform inversions (Figure 5-2b) suggests that significant coseismic slip may have occurred along major splay faults [*Kato*, 1983; *Sagiya and Thatcher,* 1999; *Cummins and Kaned*a, 2000; *Park et al.,* 2000; *Tanioka and Satake,* 2001; *Kikuchi et al.,* 2003]. This inference is consistent with theoretical studies suggesting that rupture is likely to branch along such structures [*Sekiguchi et al.,* 2000; *Kame et al.,* 2003]. Seismic reflection data has revealed a major, active OOST, or megasplay fault [*Park et al.,* 2002; *Moore et al.,* 2007; *Bangs et al.*, 2009] that may accommodate long term plate motion, indicating that coseismic rupture and strain accumulation is not limited to the décollement. Various forms of slow slip, including very low frequency earthquakes [*Ito and Obara,* 2006] and postseismic relaxation [*Sagiya and Thatcher*, 1999] have also been observed on thrusts within the accretionary prism, as well as on the décollement [*Davis et al.,* 2006]. Thus, thrusts faults within the prism are important for accommodating all types of slip and it is necessary to account for their frictional properties.

The mode of fault slip, which may range from aseismic creep earthquakes and include intermediate slow events, is controlled by frictional properties of the constituent fault material. Experimental and theoretical studies have shown that the mode of fault slip is a manifestation of frictional stability, which can be quantified by measuring the response of friction to slip velocity perturbations in laboratory experiments [e.g. *Marone*, 1998; *Scholz*, 2002]. Previous work on synthetic mixtures used as analogs for natural fault gouge [e.g. *Morrow et al.,* 1992; *Saffer and Marone,* 2003; *Crawford et al.,* 2008; *Ikari et al.,* 2009a] and limited studies of natural fault materials from subduction zone settings [*Brown et al.*, 2003; *Kopf and Brown*, 2003; *McKiernan et al.,* 2005; *Ikari et al.*, 2009b] have shown that clay-rich sediments are generally frictionally weak and exhibit frictionally stable behavior. This indicates that coseismic rupture propagation and slow slip occurrence in complex fault systems may depend on relatively subtle differences in fault properties. Therefore, careful characterization of the frictional properties of natural gouge from active faults under conditions approximating those in-situ [e.g. *Smith and Faulkner,* 2010], is essential for describing fault slip behavior in natural environments. Here, we report the results of shearing experiments conducted on material retrieved from the frontal thrust zone of the Nankai trough during Integrated Ocean Drilling Program (IODP) Expedition 316, and from the décollement zone during Ocean Drilling Program (ODP) Leg 190, and compare these results with those reported by *Ikari et al.* [2009b] for material retrieved from the megasplay fault zone during Expedition 316.

Geologic Setting: Nankai Subduction Zone

The Nankai accretionary complex off the coast of SW Japan is formed by subduction of the Philippine Sea plate beneath the Eurasian plate (Figure 5-1). It is one of the most extensively studied subduction zones in the world, and has been the focus of numerous ODP and IODP drilling expeditions, 3-D seismic imaging, and geodetic surveys [e.g. *Thatcher*, 1984; *Ozawa et al.,* 1999; *Sagiya and Thatcher,* 1999; *Mazzotti et al.*, 2000; *Moore et al.,* 2001; *Park et al.,* 2002; *Bangs et al.,* 2004]. This includes ODP Leg 190, which sampled the décollement zone at Site 1174 (Figure 1, 2b) and IODP Expedition 316, which sampled the megasplay fault at Site C0004 and the frontal thrust zone at Site C0007 (Figure 5-1, 5-2a).

Megasplay Thrust Fault

The megasplay, a major out-of-sequence splay fault bounding the seaward edge of the Kumano forearc basin was drilled at Site C0004 during IODP Expedition 316, part of the Nankai Trough Seismogenic Zone Experiment (NanTroSEIZE) [*Kimura et al.,* 2008]. The megasplay branches from the main décollement ~50-55 km landward of the deformation front and terminates near the seafloor ~25 km from the deformation front [*Moore et al.*, 2007, 2009] (Figure 5-2a). Our samples span a depth transect from 119-439 mbsf (meters below sea floor) (Figure 5-3). The hanging wall (lithologic Unit II, Figure 5-2) is mostly composed of late- to middle-Pliocene hemipelagic mudstones, and extends from 78–258 mbsf. Lithologic Unit III is a fault-bounded package between 258 and 308 mbsf defined by biostratigraphic age reversals [*Kimura et al.,* 2008; *Expedition 316 Scientists,* 2009a]. This is considered to be the main fault zone of the megasplay and is composed of fractured and brecciated mid-Pliocene hemipelagic muds with minor interbedded volcanic ash. The footwall (lithologic Unit IV) is overridden slope apron sediment, consisting of early Pleistocene fine-grained hemipelagic claystones with some sand turbidite layers [*Kimura et al.,* 2008; *Expedition 316 Scientists,* 2009a]. Within the depth interval of our samples, total clay mineral content generally ranges between ~40%-70%, combined quartz and plagioclase content ranges from ~25%-55%, and minor calcite is present throughout the section (Figure 3). The highest clay contents (and lowest plagioclase contents) occur within the fault zone, and we observe a distinct reduction in clay and increase in quartz and plagioclase at the lower boundary of Unit III (Figure 2) [*Expedition 316 Scientists*, 2009a]. We conducted friction and permeability measurements on two samples from the hanging wall, four from the fault zone, and two from the footwall.

Frontal Thrust System

Site C0007 samples the frontal thrust zone near the toe of the prism along the same transect as Site C0004 (Figure 5-2a). A unique characteristic of this region is the multiple faults penetrated within a small depth interval, in contrast to the single major faults at Sites C0004 and 1174 (Figure 5-4). These three fault zones are located at depths of 237.5-259.3 mbsf, 341.5-362.3 mbsf, and 399-446 mbsf [*Kimura et al.*, 2008; *Expedition 316 Scientists,* 2009b]. Lithologic Unit II is an accreted trench wedge facies, a coarsening-upward sequence composed of mudstones with decreasing contents of sand and gravel with depth from 34-362 mbsf. Unit III extends from 362-439 mbsf and is composed of Pliocene hemipelagic sediments with small ash layers found primarily at the top of the unit. Unit III is considered to be the stratigraphic equivalent of the Upper Shikoku Basin facies identified at Site 1174 [*Kimura et al.*, 2008; *Shipboard Scientific Party*, 2001]. For the upper ~150 m of the section at Site C0007, quartz + plagioclase ranges from ~50-75% and clay content is ~25-50% (Figure 5-4). Below ~200 mbsf, quartz + plagioclase content declines approximately linearly from ~50% to ~30% while clay content increases from ~40% to near 70%. Calcite content is low throughout the section. Our samples from Site C0007 span a depth range of 104-437 mbsf and include one sample from the shallowest fault zone (Fault Zone 1) and two samples from the deepest fault zone (Fault Zone 3)(Figure 5-4).

Décollement Zone

Site 1174 penetrates the décollement zone along the Muroto Transect drilled during ODP Leg 190 (Figure 5-2b). The samples tested from this site are significantly deeper than those from Sites C0004 and C0007, ranging from 660-968 mbsf (Figure 5-5). The shallowest sample we tested comes from near the base of Unit III (Upper Shikoku Basin facies) which is a silty claystone/clayey siltstone with some volcanic ash beds. 661 mbsf marks the base of Unit III and the top of Unit IV (Lower Shikoku Basin facies) which is a fairly homogeneous section of Miocece to Pliocene silty claystone/clayey siltstone [*Shipboard Scientific Party*, 2001]. The décollement is located within Unit IV from 808-840 mbsf. From ~500-1100 mbsf, quartz + plagioclase content declines slightly, dropping from ~55% to ~30%, with scattered lower values (Figure 5-5). Clay content simultaneously increases slightly from ~40% to ~60%. Calcite contents are mostly low, but can be as high as ~25% above the décollement and ~75% below. We tested three hanging wall samples, three samples within the décollement, and four footwall samples, which includes one sample within 1.3 m of the décollement.

Experimental Methods

We conducted experiments using a true-traixial testing machine with servo-hydraulic control [*Ikari et al.,* 2009a; *Samuelson et al.,* 2009]. Friction and permeability normal to the shear direction were measured under saturated and controlled pore pressure conditions in the double-direct shear configuration [e.g., *Ikari et al.,* 2009a] (inset, Figure 5-6a). When feasible, samples were tested as intact wafers trimmed from whole-round cores and sheared in a direction perpendicular to the core axis (i.e., parallel to bedding). Other samples were obtained as brecciated mud, these samples were either remolded or run as powdered gouge. Samples tested as powdered gouge were dried at ~40°C, disaggregated by hand, and sieved to a grain size of <106 µm. Upon saturation and application of normal stress (prior to shearing), layer thickness of the disaggregated gouge was ~1.5 mm (Table 5-1). The fragile nature of the intact wafers required the use of thicker samples (2.5 to 4 mm prior to shearing).

In each experiment, shear was implemented as a displacement rate boundary condition (~10 µm/s) at the gouge layer boundary. Effective normal stress was maintained at 25 MPa, and includes the combined effects of confining pressure (P_c), externally applied normal load, and pore pressure (P_p). During shear, P_c was held constant at 6 MPa, pore pressure at the upstream end of the sample (Pp_a) was held constant at 5 MPa, and the downstream pore pressure (Pp_b) was set to a no-flow (undrained) condition in order to monitor pore pressure in the layer [e.g., *Ikari et al*., 2009a]. In order to simulate in-situ conditions, we used 3.5 wt% NaCl brine as pore fluid. After attainment of steady-state shear stress (typically at shear strain of ~5), a velocity-stepping sequence in the range 0.03-100 µm/s was performed to measure friction constitutive parameters. At the end of shearing, a constant pore pressure gradient was applied across the layer perpendicular to the shear direction, and after reaching a steady-state, the resulting flow rate was used to calculate the permeability (k) by Darcy's law.

We measure the steady-state shear stress (τ) prior to the initiation of velocity steps (Figure 6a). The coefficient of sliding friction μ is calculated by:

$$\tau = \mu \sigma_n ' + c \tag{1}$$

[*Handin*, 1969] where c is cohesion (assumed to be negligible), and σ_n' is the effective normal stress, computed using the average of the pore pressures at the drained and undrained boundaries. We quantify frictional stability using the friction rate parameter (*a-b*):

$$a - b = \frac{\Delta\mu_{ss}}{\ln\left(V / V_o \right)} \tag{2}$$

where $\Delta\mu_{ss}$ is the change in the steady state coefficient of friction upon an instantaneous change in sliding velocity from V_o to V [*Tullis and Weeks*, 1986; *Marone*, 1998]. A material exhibiting a positive value of *a-b* is said to be velocity-strengthening, and will tend to slide stably and inhibit propagation of seismic rupture. A material with negative *a-b* is termed velocity-weakening, which is considered a prerequisite for frictional instability resulting in earthquake nucleation [*Scholz*, 2002]. We determined values of the friction rate parameter *a-b* and other constitutive parameters using an inverse modeling technique with an iterative least-squares method, using *Dieterich's* [1979, 1981] constitutive law for friction with two state variables:

$$\mu = \mu_o + a \ln\left(\frac{V}{V_o}\right) + b_2 \ln\left(\frac{V_o \Theta_1}{D_{c2}}\right) + b_2 \left(\frac{V_o \Theta_2}{D_{c2}}\right) \tag{3}$$

$$\frac{d\Theta}{dt} = 1 - \frac{V\Theta_1}{D_{c2}} - \frac{V\Theta_2}{D_{c2}} \tag{4}$$

where a, b_1 and b_2 are empirically derived constants (unitless), Θ_1 and Θ_2 are the state variables (units of time), and D_{c1} and D_{c2} are the critical slip distances. The state variables are inferred to be the average lifetime of contact points that control friction, and the critical slip distance is the displacement over which those contacts are renewed. The allowance of two state variables where necessary represents a more rigorous quantification of velocity-dependent friction parameters than those reported in *Ikari et al.* [2009b] who used only a one state variable model. In many cases, the friction data from an individual velocity step are well fit using only one state variable, in this case equations 3 and 4 are simplified by setting $\Theta_2 = 0$, eliminating the final term on the right hand side of each equation. In our use of the parameter *a-b*, we consider $b = b_1 + b_2$ to account for the possibility of using either 1 or 2 state variables. These equations are coupled with an expression describing machine stiffness:

$$\frac{d\mu}{dt} = K(V_{lp} - V) \tag{7}$$

where K is the stiffness of the fault surroundings (in this case the testing apparatus and sample blocks) normalized by normal stress (K = ~3x10^{-3} μm^{-1} at 25 MPa normal stress), V_{lp} is the load point velocity, and V is the true slip velocity [*Reinen and Weeks*, 1993; *Saffer and Marone*, 2003; *Ikari et al.,* 2009a]. An example of a velocity step in friction data and the corresponding modeled friction are shown in Figure 5-6b. After the velocity-step tests, we conducted slide-hold-slide tests, the results of which are not included in this report. Continuous acoustic measurements of P-wave (V_p) and S-wave velocity (V_s) were also made during many of these experiments in order to investigate the effects of shear strain and stress perturbations on elastic properties [*Knuth et al.*, 2009]. The results of these measurements will be reported elsewhere by M.W. Knuth.

Results

Frictional Strength

For all three sites, almost all of the samples we tested are frictionally weak, with a coefficient of friction $\mu \leq 0.46$ (Figure 5-7). From the megasplay (Site C0004), the weakest samples are from within the fault zone ($0.36 \leq \mu \leq 0.44$), and these have significantly lower strength than the surrounding wall rocks ($0.41 \leq \mu \leq 0.46$) as reported by *Ikari et al.* [2009b] (Figure 5-7). Samples from the frontal thrust (Site C0007) are consistently weaker than those from the megasplay, with $0.32 \leq \mu \leq 0.40$ for all samples except sample C0007C-11X-4 (μ = 0.54). This sample is especially clay-poor (~30% clay) and is the only sample where we observe $\mu > 0.46$. Unlike the megasplay, we observe no frictional strength difference between fault zone material and wall rock. There is a general trend of slightly decreasing friction as a function of depth (Figure 5-7). The samples from Site 1174 are significantly weaker than those from the other two sites, with $0.20 \leq \mu \leq 0.28$. Similar to Site C0007, the samples from within the décollement have similar frictional strength to those of the wall rock. Strength appears to decrease slightly with depth, but this effect is weaker than it is in the frontal thrust. For samples from all three sites, there is no significant difference in friction between samples tested as intact wafers and granular gouge, with a maximum difference of 0.05 observed between two samples of C0007D-24R-1.

Velocity Dependence of Friction

The frictional velocity dependence *a-b* is fairly consistent between all three sites (Figure 5-8, Table 5-2). All samples are generally velocity-strengthening (*a-b* > 0) with a few exceptions: 1 instance of velocity-weakening in the megasplay samples (C0004D-42R-3, *a-b* = -

0.0001) and 3 instances of velocity-weakening in the frontal thrust samples (C0007D-24R-1 and C0007D-27R-1, minimum *a-b* = -0.0005). The décollement zone samples exhibit strictly velocity-strengthening behavior. Values of *a-b* range up to ~0.006 for all three sites. We observe no systematic dependence of *a-b* on depth, lithification state, or position in the fault zone. However, we do observe a strong dependence of *a-b* on slip velocity (Figure 5-9). At all three sites, we observe minimum values of a-b, including all instances of velocity-weakening, at slip velocities of 1-3 μm/s. These lower values also show a tendency to be better fit by a two state variable constitutive model (Table 5-2). At velocities > 3 μm/s, *a-b* shows a strong positive dependence on slip velocity.

Discussion

Comparison of Frictional Behavior

The low overall values of friction and positive values of *a-b* we observe are consistent with previous experimental studies of saturated clay-rich gouges [e.g. *Morrow et al.,* 1992*; Brown et al.,* 2003*; Kopf and Brown,* 2003*; Ikari et al.,* 2009]. We observe significant strength differences between the three sites, although the samples we tested are primarily hemipelagic silty claystones/clayey siltstones and therefore lithologically similar. Samples obtained from the megasplay are consistently stronger than those from both the frontal thrust zone and the décollement zone, and the décollement zone samples are the weakest in this study. The shallow angle of the décollement and steeper incline of the megasplay indicate that there is a correlation between frictional strength and faulting angle, consistent with Coulomb wedge theory [*Davis et al.,* 1983; *Davis and von Huene,* 1987; *Wang and Hu*, 2006].

We observe that material from within the fault zone is weaker than the wall rocks in the megasplay fault zone, but this behavior is absent from the other two settings. This can be attributed to slight mineralogic variations between sites and also within individual sites. At Site C0004, the low fault zone friction compared to the wall rock can be explained by high clay contents (and low quartz + plagioclase contents) located within the fault zone, as well as the sharp step changes in mineralogy at the lower boundary of the fault zone (Figure 5-3). In contrast, the décollement and fault zones within the frontal thrust region do not show increased clay within shear zones, consistent with our friction measurements that show little difference between fault rock and wall rock friction at these two sites. The decrease in friction with depth at Site C0007 is the result of increasing clay content with depth (Figure 5-4); similarly the slight decrease in friction with depth at Site 1174 corresponds to the slight increase in clay content with depth Figure 5-5). This illustrates the magnitude with which sediment lithology controls frictional strength. We also observe little difference in friction between samples trimmed as wafers with minimal disturbance to in-situ fabric and consolidation state, and those tested either as powders or remolded sediment (Figure 5-7). This applies to both Site C0007 and 1174, and is consistent with previous findings from C0004. This indicates that at depths of up to ~1 km, fabric development and consolidation have not advanced to the point that they exert a significant influence on fault friction.

We expand on the results of *Ikari et al.* [2009b] by allowing use of a two state variable constitutive law, if necessary, in order to better quantify frictional stability. In contrast to frictional strength, the velocity dependence of friction shows little dependence on mineralogic fluctuations or position across the fault zone (Figure 5-8). This is consistent with previous work showing that *a-b* is less sensitive to changes in clay mineral content than is frictional strength [*Ikari et al.,* 2007]. Our observation of mostly velocity-strengthening behavior is in agreement with several studies which demonstrate that clay-rich gouges are generally velocity-strengthening [e.g., *Logan and Rauenzahn*, 1987; *Morrow et al.,* 1992; *Saffer and Marone*, 2003; *Ikari et al.*, 2009; *Tembe et al.*, 2010] and others that have concluded that seismic slip is not expected to occur at shallow depths [*Marone and Scholz*, 1988; *Hyndman*, 2007]. The few occurrences of velocity-weakening are unexpected given the weak, clay-rich nature of our samples, although we note that the magnitude of velocity-weakening is very small (a-$b \geq 0.0005$). We note that low values of *a-b* (including all the instances of velocity-weakening) appear to be better fit by a two state variable constitutive law. This may indicate a change in underlying frictional mechanisms at the grain scale, but verification of this will require further research, as the physical processes described by the two state variable friction law are poorly understood. Slip velocity exerts a much stronger control on *a-b*, which will be discussed in more detail in the following section.

Implications for Slip at Shallow Depths

Due to the overall velocity-strengthening behavior we observe, seismic slip is not expected to nucleate at the shallow depths of all three fault zone settings in this study. Moreover, coseismic slip initiated at some depth along the subduction megathrust will decelerated by shallow clay-rich sediments, making it difficult for seismic slip to reach the seafloor [*Rubin*, 2008]. Since the *a-b* values are almost indistinguishable between the three settings, resistance to seismic slip propagation will be similar which could make predictions of rupture propagation paths difficult.

We have previously noted [*Ikari et al.*, 2009b] that the velocity range at which we observe minimum values of *a-b* in the megasplay corresponds to rates observed during slow slip events in both Japan and on the San Andreas fault in California [*Linde et al.*, 1997; *Ide et al.*, 2007]. The velocity-dependent frictional behavior of samples from both the frontal thrust and the décollement zones are strikingly similar to that of the megasplay. Combining data from all three fault zone settings, the stability minima occurs at the velocity range of 1-3 μm/s (or 0.1-0.3 m/day). This indicates that in addition to the megasplay, slow slip events such as low frequency earthquakes [*Ito and Obara*, 2006] and earthquake afterslip [*Thatcher*, 1984; *Marone et al.,* 1991; *Perfettini and Ampuero*, 2008] are likely to occur on other shallow fault zone settings including the décollement [e.g. *Davis et al.*, 2006]. Propagation of slow slip events could be further assisted by pore pressure transients resulting from low permeability sediments. We measured fault-perpendicular permeability after shearing and observed consistently low values of $\leq 7\text{x}10^{-19}$ m^2. This low permeability could both trigger slow slip events and allow them to propagate further than expected.

Conclusions

We observe low values of friction for nearly all samples in this study, however samples from the décollement zone at Site 1174 are consistently lower than those from the frontal thrust area at Site C0007, which in turn are consistently lower than those from the megasplay fault zone at Site C0004. Mineralogy exerts a strong first-order control on frictional strength, as variations in clay content can explain: 1. the weakness of the megasplay fault zone relative to the wall rocks, 2. the absence of such a trend in the frontal thrust and décollement zones, and 3. the decrease in friction as a function of depth in the frontal thrust and décollement zones. Frictional stability, however is largely independent of mineralogic variation, depth, or position across fault zones. Values of *a-b* are generally positive indicating velocity-strengthening behavior, which indicates resistance to seismic slip propagation and precludes earthquake nucleation. However, minima in frictional stability are observed in the range 1-3 μm/s at all three sites, strongly indicating that all fault settings in accretionary prisms are susceptible to slow slip events.

Figures

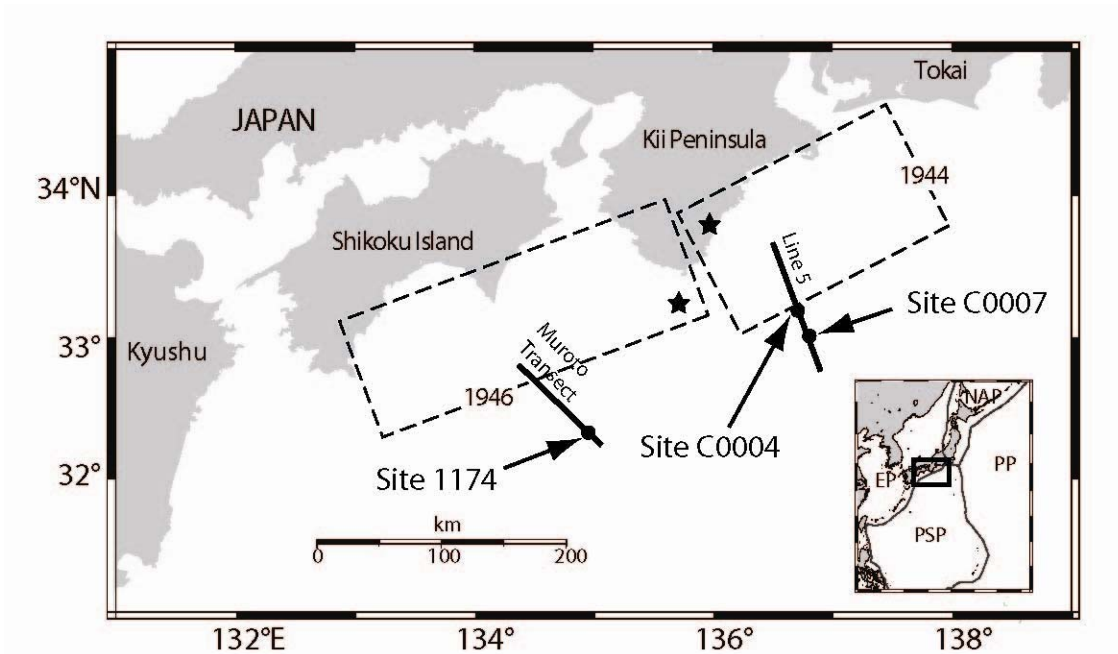

Figure 5-1: A. Map of the Nankai area showing location of drill sites C0004, C0007, and 1174 as well as the rupture areas (dashed boxes) and epicenters (stars) of the 1944 Tonankai and 1946 Nankaido earthquakes (modified from *Kimura et al.,* [2008]).

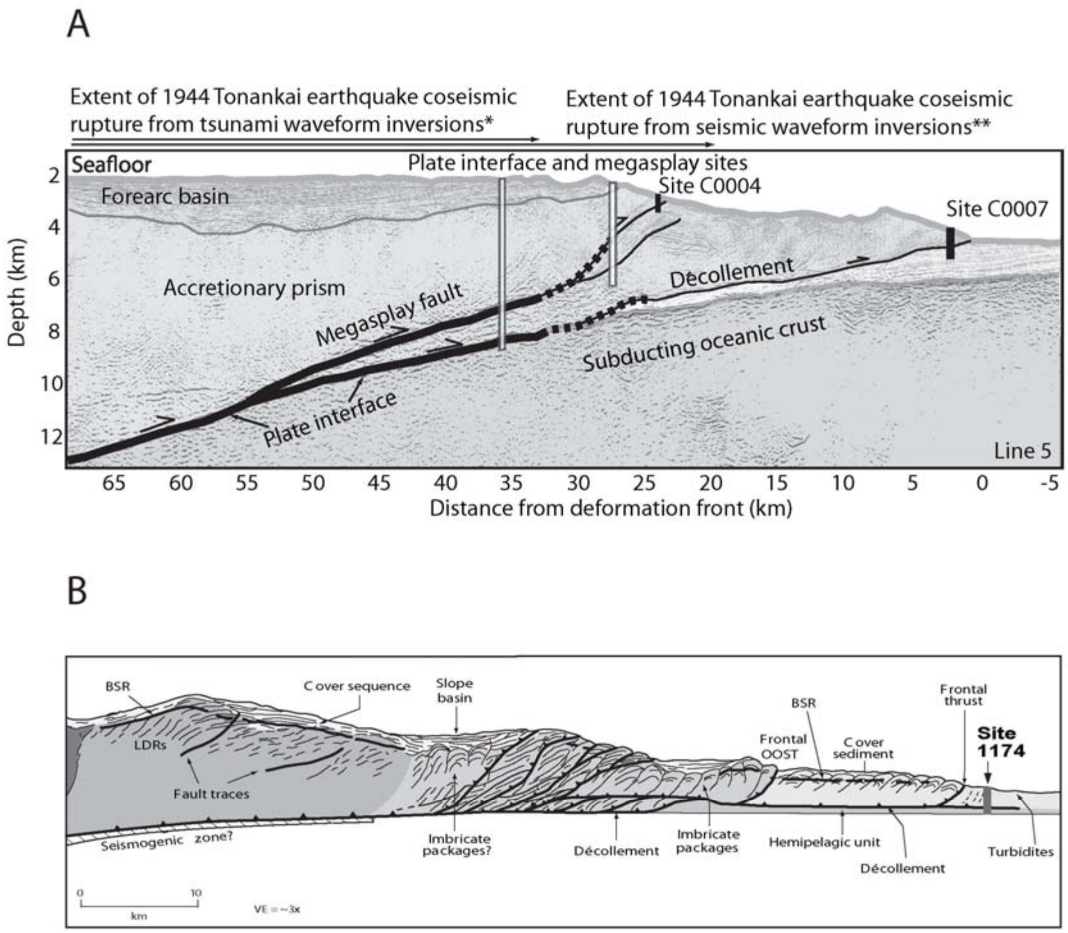

Figure 5-2: A. Profile of the accretionary prism along Line 5 in Figure 1A, showing drill site C0004 and C0007 and approximate sampling area. Also shown are estimates of the updip extent of coseismic slip inferred for the 1944 Tonankai earthquake [**Tankioka and Satake*, 2001; ***Kikuchi et al.,* 2003], (modified from *Kimura et al.,* [2008]). B. Profile of the accretionary prism along the Muroto transect, showing drill site 1174 (Modified from *Shipboard Scientific Party,* [2001a]).

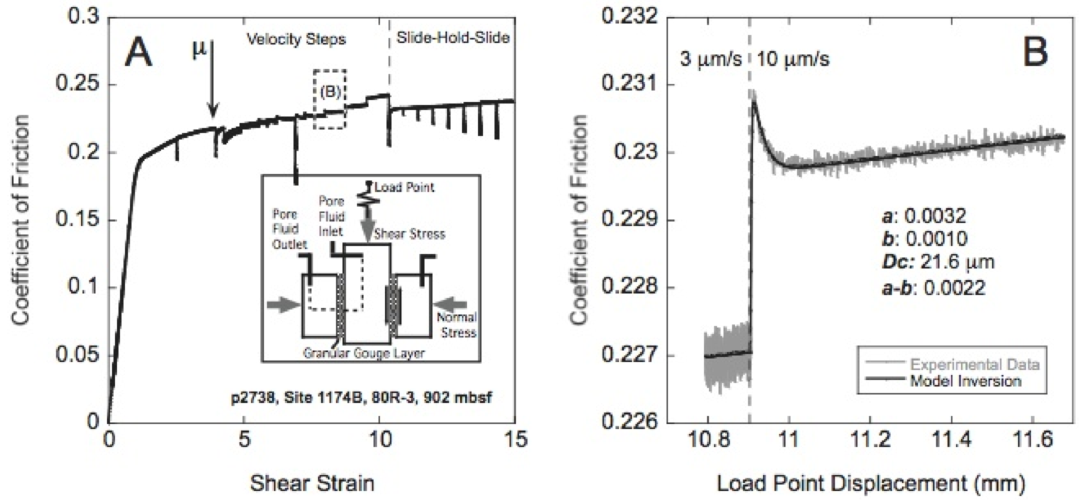

Figure 5-3: A. Example of a friction-strain curve from a typical experiment showing measurement of the coefficient of friction μ, velocity step test, and slide-hold-slide sequence. Dashed box shows velocity-step shown in Figure 3b. Inset shows double direct-shear configuration with applied stresses and pore fluid ports. B. Example of a velocity step with the model inversion superimposed on experimental data.

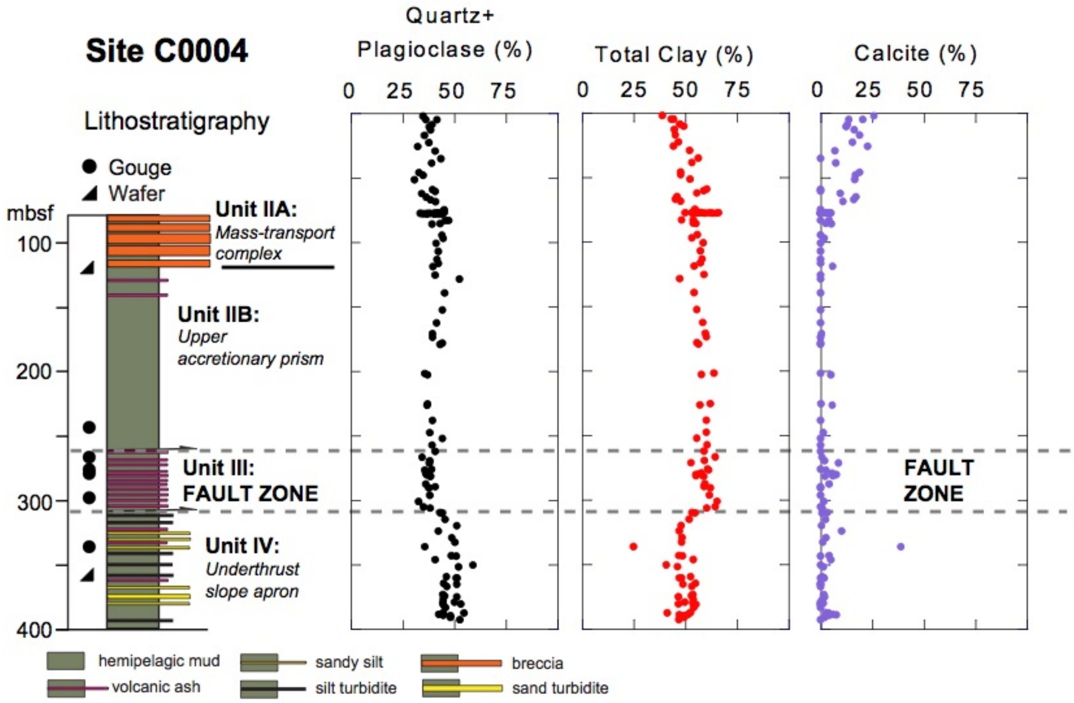

Figure 5-4: Summary of sample locations and lithostratigraphy (Left column), and mineralogy data (Right columns) at Site C0004. The lithostratigraphy is modified from M.B. Underwood (unpub. data). Symbols show experimental sample locations at the appropriate depth.

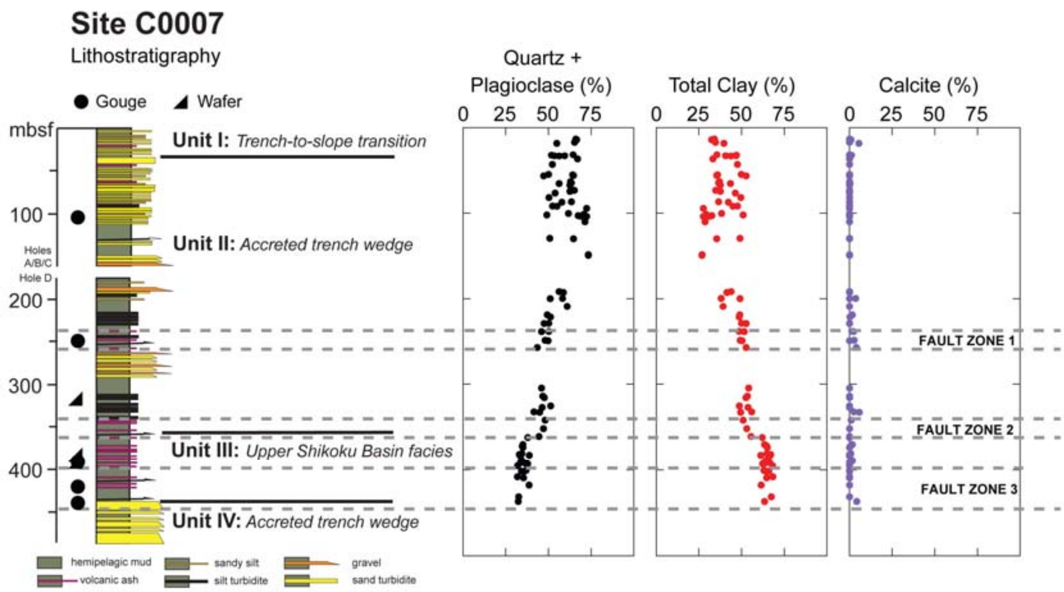

Figure 5-5: Summary of sample locations and lithostratigraphy (Left column), and mineralogy data (Right columns) at Site C0007. The lithostratigraphy is modified from M.B. Underwood (unpub. data). Symbols show experimental sample locations at the appropriate depth.

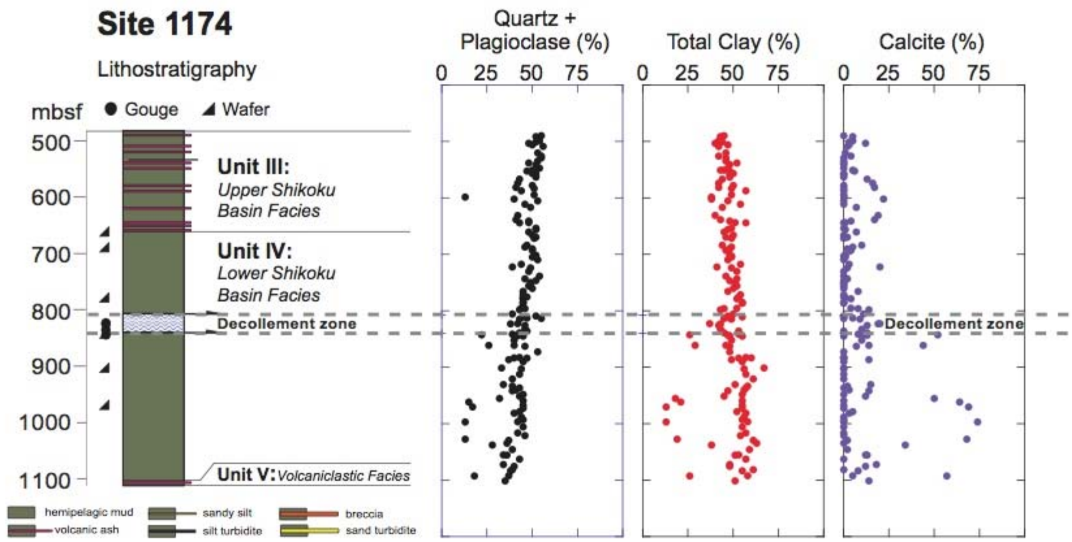

Figure 5-6: Summary of sample locations and lithostratigraphy (Left column), and mineralogy data (Right columns) at Site 1174. The lithostratigraphy is modified from *Shipboard Scientific Party* [2001b]. Symbols show experimental sample locations at the appropriate depth.

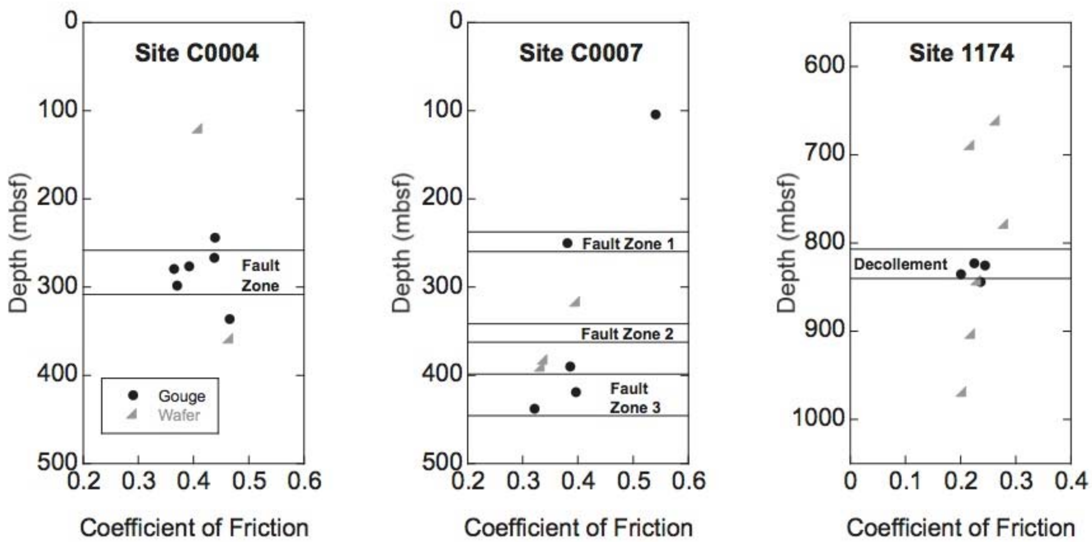

Figure 5-7: Coefficient of friction μ as a function of depth for Site C0004, C0007, and 1174. Samples tested as granular gouge or intact wafers as indicated.

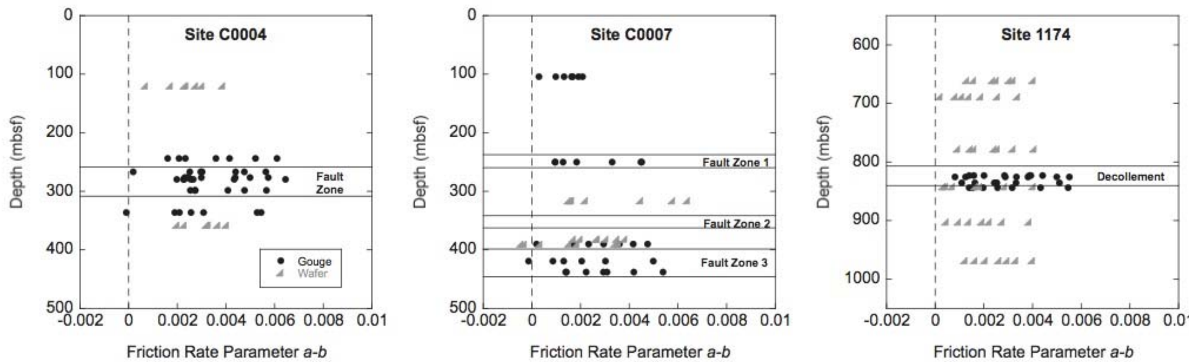

Figure 5-8: Friction rate parameter a-b as a function of depth for Site C0004, C0007, and 1174. Samples tested as granular gouge or intact wafers as indicated.

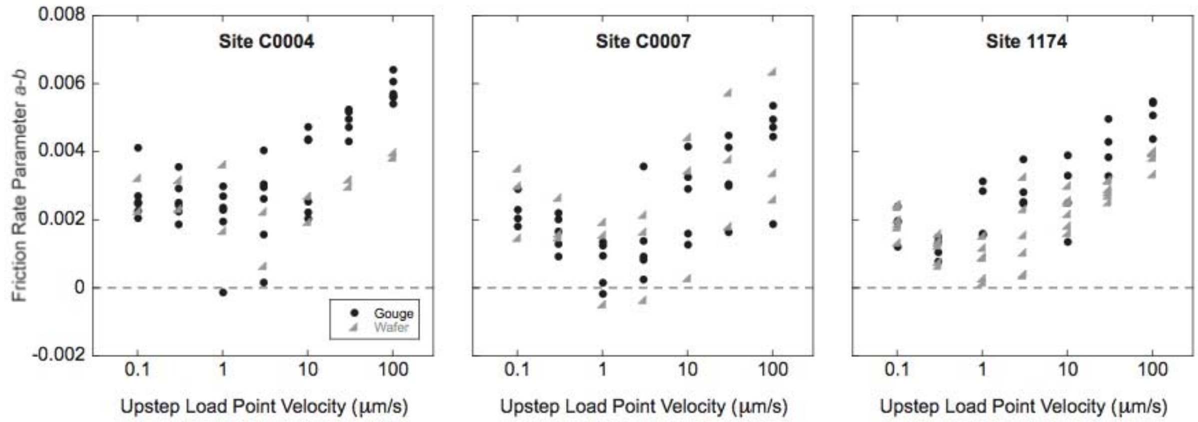

Figure 5-9: Friction rate parameter a-b as a function of upstep load point velocity for Site C0004, C0007, and 1174. Samples tested as granular gouge or intact wafers as indicated.

Tables

Experiment	Sample	Depth (mbsf)	State	σ_n' (MPa)	P_c (MPa)	Pp_a (MPa)	Sample Thickness Under Load (mm)	Maximum Shear Strain
p2118	C0004C-15X-2	119.28	wafer	25	6	5	2.42	6.1
p2627	C0004D-22R-1	243.10	powdered	25	6	5	1.39	20.5
p2102	C0004D-27R-1	266.16	powdered	25	6	5	1.14	16.0
p2069	C0004D-29R-2	275.73	powdered	25	6	5	1.07	14.4
p2067	C0004D-30R-1	278.75	powdered	25	6	5	0.86	19.9
p2068	C0004D-34R-1	297.55	powdered	25	6	5	1.06	15.7
p2121	C0004D-42R-3	335.42	powdered	25	6	5	1.41	10.8
p2112	C0004D-47R-2	357.11	wafer	25	6	5	3.88	3.7
p2654	C0007C-11X-4	103.61	remolded	25	6	5	4.58	7.0
p2777	C0007D-9R-2	249.37	remolded	25	6	5	2.52	14.6
p2640	C0007D-16R-2	315.42	wafer (fractured)	25	6	5	3.45	10.0
p2639	C0007D-23R-2	381.14	wafer	25	6	5	3.43	14.0
p2655	C0007D-24R-1	389.28	wafer (fractured)	25	6	5	3.79	21.0
p2656	C0007D-24R-1	389.28	powdered	25	6	5	2.20	22.3
p2644	C0007D-27R-1	418.42	breccia	25	6	5	3.59	12.4
p2641	C0007D-29R-1	437.19	powdered	25	6	5	2.15	29.3
p2720	1174B-55R-1	660.35	wafer	25	6	5	8.13	6.8
p2721	1174B-57R-CC	688.07	wafer	25	6	5	1.81	15.6
p2642	1174B-67R-3	777.24	wafer	25	6	5	2.35	18.0
p2705	1174B-72R-1	822.20	powdered	25	6	5	2.83	11.4
p2704	1174B-72R-2	824.53	powdered	25	6	5	2.26	14.9
p2706	1174B-73R-2	834.60	powdered	25	6	5	2.90	12.5
p2707	1174B-73R-CC	841.47	wafer (fractured)	25	6	5	1.81	17.7
p2690	1174B-74R-2	843.30	powdered	25	6	5	3.24	10.3
p2738	1174B-80R-3	902.00	wafer	25	6	5	1.99	15.0
p2752	1174B-87R-1	967.80	wafer	25	6	5	1.96	15.3

Table 5-1. Experiment parameters.

Experiment	Sample	Depth (mbsf)	V_o (μm/s)	V (μm/s)	a	b_1	D_{c1} (μm)	b_2	D_{c2} (μm)	a-b	a SD	b_1 SD	D_{c1} SD	b_2 SD	D_{c2} SD
p2118	15X-2	119.28	0.03	0.1	0.0056	0.0034	11.7			0.0023	0.00058	0.00057	2.78		
p2118	15X-2	119.28	0.1	0.3	0.0075	0.0035	7.6	0.0017	69.2	0.0023	0.00074	0.00007	2.99	0.00036	17.91
p2118	15X-2	119.28	0.3	1	0.0060	0.0028	15.2	0.0015	89.1	0.0017	0.00020	0.00025	2.50	0.00022	13.07
p2118	15X-2	119.28	1	3	0.0049	0.0022	17.6	0.0020	129.0	0.0007	0.00005	0.00006	0.80	0.00004	3.25
p2118	15X-2	119.28	3	10	0.0061	0.0025	6.4	0.0008	39.2	0.0027	0.00011	0.00011	0.54	0.00009	3.92
p2118	15X-2	119.28	10	30	0.0071	0.0027	4.5	0.0015	28.2	0.0030	0.00011	0.00010	0.31	0.00007	1.10
p2118	15X-2	119.28	30	100	0.0068	0.0030	16.6			0.0038	0.00006	0.00006	0.42		
p2627	22R-1	243.10	0.03	0.1	0.0081	0.0040	10.3			0.0041	0.00134	0.00134	5.38		
p2627	22R-1	243.10	0.1	0.3	0.0080	0.0044	9.1			0.0036	0.00172	0.00172	6.17		
p2627	22R-1	243.10	0.3	1	0.0079	0.0039	8.7	0.0016	45.8	0.0023	0.00152	0.00191	11.16	0.00182	64.79
p2627	22R-1	243.10	1	3	0.0075	0.0032	3.8	0.0026	38.0	0.0016	0.00019	0.00017	0.32	0.00006	0.94
p2627	22R-1	243.10	3	10	0.0069	0.0020	5.8	0.0028	74.5	0.0020	0.00018	0.00017	0.75	0.00006	1.99
p2627	22R-1	243.10	10	30	0.0072	0.0020	9.1			0.0052	0.00011	0.00011	0.62		
p2627	22R-1	243.10	30	100	0.0073	0.0013	24.0			0.0061	0.00011	0.00011	2.87		
p2102	27R-1	266.16	0.03	0.1	0.0066	0.0042	10.2			0.0025	0.00031	0.00031	1.01		
p2102	27R-1	266.16	0.1	0.3	0.0076	0.0046	11.6			0.0029	0.00033	0.00033	1.12		
p2102	27R-1	266.16	0.3	1	0.0076	0.0046	9.5			0.0030	0.00037	0.00035	1.24		
p2102	27R-1	266.16	1	3	0.0063	0.0028	13.7	0.0034	68.7	0.0002	0.00006	0.00009	0.70	0.00008	1.49
p2102	27R-1	266.16	3	10	0.0062	0.0018	10.2			0.0044	0.00009	0.00009	0.66		
p2102	27R-1	266.16	10	30	0.0069	0.0021	10.1			0.0047	0.00006	0.00005	0.34		
p2102	27R-1	266.16	30	100	0.0077	0.0021	10.1			0.0056	0.00153	0.00015	1.02		
p2069	29R-2	275.73	0.03	0.1	0.0055	0.0032	9.8			0.0023	0.00009	0.00009	0.35		
p2069	29R-2	275.73	0.1	0.3	0.0067	0.0042	6.7			0.0025	0.00016	0.00016	0.31		
p2069	29R-2	275.73	0.3	1	0.0061	0.0025	7.0	0.0013	31.4	0.0024	0.00020	0.00028	1.41	0.00030	5.63
p2069	29R-2	275.73	1	3	0.0063	0.0022	5.1	0.0011	38.2	0.0030	0.00078	0.00075	4.05	0.00047	21.10
p2069	29R-2	275.73	3	10	0.0062	0.0015	6.3	0.0004	3.7	0.0044	0.00037	0.00018	1.53	0.00019	22.78
p2069	29R-2	275.73	10	30	0.0065	0.0015	6.9			0.0050	0.00011	0.00011	0.66		
p2069	29R-2	275.73	30	100	0.0064	0.0007	12.3			0.0057	0.00018	0.00018	4.71		
p2067	30R-1	278.75	0.03	0.1	0.0046	0.0021	11.2			0.0025	0.00009	0.00009	0.62		
p2067	30R-1	278.75	0.1	0.3	0.0047	0.0024	16.0			0.0023	0.00011	0.00011	1.01		
p2067	30R-1	278.75	0.3	1	0.0050	0.0014	6.7	0.0016	54.4	0.0020	0.00044	0.00043	4.42	0.00025	9.63
p2067	30R-1	278.75	1	3	0.0047	0.0021	54.7			0.0026	0.00013	0.00013	6.62		
p2067	30R-1	278.75	3	10	0.0046	0.0023	75.8			0.0022	0.00014	0.00014	9.05		
p2067	30R-1	278.75	10	30	0.0054	0.0010	76.8			0.0043	0.00003	0.00003	4.50		
p2067	30R-1	278.75	30	100	0.0060	-0.0004	14.4			0.0064	0.00014	0.00014	7.94		
p2068	34R-1	297.55	0.03	0.1	0.0055	0.0028	11.4			0.0027	0.00009	0.00009	0.47		
p2068	34R-1	297.55	0.1	0.3	0.0059	0.0034	10.3			0.0025	0.00013	0.00013	0.52		
p2068	34R-1	297.55	0.3	1	0.0053	0.0026	13.2			0.0027	0.00008	0.00008	0.56		
p2068	34R-1	297.55	1	3	0.0052	0.0012	13.3			0.0041	0.00004	0.00004	0.57		
p2068	34R-1	297.55	3	10	0.0051	0.0003	8.6			0.0047	0.00011	0.00011	4.30		
p2068	34R-1	297.55	30	100	0.0064	0.0007	4.7			0.0056	0.00029	0.00029	2.81		
p2121	42R-3	335.42	0.03	0.1	0.0069	0.0048	3.2			0.0021	0.00042	0.00042	0.37		
p2121	42R-3	335.42	0.1	0.3	0.0103	0.0062	1.5	0.0022	16.9	0.0019	0.00169	0.00154	0.63	0.00039	3.60
p2121	42R-3	335.42	0.3	1	0.0101	0.0067	1.9	0.0035	43.9	-0.0001	0.00182	0.00175	0.74	0.00028	5.89
p2121	42R-3	335.42	1	3	0.0085	0.0054	10.8			0.0031	0.00024	0.00023	0.64		
p2121	42R-3	335.42	3	10	0.0078	0.0029	5.7	0.0024	52.1	0.0025	0.00036	0.00035	1.28	0.00019	5.23
p2121	42R-3	335.42	10	30	0.0078	0.0025	9.9			0.0053	0.00005	0.00005	0.24		
p2121	42R-3	335.42	30	100	0.0083	0.0029	13.3			0.0054	0.00008	0.00008	0.52		
p2112	47R-2	357.11	0.03	0.1	0.0066	0.0034	9.7			0.0033	0.00075	0.00075	3.06		
p2112	47R-2	357.11	0.1	0.3	0.0077	0.0045	6.7			0.0032	0.00118	0.00118	2.44		
p2112	47R-2	357.11	0.3	1	0.0093	0.0057	9.6			0.0036	0.00079	0.00078	1.84		
p2112	47R-2	357.11	1	3	0.0090	0.0047	7.1	0.0021	43.1	0.0023	0.00058	0.00057	1.40	0.00028	4.10
p2112	47R-2	357.11	3	10	0.0083	0.0048	9.6	0.0015	102.9	0.0020	0.00014	0.00014	0.44	0.00006	5.24
p2112	47R-2	357.11	10	30	0.0084	0.0052	10.3			0.0032	0.00008	0.00008	0.19		
p2112	47R-2	357.11	30	100	0.0108	0.0068	10.3			0.0040	0.00013	0.00013	0.25		

Table 5-2A: Constitutive friction parameters: Site C0004.

Experiment	Sample	Depth (mbsf)	V_o (μm/s)	V (μm/s)	a	b_1	D_{c1} (μm)	b_2	D_{c2} (μm)	a-b	a SD	b_1 SD	D_{c1} SD	b_2 SD	D_{c2} SD
p2654	C0007D-11X4	103.61	0.03	0.1	0.0068	0.0048	11.8			0.0021	0.00033	0.00032	1.10		
p2654	C0007D-11X4	103.61	0.1	0.3	0.0061	0.0048	21.9			0.0013	0.00024	0.00024	1.60		
p2654	C0007D-11X4	103.61	0.3	1	0.0076	0.0046	7.1	0.0021	40.7	0.0010	0.00036	0.00037	1.09	0.00032	5.55
p2654	C0007D-11X4	103.61	1	3	0.0081	0.0050	7.6	0.0029	79.8	0.0003	0.00035	0.00033	0.57	0.00008	2.75
p2654	C0007D-11X4	103.61	3	10	0.0075	0.0059	14.6			0.0016	0.00021	0.00021	0.70		
p2654	C0007D-11X4	103.61	10	30	0.0079	0.0062	24.8			0.0017	0.00007	0.00007	0.36		
p2654	C0007D-11X4	103.61	30	100	0.0101	0.0044	9.5	0.0039	82.0	0.0019	0.00533	0.00506	52.60	0.00263	86.03
p2777	C0007D-9R-2	249.37	0.03	0.1	0.0063	0.0045	5.1			0.0018	0.00011	0.00011	0.15		
p2777	C0007D-9R-2	249.37	0.1	0.3	0.0063	0.0043	5.3	0.0011	59.8	0.0009	0.00013	0.00013	0.25	0.00006	4.03
p2777	C0007D-9R-2	249.37	0.3	1	0.0081	0.0046	2.8	0.0023	23.9	0.0013	0.00028	0.00024	0.25	0.00010	1.02
p2777	C0007D-9R-2	249.37	1	3	0.0066	0.0039	9.9	0.0018	89.8	0.0009	0.00006	0.00006	0.26	0.00003	2.00
p2777	C0007D-9R-2	249.37	3	10	0.0076	0.0027	4.6	0.0017	41.3	0.0033	0.00038	0.00035	1.08	0.00016	4.27
p2777	C0007D-9R-2	249.37	10	30	0.0072	0.0027	13.9			0.0045	0.00005	0.00005	0.33		
p2777	C0007D-9R-2	249.37	30	100	0.0090	0.0027	5.1	0.0018	38.7	0.0045	0.00027	0.00025	0.83	0.00012	2.53
p2640	C0007D-16R2	315.42	0.03	0.1	0.0044	0.0029	12.5			0.0015	0.00011	0.00011	0.61		
p2640	C0007D-16R2	315.42	0.1	0.3	0.0060	0.0032	9.2	0.0011	49.4	0.0016	0.00014	0.00017	0.87	0.00016	5.87
p2640	C0007D-16R2	315.42	0.3	1	0.0047	0.0031	30.7			0.0016	0.00008	0.00008	1.03		
p2640	C0007D-16R2	315.42	1	3	0.0070	0.0028	9.8	0.0021	67.7	0.0022	0.00011	0.00010	0.68	0.00007	2.34
p2640	C0007D-16R2	315.42	3	10	0.0071	0.0027	12.2			0.0044	0.00011	0.00011	0.66		
p2640	C0007D-16R2	315.42	10	30	0.0082	0.0024	7.1			0.0058	0.00012	0.00012	0.41		
p2640	C0007D-16R2	315.42	30	100	0.0077	0.0013	19.3			0.0064	0.00010	0.00010	1.88		
p2639	C0007D 23R2	381.14	0.03	0.1	0.0041	0.0011	19.3			0.0030	0.00013	0.00013	3.41		
p2639	C0007D 23R2	381.14	0.1	0.3	0.0049	0.0023	15.0			0.0027	0.00011	0.00011	1.00		
p2639	C0007D 23R2	381.14	0.3	1	0.0065	0.0026	2.3	0.0019	48.4	0.0020	0.00057	0.00054	0.63	0.00007	2.23
p2639	C0007D 23R2	381.14	1	3	0.0043	0.0026	73.5			0.0017	0.00002	0.00002	0.83		
p2639	C0007D 23R2	381.14	3	10	0.0053	0.0013	8.9	0.0006	75.8	0.0035	0.00015	0.00015	1.86	0.00008	13.45
p2639	C0007D 23R2	381.14	10	30	0.0052	0.0014	25.5			0.0038	0.00003	0.00003	0.74		
p2639	C0007D 23R2	381.14	30	100	0.0059	0.0011	33.3	0.0022	146.7	0.0026	0.00006	0.00012	5.00	0.00011	8.70
p2655	C0007D-24R-1	389.28	0.03	0.1	0.0040	0.0005	44.2			0.0035	0.00020	0.00020	44.28		
p2655	C0007D-24R-1	389.28	0.1	0.3	0.0035	0.0020	27.1			0.0015	0.00027	0.00026	6.30		
p2655	C0007D-24R-1	389.28	0.3	1	0.0039	0.0018	11.9	0.0026	136.0	-0.0005	0.00023	0.00023	2.66	0.00010	8.78
p2655	C0007D-24R-1	389.28	1	3	0.0043	0.0020	16.3	0.0026	136.5	-0.0003	0.00010	0.00011	1.59	0.00007	5.06
p2655	C0007D-24R-1	389.28	3	10	0.0045	0.0020	10.2	0.0022	83.5	0.0003	0.00015	0.00015	1.31	0.00009	3.47
p2655	C0007D-24R-1	389.28	10	30	0.0060	0.0025	7.4	0.0017	63.5	0.0018	0.00009	0.00008	0.41	0.00004	1.71
p2655	C0007D-24R-1	389.28	30	100	0.0059	0.0016	18.9	0.0009	102.5	0.0034	0.00007	0.00009	1.97	0.00009	9.04
p2656	C0007D-24R-1	389.28	0.03	0.1	0.0042	0.0012	4.8	0.0006	43.2	0.0023	0.00069	0.00066	6.51	0.00033	29.23
p2656	C0007D-24R-1	389.28	0.1	0.3	0.0049	0.0022	4.3	0.0010	47.8	0.0017	0.00098	0.00092	3.67	0.00029	18.40
p2656	C0007D-24R-1	389.28	0.3	1	0.0035	0.0018	13.7	0.0016	125.0	0.0002	0.00034	0.00034	5.19	0.00019	22.34
p2656	C0007D-24R-1	389.28	1	3	0.0061	0.0025	35.6			0.0036	0.00032	0.00032	6.60		
p2656	C0007D-24R-1	389.28	3	10	0.0046	0.0017	19.2			0.0029	0.00029	0.00029	4.79		
p2656	C0007D-24R-1	389.28	10	30	0.0059	0.0018	13.5			0.0041	0.00013	0.00013	1.33		
p2656	C0007D-24R-1	389.28	30	100	0.0063	0.0016	12.3			0.0047	0.00015	0.00015	1.58		
p2644	C0007D-27R1	418.42	0.1	0.3	0.0056	0.0017	6.6	0.0019	46.4	0.0020	0.00132	0.00127	17.95	0.00083	23.67
p2644	C0007D-27R1	418.42	0.3	1	0.0053	0.0018	12.5	0.0037	106.5	-0.0002	0.00041	0.00041	5.97	0.00024	8.66
p2644	C0007D-27R1	418.42	1	3	0.0062	0.0033	8.5	0.0021	76.4	0.0008	0.00012	0.00012	0.52	0.00006	2.54
p2644	C0007D-27R1	418.42	3	10	0.0079	0.0038	4.1	0.0028	51.0	0.0013	0.00030	0.00028	0.44	0.00008	1.66
p2644	C0007D-27R1	418.42	10	30	0.0065	0.0019	9.4	0.0016	62.3	0.0030	0.00009	0.00009	0.85	0.00007	2.49
p2644	C0007D-27R1	418.42	30	100	0.0053	0.0003	108.3			0.0050	0.00003	0.00003	23.27		
p2641	C0007D-29R1	437.19	0.03	0.1	0.0041	0.0012	36.6			0.0029	0.00020	0.00020	10.55		
p2641	C0007D-29R1	437.19	0.1	0.3	0.0039	0.0017	41.3			0.0022	0.00013	0.00013	4.67		
p2641	C0007D-29R1	437.19	0.3	1	0.0039	0.0025	48.8			0.0014	0.00005	0.00004	1.37		
p2641	C0007D-29R1	437.19	1	3	0.0042	0.0028	104.2			0.0014	0.00001	0.00001	0.93		
p2641	C0007D-29R1	437.19	3	10	0.0048	0.0007	82.0			0.0042	0.00004	0.00004	11.75		
p2641	C0007D-29R1	437.19	10	30	0.0054	0.0024	127.0			0.0031	0.00001	0.00001	1.38		
p2641	C0007D-29R1	437.19	30	100	0.0065	0.0012	93.6			0.0054	0.00002	0.00002	2.36		

Table 5-2B: Constitive friction parameters: Site C0007.

Experiment	Sample	Depth (mbsf)	V_o (μm/s)	V (μm/s)	*a*	b_1	D_{c1} (μm)	b_2	D_{c2} (μm)	*a-b*	*a* SD	b_1 SD	D_{c1} SD	b_2 SD	D_{c2} SD
p2720	1174B-55R1	660.35	0.03	0.1	0.0044	0.0019	9.9			0.0025	0.00016	0.00016	1.03		
p2720	1174B-55R1	660.35	0.1	0.3	0.0043	0.0019	10.0	0.0011	58.7	0.0013	0.00024	0.00027	2.90	0.00024	11.58
p2720	1174B-55R1	660.35	0.3	1	0.0088	0.0055	1.2	0.0018	71.6	0.0016	0.00005	0.00005	0.22	0.00010	6.33
p2720	1174B-55R1	660.35	1	3	0.0072	0.0034	3.1	0.0014	186.9	0.0023	0.00044	0.00043	0.48	0.00003	10.67
p2720	1174B-55R1	660.35	3	10	0.0053	0.0023	5.4			0.0030	0.00027	0.00027	0.89		
p2720	1174B-55R1	660.35	10	30	0.0050	0.0018	9.9			0.0032	0.00010	0.00010	0.71		
p2720	1174B-55R1	660.35	30	100	0.0056	0.0016	9.1			0.0040	0.00011	0.00011	0.79		
p2721	1174B-57R-CC	688.07	0.03	0.1	0.0025	0.0011	7.2			0.0014	0.00015	0.00015	1.30		
p2721	1174B-57R-CC	688.07	0.1	0.3	0.0025	0.0017	10.4			0.0008	0.00017	0.00017	1.45		
p2721	1174B-57R-CC	688.07	0.3	1	0.0039	0.0020	3.4	0.0017	100.5	0.0002	0.00050	0.00049	1.17	0.00008	7.54
p2721	1174B-57R-CC	688.07	1	3	0.0043	0.0015	6.3	0.0018	175.4	0.0011	0.00021	0.00021	1.25	0.00004	8.47
p2721	1174B-57R-CC	688.07	3	10	0.0052	0.0022	1.6	0.0012	31.9	0.0019	0.00085	0.00083	0.95	0.00011	3.40
p2721	1174B-57R-CC	688.07	10	30	0.0043	0.0017	7.0			0.0025	0.00008	0.00008	0.39		
p2721	1174B-57R-CC	688.07	30	100	0.0044	0.0011	10.1			0.0034	0.00009	0.00009	1.07		
p2642	1174B-67R3	777.24	0.03	0.1	0.0039	0.0015	10.9			0.0024	0.00026	0.00025	2.90		
p2642	1174B-67R3	777.24	0.1	0.3	0.0035	0.0012	8.6	0.0009	56.2	0.0014	0.00023	0.00025	3.67	0.00019	12.09
p2642	1174B-67R3	777.24	0.3	1	0.0037	0.0013	10.6	0.0015	83.5	0.0009	0.00010	0.00010	1.53	0.00007	4.33
p2642	1174B-67R3	777.24	1	3	0.0038	0.0011	11.7	0.0011	100.0	0.0016	0.00005	0.00005	0.91	0.00003	3.08
p2642	1174B-67R3	777.24	3	10	0.0039	0.0014	19.3			0.0025	0.00004	0.00004	0.79		
p2642	1174B-67R3	777.24	10	30	0.0047	0.0015	16.5			0.0032	0.00004	0.00004	0.53		
p2642	1174B-67R3	777.24	30	100	0.0053	0.0012	18.5			0.0040	0.00005	0.00005	0.93		
p2705	1174B-72R1	822.20	0.03	0.1	0.0028	0.0008	12.8			0.0020	0.00005	0.00005	0.99		
p2705	1174B-72R1	822.20	0.1	0.3	0.0028	0.0007	9.1	0.0007	83.5	0.0014	0.00006	0.00006	1.41	0.00003	4.75
p2705	1174B-72R1	822.20	0.3	1	0.0032	0.0006	7.1	0.0010	119.0	0.0016	0.00007	0.00007	1.37	0.00002	3.78
p2705	1174B-72R1	822.20	1	3	0.0031	0.0002	7.3			0.0028	0.00006	0.00006	2.81		
p2705	1174B-72R1	822.20	3	10	0.0031	-0.0008	185.4			0.0039	0.00002	0.00002	10.37		
p2705	1174B-72R1	822.20	10	30	0.0037	-0.0002	71.8			0.0039	0.00004	0.00004	33.67		
p2705	1174B-72R1	822.20	30	100	0.0040	-0.0004	6.0			0.0044	0.00019	0.00019	4.81		
p2704	1174B-72R2	824.53	0.03	0.1	0.0022	0.0010	36.4			0.0012	0.00017	0.00017	10.20		
p2704	1174B-72R2	824.53	0.1	0.3	0.0020	0.0012	17.7			0.0008	0.00028	0.00028	6.79		
p2704	1174B-72R2	824.53	0.3	1	0.0043	0.0014	44.8			0.0029	0.00019	0.00019	9.69		
p2704	1174B-72R2	824.53	1	3	0.0050	0.0012	5.4			0.0038	0.00029	0.00029	1.66		
p2704	1174B-72R2	824.53	3	10	0.0041	0.0009	2.9	-0.0001	56.8	0.0033	0.00045	0.00043	2.36	0.00007	55.32
p2704	1174B-72R2	824.53	10	30	0.0057	0.0018	1.3	-0.0011	121.5	0.0050	0.00002	0.00002	0.35	0.00003	6.21
p2704	1174B-72R2	824.53	30	100	0.0046	-0.0009	72.9			0.0055	0.00005	0.00005	6.54		
p2706	1174B-73R2	834.60	0.03	0.1	0.0030	0.0005	4.3			0.0024	0.00011	0.00011	1.11		
p2706	1174B-73R2	834.60	0.1	0.3	0.0034	0.0011	2.2	0.0012	107.9	0.0011	0.00028	0.00028	0.70	0.00002	2.85
p2706	1174B-73R2	834.60	0.3	1	0.0028	0.0011	83.6			0.0016	0.00002	0.00002	2.35		
p2706	1174B-73R2	834.60	1	3	0.0031	0.0007	20.7			0.0025	0.00005	0.00005	2.08		
p2706	1174B-73R2	834.60	3	10	0.0033	0.0008	39.9			0.0025	0.00004	0.00004	2.97		
p2706	1174B-73R2	834.60	10	30	0.0036	0.0003	133.5			0.0033	0.00003	0.00003	25.67		
p2706	1174B-73R2	834.60	30	100	0.0043	-0.0008	991.5			0.0051	0.00003	0.00147	9079.89		
p2707	1174B-73R-CC	841.47	0.03	0.1	0.0025	0.0007	19.1			0.0018	0.00003	0.00003	1.17		
p2707	1174B-73R-CC	841.47	0.1	0.3	0.0024	0.0011	19.5	0.0007	112.8	0.0007	0.00004	0.00005	1.57	0.00005	8.13
p2707	1174B-73R-CC	841.47	0.3	1	0.0028	0.0010	11.5	0.0015	61.6	0.0003	0.00007	0.00009	1.93	0.00008	2.77
p2707	1174B-73R-CC	841.47	1	3	0.0028	0.0008	21.4	0.0016	79.9	0.0004	0.00004	0.00009	3.10	0.00010	3.43
p2707	1174B-73R-CC	841.47	3	10	0.0034	0.0011	15.9	0.0006	68.6	0.0016	0.00006	0.00009	2.08	0.00010	8.17
p2707	1174B-73R-CC	841.47	10	30	0.0040	0.0011	20.7			0.0028	0.00005	0.00005	1.25		
p2707	1174B-73R-CC	841.47	30	100	0.0049	0.0009	18.3			0.0040	0.00011	0.00011	3.17		
p2690	1174B-74R2	843.30	0.03	0.1	0.0026	0.0003	5.8	0.0003	7.5	0.0020	0.00058	0.00029	30350.51	0.00029	993.69
p2690	1174B-74R2	843.30	0.1	0.3	0.0026	0.0004	4.8	0.0006	14.3	0.0015	0.00073	0.00211	1060.27	0.00239	74.97
p2690	1174B-74R2	843.30	0.3	1	0.0056	0.0017	2.0	0.0007	77.4	0.0031	0.00137	0.00135	2.88	0.00013	22.02
p2690	1174B-74R2	843.30	1	3	0.0041	0.0028	30.1	-0.0012	52.5	0.0025	0.00005	0.00002	1.22	0.00002	3.07
p2690	1174B-74R2	843.30	3	10	0.0028	0.0007	9.1	0.0007	83.5	0.0014	0.00006	0.00006	1.41	0.00003	4.75
p2690	1174B-74R2	843.30	10	30	0.0039	-0.0004	90.9			0.0043	0.00003	0.00003	8.84		
p2690	1174B-74R2	843.30	30	100	0.0046	-0.0009	100.9			0.0054	0.00004	0.00003	7.62		
p2738	1174B-80R3	902.00	0.03	0.1	0.0025	0.0006	21.0			0.0019	0.00006	0.00006	3.02		
p2738	1174B-80R3	902.00	0.1	0.3	0.0029	0.0009	3.7	0.0007	41.1	0.0013	0.00034	0.00032	2.74	0.00011	8.01
p2738	1174B-80R3	902.00	0.3	1	0.0037	0.0012	13.1	0.0016	109.7	0.0009	0.00026	0.00024	3.66	0.00007	5.86
p2738	1174B-80R3	902.00	1	3	0.0028	0.0007	14.6	0.0016	182.8	0.0004	0.00006	0.00006	2.08	0.00002	5.55
p2738	1174B-80R3	902.00	3	10	0.0032	0.0010	21.6			0.0022	0.00004	0.00004	1.28		
p2738	1174B-80R3	902.00	10	30	0.0036	0.0008	26.1			0.0027	0.00007	0.00007	2.98		

Table 5-2C: Constitutive friction parameters: Site 1174.

Experiment	Sample	Depth (mbsf)	V_o (µm/s)	V (µm/s)	*a*	b_1	D_{c1} (µm)	b_2	D_{c2} (µm)	*a-b*	*a* SD	b_1 SD	D_{c1} SD	b_2 SD	D_{c2} SD
p2738	1174B-80R3	902.00	30	100	0.0045	0.0006	19.2			0.0038	0.00005	0.00005	2.04		
p2752	1174B-87R1	967.80	0.03	0.1	0.0024	0.0004	37.3			0.0020	0.00005	0.00005	7.04		
p2752	1174B-87R1	967.80	0.1	0.3	0.0025	0.0009	30.7			0.0016	0.00007	0.00007	3.55		
p2752	1174B-87R1	967.80	0.3	1	0.0022	0.0010	68.2			0.0012	0.00007	0.00007	8.17		
p2752	1174B-87R1	967.80	1	3	0.0038	0.0005	47.8			0.0033	0.00013	0.00013	13.88		
p2752	1174B-87R1	967.80	3	10	0.0033	0.0007	28.8			0.0026	0.00011	0.00011	7.19		
p2752	1174B-87R1	967.80	10	30	0.0035	0.0006	31.4			0.0029	0.00002	0.00002	2.04		
p2752	1174B-87R1	967.80	30	100	0.0043	0.0003	65.3			0.0040	0.00002	0.00002	7.74		

Table 2C contd.

Chapter 6

ON THE RELATION BETWEEN FAULT STRENGTH AND FRICTIONAL STABILITY

Abstract

A fundamental problem in fault mechanics is whether slip instability associated with earthquake nucleation depends on absolute fault strength. We present laboratory experimental evidence for a systematic relationship between frictional strength and stability for a wide range of constituent minerals relevant to natural faults. All of the frictionally weak gouges ($\mu < 0.5$) are composed of phyllosilicate minerals and exhibit increased friction with slip velocity, known as velocity-strengthening behavior, which suppresses frictional instability. In contrast, fault gouges with higher frictional strength exhibit both velocity-weakening and velocity-strengthening frictional behavior. These materials are dominantly quartzo-feldspathic in composition, but in some cases are phyllosilicate-rich. We also find that frictional velocity-dependence evolves systematically with shear strain, such that a critical shear strain is required to allow slip instability. As applied to tectonic faults, our results suggest that seismic behavior and the mode of fault slip may evolve predictably as a function of accumulated offset.

Introduction

A common assumption in many studies of fault and earthquake mechanics is that earthquakes nucleate on mechanically strong portions of faults (asperities), whereas aseismic slip occurs on weak patches (e.g. Ruff and Kanamori, 1983; Tichelaar and Ruff 1993; but see Scholz, 1992). Theoretical treatments and experimental results, however, have repeatedly demonstrated that earthquake source parameters and stick-slip frictional instability are independent of absolute fault strength, and depend only on the relative change in strength (e.g. Brune, 1970; Johnson and Scholz, 1976; Tullis, 1988). To date, there is little direct evidence linking the stability of fault slip with absolute frictional strength, although some theoretical arguments suggest this might be the case (e.g., Beeler, 2007).

Previous laboratory studies have shown that the mineralogy of fault gouge exerts a first-order control on the frictional properties of faults, including both strength and sliding stability (Shimamoto and Logan, 1981a,b; Logan and Rauenzahn, 1987; Morrow et al., 1992, 2000; Ikari et al., 2007). Other laboratory studies have highlighted the importance of net shear strain in determining frictional properties, with higher strain and increased shear localization leading to unstable slip (e.g. Byerlee et al., 1978; Marone et al., 1992; Logan et al., 1992; Beeler et al., 1996; Scruggs and Tullis, 1998; Marone, 1998; Mair and Marone, 1999). These observations are consistent with field data showing systematic changes in fault properties as a function of maturity, including development of internal fabric, shear localization, and evolution of structural complexity (Wesnousky, 1988; Cowie and Scholz, 1992; Collettini and Holdsworth, 2004; Sagy et al., 2007; Frost et al., 2009). However, neither the general relationship between fault stability and shear strain nor the underlying processes are well understood.

Here, we investigate the relationships between fault strength, stability, and shear strain using laboratory experiments on a suite of gouge compositions relevant to natural faults. Specifically, we: (1) provide a critical assessment of the hypothesized link between fault strength and frictional stability; and (2) evaluate the effects of shear strain on frictional behavior, for shear strains γ of over 100 (10,000%), normal stresses up to 50 MPa, and slip velocities relevant to earthquake nucleation.

Methods

We studied the frictional properties of synthetic and natural fault gouges spanning a wide range of compositions and mineralogies that are common in major fault zones (e.g., Vrolijk and van der Pluijm, 1999; Solum et al., 2003; Underwood, 2007; Smith and Faulkner, 2010). The natural materials include illite shale, chlorite schist, biotite schist, talc schist, serpentinite, andesine feldspar, and Westerly granite. Synthetic gouges included monomineralic and bimineralic mixtures prepared from commercially obtained powders of Ca-montmorillonite (mean grain size 60 μm), kaolinite (maximum grain size 4 μm), muscovite (maximum grain size 90 μm), and quartz (mean grain size 130 μm). The natural gouges were prepared from rock samples ground in a rotary mill and sieved to < 106 μm or (for Westerly granite) < 150 μm.

Gouge layers were prepared to a uniform thickness and deformed in the double-direct shear configuration (Figure 6-1A inset). In this configuration, the nominal frictional contact area and the normal stress are constant throughout shearing. We sheared layers using a displacement rate boundary condition (11 μm/s) imposed at the edge of the gouge layer via a fast-acting servo-hydraulic controller. All experiments were conducted at room temperature and humidity (see Ikari et al., 2007 for additional details of the experimental arrangement).

Our goals were to measure frictional strength and stability over a wide range of shear strains. Frictional stability is determined by the dependence of sliding friction on slip velocity and thus our experiments included measurements of the friction rate parameter $a\text{-}b = \Delta\mu/\Delta lnV$ (e.g., Dieterich, 1979; Scholz, 2002). To facilitate comparison between experiments we conducted velocity step tests over the range from 1-300 μm/s at specified shear strains in the range of $\gamma = 5$ to 100 in each experiment. Shear strain was determined from the integral of shear displacement divided by instantaneous layer thickness. Due to variable layer thinning among samples, not all samples reached the same shear strains, but strains of $\geq$ ~50 were attained in all experiments. The coefficient of sliding friction μ was determined from the ratio of shear stress τ over normal stress σ_n and assuming that cohesion is zero.

Results

Figure 6-1 shows the coefficient of friction during steady sliding for our suite of samples. The data show that phyllosilicate gouges (biotite, montmorillonite, and talc) are frictionally weak ($\mu < 0.5$) whereas gouges rich in framework silicate minerals (quartz, andesine feldspar, Westerly granite) are stronger ($\mu > 0.6$). However, phyllosilicate gouges are not uniformly weak (Figure 1A); those containing muscovite, montmorillonite/quartz, illite, and chlorite exhibit a range of friction coefficients between that of talc (μ = ~0.25) and quartz (μ = ~0.60). Kaolinite, kaolinite/quartz and serpentine gouges are uniformly strong ($\mu \sim 0.65$). Some of these materials also exhibit significant strain-hardening (e.g. montmorillonite/quartz, chlorite), which results in larger ranges of the friction values (Figure 6-1A); however, steady-state friction is generally reached for $\gamma \leq 10$. With the exception of montmorillonite, friction values are nearly identical at 20 and 50 MPa normal stress.

Examination of the friction rate parameter *a-b* (Figure 6-1B) over the range of gouge compositions reveals two distinct populations; gouges that exhibit strictly velocity-strengthening behavior, and gouges that exhibit both velocity-strengthening and velocity-weakening, depending on experimental conditions. Values of *a-b* for strictly velocity-strengthening gouges ranges from ~0 (montmorillonite, 20 MPa) to 0.011 (montmorillonite, 20 MPa and biotite, 20 MPa), and values of *a-b* for gouges that exhibit some velocity-weakening range from to -0.006 (serpentine, 20 MPa) to 0.004 (quartz, 20 MPa). Notably, the weakest gouges are uniformly velocity-strengthening, whereas the frictionally stronger gouges exhibit both velocity-weakening and velocity-strengthening (Figure 6-2). The velocity-strengthening gouges are all rich in phyllosilicate minerals, whereas the set of velocity-weakening gouges includes those rich in framework minerals, but also some phyllosilicates (kaolinite, kaolinite/quartz, serpentine). For all gouges, fault frictional stability at 50 MPa is nearly identical to that observed at 20 MPa.

We also find a clear dependence of *a-b* on shear strain for the gouges that exhibit velocity-weakening behavior (Figure 6-3). For example, in Westerly Granite gouge at 50 MPa, *a-b* evolves from velocity-strengthening (values up to 0.0027) to velocity-weakening (values as low as -0.0037) over shear strains from 0 to ~30 (Figure 6-3A). In contrast, the effect of shear strain on the parameter *a-b* is minimal for exclusively velocity-strengthening gouges (e.g. chlorite gouge at 20 MPa, Figure 6-3B). We note however, that the range of *a-b* values at a given shear strain can be large, especially for the velocity-strengthening gouges (Figure 6-3B).   This is a consequence of increasing *a-b* values as slip velocity increases, which is a consistent observation (e.g., Saffer and Marone, 2003).

Discussion

Our data demonstrate a systematic relationship between frictional strength and stability that carries important implications for linkages between absolute fault strength and slip stability (Figures 6-1, 6-2). For a wide range of materials relevant to natural faults, velocity-strengthening frictional behavior can occur in materials of any frictional strength, but velocity-weakening occurs only in strong gouges, with $\mu > 0.5$ (Figures 6-1, 6-2). Recalling that $a\text{-}b = \Delta\mu/\Delta lnV$, many previous works have pointed out that: 1) frictional instability and thus the potential for seismic slip depends on the relative change rather than the absolute value of strength; and 2) there is no *a priori* reason to assume a relationship between frictional strength and stability. This is a consequence of the individual parameters *a* and *b* being treated as empirically derived constants and assumed to be independent of fault strength. If instead these parameters are considered functions of the overall friction level (e.g. Beeler, 2007), rate- and state- friction laws are consistent with a dependence of fault stability on frictional strength, as supported by our experimental results.

The links between frictional strength, net shear strain, and slip stability have important implications for slip behavior on natural faults (Figure 6-4). For example, our results suggest that immature faults hosted in phyllosilicate-rich rocks should exhibit low frictional strength and a tendency for stable creep, due to velocity-strengthening frictional behavior (path 1 in Figure 4). In this case, aseismic slip is expected to persist with increasing fault offset because the velocity dependence of friction for these materials is largely independent of shear strain (Figure 6-3). Unstable slip on such a fault would require modification of the gouge composition, or mechanisms that change its physical properties or increase its frictional strength, such as cementation or consolidation (Bernabé et al., 1992; Moore and Saffer, 2001; Marone and Saffer, 2007) (path 2, Figure 6-4). Immature faults in strong minerals, such as those with a non-phyllosilicate protolith, may evolve from being frictionally stable (velocity-strengthening) to unstable (velocity-weakening) with increased shear strain (Figure 6-3A; path 3 in Figure 6-4). A transition from stable to unstable behavior as a function of increasing fault maturity and offset is consistent with shear localization, as noted in previous works (Byerlee et al., 1978; Shimamoto and Logan, 1981a,b; Logan et al., 1992; Marone et al., 1992; Beeler et al., 1996; Scruggs and Tullis, 1998; Mair and Marone, 1999). A mature fault with velocity-weakening frictional behavior could also be forced back into the stable regime. This could occur via brecciation during seismic slip, which would disrupt the fault structure (Sibson, 1986), or by authigenic growth of weak, velocity-strengthening minerals (e.g. Wintsch et al., 1995; Vrolijk and van der Pluijm, 1999; Warr and Cox, 2001) (path 4, Figure 6-4). Previous work has shown that only a small fraction of a weak, stable mineral phase need be present in the bulk gouge in order to control its frictional behavior (Logan and Rauenzahn, 1987), and extremely low abundances of a weak phase may cause significant weakening if the weak mineral occurs as a thin lining or film on slip surfaces in foliated fault rock (Colletini et al., 2009; Niemeijer et al., 2010; Smith and Faulkner, 2010; Schleicher et al., 2010).

Conclusions

We find a systematic relationship between absolute frictional strength and the potential for unstable fault slip. Weak gouges, with friction $\mu < 0.5$, exhibit only stable sliding behavior, whereas strong gouges, with a coefficient of friction $\mu > 0.5$, exhibit both stable and unstable slip. Weak gouges are those rich in phyllosilicate minerals. Strong gouges are rich in quartzo-feldspathic minerals and exhibit a systematic decrease in the frictional stability parameter, *a-b*, with increasing shear strain. A key implication of our work is that absolute fault strength and sliding stability are linked for a wide range of materials common in natural faults, even though no such relationship is predicted by theoretical or previous experimental studies. Our observation that *a-b* evolves with shear strain suggests that immature, low-offset faults in quartzo-feldspathic rock may become seismogenic with increasing displacement. In contrast, most phyllosilicate-rich faults are expected to exhibit stable creep unless the gouge mineralogy changes or strengthening of gouge occurs and slip becomes localized.

Figures

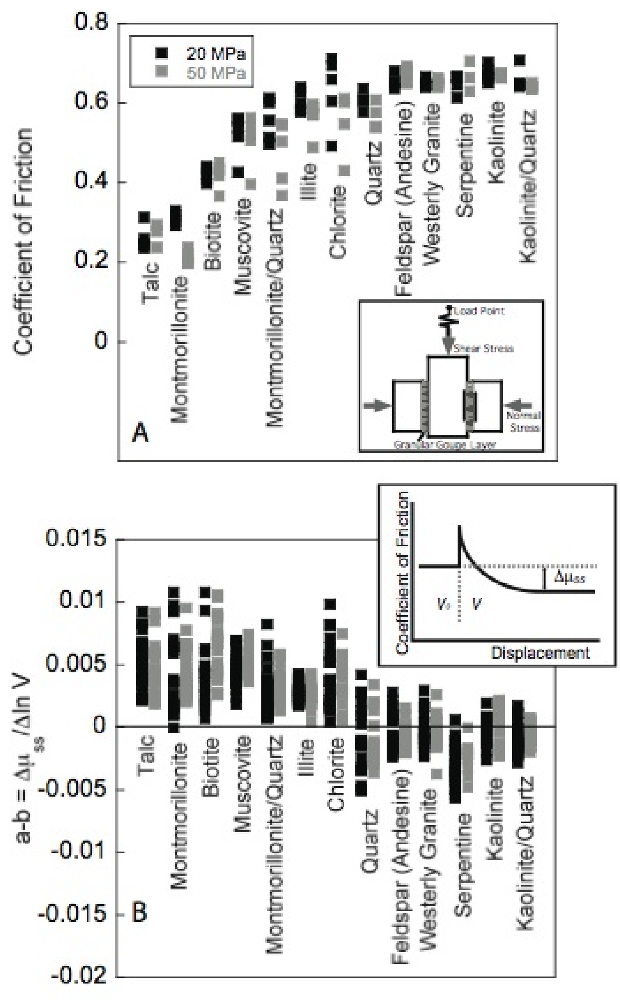

Figure 6-1: A. Measured coefficient of friction for all gouges in this study. Inset shows double-direct shear geometry. B. *a-b* for all gouges in this study. Inset shows an example of a velocity-step sequence and measurement of $\Delta\mu_{ss}$, used to calculate *a-b*.

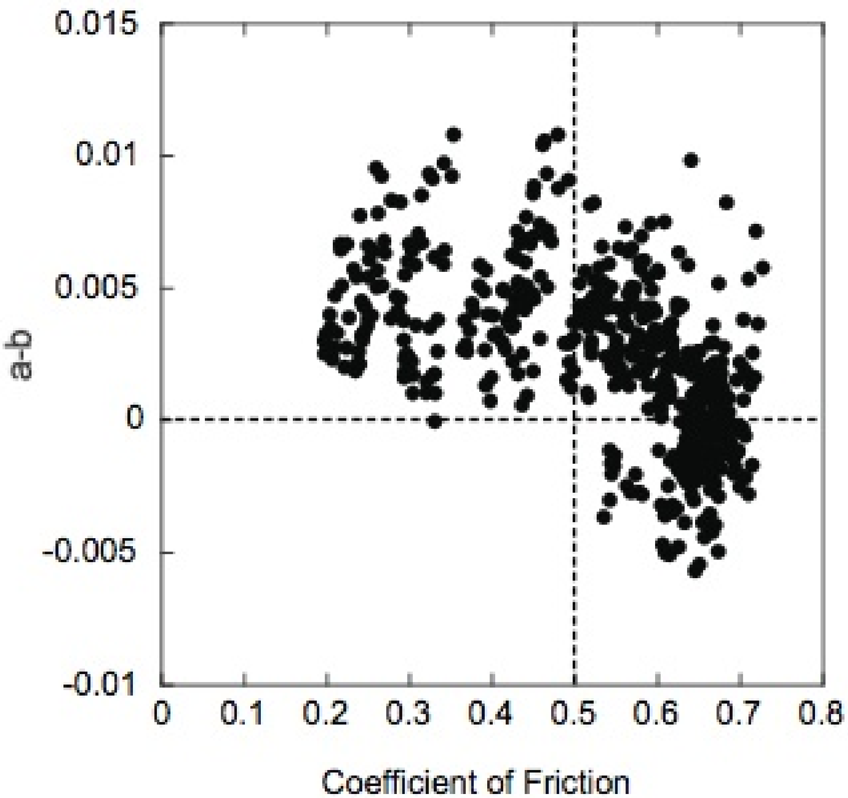

Figure 6-2: *a-b* as a function of coefficient of friction for all gouges in this study.

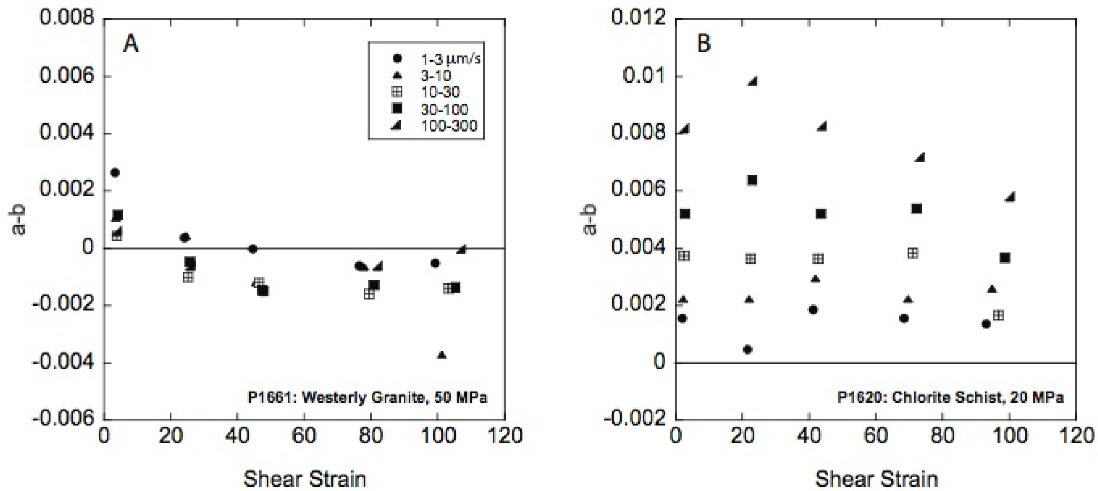

Figure 6-3: *a-b* as a function of shear strain for: A. Westerly granite at 50 MPa as an example of the velocity-weakening group, and B. chlorite gouge at 20 MPa as an example of the velocity-strengthening group.

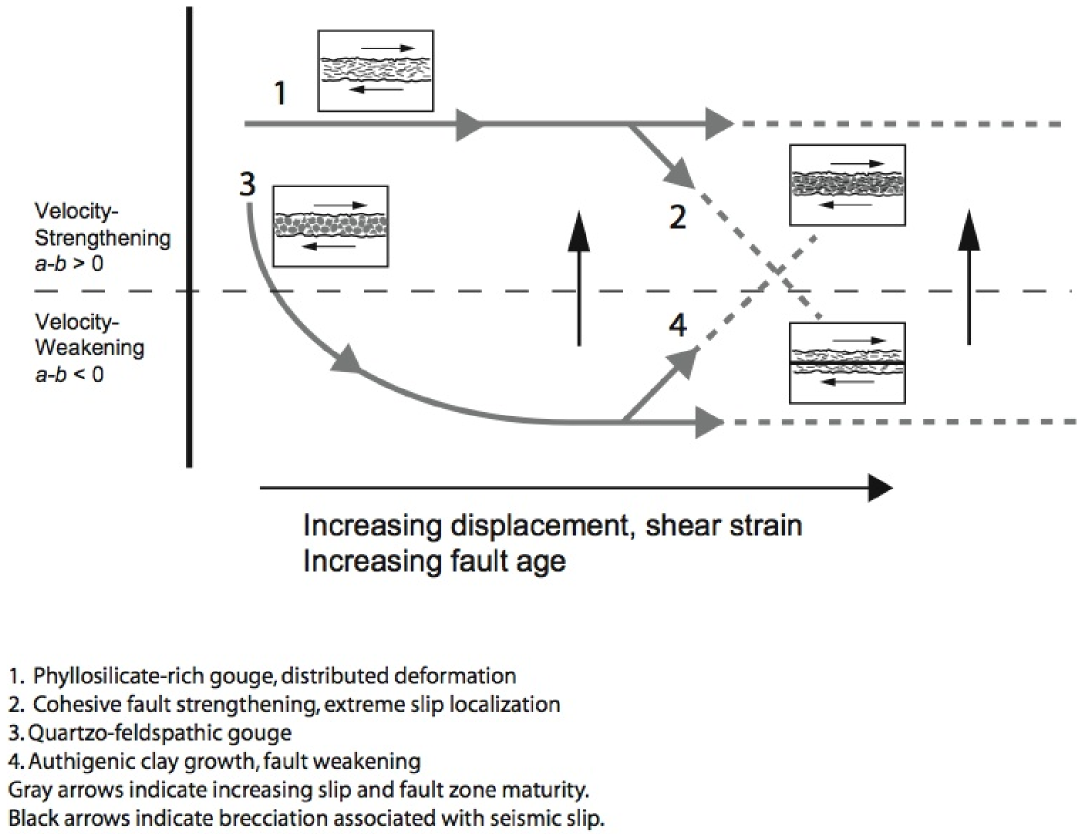

Figure 6-4: Schematic illustration of the evolution of fault frictional stability for fault gouges that are derived from phyllosilicate-rich protolith (initially phyllosilicate-rich gouge) and gouges derived from quartzo-feldspathic protolith (gouges initially containing no phyllosilicates). Initially phyllosilicate rich gouge will remain velocity-strengthening (path 1) but may transition to velocity-weakening if cohesive strengthening and extreme slip localization will occur (path 2). Strong, quartzo-feldspathic gouge will become velocity-weakening with a critical amount of accumulated shear strain (path 3) but may transition to velocity-strengthening if fault weakening due to authigenic clay growth occurs (path 4).

Chapter 7

COMPARISON OF GRANULAR AND LITHIFIED FAULT ROCK ANALOGUES: FRICTIONAL SLIP BEHAVIOR AND MICROSTRUCTURE

Abstract

Slip on faults at seismogenic depths occurs under conditions in which fault rocks are lithified cataclasites and ultracataclasites. We examine the frictional behavior of a wide range of lithified fault rock analogues and compare them with gouge powders commonly used in experimental fault mechanics. At 50 MPa normal stress, the frictional strength of lithified, isotropic hard rocks (granite, sandstone, limestone, marble) is generally at least 0.05 higher than powdered gouge, whereas foliated phyllosilicate-rich rock strength (slate, shale, schists) is similar to or weaker than powdered gouge, depending on the intensity of foliation. This highlights the importance of fault rock structure as well as rock type in controlling slip behavior. Measurements of frictional stability using rate- and state-dependent constitutive modeling show that both lithified and granular phyllosilicate-rich gouges are strongly velocity-strengthening (stable sliding), and velocity-weakening behavior is limited to phyllosilicate-poor samples, suggesting that lithification of phyllosilicate-rich fault gouge is insufficient to allow earthquake nucleation.. Microstructural observations show prominent through-going Reidel shear planes in most samples but are notably absent in lithified muscovite schist, indicating foliation-parallel slip. Both lithified and powdered samples of non-foliated hard rock show significant comminution of grains in the vicinity of Reidel shears and some evidence of boundary shear, and also higher maximum angles of Reidel shears when compared with phyllosilicate-rich faults materials. We observe a

strong effect of fault zone thickness on frictional strength, where comparison of thick and thin granular gouge layers shows higher angle Reidel shears and a significant reduction in the measured apparent coefficient of friction in thick fault zones. This suggests that the difference between the measured apparent friction and the true internal friction is related to the orientation of Reidel shears.

Introduction

Fault slip is known to be generally accommodated within finite volumes of rock or sediment (the "fault zone"), and the frictional properties of the fault zone material are considered to be a first-order control on both the overall fault strength and the style of fault slip, which can range from aseismic creep to destructive, large-magnitude earthquakes. Numerous experimental studies have been performed using both natural fault gouge and fault gouge analogues in order to measure fault strength and fault stability, which is a quantification of the likelihood of seismic slip. Many of these studies show that frictional slip behavior is strongly dependent on gouge mineralogy. Granular gouges consisting of non-phyllosilicate minerals such as quartz and feldspar are frictionally strong and may have the potential for seismic slip [*Beeler et al.*, 1996; *Scruggs and Tullis*, 1998; *Mair and Marone*, 1999], while gouges composed primarily of phyllosilicate minerals (clays and micas) have been shown to be both frictionally weak and tend toward aseismic behavior over a large range of conditions [*Morrow et al.,* 1992; *Saffer and Marone*, 2003; *Brown et al.*, 2003; *Niemeijer and Spiers*, 2006; *Ikari et al.*, 2007, 2009].

The majority of previous studies investigating fault friction simulate faults as a volume of granular, unlithified fault gouge. However, non-cohesive fault gouge is restricted to shallow levels in the crust, giving way to cataclasites and ultracataclasites within ~5 km of depth [*Sibson*, 1986a]. This transition has been observed to correlate with seismicity levels in the San Andreas fault [*Marone and Scholz,* 1988], leading to the hypothesis that consolidation and lithificatiton of fault rock is a necessary condition for seismic slip [*Moore and Saffer*, 2001; *Marone and Saffer,* 2007]. Therefore, studies of unlithified granular gouge may be of limited applicability. Other studies simulate faults as a discrete planar surface between two pieces of intact rock [e.g. *Dieterich*, 1979; *Tullis and Weeks*, 1986; *Savage and Marone*, 2008]. While these studies have been useful in showing that unstable, potentially seismic slip along pre-existing faults may be associated with localized slip in cohesive rock, the sample type is generally limited to a phyllosilicate-poor rock, such as granite or sandstone. In phyllosilicate-rich rock or foliated fault rocks in general, fabric can have a significant effect on frictional behavior by allowing slip on planes of weakness [*Collettini et al*., 2009; *Niemeijer et al.*, 2010; *Smith and Faulkner*, 2010; *Schleicher et al.*, 2010].

In this study, we report on the results of friction experiments in which we measure the frictional strength and stability of a wide range of rocks used as analogues for cataclastic fault rocks at seismogenic depths. We compare the frictional behavior of intact, lithified rock wafers with powdered, granular versions of the same rocks in order to determine if the lithification state of fault material influences its slip behavior. Specifically, we aim to investigate 1. The competing effects of strengthening from fault rock lithification and weakening due to structural anisotropy, and 2. If the lithification of phyllosilicate-rich gouge is sufficient to allow potentially seismic slip behavior. We compare microstructures developed during shear in order to investigate qualitative differences between lithified and unlithified fault rock after shearing. Additionally, we compare the frictional and microstructure of thick and thin fault zones to investigate the effect of fault thickness on the measured apparent fault strength.

Methods

Experimental Procedure

We conducted experiments using wafers of both foliated, phyllosilicate-rich rocks and non-foliated, phyllosilicate-poor rocks, as well as powdered, granular versions of the same rocks (Figure 7-1, Table 7-1). The non-foliated rocks were Westerly granite, Berea sandstone, Vermont marble, and Indiana limestone. The foliated, phyllosilicate-rich rocks were biotite schist (Bancroft, Ontario), muscovite schist, chlorite schist (Madison County, North Carolina), illite shale (Rochester, New York), and Pennsylvania black slate. The Pennsylvania slate is a foliated rock, but X-Ray Diffraction (XRD) has shown that it is composed of only ~10% phyllosilicate minerals. Thus, we consider this sample to be transitional between the two groups. Intact rock samples were cut into 5 x 5 cm wafers and tested as lithified fault rock. These samples were surface ground to a thickness of ~6-8 mm with a 60 grit grinding wheel, except for more friable samples such as the mica schists, which were separated along cleavage planes. Phyllosilicate-rich wafers were sheared with fabric approximately parallel to the shear direction. For non-cohesive granular gouge samples, rocks were crushed in a disk mill and sieved to a grain size of <106 μm. These samples were constructed in a leveling jig to be a uniform area (5 x 5 cm) and to compact under load to a thickness similar to the lithified wafers to facilitate a more direct comparison. We also ran a subset of experiments on thinner granular gouge layers (2-3 mm under load) to investigate the effects of gouge thickness on friction [e.g. *Scott et al.,* 1994](Table 7-1). We conducted experiments in a biaxial testing apparatus to measure frictional behavior under controlled normal stress and sliding velocity [e.g. *Ikari et al.,* 2007] (inset, Figure 2a). Two layers of sample fault gouge were sheared within a three-piece steel block assembly in a double-direct shear configuration (inset, Figure 7-2a). The block-sample contact surfaces were grooved to ensure that shearing occurred within the layer and not at the layer-block interface. In all experiments, the normal stress σ_n was maintained at 50 MPa and the contact area was maintained at 25 cm^2. All experiments were conducted under conditions of room humidity and temperature.

In each experiment, the sample was sheared at a constant velocity of 11 μm/s until attainment of residual shear stress, generally at shear strains of < 3. Upon reaching residual stress levels, a velocity-stepping test was initiated, which consists of an initial background velocity of 10 μm/s followed by a drop to 1 μm/s and subsequent instantaneous increases in velocity to 3, 10, 30, 100, and 300 μm/s. Shear displacement during each velocity step was 500 μm. At the conclusion of each experiment, the stresses were removed and the sample end product was recovered. These post-shearing samples were then set into epoxy (Buehler EpoThin© resin and hardener), cut parallel to the shear direction, and analyzed with a scanning electron microscope (SEM).

Friction Measurements and Constitutive Parameters

Figure 7-2a shows an example of a friction-displacement curve in which measurements of failure friction, residual friction, and the velocity-dependent frictional response are measured. We report values of the apparent coefficient of friction μ_a at failure, and at attainment of residual friction calculated as:

$$\tau = \mu_a \sigma_n + c \tag{1}$$

Where c is the cohesion [*Handin*, 1969]. We assume the cohesion to be zero for granular gouge, and that for intact rock wafers cohesion is lost by the time residual friction is achieved. Failure friction is taken as either the peak friction, or, in the absence of a clear peak, the point when the change in friction with displacement becomes steady (Figure 7-2b). Residual friction is measured at low shear strains ranging from 0.6-2.8 to facilitate comparison between lithified rock and granular gouge. Since the thickness of the experimental fault zone has been shown to have a significant effect on the measured apparent friction, we correct our measured friction values following *Scott et al.* [1994], using the equation:

$$\mu_a = \frac{RF\sin\phi + 2T(1-\alpha)}{RF^2 - T(1+\alpha)[RF\sin\phi + 2T(1-\alpha)} \tag{2}$$

Where μ_a is the apparent friction, R is a unitless, experimentally derived constant with a value of 1.2, $F = [1+T^2(1+\alpha)^2]^{1/2}$, φ is the angle of internal friction, T is the measured local rate of fault zone thinning -*Δh/Δx*, where *h* is the layer thickness and *x* is the shear displacement, and *α* is a unitless parameter describing the mechanism of fault zone thinning, which ranges from 0 (strictly density changes) to 1 (strictly gouge extrusion). The parameter *α* is calculated as:

$$\alpha = -\frac{h}{LT} = -\frac{T_{GT}}{T} \tag{3}$$

Where *L* is the length of the sample (5 cm in this case), and $T_{GT} = h/L$ and represents the theoretical maximum rate of geometric thinning [*Scott et al.,* 1994]. The true coefficient of internal friction *μ* is calculated as *μ* = tan *φ*. Note that effects of shear localization are neglected in this correction.

From the velocity-stepping tests, we are able to quantify frictional stability using the friction rate parameter *a-b*; defined as:

$$a - b = \frac{\Delta\mu_{ss}}{\ln\left(V / V_o \right)} \tag{4}$$

Where $\Delta\mu_{ss}$ is the change in the steady state coefficient of friction upon an instantaneous change in sliding velocity from V_o to *V* [*Tullis and Weeks*, 1986; *Marone*, 1998]. A material exhibiting a positive value of *a-b* is said to be velocity-strengthening, and will tend to slide stably and inhibit propagation of seismic rupture. A material with negative *a-b* is termed velocity-weakening, which is considered a prerequisite for frictional instability resulting in earthquake nucleation [*Scholz*, 2002]. We determined values of the friction rate parameter *a-b* and other constitutive parameters using an inverse modeling technique with an iterative least-squares method, using *Dieterich's* [1979, 1981] constitutive law for friction with two state variables:

$$\mu = \mu_o + a\ln\left(\frac{V}{V_o}\right) + b_2\ln\left(\frac{V_o\Theta_1}{D_{c2}}\right) + b_2\left(\frac{V_o\Theta_2}{D_{c2}}\right) \tag{5}$$

$$\frac{d\Theta}{dt} = 1 - \frac{V\Theta_1}{D_{c2}} - \frac{V\Theta_2}{D_{c2}} \tag{6}$$

where a, b_1 and b_2 are empirically derived constants (unitless), Θ_1 and Θ_2 are the state variable (units of time), and D_{c1} and D_{c2} are the critical slip distances. The state variables are inferred to be the average lifetime of contact points that control friction, and the critical slip distance is the displacement over which those contacts are renewed. In some cases, the friction data from an individual velocity step is well fit using only one state variable, in this case equations 5 and 6 are simplified by setting $\Theta_2 = 0$, eliminating the final term on the right hand side of each equation. In our use of the parameter a-b, we consider $b = b_1 + b_2$ to account for the possibility of using either 1 or 2 state variables. These equations are coupled with an expression describing machine stiffness:

$$\frac{d\mu}{dt} = K(V_{lp} - V) \tag{7}$$

where K is the stiffness of the fault surroundings (in this case the testing apparatus and sample blocks) normalized by normal stress (K = ~3×10^{-3} μm^{-1} at 25 MPa normal stress), V_{lp} is the load point velocity, and V is the true slip velocity [*Reinen and Weeks*, 1993; *Saffer and Marone*, 2003; *Ikari et al.,* 2009]. An example of a velocity step in friction data and the corresponding modeled friction are shown in Figure 3c.

Results

Friction Measurements

The frictional strength of our suite of fault material is highly variable, but both residual and failure friction of isotropic, phyllosilicate-poor hard rocks are consistently higher than that of foliated, phyllosilicate-rich rocks (Figure 7-3). For the phyllosilicate-poor samples, values of residual friction range from $0.47 \le \mu_a \le 0.57$ for lithified samples and $0.42 \le \mu_a \le 0.48$ for granular samples. Residual friction ranges from $0.15 \leq \mu_a \leq 0.44$ for lithified rocks and from $0.24 \leq \mu_a \leq 0.42$ for granular samples of foliated, phyllosilicate-rich rocks (Figure 3a). Values of failure friction range for phylloslicate-poor samples from $0.50 \leq \mu_a \leq 0.63$ for lithified rocks and from $0.40 \leq \mu_a \leq 0.46$ for granular gouges. Failure friction is $0.15 \leq \mu_a \leq 0.49$ for lithified and $0.21 \leq \mu_a \leq 0.36$ for granular phyllosilicate-rich fault materials (Figure 7-3b).

In comparing the lithified samples with the granular samples, we observe that the failure friction of lithified samples can be significantly higher than the residual friction, but in granular samples the failure friction is consistently lower than residual friction (Figure 7-4a). This is due to the presence of a pronounced peak in friction for some lithified rocks, while granular gouges exhibit rollover and subsequent strain hardening. Figure 7-5a shows an example of this type of behavior in Berea sandstone. We also note that both the residual and failure friction are higher for lithified rocks, with notable exceptions being the mica schists (Figure 7-4b, 7-5b). The strength discrepancy appears to be somewhat lower for phyllosilicate-rich samples in general.

Estimates of Internal Friction

Measured values of residual friction for a subset of thin granular samples (pre-shear thickness under normal load 1.5-3mm) are all consistently higher than those of granular samples with greater thicknesses similar to the lithified wafers (> 6mm) (Figure 7-6). Comparison of a friction-strain curve for thick and thin granular illite shale is shown in Figure 7-6a as an example. Residual friction of initially thin samples ranges from $0.56 \leq \mu_a \leq 0.70$ for non-foliated rocks and from $0.32 \leq \mu_a \leq 0.55$ for phyllosilicate-rich samples. Additionally, the rate of strain hardening is observed to be significantly higher for the initially thick samples (Figure 7-6a).

In thick experimental fault zones, the measured apparent friction can be significantly lower than the true internal friction [e.g. *Scott et al.*, 1994] due to rotation of the principal stress axes during shear [*Mandl et al.*, 1977; *Byerlee and Savage*, 1992]. We estimate the residual value of true internal friction for our sample set by applying a correction for friction following *Scott et al.* [1994]. In applying this correction, we use three values of the parameter α: $\alpha = 0$ (all sample thinning attributed to increasing density), $\alpha = 1$ (all sample thinning attributed to extrusion of material), and α calculated using Equation 3 (Figure 7-7, Table 7-2). Internal friction calculated using $\alpha = 0$ results in extremely high friction values, up to $\mu = 1.45$. More reasonable friction values ($\mu \leq 0.85$ [*Byerlee*, 1978]) are obtained using $\alpha = 1$ and calculated α. Using calculated α, friction ranges from $0.11 \leq \mu \leq 0.93$ and from $0.16 \leq \mu \leq 0.91$ using $\alpha = 1$ for all samples in this study. Unusually high corrected friction ($\mu > 0.85$) is observed for lithified Berea sandstone and calcite samples (limestone and marble).

Friction Rate Dependence and Constitutive Parameters

The velocity dependence of friction, as measured by the parameter *a-b*, is positive for all the phyllosilicate-rich rocks, both lithified and granular, ranging from $0.0013 \leq a\text{-}b \leq 0.0070$ (Figure 7-8a). As with the friction values, the velocity dependence of friction is highly variable between samples. Lithified versions of most samples (biotite, muscovite, chlorite) show consistently higher *a-b* values than the granular samples. Exceptions include illite, in which the granular *a-b* is higher, and slate, in which the *a-b* values are indistinguishable between granular and lithified samples. Many of these samples show a strong positive velocity dependence of *a-b* (muscovite, chlorite, slate) in both lithified and granular form. Unlike the foliated rocks, the non-foliated rock samples show both velocity-strengthening and velocity-weakening behavior. Velocity-weakening is observed in lithified limestone ($-0.0018 \leq a\text{-}b \leq -0.0007$) and lithified sandstone ($-0.0015 \leq a\text{-}b \leq 0$). Values of *a-b* for all other non-foliated rocks ranges from $0.0003 \leq a\text{-}b \leq 0.0045$ for both lithified and granular samples. The friction rate parameter D_c shows no discernible pattern but values are generally < 100 μm (Figure 7-8b). The parameters *a* and *b* are elevated for both granular and lithified phyllosilicate-poor rocks compared to the phyllosilicate-rich samples (Figures 7-8c,d). Negative values of *b* are observed for samples of chlorite, biotite, and muscovite. In comparing initially thick granular samples with initially thin samples, we observe that values of a-b are similar in both magnitude and range (Figure 7-9). An exception is the thin Westerly granite, which exhibits some velocity-weakening that is not observed for the thick gouge. All constitutive parameters and standard deviations are listed in Table 3.

Microstructural Observations

In the following, we will present and discuss the microstructures of our experimentally deformed lithified samples wafers and their granular analogues. For clarity, we divide the experiments in four groups (isotropic lithified, phyllosilicate-poor granular, foliated lithified, and phyllosilicate-rich granular samples) and discuss the general microstructures of each individual group. In the final section, we compare the microstructures of thin and thick granular samples. We applied the nomenclature for the different localization features as used by *Logan et al.* [1992] and schematically represented in Figure 7-10.

Isotropic Lithified Samples

In Figure 7-11, we show mosaics of back scattered electron scanning electron microscope (BSE-SEM) images of deformed samples of lithified Westerly granite, Berea sandstone, Indiana Limestone and Vermont marble. A common feature about all microstructures shown in Figure 7-

11 is the heterogeneity of deformation. The microstructures can be roughly subdivided in regions of intense grain size reduction (GSR) and spectator regions (S). In back-scatter, intense grain size reduction is identified by a lower gray scale as a result of higher porosity in areas containing small grains which reduces the average atomic weight. Identification of individual particles is not straightforward and deformation produced very fine fragments as small as <1 μm in localized zones. The localized zones of GSR typically are oriented in a Riedel shear orientation although the angles of the zones vary between ~5 – 25 º, with lower angles tending to be located near the boundaries. In the sample of Berea sandstone we observe localized areas of GSR also along the boundaries of the samples (Y or B-shears) but they are not continuous along the length of the sample. We did not observe a consistent variability of the angles between different non-foliated rock types. The boundaries between the zones of GSR and spectator regions can be sharp as sometimes evidenced by through-going fractures (possibly from decompression, Figure 7-2a) or more diffuse with a gradation in the amount of GSR increasing towards the localized zone (Figure 7-11b, 7-11d). In addition, the sample of Westerly granite shows fracturing of the spectator regions at angles sub-parallel to the normal stress in the R2 and, less commonly, in the X orientation with a smaller amount of fine grains, i.e. with a reduced amount of GSR. These types of fractures are also present to a lesser degree in the Vermont marble but generally seem to mostly absent or less pronounced in the calcite samples.

Figure 7-12 shows details of the localized zones of intense GSR and the transition zones for the samples of Westerly granite and Berea sandstone. These microstructures demonstrate the intense grain size reduction that occurred in these samples. Larger clasts are sometimes intensely fractured (Figure 7-12a), showing numerous intra- and transgranular fractures. The grain size is highly variable and grains as small as <1 μm are present (Figure 7-12d). The amount of fine-grained material increases towards the gouge-cutting fractures in the Riedel orientation, while the number and size of clasts decreases.

Phyllosilicate-poor Granular Samples

Figure 7-13 shows mosaics of four deformed samples of powders of Westerly granite, Berea sandstone, Indiana limestone and Vermont marble. The figure shows four very similar microstructures despite the differences in mineralogy. All samples are characterized by one or more gouge-cutting fractures in a Riedel (R1) orientation and heterogeneous grain size reduction. The spacing of the Riedel shear fractures varies from more than 15 mm (Westerly granite, Figure 7-13a) down to about 5 mm (Indiana limestone, Figure 7-13c). The other two samples show an intermediate Riedel fracture spacing of 6-7 mm. Moreover, the orientation of the Riedel fractures is not constant across the fault gouge, i.e. the fractures are not straight, but are somewhat anastomosing and in the case of the calcite-bearing samples have a step-like appearance. Zones of intense grain size reduction surround the Riedel fractures in all cases. Another zone of grain size reduction is located at the interface between the gouge and the forcing block, but does not appear to be continuous. This zone in a B-shear orientation is more pronounced in the samples of Westerly granite and Berea sandstone (Figure 7-13a,b). In addition to the obvious Riedel fractures, the two calcite-bearing samples show some discontinuous fractures and areas of grain size reduction in orientations between R1 and Y-shear, which seem to be absent in the samples of Westerly granite and Berea sandstone.

Due to practical reasons associated with epoxy impregnation in the thick granular samples, we show the details of the thin samples at high magnification. Figure 7-14 shows details of the Riedel fractures seen in the samples of the initially thin samples of Westerly granite (Figure 7-14a,b) and Indiana limestone (Figure 7-14c,d). The zone of GSR surrounding the fracture in the sample of Westerly granite is narrow, extending into the gouge only 50-150 μm. Larger clasts are present in close proximity to the boundary of the fracture. In contrast, the area of GSR surrounding the Riedel fracture in the sample of Indiana limestone is wider and appears to extend up to several 100s of microns into the gouge, especially at the bottom of the fracture. The fine-grained nature of the zone is apparent from the more detailed views in Figures 7-14b and 7-14d, showing a large variation in grain size, with micron to sub-micron scale grains forming the matrix.

Foliated Lithified Samples

In Figure 7-15, we show BSE-SEM mosaics of deformed samples of Pennsylvania slate, illite shale, biotite schist and muscovite schist. Both the sample of Pennsylvania slate and the illite shale show intense fracturing. Through-going shear fractures in the R1 Riedel orientation are visible in both samples and are filled with fine-grained material. The fractures are continuous, but larger pods of nearly intact material occur along the fracture. The illite shale shows evidence for shear-parallel fracturing along pre-existing foliaton. Smaller fractures extend from the large Riedel fracture to the gouge boundaries at an angle almost parallel to the applied normal stress which is close to the orientation for R2-type Riedel shears. There are no clear conjugate sets of R2 fractures visible. The matrix is characterized by an extremely fine-grained material (sub-micron) with some larger clasts (Figure 7-16a,b). Individual grains are difficult to distinguish.

In contrast, the biotite and muscovite schist (Figures 7-15c,d; Figure 7-16c,d) lack fine-grained material. Instead, these samples are characterized by fracturing perpendicular to the applied normal stress (parallel to foliation), with some fractures in the R1 orientation in the biotite schist. Note that the muscovite schist does not show any fractures in the R1 orientation. The network of fracturing is more complex in the biotite schist than in the muscovite schist, which only shows fracturing parallel or sub-parallel to the shear direction and some tensile fracturing of the mica sheets. Many of these fractures are continuous over the entire length of the sample (Figure 7-15d). The biotite schist, on the other hand shows shearing-parallel fractures that terminate against R1 Riedel fractures or change orientation and terminate at the sample boundary. Folded and buckled fractures are visible at all scales (Figure7-15c; 7-16c,d) and some fine-grained material can be observed at the boundaries of some fractures. This material is very fine-grained (sub-micron) but is not as abundant as in the Pennsylvania slate and illite shale. No fine-grained material was observed in the muscovite schist sample.

Phyllosilicate-rich Granular Samples

Mosaics of SEM-BSE images of four foliated granular samples (Pennsylvania slate, illite shale, biotite schist and muscovite schist) are shown in Figure 7-17. All samples are characterized by one or more through-going fracture in a R1 Riedel orientation. The fractures are not smooth but show bending (i.e. a change in angle) and steps in the Pennsylvania slate (Figure 7-17), whereas the fractures in the other three samples do not show pronounced steps. Fractures in the biotite and muscovite schists appear to have listric shape, with the fracture angle decreasing into an almost boundary-parallel orientation at the bottom of the gouge layer. Numerous subsidiary fractures in different orientations (P and Y shears) exist in all samples. Longer scale fractures can be seen in a boundary-parallel orientation but with a wavy appearance. An especially long and pronounced wavy fracture can be seen in the muscovite schist (Figure 7-17d), but whether this fracture represents a Y shear or a low angle R_1 Riedel shear is not clear. Note that this is an image of the thin fault gouge of muscovite, since we were unable to image the thick gouge.

Figure 7-18 shows details of the microstructures for the thin gouge layers of the same sample type as in Figure 7-17. We were unable to achieve full impregnation of the illite shale samples, likely due to intense grain size reduction that results in very low permeability. Grain size reduction was also found to be intensive in the sample of Pennsylvania slate, which we were able to fully impregnate and image due to the more heterogeneous deformation of this sample (Figure 7-17a). The samples showed intense grain size reduction with an increasing intensity approaching the Riedel shear. Very fine grained material (down to sub-micron size) surrounds the boundaries of the Riedel shear on both sides, with a varying lateral extent between 20 to 100 μm (Figure 7-18a,b). Biotite and muscovite schists show little fine-grained material (Figure 7-18c,d), although some pockets of fine-grained material are present close to the fractures. The majority of the grains, however, seem to reflect the starting grain size, with the long axis of the grains extending up to 100 μm in size. The grains have a mild shape preferred orientation at parallel to sub-parallel to the shear direction. No grain shapes were observed with a high angle to the shearing direction.

Comparison of Thick and Thin Granular Samples

In Figure 7-18, we show two examples of the microstructures obtained from experiments on thin fault gouges, one phyllosilicate-poor (Vermont marble, Figure 7-19a) and one phyllosilicate-rich (biotite schist, Figure 7-19b). Comparing Figure 7-19a and Figure 7-13d, it is immediately clear that the microstructure of the thick granular sample is very similar to the thin sample. Both are dominated by obvious fractures in the R_1 Riedel orientation with intervening areas affected by grain size reduction. The areas of intense grain size reduction are larger for the thinner samples, which is probably related to the higher shear strain achieved for these samples. Additionally, the angle of the Riedel fracture appears to be higher in the thick granular sample. For the phyllosilicate-rich samples (compare Figure 7-19b, 7-17c), a similar observation can be made: the microstructures of the thick and thin granular samples are very similar, except that the angle of the Riedel fractures is larger in the thicker samples. We will quantify this difference in angle and relate it to the apparent friction in the discussion.

Discussion

Micromechanical Controls on Friction

Analysis of measurements of both residual and failure apparent friction reveals several key observations. Phyllosilicate-rich fault materials are in general much weaker than those with low phyllosilicate contents, an expected result based on previous experimental work. Lithification significantly increases the strength of isotropic hard rocks, but we observe either minimal strengthening or weakening due to lithification of foliated, phyllosilicate-rich rocks. This implies that the foliated nature of the rock provides a mechanism for weakening that offsets with the strengthening effect of cementation and consolidation associated with the lithification process. The weakening effect of foliation appears to depend on its intensity, and in intensely foliated rocks such as books of mica sheets the lithified rock is significantly weaker than granular mica gouge with no pre-existing structure. In fact, the lithified mica schists are the two weakest fault materials in this study with residual friction values < 0.16.

Microstructural observations reveal clear differences in deformation between the isotropic and foliated lithified fault rocks. In the isotropic hard rocks, shearing is accommodated on one or two prominent through-going zones at the R1 orientation (Figure 7-11). The thickness of this zone may increase with shear strain (e.g. Vermont marble). However, foliated rocks such as Pennsylvania slate and illite shale show pervasive fracturing at angles that range from low R1 to shear-parallel. Muscovite schist shows little evidence of deformation except for tensile fracturing of mica sheets, indicating that slip was accommodated on pre-existing foliation planes. Biotite schist, despite its similarity in frictional behavior to muscovite, exhibits more complicated deformation that includes R1 fractures, folding, and kinking, which is consistent with previous microstructural observations in biotite schists [*Shea and Kronenberg*, 1993]. The cause of this difference is unknown, but could be related to small quartz impurities or a less continuous foliation than that in muscovite schist.

The higher frictional strength of the lithified isotropic phyllosilicate-poor rocks compared to granular phyllosilicate-poor gouge is clearly the result of comminution of large grains and cemented grain aggregates. Discrete fracturing is pervasive in the Westerly granite and to a lesser degree in the Vermont marble, indicating a high cohesive strength resulting in a pronounced friction peak (high failure strength). For the foliated rocks, granular samples of Pennsylvania slate and illite shale show significantly less fracturing and absence of shear-parallel fractures. Since the frictional strengths of the lithified and granular samples are similar, it appears that the strength increase from lithification is approximately balanced by strength reduction from pre-existing foliation. Granular mica gouges also deform in a similar fashion to the other granular gouges in this study, along a small number of angled shears. The marked strength reduction in lithified mica schist below that of the granular gouge is clearly due to the different deformation mechanisms: bending, fracturing, and kinking in the case of biotite and foliation-parallel slip in the muscovite.

Relationship Between Fault Zone Thickness, Reidel Shear Angle, and Apparent Friction

Many of our results compare favorably with previous studies that have measured residual apparent friction at similar conditions, although our friction measurements for our intact rock samples and thick granular layers are consistently lower due to the effects of high layer thickness on apparent friction. Comparisons to previous data are limited by the lack of data for samples of intact rock deformed in simple shear, so we use our thin granular gouge layers for comparison. *Shimamoto and Logan* [1981a] report coefficient of friction values of 0.48 for illite and 0.42 for chlorite, consistent with our measured value of apparent residual friction for illite shale of 0.49

and chlorite schist of 0.37. Our illite friction value is also is similar to the ~0.5 measured by *Saffer and Marone* [2003] and ~0.45 measured by *Morrow et al.* [1992]. *Morrow et al.*, [2000] report dry frictional strengths of chlorite (~0.45-0.60), muscovite (~0.30-0.50) and biotite (~0.40-0.45) gouges, broadly consistent with our results for chlorite and muscovite but is higher for biotite gouge. However, our friction values of 0.45 for muscovite and 0.32 for biotite are within the range of 0.25-0.45 reported by *Scruggs and Tullis* [1998] for these two gouges. Our measured friction value for Westerly granite gouge of 0.60 is on the low end of the range reported by *Beeler et al.* [1996] of 0.60-0.68 but is more consistent with the range reported by *Dieterich* [1981] of 0.55-0.65 for 2 mm thick gouge layers. Berea sandstone is composted of 83% quartz and 7% feldspar [*Menéndez et al.*, 1996], so we compare our friction of granular Berea sandstone gouge to previous work on nearly pure quartz sand. Our reported residual friction value of 0.56 is lower than the 0.7 reported by *Shimamoto and Logan* [1981b] but matches the range of 0.56-0.60 reported by *Mair and Marone* [1999]. *Shimamoto and Logan* [1981b] also reported a friction value of 0.74 for calcite gouge, which compares well with a measured value of 0.70 observed for both Vermont marble and Indiana limestone.

We attribute low values of friction for intact rock wafers and thick granular gouges to effects of gouge thickness on apparent friction. Gouge zone thickness has previously been shown to have significant weakening effect on the measured apparent coefficient of friction in gouge zones thicker than ~0.5 mm [*Dieterich*, 1981; *Marone et al.*, 1990; *Scott et al.*, 1994]. This has been attributed to rotation of the principal stress axes within the gouge layer compared to the externally applied stresses, such that the apparent coefficient of friction $\mu_a = \sin \varphi$, rather than $\tan \varphi$ [*Byerlee and Savage*, 1992]. We corrected our measured values of apparent residual and failure friction following *Scott et al.* [1994], obtaining estimates of true internal friction (Figure 7-7). We find that values of $\alpha = 1$ or calculated values of α using measured values of the thinning rate T provide the most reasonable values of μ. Calculated values of α range from 0.67 to 2.25, implying that gouge extrusion is the dominant mechanism of thinning (as opposed to density increases, represented by values of α ~0). *Scott et al.* [1994] asserted that α ranges from 0 to 1, however their correction neglected effects of shear localization. If slip localization occurs, the measured thinning rate T will not reach the theoretical rate T_{GT}, making $\alpha > 1$ as noted in Equation 3. In the limiting case of pure boundary parallel shear, $\alpha \rightarrow \infty$ and $\mu_a = \mu$, meaning no correction is necessary and the measured apparent friction is the true internal friction.

If the weakening effect of fault zone thickness depends on the gouge thinning rate and deviation from pure boundary-parallel shear, we expect that the measured apparent friction depends on the orientation of shear slip planes internal to the gouge layer. Figure 7-20 shows the residual value of measured apparent friction as a function of the maximum observed R1 Reidel shear angle observed in SEM images. This figure includes all samples in this study with the exception of the lithified muscovite schist, which exhibited no R1 shears, and initially thin granular chlorite schist, within which we could not distinguish R1 shears. High friction is observed for thin gouge layers, which also have the lowest R1 angles. High R1 angles are observed in thick fault samples, where the friction tends to be lower. This implies that thick fault zones in which deformation occurs along well-developed through-going Reidel shears, greater R1 angles correlate to lowering of the apparent friction, which has previously been suggested by *Gu and Wong* [1994] and *Tembe et al.* [2010]. This is also supported by our observations of large amounts of strain hardening in the thick granular gouges, which may be the result of flattening of R1 shears as shearing progresses and an initially high thinning rate declines.

If the angle of R1 shears is related to the weakening of apparent friction due to fault thickness, the true internal friction of the fault material would be the strength required to deform along a plane at the R1 angle. Assuming that R1 shears are Coulomb failure planes, we can use estimations of the R1 angle β to apply a two-dimensional stress transformation and calculate the shear stress τ^* and normal stress σ_n^* resolved on the plane of the R1 shear [*Hibbeler*, 1997]. In our biaxial experimental configuration, the layer is unconfined at the leading and trailing edges of the sample, so we assume that these are free surfaces and the only stresses transferred to the R1 plane are the remotely applied normal stress σ_n and the remotely measured shear stress τ (Figure 7-21). In this simplified configuration, the shear and normal stresses resolved on the R1 plane are calculated by:

$$\sigma_n{}^* = \sigma_n \cos^2 \beta + \frac{\tau}{2} \sin 2\beta \tag{8}$$

and

$$\tau^* = \frac{\sigma_n}{2} \sin 2\beta + \tau \cos^2 \beta \,. \tag{9}$$

In the limiting case of strictly boundary-parallel shear ($\beta = 0$), the original values of remotely applied normal stress σ_n and the remotely measured shear stress τ are recovered. Using this technique, the calculated coefficient of internal friction $\mu^* = \tau^*/\sigma_n{}^*$ ranges from 0.82 for lithified Berea sandstone to 0.50 for thick granular chlorite gouge (Table 7-4). While reasonable friction values are produced for high strength gouges, this correction tends to overestimate the frictional strength of weaker gouges such as clays and micas. This is likely due to the fact that no provision is made for simultaneous deformation along shear fractures of differing orientation. Therefore, the μ^* values represent upper bounds on true internal friction. This may be inaccurate for fault material with complicated internal deformation structures (e.g. lithified illite shale and biotite) but may be sufficient to characterize fault rock with well developed, distinct Reidel shears (e.g. Berea sandstone and Westerly granite).

Stability of Frictional Slip

Results of constitutive modeling from which we obtain and analyze rate- and state-dependent friction parameters reveal mostly velocity-strengthening behavior (*a-b* > 0), consistent with previous work on phyllosilicate gouges [*Morrow et al.*, 1992; *Brown et al.*, 2003; *Ikari et al.,* 2009] and quartzo-feldspathic gouge at low shear strains [*Beeler et al.,* 1996; *Mair and Marone*, 1999]. Instances of velocity-weakening behavior (*a-b* < 0) are observed in lithified Berea sandstone and Indiana limestone. Microstructural analysis of the Berea sandstone indicates areas of GSR consistent with localization on Y and B-type shears, which have previously been associated with unstable frictional slip [*Shimamoto and Logan,* 1986; *Logan et al.*, 1992; *Marone et al.*, 1992; *Beeler et al.,* 1996; *Scruggs and Tullis*, 1998; *Niemeijer and Spiers*, 2005]. Indiana limestone exhibits GSR and fracturing in the R1 orientation and perhaps localization at angles intermediate to that of the R1 and boundary-parallel shear. This is consistent with the observations of deformation by *Friedman and Higgs* [1981] in calcite gouge at 25°C. They also observed stick-slip behavior under these conditions, consistent with our observations of velocity-weakening behavior. This indicates that limestone may be frictionally unstable enough that deformation on Reidel shears is sufficient to allow unstable slip behavior.

It has been previously suggested that the velocity-strengthening nature of unconsolidated, clay-rich sediments requires that fault gouge become lithified before seismogenic slip can nucleate within them [e.g. *Marone and Saffer*, 2007]. We observe strictly velocity-strengthening behavior in lithified foliated, phyllosilicate-rich rock, note that in some cases *a-b* for these samples are higher than those for granular phyllosilicate-rich fault gouge. This is true even for fault rocks with evidence of foliation-parallel fracturing and/or slip. This indicates that fault rock lithification is insufficient as a sole mechanism for the transition from stable to unstable slip at the updip limit of the seismogenic zone. Since the pressure and temperature conditions at seismogenic depths generally ensure that fault rocks are lithified, other processes along with fault rock lithification appear to be required before unstable slip is able to nucleate. These may include any number of diagenetic and low-grade metamorphic reactions [*Moore and Saffer*, 2001; *Moore et al.*, 2007], localized fault structure development at a critical shear strain, or an increase in fault frictional strength [*Ikari et al.*, 2010].

It was suggested by *Ikari et al.*, [submitted 2010] that fault slip stability may be related to fault frictional strength, such that velocity-weakening behavior is suppressed in weak fault materials [$\mu < 0.5$]. Our data show trends consistent with this assertion, and we note that the only samples in this study which exhibit velocity-weakening behavior, lithified Berea sandstone and Indiana limestone, are two of the strongest samples (residual $\mu_a = 0.52$ and 0.56, respectively). Additionally, we observe instances of negative values of b in the weakest samples (chlorite, muscovite, and biotite schists), which guarantee velocity-strengthening behavior and are thought to result from saturation of real area of contact in weak, phyllosilicate-rich gouge [*Saffer and Marone*, 2003; *Ikari et al.,* 2009]. Moreover, *a-b* values obtained from our subset of experiments on thin granular gouges are nearly identical to the *a-b* values of thick granular gouges, indicating that *a-b* is independent of the apparent friction and, by extension, factors that affect the apparent friction such as fault zone thickness and Reidel shear angle. However, we do observe some velocity-weakening behavior in thin Westerly granite samples that is not observed in the thicker sample. This could be due to a more well-developed Reidel shear in the thin sample of granular Westerly granite, as observed in SEM images. If *a-b* is related to frictional strength as suggested by *Ikari et al.* [2010], it appears to be related to the true internal friction, meaning that the velocity-weakening we observe occurs in a gouge with a frictional strength $\mu = \sim 0.85$. We note however that these results and those of *Ikari et al.* [2010] were conducted at sub-saturated, room temperature conditions and may only be applicable to purely brittle-frictional faulting.

Implications for Slip Behavior in Natural Fault Systems

Our experimental results indicate that the strength of natural faults can experience a complicated history and is subject to change as a function of numerous competing effects, which may include changes in lithification state, composition, fault width, and internal structure. Faults that are strong, due to advanced lithification and/or intrinsically strong mineralogy (calcite, quartz, feldspar) can be substantially weakened by a variety of mechanisms. In seismogenic faults, brecciation during a seismic event would destroy fault rock cohesive strength [*Sibson*, 1986b], regeneration of which would then be a function of the recurrence interval [*Scholz*, 2002]. Another mechanism for weakening is the authigenic formation of weak, phyllosilicate phases, aided by fluid-rock interactions [*Wintsch et al.,* 1995; *Vrolijk and van der Pluijm,* 1999; *Warr and Cox*, 2001] which has been observed in fault systems such as the San Andreas [*Evans and Chester*, 1995; *Schleicher et al.*, 2009]. The presence of phyllosilicate minerals can also contribute to weakening by developing strong foliation in the rock. Based on our friction measurements, if foliation develops to the point of being similar to that of nearly pure mica schists, the strength could be sufficiently reduced to satisfy the heat flow constraint on the San Andreas [*Lachenbruch and Sass*, 1980].

We note that the width of the fault zone can have a significant effect on the apparent friction of a fault, such that very thick faults may appear to be weak in response to far-field stresses while being composed of frictionally strong material. As faults grow and mature, one would then expect faults to weaken with accumulated offset if a linear displacement-thickness relationship is assumed [*Scholz*, 1987], although the validity of such relationships is still a subject of debate [*Evans*, 1990]. However, this is complicated by the observation that the discrepancy between apparent and true internal friction may depend on the orientation of shear planes internal to the fault zone. Localized deformation on low angles approaching the orientation of the fault itself brings the apparent friction nearer to its true value. Therefore, the strength of wide fault zones depends not only on their net thickness but also their internal structure and distribution of deformation, which is often complicated [*Hull*, 1988; *Means*; 1995; *Caine et al.*, 1996].

Conclusions

Results of friction experiments on lithified and granular fault materials composed of a wide variety of rock types and varying thickness reveal several systematic effects on fault slip behavior. Fault strength as measured by the apparent coefficient of friction is strongly dependent on fault composition, with phyllosilicate-rich gouges significantly weaker than those lacking phyllosilicate minerals. The strengthening effect of lithification is seen most strongly in Isotropic hard rocks such as Westerly granite and Berea sandstone, but this effect is reduced in rocks containing pre-existing foliation (e.g. Pennsylvania slate and illite shale), and intensely foliated rocks such as mica schists are significantly weaker than their granular counterparts. We compare initially thick (> 6 mm) and thin (< 3 mm) granular gouge layers and find that the apparent coefficient of friction is reduced significantly reduced in thick gouges. Microstructural analysis reveals that the angle of R1 Reidel shears is positively correlated with fault thickness. Reasonable estimates of true internal friction are obtained by correcting measured values of apparent friction by two methods: using measured rates of gouge thinning following *Scott et al.*, [1994], and using plane-strain stress transformation using measured R1 angles. However, more accurate estimates of true internal friction will require more sophisticated methods that account for effects of shear localization and heterogeneous deformation. The strength of natural faults will be affected by a number of competing time- and displacement-variable effects that include fault composition, lithification state, thickness, and internal structure that are complicated in nature. Observations of mostly velocity-strengthening behavior suggest that other mechanisms in addition to fault rock lithification are required for the nucleation of seismogenic fault slip. We note that although fault strength may be affected by fault zone thickness, and lithification state, fault stability will be primarily a function of fault material composition and shear localization.

Figures

Figure 7-1. Examples of sample fault materials. Top left: Lithified, non-foliated rock (Westerly granite). Top right: Lithified, foliated rock (biotite schist). Bottom left: granular Westerly granite. Bottom right: granular biotite schist.

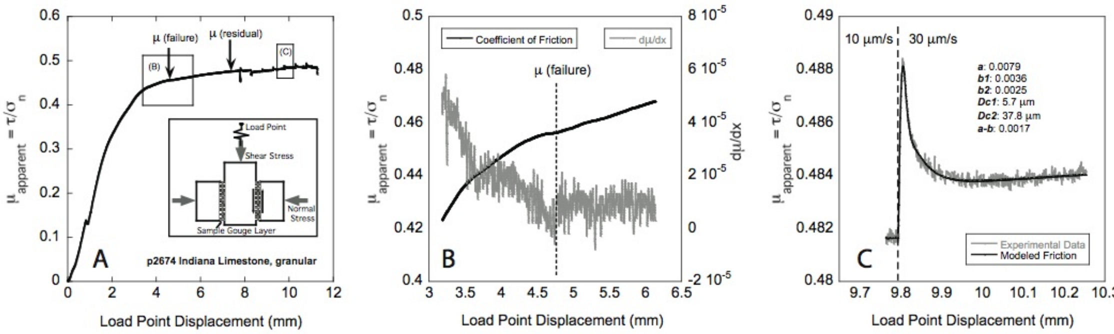

Figure 7-2. (a) Example of a friction-displacement curve for a typical experiment. Inset shows double-direct shear geometry. (b) Portion of friction curve in (a) showing measurement of failure friction as coincident with a constant value of $\Delta\mu/\Delta x$. (c) Enhanced view of a velocity step as indicated in (a). Friction data is overlain by a best-fit model.

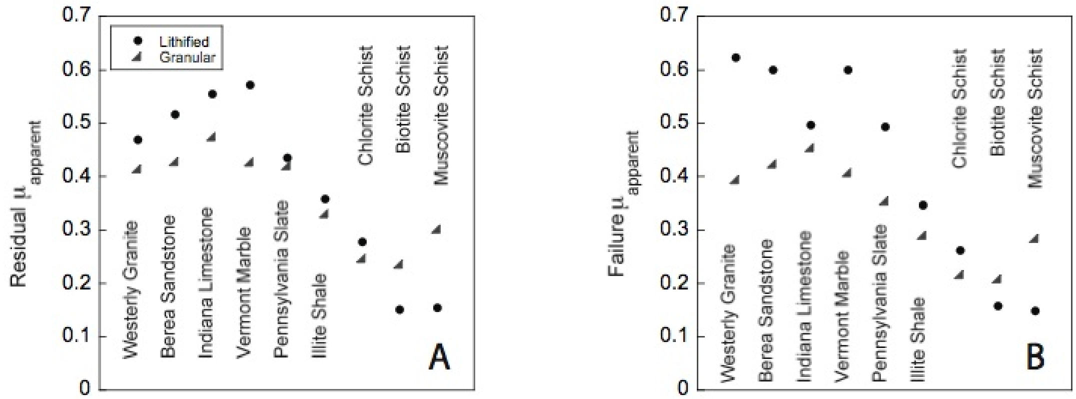

Figure 7-3. Measurements of (a) residual apparent friction, and (b) failure apparent friction.

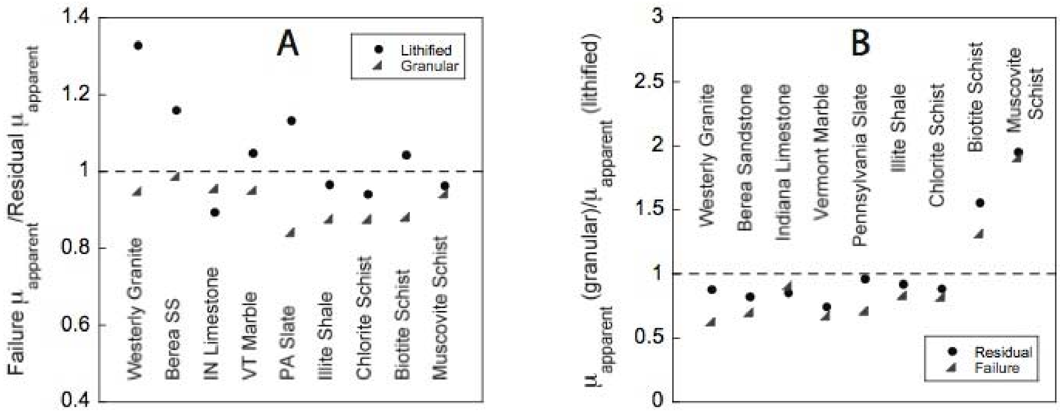

Figure 7-4. (a) Apparent friction at failure with respect to residual friction, and (b) Effect of lithification state on failure and residual friction.

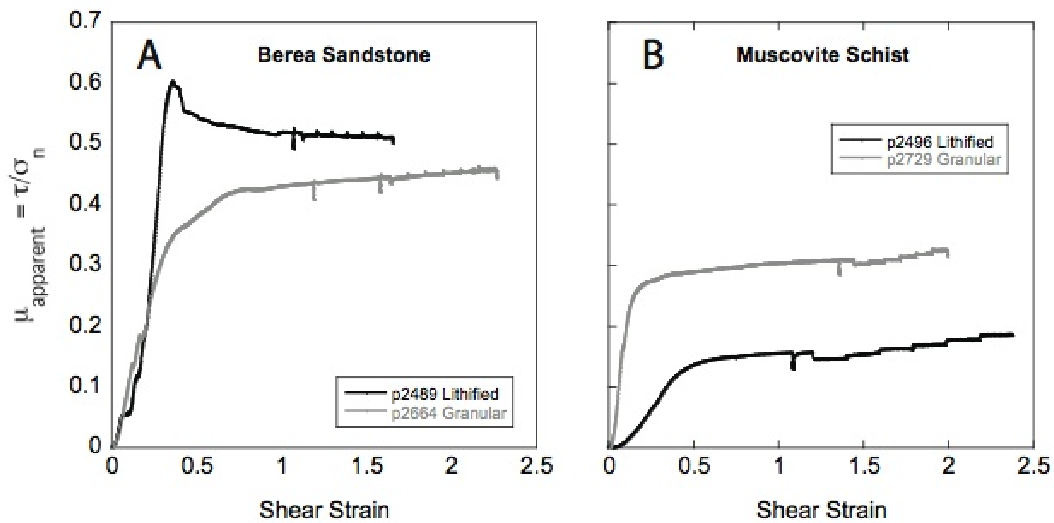

Figure 7-5. Comparison between friction-strain curves for lithified and granular samples of (a) Berea sandstone, and (b) muscovite schist.

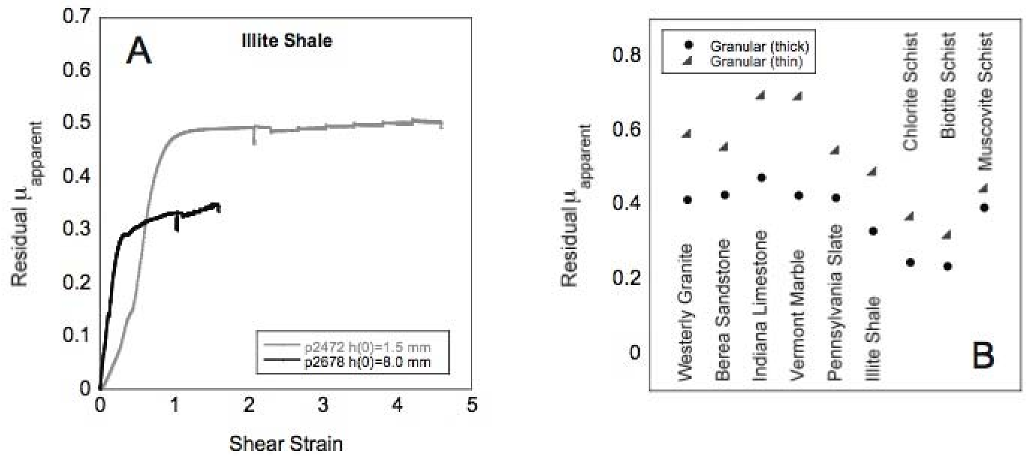

Figure 7-6. (a) Comparison between friction-strain curves for initially thick (~8.0 mm under load) and initially thin (~1.5 mm under load) samples of granular illite shale. (b) Effect of gouge thickness for all granular samples in this study.

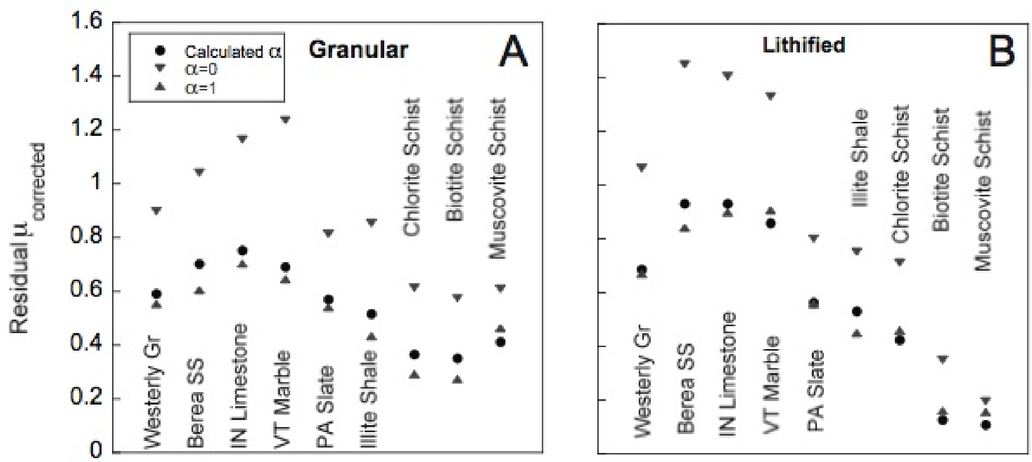

Figure 7-7. Residual friction using *Scott et al.'s* [1994] correction for gouge thickness effects for (a) granular and (b) lithified fault material.

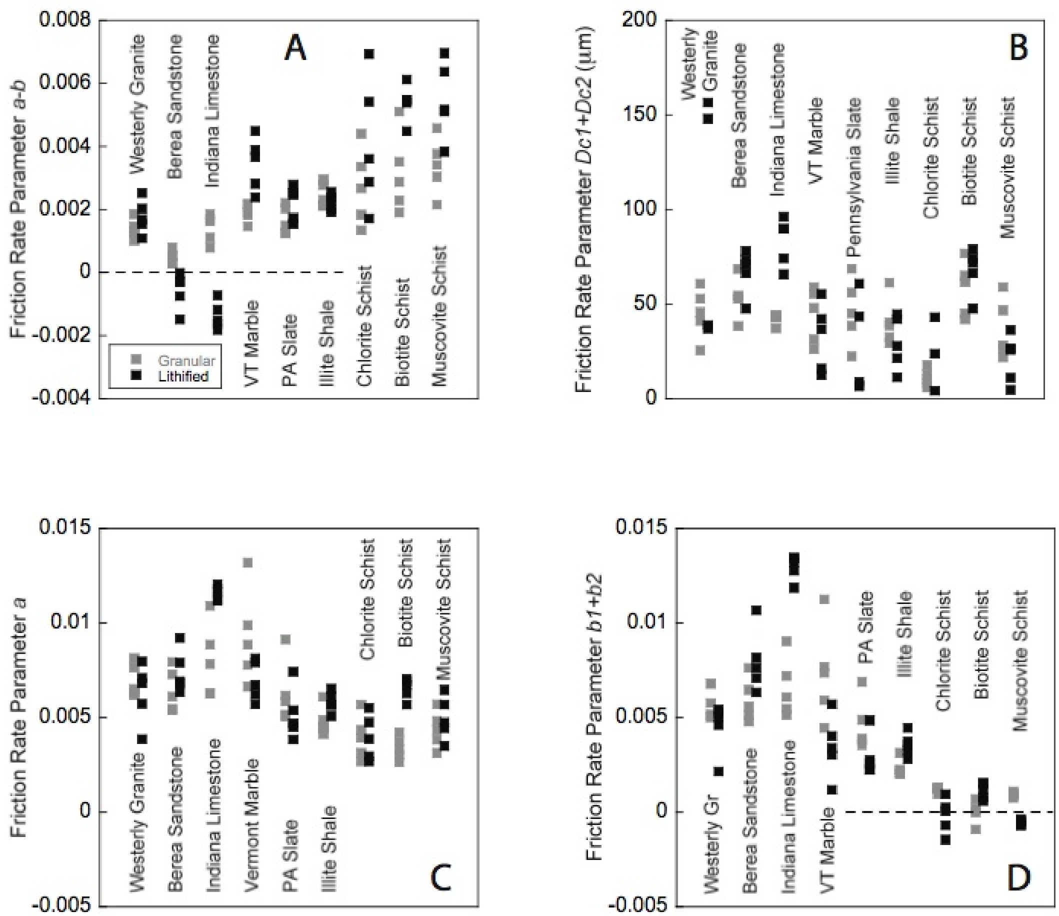

Figure 7-8. Modeled rate-and state-dependent constitutive parameters: (a) *a-b*, (b) $D_{c1}+D_{c2}$, (c) *a*, and (d) b_1+b_2.

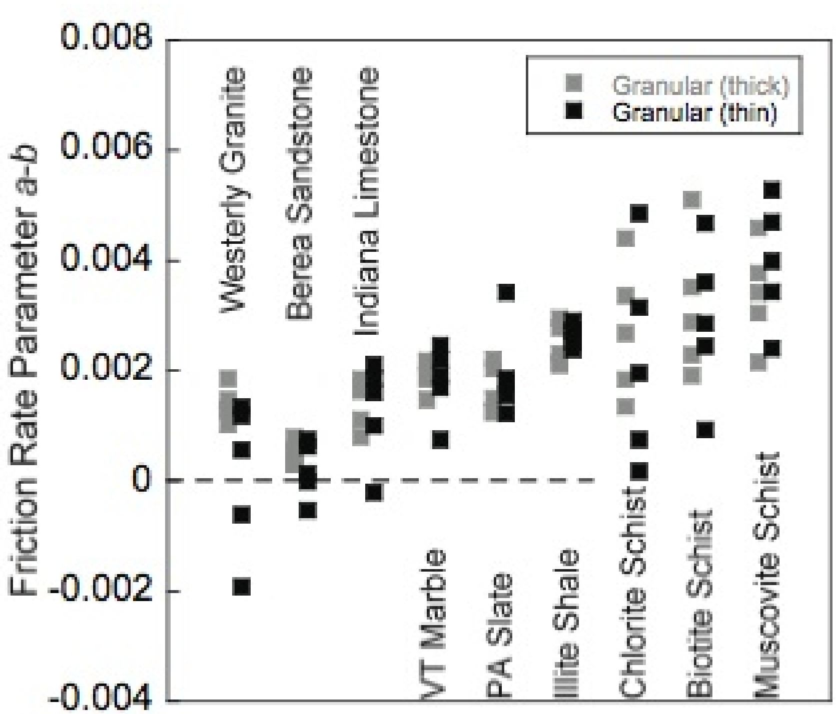

Figure 7-9. Comparison between values of *a-b* for initially thin and initially thick granular samples.

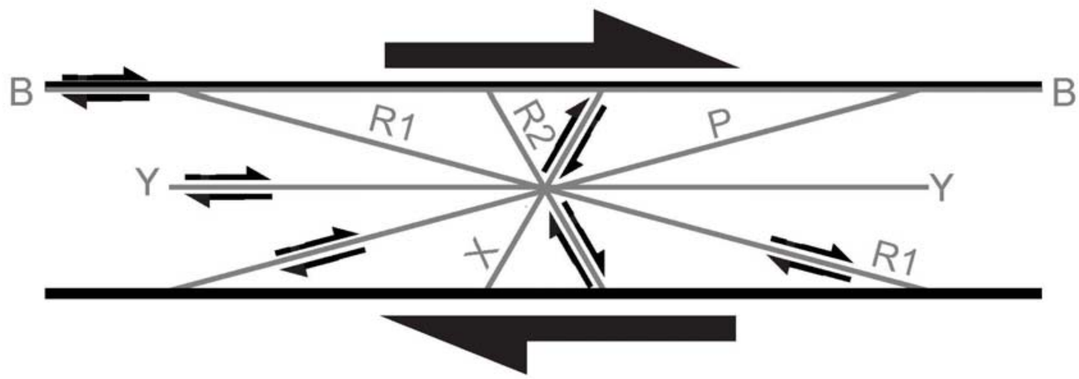

Figure 7-10. Schematic representation of the microstructure of a deformed sample showing the orientation of potential deformation localization features and their nomenclature [after *Logan et al.*, 1992].

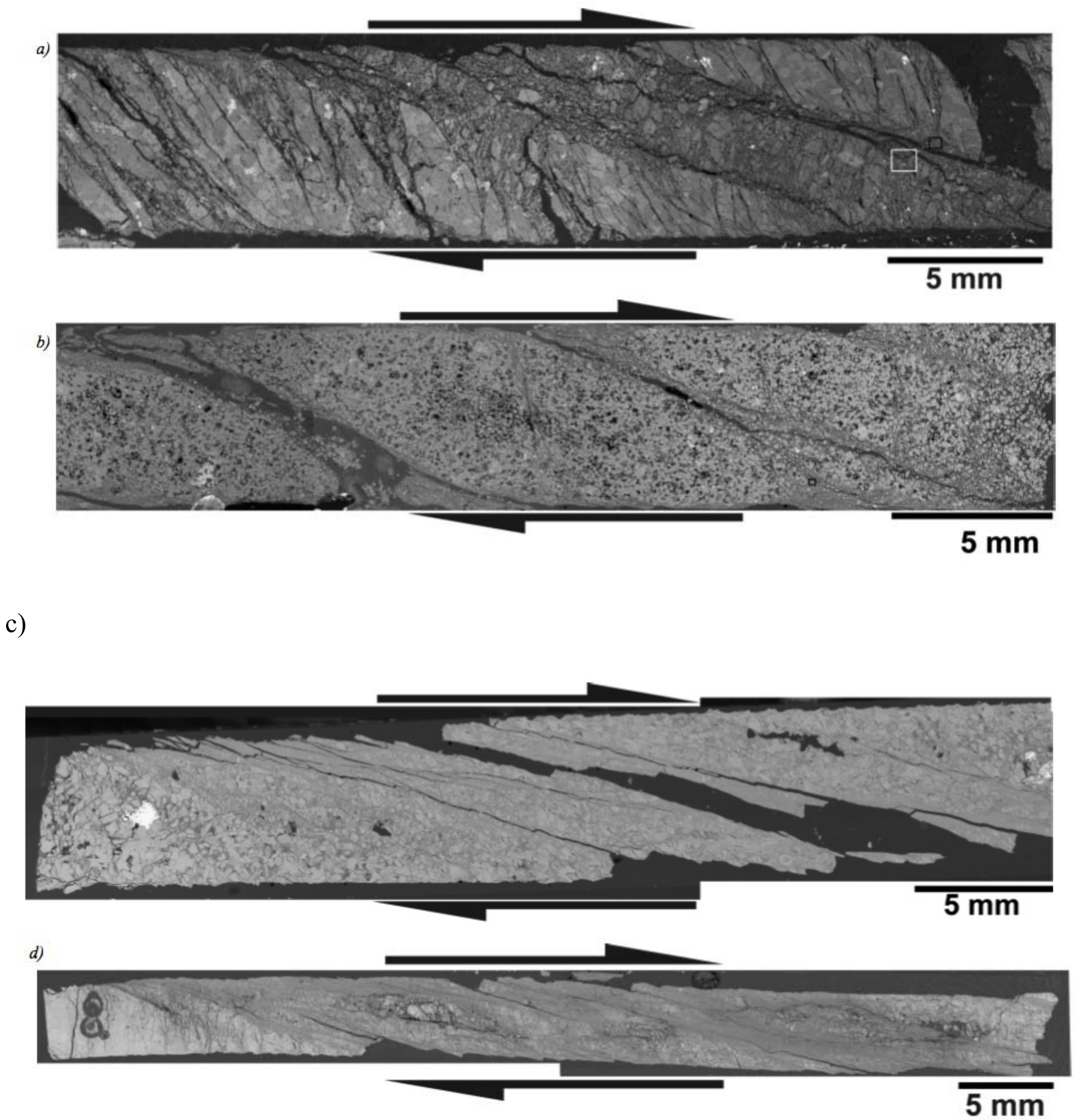

Figure 7-11. Backscattered Scanning Electron Microscope (BSE-SEM) mosaics of four deformed non-foliated and lithified samples. Arrows indicate sense of shear. (a) Westerly granite (p2548). Shear strain is 3.8. The white and black boxes indicate the locations of figure 3a and 3b, respectively. (b) Berea sandstone (p2489). Shear strain is 1.7. The black box indicates the location of Figure 3c. (c) Indiana limestone (p2491). Shear strain is 1.7. (d) Vermont marble (p1696). Shear strain is 6.8.

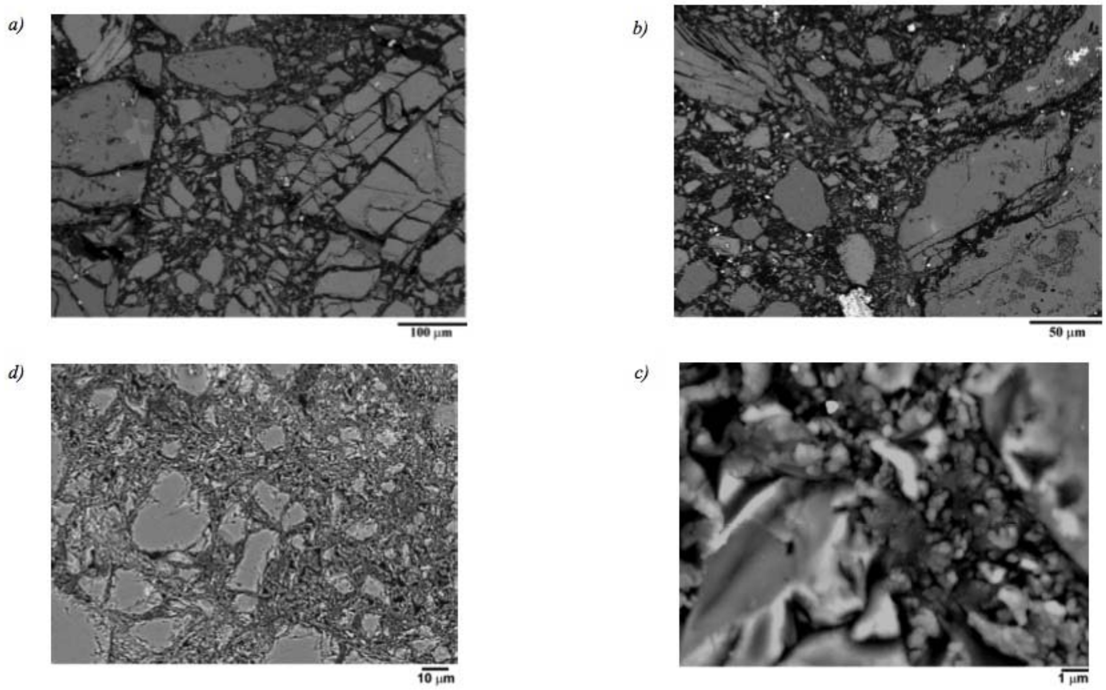

Figure 7-12. (a) Detail of the transition zone between a localized zone and a spectator region for Westerly granite. Transgranular and intragranular fractures in the larger clasts of quartz grains are apparent. Only a few larger grains of feldspar are present. No fracturing is evident in the muscovite grains. (b) Same as (a) but closer to the localized zone of GSR. Note the large variability in grain size. (c) Detail of the zone of grain size reduction in a Riedel (R1) shear orientation for Berea sandstone. Grain size is highly variable and porosity is high. (d) Same as (c) but at high magnification showing sub-micron sized grains.

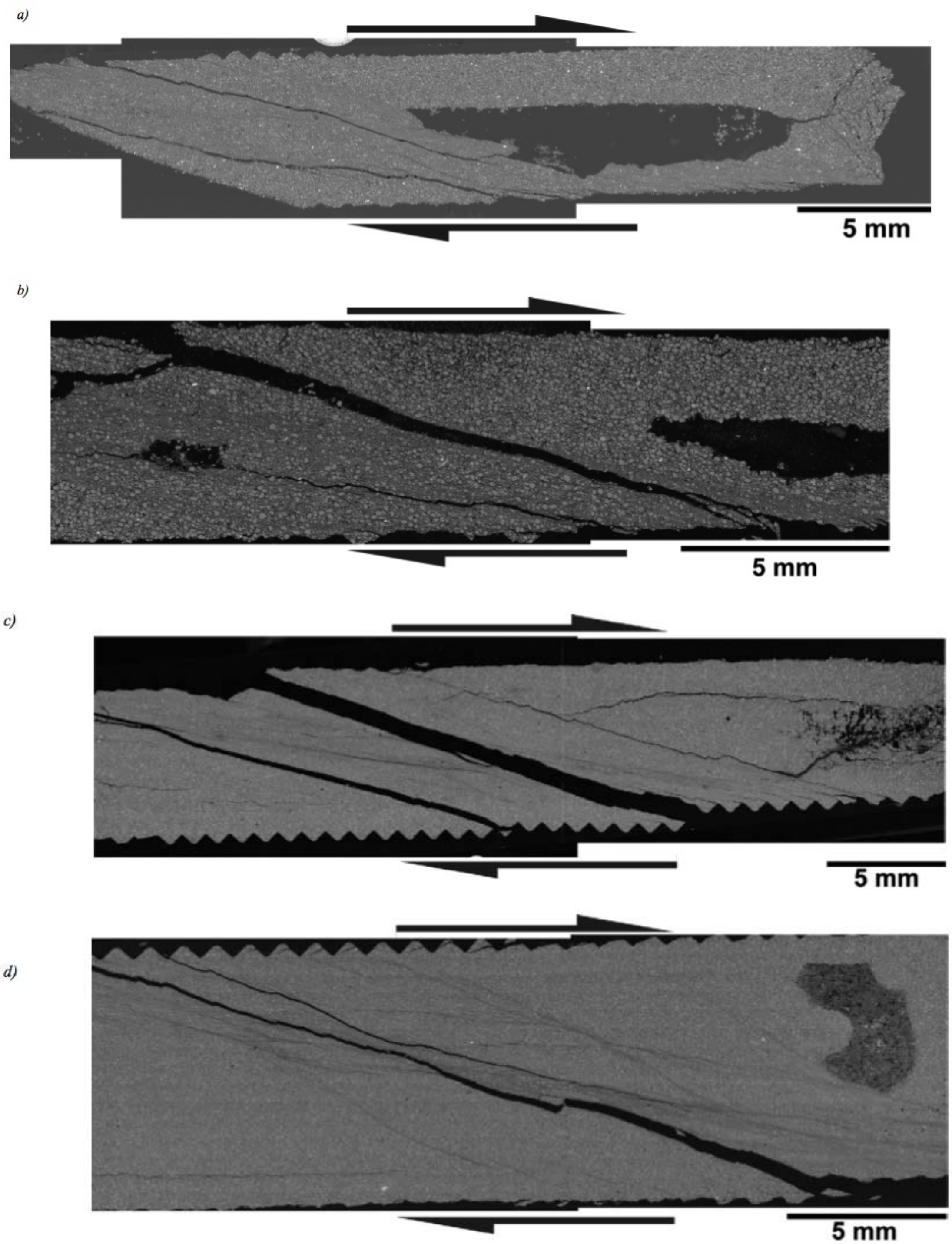

Figure 7-13. BSE-SEM mosaics of four deformed thick non-foliated and granular samples. Normal stress was 50 MPa in all cases and shear sense as indicated. (a) Westerly granite (p2675). Shear strain is 2.1. (b) Berea sandstone (p2664). Shear strain is 2.3. (c) Indiana limestone (p2674). Shear strain is 1.7. (d) Vermont marble (p2676). Shear strain is 1.3.

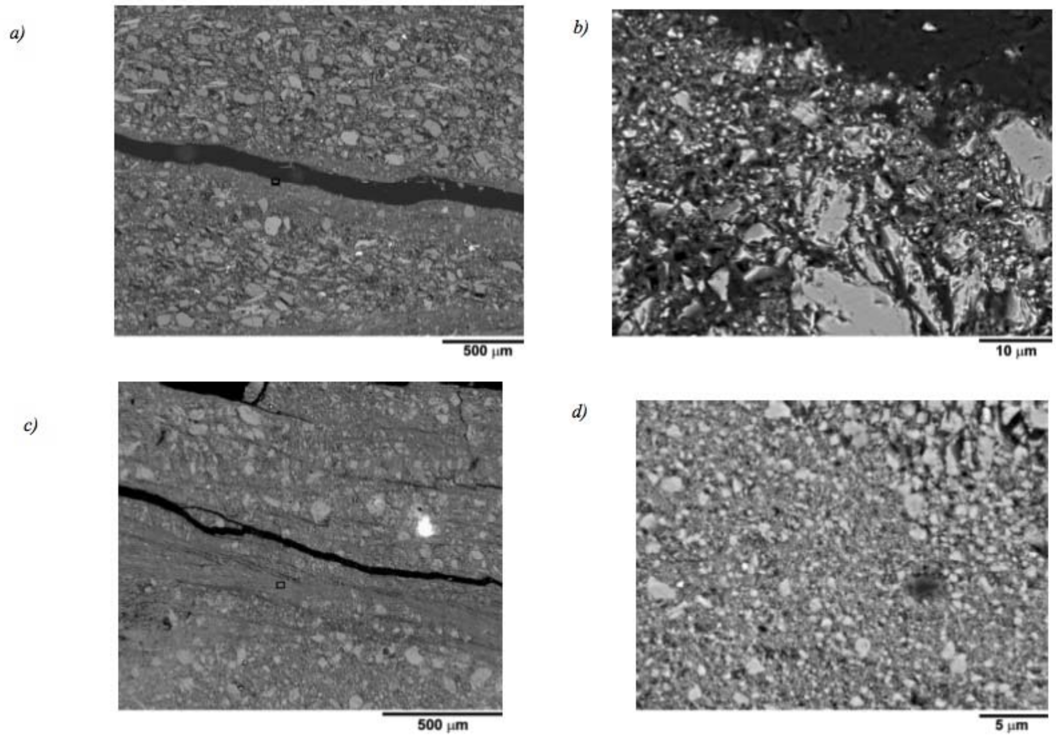

Figure 7-14. BSE-SEM images showing details of the localized zones of intense grain size reduction in deformed non-foliated and granular samples of Westerly granite and Indiana limestone. (a) Detail of a zone of intense grain size reduction surrounding a fracture in the Riedel (R1) orientation in powdered Westerly granite. Note that the thickness of the zone of GSR varies in the range ~10 µm – 350 µm. The box indicates the location of figure 5b. (b) Close-up of the boundary of the zone of GSR with the fracture shown in (a). Note the presence of (sub)micron-size particles. (c) Overview of a part of the gouge thickness of powdered Indiana limestone showing a Riedel fracture with areas of GSR surrounding it. The box indicates the location of figure 5d. (d) Detail of the zone of GSR of (c) showing a large variability in grain size down to the (sub)micron size.

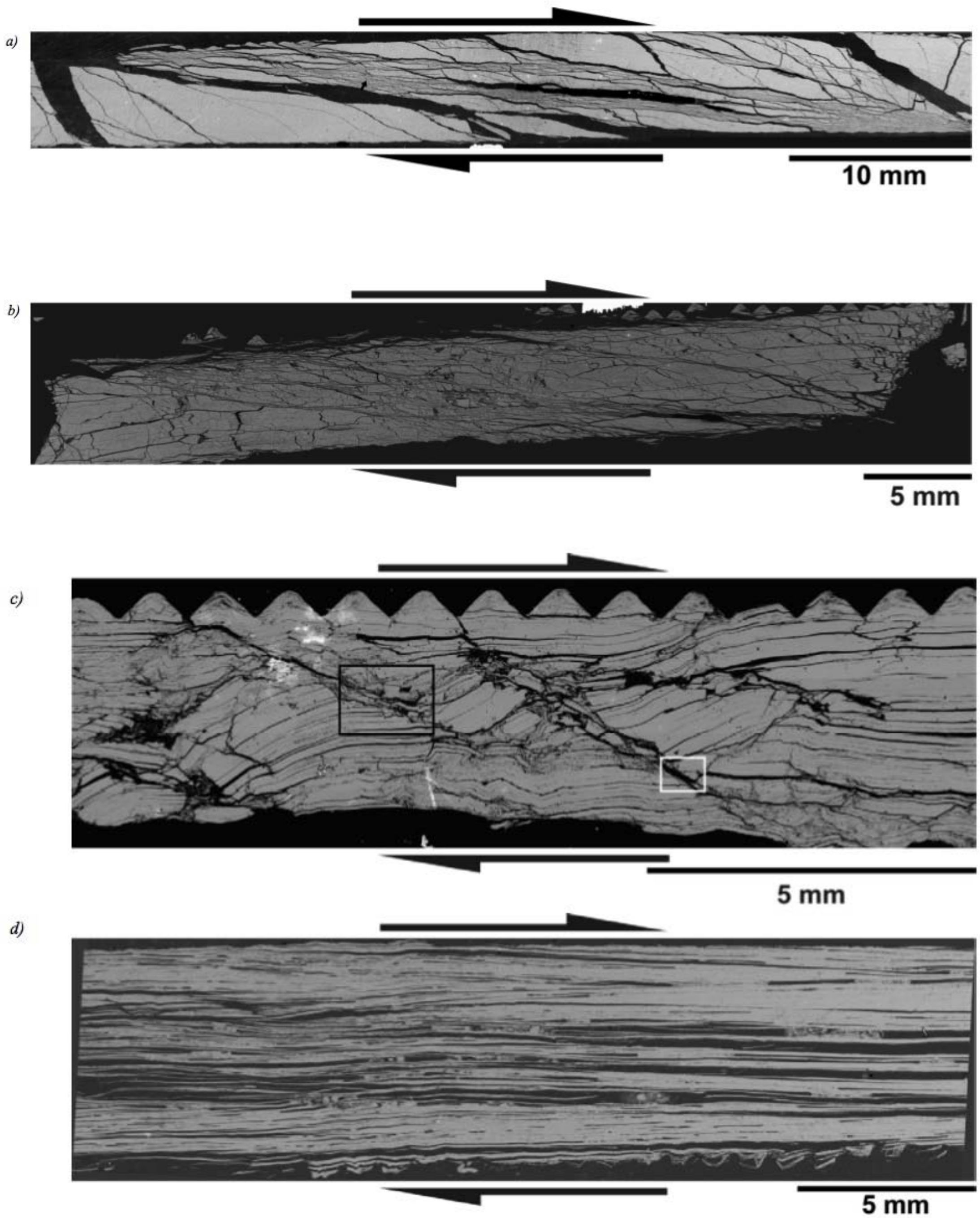

Figure 7-15. BSE-SEM mosaics of four deformed foliated and lithified samples. (a) Pennsylvania slate (p2488). Shear strain is 5.7. Arrow indicates the locations of Figure 16a and 16b. (b) Illite shale (p2317). Shear strain is 6.5. (c) Biotite schist (p2553). Shear strain is 6.9. The black and white boxes indicate the locations of Figure 16c and 16d, respectively. (d) Muscovite schist (p2496). Shear strain is 2.7.

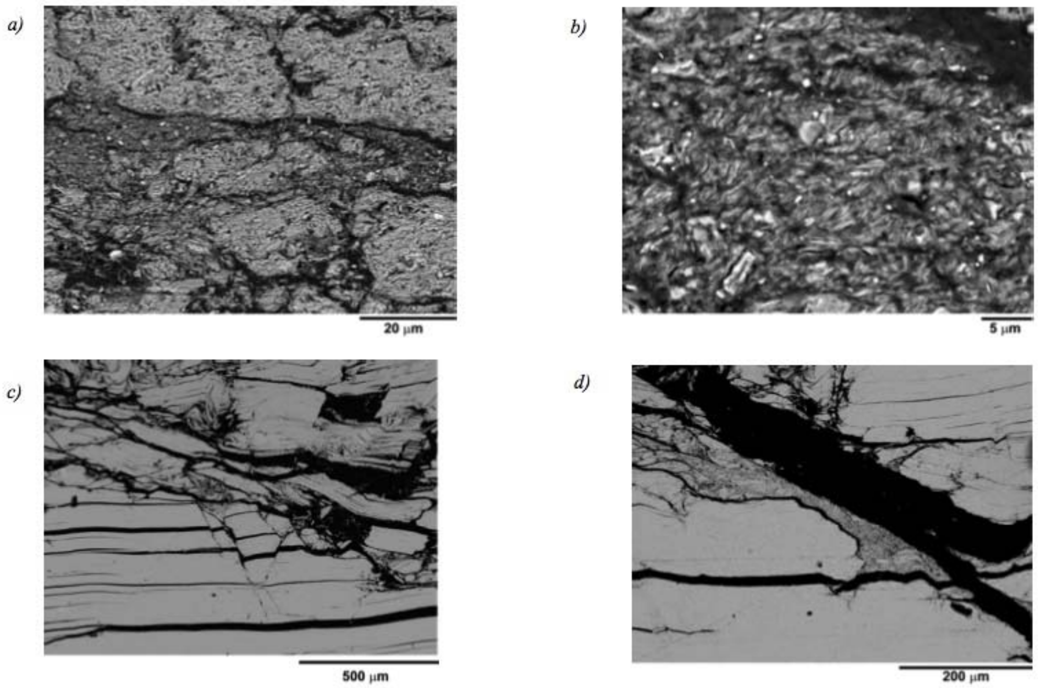

Figure 7-16. BSE-SEM images showing details of the microstructures of deformed foliated and lithified samples of Pennsylvania slate and biotite schist. Shear sense is as in Figure 15. (a) Detail of the fine-grained portion of the microstructure of Pennsylvania slate showing a heterogeneous mixture of fine-grained material and relict portions of the original lithified sample. (b) Close-up of the fine-grained portion of Figure 16a showing comminuted grains down to the (sub)micron scale. (c) Detail of the microstructure of biotite schist showing fractures in the Y orientation terminating against a R_1 fracture. No fine-grained material surrounds the R_1 fracture. (d) Detail of the microstructure of biotite schist showing fractures in the Y orientation terminating against a R_1 fracture and a pocket of fine-grained material surrounding the R_1 fracture.

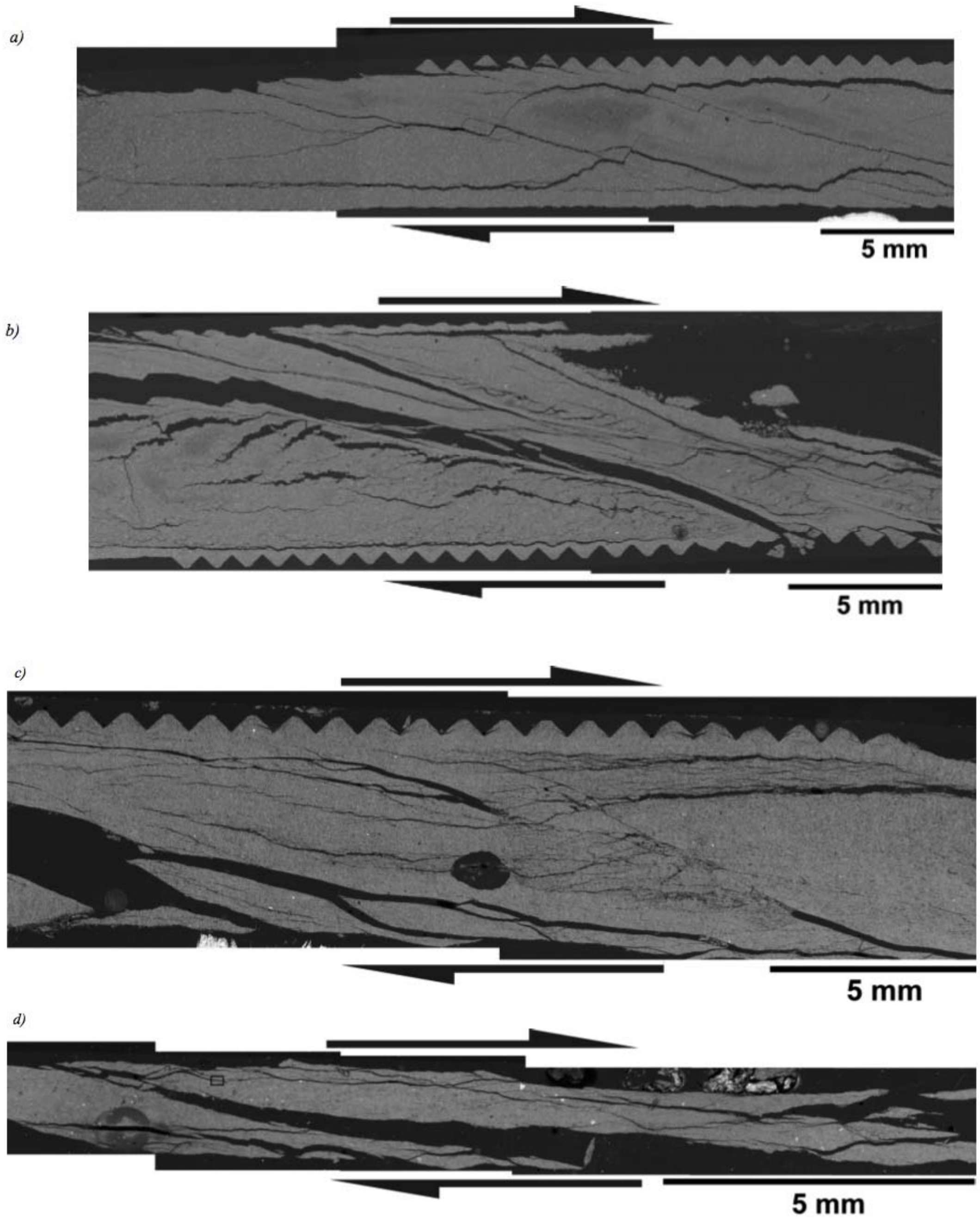

Figure 7-17. BSE-SEM mosaics of three deformed granular, phyllosilicate-rich samples and one thin phyllosilicate-rich sample. Normal stress was 50 MPa in all cases and shear sense as indicated. (a) Pennsylvania slate (p2673). Shear strain is 2.5. (b) Illite shale (p2678). Shear strain is 1.6. (c) Biotite schist (p2679). Shear strain is 2.1. (d)Muscovite schist (p2507). Shear strain is 3.5. The box indicates the location of Figure 18d.

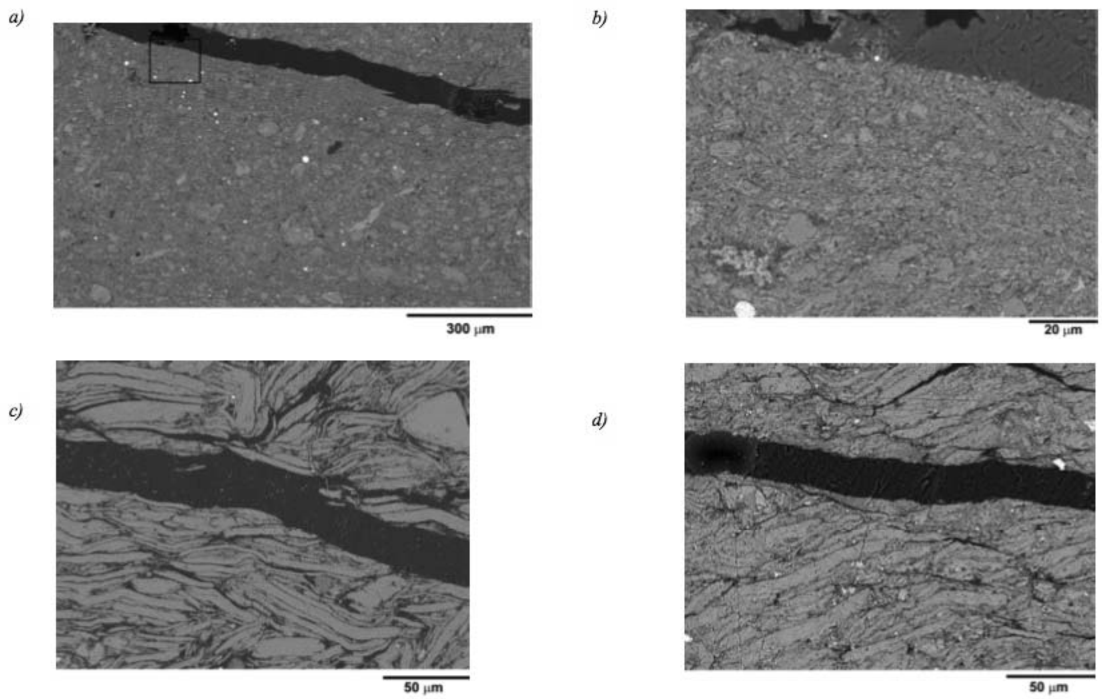

Figure 7-18. BSE-SEM images showing details of the microstructures of deformed thin, granular samples of Pennsylvania slate, biotite schist and muscovite schist. Shear sense is as in Figure 17. (a) Area surrounding a R_1 fracture in Pennsylvania slate (p2478, shear strain is 4.1) showing a decrease in grain size with proximity to the fracture. The box indicates the location of Figure 18b. (b) Detail of the edge of the R_1 fracture shown in Figure 18a showing very fine-grained material (down to sub-micron size) surrounding the fracture. (c) Detail of an R_1 fracture in biotite schist (p2508, shear strain is 3.2) showing the absence of fine-grained material around the fracture. (d) Detail of a low angle fracture in muscovite schist showing a small amount of fine-grained material around the fracture and a mild grain-shape preferred orientation.

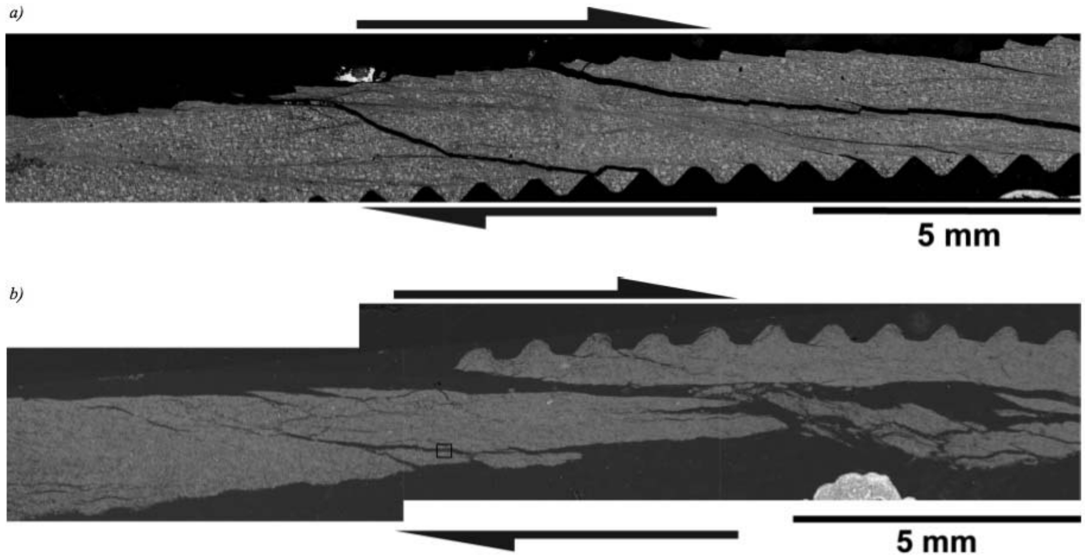

Figure 7-19. BSE-SEM mosaics of two deformed thin granular samples. Normal stress was 50 MPa in both cases and shear sense as indicated. (a) Vermont marble (2476, shear strain is 4.1). (b) Biotite schist (2508, shear strain is 3.2). The box indicates the location of Figure 18c.

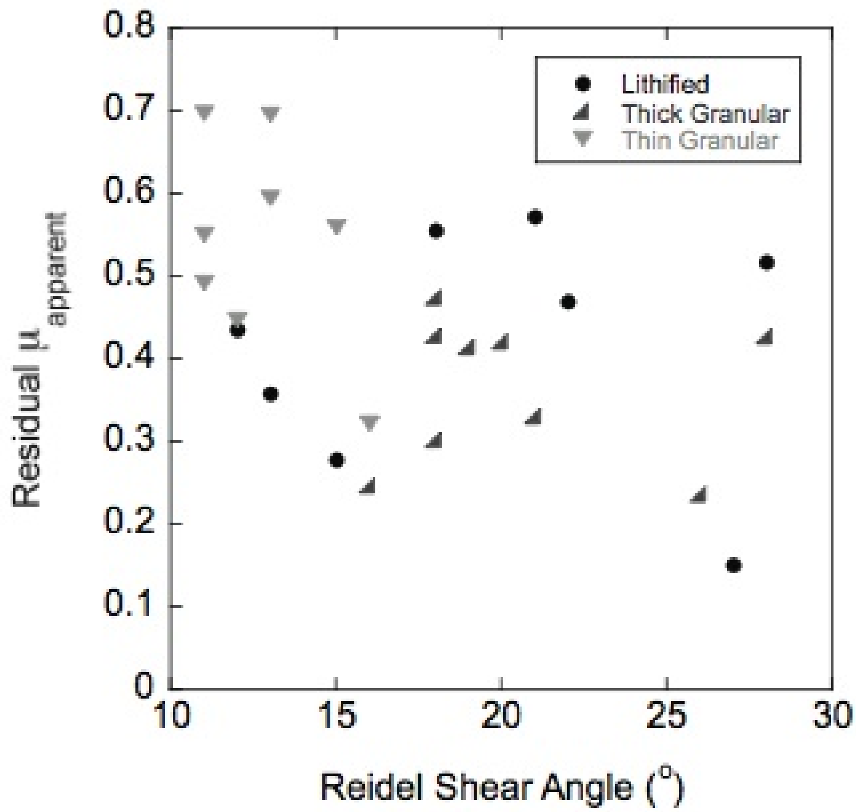

Figure 7-20. Measured value of residual apparent friction as a function of R1 shear angle for all samples in this study. Note that the angle used is the maximum measured R1 angle as observed in the microstructure images.

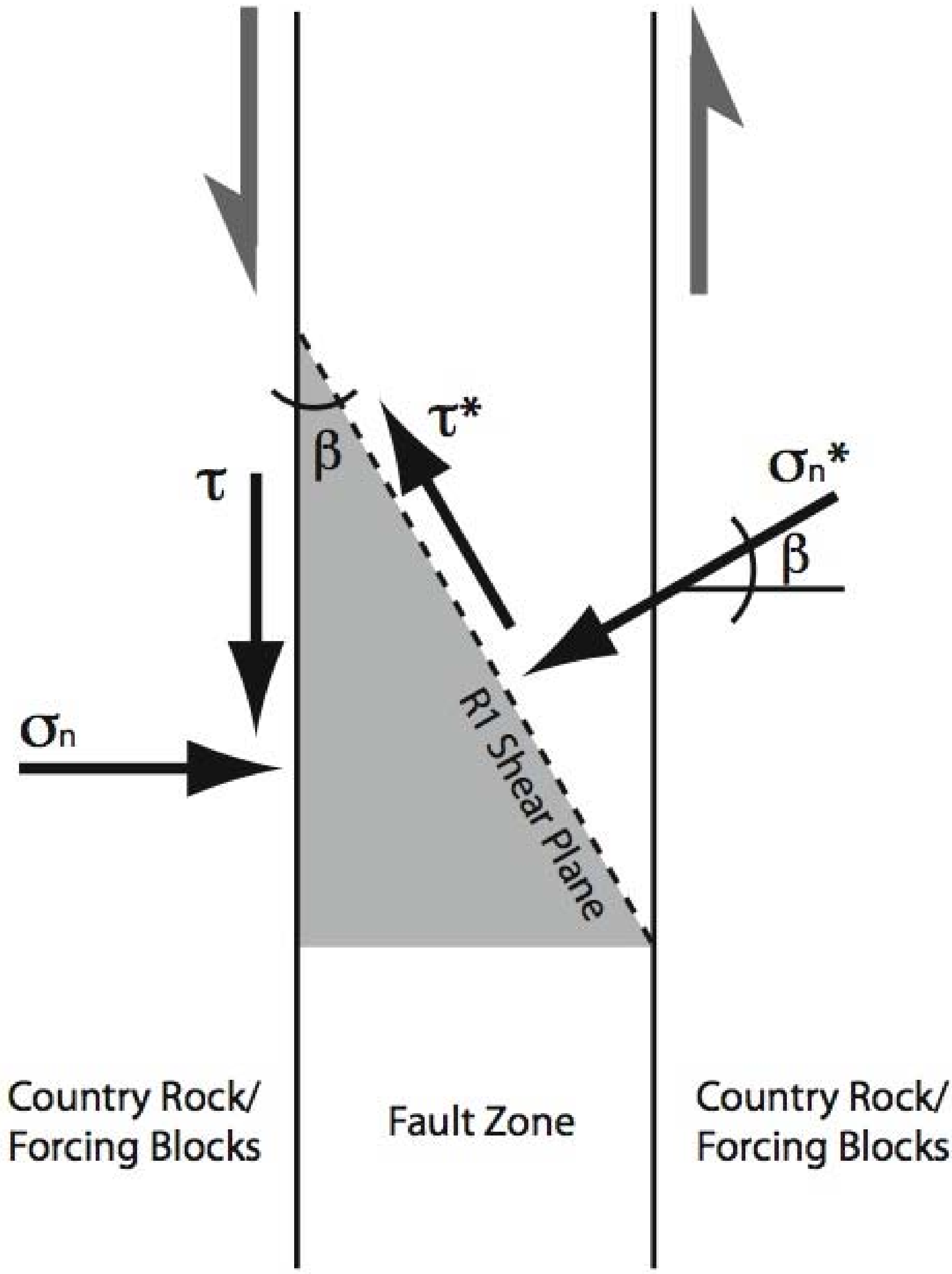

Figure 7-21. Illustration of remotely applied and resolved stresses used in plane-strain stress transformation for our experimental fault zones.

Tables

Experiment	Sample	State	Normal Stress (MPa)	Layer Thickness Under Load (mm)	Maximum Shear Strain
p2548	Westerly Granite	Lithified	49.9	7.81	3.79
p2489	Berea Sandstone	Lithified	49.8	7.07	1.66
p2491	Indiana Limestone	Lithified	49.9	6.80	1.71
p1696	Vermont Marble	Lithified	49.9	9.23	6.78
p2488	Pennsylvania Slate	Lithified	49.9	5.65	1.91
p2324	Chlorite Schist	Lithified	51.3	5.85	3.20
p2317	Illite Shale	Lithified	51.3	6.45	2.30
p2553	Biotite Schist	Lithified	49.3	6.93	3.11
p2496	Muscovite Schist	Lithified	50.0	2.67	2.38
p2675	Westerly Granite	Granular (thick)	50.0	7.54	2.10
p2664	Berea Sandstone	Granular (thick)	50.0	6.46	2.26
p2674	Indiana Limestone	Granular (thick)	50.0	7.50	1.73
p2676	Vermont Marble	Granular (thick)	49.9	9.75	1.33
p2673	Pennsylvania Slate	Granular (thick)	49.9	6.11	2.52
p2677	Chlorite Schist	Granular (thick)	50.0	6.78	1.37
p2678	Illite Shale	Granular (thick)	50.0	7.99	1.59
p2679	Biotite Schist	Granular (thick)	49.8	7.04	2.09
p2729	Muscovite Schist	Granular (thick)	49.8	7.02	2.00
p2477	Westerly Granite	Granular (thin)	49.9	2.75	3.50
p2506	Berea Sandstone	Granular (thin)	49.8	2.97	2.57
p2475	Indiana Limestone	Granular (thin)	49.9	2.25	4.73
p2476	Vermont Marble	Granular (thin)	49.9	2.58	4.14
p2487	Pennsylvania Slate	Granular (thin)	49.9	2.33	4.14
p2473	Chlorite Schist	Granular (thin)	49.6	1.64	5.98
p2472	Illite Shale	Granular (thin)	50.0	1.55	4.59
p2508	Biotite Schist	Granular (thin)	50.0	2.16	3.17
p2507	Muscovite Schist	Granular (thin)	50.0	1.94	3.48

Table 7-1: Experiment parameters.

Experiment	Sample	State	Shear Strain	Residual μ_a	T	h (mm)	T_{gt}	α	F	R	sin ϕ	ϕ (^{o})	μ	μ (α=0)	μ (α=1)
p2548	Westerly Granite	Lithified	2.0	0.47	-0.135	6.37	-0.127	0.94	1.03	1.2	0.57	34.5	0.69	1.07	0.67
p2489	Berea Sandstone	Lithified	1.0	0.52	-0.154	5.94	-0.119	0.77	1.04	1.2	0.68	43.0	0.93	1.45	0.84
p2491	Indiana Limestone	Lithified	1.1	0.56	-0.128	5.79	-0.116	0.90	1.03	1.2	0.68	43.0	0.93	1.41	0.90
p1696	Vermont Marble	Lithified	2.5	0.57	-0.111	6.55	-0.131	1.18	1.03	1.2	0.65	40.7	0.86	1.33	0.91
p2488	Pennsylvania Slate	Lithified	1.2	0.44	-0.101	4.90	-0.098	0.97	1.02	1.2	0.49	29.4	0.56	0.80	0.56
p2317	Illite Shale	Lithified	2.0	0.36	-0.134	4.56	-0.091	0.68	1.03	1.2	0.47	28.0	0.53	0.75	0.45
p2324	Chlorite Schist	Lithified	0.6	0.28	-0.114	3.82	-0.076	0.67	1.02	1.2	0.36	21.2	0.39	0.55	0.32
p2553	Biotite Schist	Lithified	1.5	0.15	-0.106	6.36	-0.127	1.20	1.03	1.2	0.13	7.3	0.13	0.35	0.16
p2496	Muscovite Schist	Lithified	1.0	0.16	-0.023	2.58	-0.052	2.25	1.00	1.2	0.11	6.3	0.11	0.20	0.16
p2675	Westerly Granite	Granular (thick)	1.5	0.42	-0.136	5.84	-0.117	0.86	1.03	1.2	0.51	30.7	0.59	0.90	0.56
p2664	Berea Sandstone	Granular (thick)	1.0	0.43	-0.156	5.48	-0.110	0.70	1.03	1.2	0.58	35.2	0.71	1.05	0.61
p2674	Indiana Limestone	Granular (thick)	1.1	0.48	-0.147	6.22	-0.124	0.85	1.04	1.2	0.60	37.1	0.75	1.17	0.71
p2676	Vermont Marble	Granular (thick)	0.9	0.43	-0.186	8.12	-0.162	0.87	1.06	1.2	0.57	34.8	0.69	1.24	0.65
p2673	Pennsylvania Slate	Granular (thick)	1.7	0.42	-0.113	4.92	-0.098	0.87	1.02	1.2	0.50	29.8	0.57	0.82	0.54
p2678	Illite Shale	Granular (thick)	1.0	0.33	-0.178	6.61	-0.132	0.74	1.05	1.2	0.46	27.4	0.52	0.86	0.44
p2677	Chlorite Schist	Granular (thick)	0.8	0.25	-0.160	5.86	-0.117	0.73	1.04	1.2	0.35	20.2	0.37	0.62	0.29
p2679	Biotite Schist	Granular (thick)	1.5	0.24	-0.152	5.36	-0.107	0.71	1.03	1.2	0.33	19.5	0.35	0.58	0.28
p2729	Muscovite Schist	Granular (thick)	1.0	0.30	-0.146	6.00	-0.120	0.82	1.03	1.2	0.38	22.5	0.42	0.61	0.47
p2477	Westerly Granite	Granular (thin)	2.0	0.60	-0.058	2.33	-0.047	0.80	1.01	1.2	0.66	41.1	0.87	1.02	0.84
p2506	Berea Sandstone	Granular (thin)	1.0	0.56	-0.068	3.28	-0.066	0.97	1.01	1.2	0.61	37.9	0.78	0.97	0.77
p2475	Indiana Limestone	Granular (thin)	2.8	0.70	-0.044	1.91	-0.038	0.87	1.00	1.2	0.75	48.8	1.14	1.31	1.12
p2476	Vermont Marble	Granular (thin)	2.5	0.70	-0.048	2.20	-0.044	0.92	1.00	1.2	0.75	48.9	1.15	1.34	1.13
p2487	Pennsylvania Slate	Granular (thin)	2.0	0.55	-0.051	2.00	-0.040	0.78	1.00	1.2	0.60	36.9	0.75	0.86	0.72
p2472	Illite Shale	Granular (thin)	2.0	0.49	-0.039	1.37	-0.027	0.70	1.00	1.2	0.53	32.0	0.63	0.69	0.60
p2473	Chlorite Schist	Granular (thin)	1.5	0.37	-0.033	1.36	-0.027	0.83	1.00	1.2	0.39	23.1	0.43	0.48	0.41
p2508	Biotite Schist	Granular (thin)	1.5	0.32	-0.054	2.34	-0.047	0.87	1.01	1.2	0.35	20.3	0.37	0.46	0.36
p2507	Muscovite Schist	Granular (thin)	1.5	0.45	-0.051	2.11	-0.042	0.83	1.00	1.2	0.48	29.0	0.55	0.65	0.54

Table 7-2: Parameters for friction correction (geometric thinning method).

Experiment	Sample	V_o (μm/s)	V (μm/s)	*a*	b_1	D_{c1} (μm)	b_2	D_{c2} (μm)	*a-b*	*a* SD	b_1 SD	D_{c1} SD	b_2 SD	D_{c2} SD
p2548	Westerly Granite	1	3	0.0069	0.0016	9.5	0.0037	27.9	0.0016	0.00011	0.00040	2.55	0.00044	1.82
p2548	Westerly Granite	3	10	0.0080	0.0033	9.1	0.0022	416.7	0.0026	0.00017	0.00016	0.77	0.00626	10555.64
p2548	Westerly Granite	10	30	0.0071	0.0022	8.0	0.0029	31.3	0.0021	0.00007	0.00009	0.62	0.00011	0.78
p2548	Westerly Granite	30	100	0.0058	0.0026	78.5	0.0021	78.4	0.0011	0.00003	0.00001	0.80	0.00001	0.98
p2548	Westerly Granite	100	300	0.0039	0.0013	13.1	0.0009	135.3	0.0017	0.00008	0.00007	1.50	0.00005	30.96
p2489	Berea Sandstone	1	3	0.0064	0.0038	11.9	0.0026	66.7	0.0000	0.00006	0.00008	0.43	0.00007	1.85
p2489	Berea Sandstone	3	10	0.0069	0.0042	9.2	0.0029	62.4	-0.0003	0.00011	0.00010	0.41	0.00008	1.84
p2489	Berea Sandstone	10	30	0.0070	0.0050	8.3	0.0027	65.5	-0.0007	0.00013	0.00012	0.35	0.00008	2.28
p2489	Berea Sandstone	30	100	0.0080	0.0055	7.3	0.0027	40.8	-0.0002	0.00031	0.00030	0.78	0.00027	3.50
p2489	Berea Sandstone	100	300	0.0093	0.0065	6.5	0.0042	60.4	-0.0015	0.00036	0.00032	0.53	0.00014	2.41
p2491	Indiana Limestone	1	3	0.0117	0.0107	10.1	0.0028	86.5	-0.0018	0.00008	0.00008	0.13	0.00005	2.32
p2491	Indiana Limestone	3	10	0.0113	0.0099	10.1	0.0029	64.5	-0.0015	0.00013	0.00013	0.25	0.00011	2.67
p2491	Indiana Limestone	10	30	0.0119	0.0085	9.2	0.0049	57.0	-0.0016	0.00009	0.00008	0.17	0.00007	0.83
p2491	Indiana Limestone	30	100	0.0112	0.0075	11.7	0.0044	78.5	-0.0007	0.00015	0.00015	0.41	0.00010	2.00
p2491	Indiana Limestone	100	300	0.0121	0.0070	10.0	0.0063	80.2	-0.0012	0.00023	0.00021	0.56	0.00013	2.13
p1696	Vermont Marble	1	3	0.0063	0.0034	12.9			0.0028	0.00016	0.00016	0.57		
p1696	Vermont Marble	3	10	0.0081	0.0036	7.5	0.0022	35.3	0.0024	0.00015	0.00016	0.65	0.00017	2.18
p1696	Vermont Marble	10	30	0.0080	0.0041	16.3			0.0039	0.00004	0.00004	0.21		
p1696	Vermont Marble	30	100	0.0068	0.0031	37.2			0.0037	0.00004	0.00004	0.72		
p1696	Vermont Marble	100	300	0.0057	0.0012	55.7			0.0045	0.00005	0.00005	4.39		
p2488	Pennsylvania Slate	1	3	0.0039	0.0018	6.8	0.0005	54.5	0.0016	0.00007	0.00008	0.51	0.00005	6.49
p2488	Pennsylvania Slate	3	10	0.0045	0.0028	7.0			0.0018	0.00010	0.00010	0.34		
p2488	Pennsylvania Slate	10	30	0.0048	0.0023	7.5			0.0025	0.00007	0.00007	0.31		
p2488	Pennsylvania Slate	30	100	0.0054	0.0026	9.4			0.0028	0.00020	0.00020	0.95		
p2488	Pennsylvania Slate	100	300	0.0075	0.0037	4.8	0.0012	39.1	0.0026	0.00026	0.00024	0.53	0.00012	4.29
p2317	Illite Shale	1	3	0.0051	0.0028	11.9			0.0023	0.00006	0.00006	0.30		
p2317	Illite Shale	3	10	0.0057	0.0021	6.8	0.0016	35.8	0.0019	0.00130	0.00014	0.85	0.00013	2.48
p2317	Illite Shale	10	30	0.0066	0.0026	5.7	0.0019	39.5	0.0020	0.00025	0.00023	0.93	0.00014	2.89
p2317	Illite Shale	30	100	0.0057	0.0033	21.8			0.0024	0.00025	0.00025	2.18		
p2317	Illite Shale	100	300	0.0062	0.0036	28.3			0.0026	0.00017	0.00017	1.98		
p2324	Chlorite Schist	1	3	0.0027	0.0010	4.6			0.0017	0.00013	0.00013	0.80		
p2324	Chlorite Schist	3	10	0.0030	0.0023	17.0	-0.0022	26.6	0.0029	0.00008	0.00004	1.78	0.00004	2.00
p2324	Chlorite Schist	10	30	0.0039	0.0003	496.7			0.0036	0.00003	0.00070	11024.57		
p2324	Chlorite Schist	30	100	0.0048	-0.0006	217.5			0.0054	0.00006	0.00201	9574.36		
p2324	Chlorite Schist	100	300	0.0055	-0.0014	24.2			0.0070	0.00031	0.00031	8.24		
p2553	Biotite Schist	1	3	0.0063	0.0008	74.4			0.0055	0.00002	0.00002	3.32		
p2553	Biotite Schist	3	10	0.0071	0.0016	48.1			0.0055	0.00003	0.00003	1.30		
p2553	Biotite Schist	10	30	0.0070	0.0015	66.8			0.0054	0.00002	0.00002	1.36		
p2553	Biotite Schist	30	100	0.0068	0.0006	79.5			0.0061	0.00002	0.00002	3.86		
p2553	Biotite Schist	100	300	0.0057	0.0012	72.2			0.0045	0.00002	0.00002	2.59		
p2496	Muscovite Schist	1	3	0.0035	-0.0003	5.0			0.0039	0.00014	0.00014	3.06		
p2496	Muscovite Schist	3	10	0.0045	-0.0006	27.1			0.0051	0.00005	0.00005	3.25		
p2496	Muscovite Schist	10	30	0.0048	-0.0004	11.5			0.0052	0.00010	0.00010	3.57		
p2496	Muscovite Schist	30	100	0.0057	-0.0007	36.7			0.0064	0.00006	0.00006	4.95		
p2496	Muscovite Schist	100	300	0.0065	-0.0005	26.3			0.0070	0.00010	0.00010	7.90		

Table 7-3A. Constitutive friction parameters: Lithified samples.

Experiment	Sample	V_o (μm/s)	V (μm/s)	a	b_1	D_{c1} (μm)	b_2	D_{c2} (μm)	a-b	a SD	b_1 SD	D_{c1} SD	b_2 SD	D_{c2} SD
p2675	Westerly Granite	1	3	0.0062	0.0036	9.2	0.0016	52.1	0.0010	0.00009	0.00010	0.48	0.00009	2.76
p2675	Westerly Granite	3	10	0.0065	0.0036	7.4	0.0014	34.1	0.0015	0.00009	0.00010	0.38	0.00011	1.95
p2675	Westerly Granite	10	30	0.0064	0.0037	9.4	0.0014	36.7	0.0013	0.00006	0.00010	0.41	0.00011	2.49
p2675	Westerly Granite	30	100	0.0077	0.0034	5.5	0.0024	20.5	0.0019	0.00016	0.00020	0.61	0.00025	1.33
p2675	Westerly Granite	100	300	0.0082	0.0043	7.6	0.0025	45.6	0.0013	0.00049	0.00044	1.59	0.00034	5.80
p2664	Berea Sandstone	1	3	0.0054	0.0038	10.5	0.0010	37647.0	0.0006	0.00005	0.00014	0.45	0.00015	3.61
p2664	Berea Sandstone	3	10	0.0055	0.0038	11.1	0.0014	43.7	0.0003	0.00008	0.00016	0.64	0.00017	3.77
p2664	Berea Sandstone	10	30	0.0062	0.0043	10.5	0.0013	58.4	0.0005	0.00006	0.00008	0.34	0.00007	4.19
p2664	Berea Sandstone	30	100	0.0073	0.0044	7.6	0.0021	31.2	0.0008	0.00016	0.00023	0.67	0.00026	2.91
p2664	Berea Sandstone	100	300	0.0080	0.0044	9.2	0.0033	43.9	0.0003	0.00049	0.00052	2.25	0.00053	5.96
p2674	Indiana Limestone	1	3	0.0063	0.0035	7.2	0.0017	30.4	0.0011	0.00028	0.00025	0.79	0.00021	2.58
p2674	Indiana Limestone	3	10	0.0063	0.0028	8.2	0.0027	36.0	0.0008	0.00012	0.00017	0.85	0.00019	1.88
p2674	Indiana Limestone	10	30	0.0079	0.0036	5.7	0.0025	37.8	0.0017	0.00013	0.00012	0.36	0.00008	1.20
p2674	Indiana Limestone	30	100	0.0089	0.0041	5.6	0.0031	39.1	0.0017	0.00033	0.00030	0.73	0.00016	1.96
p2674	Indiana Limestone	100	300	0.0109	0.0055	5.1	0.0036	38.1	0.0019	0.00077	0.00066	1.22	0.00034	3.59
p2676	Vermont Marble	1	3	0.0067	0.0033	10.6	0.0012	37.8	0.0022	0.00012	0.00025	1.10	0.00028	5.85
p2676	Vermont Marble	3	10	0.0078	0.0029	5.2	0.0030	26.4	0.0019	0.00019	0.00018	0.65	0.00016	1.04
p2676	Vermont Marble	10	30	0.0099	0.0038	2.4	0.0039	24.3	0.0022	0.00049	0.00046	0.41	0.00008	0.50
p2676	Vermont Marble	30	100	0.0089	0.0043	7.2	0.0031	52.2	0.0015	0.00018	0.00017	0.52	0.00010	2.22
p2676	Vermont Marble	100	300	0.0132	0.0078	3.9	0.0035	52.0	0.0019	0.00134	0.00124	0.94	0.00025	4.83
p2673	Pennsylvania Slate	1	3	0.0062	0.0033	2.6	0.0016	20.2	0.0013	0.00030	0.00026	0.36	0.00012	1.47
p2673	Pennsylvania Slate	3	10	0.0052	0.0028	7.2	0.0011	38.4	0.0013	0.00011	0.00013	0.58	0.00012	3.49
p2673	Pennsylvania Slate	10	30	0.0051	0.0023	10.5	0.0013	46.0	0.0015	0.00010	0.00014	1.09	0.00015	3.66
p2673	Pennsylvania Slate	30	100	0.0059	0.0021	9.0	0.0017	29.9	0.0021	0.00027	0.00066	4.07	0.00074	8.03
p2673	Pennsylvania Slate	100	300	0.0092	0.0050	4.7	0.0019	64.4	0.0022	0.00081	0.00076	1.10	0.00018	8.83
p2678	Illite Shale	1	3	0.0045	0.0015	4.0	0.0008	25.9	0.0022	0.00011	0.00011	0.54	0.00008	2.47
p2678	Illite Shale	3	10	0.0042	0.0013	6.8	0.0008	34.0	0.0021	0.00008	0.00010	1.02	0.00010	3.56
p2678	Illite Shale	10	30	0.0046	0.0013	5.5	0.0010	27.5	0.0023	0.00009	0.00011	0.88	0.00011	2.36
p2678	Illite Shale	30	100	0.0049	0.0013	7.7	0.0008	31.4	0.0028	0.00015	0.00028	2.54	0.00029	12.86
p2678	Illite Shale	100	300	0.0061	0.0026	6.8	0.0006	54.9	0.0030	0.00028	0.00026	1.30	0.00015	18.87
p2677	Chlorite Schist	1	3	0.0027	0.0014	18.1			0.0014	0.00005	0.00005	0.91		
p2677	Chlorite Schist	3	10	0.0032	0.0013	13.2			0.0019	0.00006	0.00006	0.83		
p2677	Chlorite Schist	10	30	0.0040	0.0013	8.5			0.0027	0.00006	0.00006	0.51		
p2677	Chlorite Schist	30	100	0.0044	0.0010	10.9			0.0034	0.00007	0.00007	0.97		
p2677	Chlorite Schist	100	300	0.0057	0.0013	6.2			0.0044	0.00053	0.00053	3.65		
p2679	Biotite Schist	1	3	0.0027	0.0007	42.4			0.0019	0.00002	0.00002	1.77		
p2679	Biotite Schist	3	10	0.0031	0.0007	45.5			0.0023	0.00002	0.00002	2.04		
p2679	Biotite Schist	10	30	0.0034	0.0000	62.1			0.0029	0.00001	0.00001	3.11		
p2679	Biotite Schist	30	100	0.0038	0.0002	77.2			0.0035	0.00002	0.00002	18.78		
p2679	Biotite Schist	100	300	0.0043	-0.0009	65.5			0.0051	0.00006	0.00006	7.75		
p2729	Muscovite Schist	1	3	0.0032	0.0010	59.5			0.0022	0.00003	0.00003	3.04		
p2729	Muscovite Schist	3	10	0.0039	0.0008	26.7			0.0031	0.00006	0.00006	2.88		
p2729	Muscovite Schist	10	30	0.0044	0.0009	22.3			0.0034	0.00003	0.00003	0.95		
p2729	Muscovite Schist	30	100	0.0048	0.0010	47.0			0.0038	0.00003	0.00003	1.85		
p2729	Muscovite Schist	100	300	0.0057	0.0011	28.8			0.0046	0.00006	0.00006	2.16		

Table 7-3B. Constitutive friction parameters: Initially thick granular samples.

Experiment	Sample	V_o (μm/s)	V (μm/s)	*a*	b_1	D_{c1} (μm)	b_2	D_{c2} (μm)	*a-b*	*a* SD	b_1 SD	D_{c1} SD	b_2 SD	D_{c2} SD
p2477	Westerly Granite	1	3	0.0077	0.0045	11.0	0.0019	57.7	0.0014	0.00008	0.00009	0.39	0.00009	2.37
p2477	Westerly Granite	3	10	0.0081	0.0048	8.3	0.0021	55.7	0.0012	0.00013	0.00012	0.39	0.00009	2.44
p2477	Westerly Granite	10	30	0.0081	0.0051	9.7	0.0024	70.9	0.0006	0.00029	0.00027	0.85	0.00014	3.36
p2477	Westerly Granite	30	100	0.0087	0.0055	8.2	0.0038	78.9	-0.0006	0.00025	0.00023	0.58	0.00011	3.01
p2477	Westerly Granite	100	300	0.0088	0.0060	10.2	0.0047	110.0	-0.0019	0.00035	0.00033	0.98	0.00015	7.22
p2506	Berea Sandstone	1	3	0.0067	0.0042	9.2	0.0019	40.8	0.0006	0.00013	0.00019	0.69	0.00020	3.35
p2506	Berea Sandstone	3	10	0.0071	0.0044	7.9	0.0019	43.7	0.0008	0.00012	0.00013	0.43	0.00012	2.55
p2506	Berea Sandstone	10	30	0.0076	0.0052	8.0	0.0022	74.3	0.0002	0.00009	0.00008	0.22	0.00005	2.07
p2506	Berea Sandstone	30	100	0.0089	0.0061	5.9	0.0029	62.4	0.0000	0.00023	0.00021	0.32	0.00008	2.18
p2506	Berea Sandstone	100	300	0.0100	0.0070	5.7	0.0036	78.4	-0.0005	0.00037	0.00034	0.40	0.00010	3.38
p2475	Indiana Limestone	1	3	0.0082	0.0047	6.3	0.0016	37.3	0.0019	0.00009	0.00009	0.22	0.00007	1.53
p2475	Indiana Limestone	3	10	0.0090	0.0048	5.7	0.0021	41.8	0.0021	0.00025	0.00022	0.48	0.00013	2.75
p2475	Indiana Limestone	10	30	0.0097	0.0052	7.1	0.0029	57.6	0.0016	0.00020	0.00019	0.45	0.00010	2.29
p2475	Indiana Limestone	30	100	0.0101	0.0046	7.2	0.0045	48.5	0.0010	0.00067	0.00063	1.96	0.00044	4.74
p2475	Indiana Limestone	100	300	0.0097	0.0052	9.0	0.0047	63.1	-0.0002	0.00056	0.00056	2.04	0.00043	6.46
p2476	Vermont Marble	1	3	0.0089	0.0044	7.6	0.0023	43.1	0.0022	0.00009	0.00009	0.28	0.00008	1.22
p2476	Vermont Marble	3	10	0.0090	0.0041	9.5	0.0024	51.7	0.0025	0.00008	0.00009	0.37	0.00008	1.54
p2476	Vermont Marble	10	30	0.0104	0.0053	7.1	0.0034	72.0	0.0017	0.00018	0.00016	0.35	0.00007	1.89
p2476	Vermont Marble	30	100	0.0107	0.0049	6.9	0.0038	54.6	0.0019	0.00042	0.00038	0.94	0.00020	2.99
p2476	Vermont Marble	100	300	0.0112	0.0063	7.6	0.0042	79.0	0.0008	0.00063	0.00059	1.20	0.00024	6.91
p2487	Pennsylvania Slate	1	3	0.0056	0.0031	5.1	0.0012	28.3	0.0012	0.00009	0.00009	0.27	0.00008	1.57
p2487	Pennsylvania Slate	3	10	0.0061	0.0032	4.7	0.0014	27.5	0.0016	0.00017	0.00016	0.45	0.00013	2.25
p2487	Pennsylvania Slate	10	30	0.0066	0.0033	5.3	0.0016	35.4	0.0018	0.00007	0.00007	0.20	0.00005	1.02
p2487	Pennsylvania Slate	30	100	0.0070	0.0037	7.1	0.0015	49.3	0.0019	0.00013	0.00013	0.43	0.00009	2.81
p2487	Pennsylvania Slate	100	300	0.0083	0.0049	9.4			0.0034	0.00014	0.00014	0.33		
p2472	Illite Shale	1	3	0.0056	0.0024	4.4	0.0009	39.8	0.0024	0.00015	0.00014	0.44	0.00007	3.27
p2472	Illite Shale	3	10	0.0061	0.0026	4.2	0.0007	28.9	0.0027	0.00024	0.00022	0.67	0.00014	5.46
p2472	Illite Shale	10	30	0.0058	0.0023	6.3	0.0010	47.7	0.0026	0.00014	0.00013	0.66	0.00008	3.95
p2472	Illite Shale	30	100	0.0064	0.0027	6.7	0.0009	48.7	0.0028	0.00019	0.00020	0.92	0.00013	14.38
p2472	Illite Shale	100	300	0.0075	0.0034	5.8	0.0011	53.0	0.0029	0.00050	0.00047	1.43	0.00022	13.79
p2473	Chlorite Schist	1	3	0.0033	0.0023	6.6	0.0008	36.6	0.0002	0.00006	0.00008	0.39	0.00007	3.00
p2473	Chlorite Schist	3	10	0.0036	0.0019	8.2	0.0009	49.2	0.0008	0.00008	0.00010	0.75	0.00008	4.43
p2473	Chlorite Schist	10	30	0.0041	0.0021	16.8			0.0020	0.00009	0.00009	0.94		
p2473	Chlorite Schist	30	100	0.0048	0.0017	14.9			0.0032	0.00016	0.00016	2.09		
p2473	Chlorite Schist	100	300	0.0068	0.0020	4.9			0.0049	0.00086	0.00086	3.12		
p2508	Biotite Schist	1	3	0.0026	0.0016	67.0			0.0009	0.00002	0.00002	1.48		
p2508	Biotite Schist	3	10	0.0030	0.0005	39.6			0.0025	0.00004	0.00003	4.29		
p2508	Biotite Schist	10	30	0.0033	0.0004	47.7			0.0029	0.00003	0.00003	7.08		
p2508	Biotite Schist	30	100	0.0039	0.0003	1176.0			0.0036	0.00003	0.00593	1.23E+13		
p2508	Biotite Schist	100	300	0.0045	-0.0002	6.9			0.0047	0.00038	0.00038	50.35		
p2507	Muscovite Schist	1	3	0.0044	0.0014	9.8	0.0006	94.0	0.0024	0.00006	0.00006	0.78	0.00003	8.22
p2507	Muscovite Schist	3	10	0.0046	0.0011	11.9			0.0035	0.00007	0.00007	0.98		
p2507	Muscovite Schist	10	30	0.0053	0.0013	10.7			0.0040	0.00007	0.00007	0.69		
p2507	Muscovite Schist	30	100	0.0059	0.0012	12.0			0.0047	0.00013	0.00013	1.70		
p2507	Muscovite Schist	100	300	0.0067	0.0014	17.3			0.0053	0.00016	0.00016	2.89		

Table 7-3C. Constitutive friction parameters: Initially thin granular samples.

Experiment	Sample	State	Shear Strain	β (^{0})	Residual μ_a	τ	σ_n	$\tau*$	σ_n*	$\mu*$
p2548	Westerly Granite	Lithified	2.0	22	0.47	23.5	49.9	37.5	51.1	0.74
p2489	Berea Sandstone	Lithified	1.0	28	0.52	25.8	49.8	40.8	49.5	0.82
p2491	Indiana Limestone	Lithified	1.1	18	0.56	27.7	49.9	39.7	53.3	0.75
p1696	Vermont Marble	Lithified	2.5	21	0.57	28.6	49.9	41.6	53.1	0.78
p2488	Pennsylvania Slate	Lithified	1.2	12	0.44	21.8	49.9	31.0	52.2	0.59
p2317	Illite Shale	Lithified	2.0	13	0.36	18.4	51.3	28.7	52.7	0.54
p2324	Chlorite Schist	Lithified	0.6	15	0.28	14.2	51.3	26.1	51.4	0.51
p2553	Biotite Schist	Lithified	1.5	27	0.15	7.5	49.3	25.9	42.2	0.61
p2496	Muscovite Schist	Lithified	1.0	0	0.15	7.7	50.0	7.7	50.0	0.15
p2675	Westerly Granite	Granular (thick)	1.5	19	0.42	20.8	50.0	34.0	51.1	0.67
p2664	Berea Sandstone	Granular (thick)	1.0	18	0.43	21.5	50.0	34.1	51.5	0.66
p2674	Indiana Limestone	Granular (thick)	1.1	18	0.48	23.8	50.0	36.2	52.2	0.69
p2676	Vermont Marble	Granular (thick)	0.9	28	0.43	21.4	49.9	37.4	47.8	0.78
p2673	Pennsylvania Slate	Granular (thick)	1.7	20	0.42	21.1	49.9	34.7	50.8	0.68
p2678	Illite Shale	Granular (thick)	1.0	21	0.33	16.6	50.0	31.2	49.1	0.63
p2677	Chlorite Schist	Granular (thick)	0.8	16	0.25	12.3	50.0	24.6	49.5	0.50
p2679	Biotite Schist	Granular (thick)	1.5	26	0.24	11.8	49.8	29.2	44.9	0.65
p2729	Muscovite Schist	Granular (thick)	1.0	18	0.30	15.1	49.8	28.3	49.5	0.57
p2477	Westerly Granite	Granular (thin)	2.0	13	0.60	29.7	49.9	39.1	53.9	0.73
p2506	Berea Sandstone	Granular (thin)	1.0	15	0.56	27.8	49.8	38.4	53.4	0.72
p2475	Indiana Limestone	Granular (thin)	2.8	11	0.70	34.8	49.9	42.9	54.6	0.79
p2476	Vermont Marble	Granular (thin)	2.5	13	0.70	34.7	49.9	43.9	55.0	0.80
p2487	Pennsylvania Slate	Granular (thin)	2.0	11	0.55	27.5	49.9	35.8	53.2	0.67
p2472	Illite Shale	Granular (thin)	2.0	11	0.49	24.4	49.6	32.8	52.4	0.63
p2473	Chlorite Schist	Granular (thin)	1.5	-	0.37	18.6	50.0	-	-	-
p2508	Biotite Schist	Granular (thin)	1.5	16	0.32	16.2	50.0	28.2	50.5	0.56
p2507	Muscovite Schist	Granular (thin)	1.5	12	0.45	22.4	50.0	31.6	52.4	0.60

Table 7-4: Parameters for friction correction (stress transformation method).

REFERENCES

Ando, M. (1975), Source mechanisms and tectonic significance of historical earthquakes along the Nankai Trough, Japan, *Tectonophys., 27,* 119-140.

Arch, J. and A. Maltman (1990), Anisotropic permeability and tortuosity in deformed wet sediments, *J. Geophys. Res., 95,* 9035-9045.

Bakun, W.H., and 18 others (2005), Implications for prediction and hazard assessment from the 2004 Parkfield earthquake, *Nature, 437,* 969-974, doi:10.1038/nature04067.

Bangs, N.L.B., G.F. Moore, S.P.S. Gulick, E.M. Pangborn, H.J. Tobin, S. Kuramoto, and A. Taira (2009), Broad, weak regions of the Nankai megathrust and implications for shallow coseismic slip, *Earth Plan. Sci. Lett., 284,* 44-49.

Bangs, N.L., T.H. Shipley, S.P.S. Gulick, G.F. Moore, S. Kuramoto, and Y. Nakamura (2004), Evolution of the Nankai Trough décollement from the trench into the seismogenic zone: Inferences from three-dimensional seismic reflection imaging, *Geology, 32*, 273-276, doi:10.1130/G20211.1.

Beeler, N.M. (2007), Laboratory-observed faulting in intrinsically and apparently weak materials, in *The Seismogenic Zone of Subduction Thrust Faults,* T.H. Dixon and J.C. Moore (eds.), Columbia Univ. Press, New York.

Beeler, N.M., R.W. Simpson, S.H. Hickman, and D.A. Lockner (2000), Pore fluid pressure, apparent friction, and Coulomb failure, *J. Geophys. Res., 105*, No. B11, 25,533-25,542.

Beeler, N.M., T.E. Tullis, M.L. Blanpied, and J.D. Weeks (1996); Frictional behavior of large displacement experimental faults, *J. Geophys. Res., 101,* 8697-8715.

Bernabé, Y., D.T. Fryer, and J.A. Hayes (1992), The effect of cement on the strength of granular rocks, *Geophys. Res. Lett., 19*, 1511-1514.

Bird, P. (1984), Hydration-phase diagrams and friction of montmorillonite under laboratory and geologic conditions, with implications for shale compaction, slope stability, and strength of fault gouge, *Tectonophysics*, *107*, 235-260.

Bizzari, A. and M. Cocco (2006a), A thermal pressurization model for the spontaneous dynamic rupture propagation on a three-dimensional fault: 1. Methodological approach, J. Geophys. Res., 111, B05303, doi:10.1029/2005JB003862.

Bizzari, A. and M. Cocco (2006b), A thermal pressurization model for the spontaneous dynamic rupture propagation on a three-dimensional fault: 2. Traction evolution and dynamic parameters, J. Geophys. Res., 111, B05304, doi:10.1029/2005JB003864.

Blanpied, M.L., C.J. Marone, D.A. Lockner, J.D. Byerlee, and D.P. King (1998), Quantitative measure of the variation in fault rheology due to fluid-rock interactions, *J. Geophys. Res., 103,* 9691-9712.

Blanpied, M.L., D.A. Lockner, J.D. Byerlee (1992), An earthquake mechanism based on rapid sealing of faults, *Nature, 358*, 574-576.

Boettcher, M.S. and C. Marone (2004), Effects of normal stress variation on the strength and stability of creeping faults, *J. Geophys. Res., 109,* B03406, doi:10.1029/2003JB002824.

Bourlange, S., L. Jouniax, and P. Henry (2004), Data report: permeability, compressibility, and friction coefficient measurements under confining pressure and strain, Leg 190, Nankai Trough, in *Proc. ODP, Sci. Results, 190/196*, H. Mikada, G.F. Moore, A. Taira, K. Becker, J.C. Moore, and A. Klaus (eds.), College Station, TX (Ocean Drilling Program), 1-16, doi:10.2973/odp.proc.sr.190196.215.2004.

Brown, K.M., A. Kopf, M.B. Underwood, and J.L. Weinberger (2003), Compositional and fluid pressure controls on the state of stress on the Nankai subduction thrust: A weak plate boundary, *Earth Planet. Sci. Lett., 214,* 589-603.

Brown, K.M. and J.C. Moore (1993), Comment on "Anisotropic permeability and tortuosity in deformed wet sediments" by J. Arch and A. Maltman, *J. Geophys. Res., 98*, 17,859-17,864.

Brune, J.N. (1970), Tectonic stress and the spectra of seismic shear waves from earthquakes, *J. Geophys. Res., 75*, 4997-5009.

Byerlee, J. (1990), Friction, overpressure, and fault normal compression, *Geophys. Res. Lett., 17*, 2109-2112.

Byerlee, J.D. (1978), Friction of rocks, *Pure Appl. Geophys.*, *116*, 215-626.

Byerlee, J.D., and J.C. Savage (1992), Coulomb plasticity within the fault zone, *Geophys. Res. Lett., 19*, 2341-2344.

Byerlee, J., V. Mjachkin, R. Summers, and O. Voevoda (1978), Structures developed in fault gouge during stable sliding and stick-slip, *Tectonophys., 44*, 161-171.

Byrne, D.E., D.M. Davis and L.R. Sykes (1988), Loci and maximum size of thrust earthquakes and the mechanics of the shallow region of subduction zones, *Tectonics, 7,* 833-857.

Byrne, T., and D. Fisher (1990), Evidence for a weak and overpressured décollement beneath sediment-dominated accretionary prisms, *J. Geophys.Res., 95*, 9081-9097.

Caine, J.S., J.P. Evans, and C.B. Forster (1996), Fault zone architecture and permeability structure, *Geology, 24*, 1025-1028.

Chester, F.M. and N.G. Higgs (1992), Multimechanism friction constitutive model for ultrafine quartz gouge at hypocentral locations, *J. Geophys. Res., 97*, 1859-1870.

Collettini, C., C. Viti, S.A.F. Smith, and R.E. Holdsworth (2009), Development of interconnected talc networks and weakening of continental low-angle normal faults, *Geology, 37,* 567-570, doi:10.1130/G25645A.1.

Collettini, C., and R.E. Holdsworth (2004), Fault zone weakening and character of slip along low-angle normal faults: insights from the Zuccale fault, Elba, Italy, *J. Geol. Soc., London, 161*, 1039-1051.

Colten-Bradley, V.A. (1987), Role of pressure in smectite dehydration–effects on geopressure and smectite-to-illite transformation, *AAPG Bull.*, *71*, 1414-1427.

Cowie, P.A., and C.H. Scholz (1992), Growth of faults by accumulation of seismic slip, *J. Geophys. Res., 97,* 11,085-11,095.

Crawford, B.R., D.R. Faulkner, and E.H. Rutter (2008), Strength, porosity, and permeability development during hydrostatic and shear loading of synthetic quartz-clay fault gouge, *J. Geophys. Res., 113,* B03207, doi:10.1029/2006JB004634.

Cummins, P.R. and Y. Kaneda (2000), Possible splay fault slip during the 1946 Nankai earthquake, *Geophys. Res. Lett., 27,* 2725-2728.

Davis, D.M., and R. von Huene (1987), Inferences on sediment strength and fault friction from structures at the Aleutian trench, *Geology, 15,* 517-522.

Davis, D., J. Suppe, and F.A. Dahlen (1983), Mechanics of fold-and-thrust belts and accretionary wedges, *J. Geophys. Res., 88,* 1153-1172.

Davis, E.E., K. Becker, K. Wang, K. Obara, Y. Ito, and M. Kinoshita (2006), A discrete episode of seismic and aseismic deformation of the Nankai trough subduction zone accretionary prism and incoming Philippine Sea plate, *Earth Plan. Sci. Lett., 242*, 73-8Deng, X. and M.B. Underwood (2001), Abundance of smectite and the location of a plate-boundary fault, Barbados accretionary prism, *Geol. Soc. Am. Bull., 113,* 495-507.

Dewhurst, D.N., K.M. Brown, M.B. Clennell, and G.K. Westbrook (1996), A comparison of the fabric and permeability anisotropy of consolidated and sheared silty clay, *Eng. Geol., 42,* 253-267.

Dieterich, J.H. (1981), Constitutive properties of faults with simulated gouge, *in* Mechanical Behavior of Crustal Rocks*, Geophys. Monogr. Ser., 24,* N.L. Carter et al. (eds.), AGU, Washington, D.C., 102-120.

Dieterich, J.H. (1979), Modeling of rock friction 1. Experimental results and constitutive equations, *J. Geophys. Res., 84*, 2161-2168.

Dieterich, J.H. and B. Kilgore (1996), Implications of fault constitutive properties for earthquake prediction, *Proc. Natl. Acad. Sci., 93*, 3787-3794.

Domenico, P.A. and M.D. Mifflin (1965), Water from low-permeability sediments and land subsidence, *Water Resources Res., 1,* 563-576.

Eberl, D.D., B. Velde, and T. McCormick, (1993), Synthesis of illite-smectite from smectite at earth surface temperatures and high pH, *Clay Minerals, 28*, 49-60.

Evans, J.P. (1990), Thickness-displacement relationships for fault zones, *J. Struct. Geol. 12,* 1061-1065.

Evans, J.P. and F.M. Chester (1995), Fluid-rock interactions in faults of the San Andreas system: Inferences from San Gabriel fault rock geochemistry and microstructures, *J. Geophys. Res., 100*, 13,007-13,020.

Expedition 316 Scientists (2009a), Expedition 316 Site C0004, *in* Kinoshita, M., H. Tobin, J. Ashi, G. Kimura, S. Lallemant, E.J. Screaton, D. Curewitz, H. Masago, K.T. Moe, and the Expedition 314/315/316 Scientists, *Proc. IODP,* 314/315/316: Washington, D.C. (Integrated Ocean Drilling Program Management International, Inc.), doi:10.2204/iodp.proc.314315316.133.2009.

Expedition 316 Scientists (2009b), Expedition 316 Site C0007, *in* Kinoshita, M., H. Tobin, J. Ashi, G. Kimura, S. Lallemant, E.J. Screaton, D. Curewitz, H. Masago, K.T. Moe, and the Expedition 314/315/316 Scientists, *Proc. IODP,* 314/315/316: Washington, D.C.

(Integrated Ocean Drilling Program Management International, Inc.), doi:10.2204/iodp.proc.314315316.135.2009.

Faulkner, D.R. and E.H. Rutter (2003), The effect of temperature, the nature of the pore fluid, and subyield differential stress on the permeability of phyllosilicate-rich fault gouge, *J. Geophys. Res., 108,* doi:10.1029/2001JB001581

Faulkner, D.R. and E.H. Rutter (2001), Can the maintenance of overpressured fluids in large strike-slip fault zones explain their apparent weakness? *J. Geophys. Res., 29*, 503-506.

Faulkner, D.R. and E.H. Rutter (2000), Comparisons of water and argon permeability in natural clay-bearing fault gouge under high pressure at 20°C, J. Geophys. Res., 105, 16,415-16,426.

Faulkner, D.R. and E.H. Rutter (1998), The gas permeability of clay-bearing fault gouge at 20°C, in *Faults, Fault Sealing and Fluid Flow in Hydrocarbon Reservoirs,* G. Jones, Q. Fisher, and R.J. Knipe (eds.), *Geol. Soc. Spec. Pub., 147,* 147-156.

Fitts, T.G., and K.M. Brown (1999), Stress-induced smectite dehydration: ramifications for patterns of freshening and fluid expulsion in the N. Barbados accretionary wedge, *Earth Planet. Sci. Lett.,172*, 179-197.

Friedman, M. and N.G. Higgs (1981), Calcite fabrics in experimental shear zones, *in* Mechanical Behavior of Crustal Rocks*, Geophys. Monogr. Ser., 24,* N.L. Carter et al. (eds.), AGU, Washington, D.C., 11-27.

Frost, E., J. Dolan, C. Sammis, B. Hacker, J. Cole, and L. Ratsbacher (2009), Progressive strain localization in a major strike-slip fault exhumed from midseismogenic depths: Structural observations from the Salzach-Ennstal-Mariazell-Puchberg fault system, Austria, *J. Geophys. Res., 114*, B04406, doi:10.1029/2008JB005763.

Frye, K.M. and C. Marone (2002), Effect of humidity on granular friction at room temperature, *J. Geophys. Res.,* Vol. 107, No. B11, 2309, 2002.

Gu, Y. and T.-F. Wong (1994), Development of shear localization in simulated quartz gouge: Effect of cumulative slip and gouge particle size, *Pure Appl. Geophys., 143*, 387-423.

Haines, S.H., B.A. van der Pluijm, M. Ikari, D. Saffer, and C. Marone (2009), Clay fabrics in natural and artificial gouge, *J. Geophys. Res., 114,* B05406, doi;10.1029/2008JB005866.

Handin, J. (1969), On the Coulomb-Mohr failure criterion. *J. Geophys. Res., 74*, 5343-5348.

Hibbeler, R.C. (1997), Mechanics of Materials, 3rd ed., Prentice Hall, Upper Saddle River, NJ.

Hickman, S.H. (1991), Stress in the lithosphere and the strength of active faults, *Rev. Geophys. Suppl.,* U.S. National Report to International Union of Geodesy and Geophysics, 759-775.

Hong, T. and C. Marone (2005), Effects of normal stress perturbations on the frictional properties of simulated faults, *Geochem. Geophys. Geosyst., 6,* Q03012, doi:10.1029/2004GC000821.

Hubbert, M.K. and W.W. Rubey (1959), Role of fluid pressure in mechanics of overthrust faulting 1. Mechanics of fluid-filled porous solids, and its application to overthrust faulting, *GSA Bull., 70*, 115-166.

Hull, J. (1988), Thickness-displacement relationships for deformation zones, *J. Struct. Geol., 10*, 431-435.

Hyndman, R.D. (2007), The seismogenic zone of subduction thrust faults: What we know and don't know, in *The Seismogenic Zone of Subduction Thrust Faults,* T.H. Dixon and J.C. Moore (eds.), Columbia Univ. Press, New York.

Hyndman, R.D., M. Yamano, and D.A. Oleskevich, (1997), The seismogenic zone of subduction thrust faults, in *The Island Arc*, *6,* 244-260.

Ide, S., G.C. Beroza, D.R. Shelly, and T. Uchide (2007), A scaling law for slow earthquakes, *Nature, 447,* 76-79, doi:10.1038/nature05780.

Ikari. M.J., C. Marone, and D.M. Saffer (2010), On the relation between fault strength and frictional stability, *Geology, in review.*

Ikari, M.J., D.M. Saffer, and C. Marone (2009a), Frictional and hydrologic properties of clay-rich fault gouge, *J. Geophys. Res.*, *114*, B05409, doi:10.1029/2008JB006089.

Ikari. M.J., D.M. Saffer, and C. Marone (2009b), Frictional and hydrologic properties of a major splay fault system, Nankai subduction zone, Geophys. Res. Lett., 36, L20313, doi:10.1029/2009GL040009.

Ikari, M.J., D.M. Saffer, and C. Marone (2007), Effect of hydration state on the frictional properties of montmorillonite-based fault gouge, *J. Geophys. Res., 112*, B06423, doi:10.1029/2006JB004748.

Irwin, W.P., and I. Barnes (1975), Effect of geologic structure and metamorphic fluids on the seismic behavior of the San Andreas fault system in central and northern California, *Geology, 3*, 713-716.

Ito, Y. and K. Obara (2006), Dynamic deformation of the accretionary prism excites very low frequency earthquakes, *Geophys. Res. Lett., 33,* L02311, doi:10.1029/2005GL02570.

Johnson T.L. and C.H. Scholz (1976), Dynamic properties of stick-slip friction of rock, *J. Geophys. Res., 81*, 881-888.

Kame, N., J.R. Rice, and R. Dmowska (2003), Effects of pre-stress state and rupture velocity on dynamic fault branching, *J. Geophys. Res., 108,* 1-19.

Karner, S.L., C. Marone, and B. Evans (1997), Laboratory study of fault healing and lithification in simulated fault gouge under hydrothermal conditions, *Tectonophys., 277,* 41-55.

Kato, T. (1983), High-angle reverse faulting associated with the 1946 Nankaido earthquake, *Tectonophys., 96*, 31-44.

Kikuchi, M., Nakamura, M., and K. Yoshikawa (2003), Source rupture processes of the 1944 Tonankai earthquake and the 1945 Mikawa earthquake derived from low-gain seismograms, *Earth Plan. Space, 55,* 159-172.

Kimura, G., E.J. Screaton, D. Curewitz, and Expedition 316 Scientists (2008), NanTroSEIZE Stage 1A: NanTroSEIZE shallow megasplay and frontal thrusts, *IODP Prel. Rept.,* 316, doi10.224/iodp.pr.316.2008.

Knuth, M.W., H.J. Tobin, C. Marone, D.M. Saffer, and Y. Hashimoto (2009), Influence of stress history on elastic and frictional properties of core material from IODP Expeditions 315 and 316, NanTroSEIZE transect: Implications for the Nankai Trough accretionary prism, *Eos Trans. AGU, 90(52)*, Fall Meet. Suppl., Abstract T12A-07.

Kopf, A. and K.M. Brown (2003), Friction experiments on saturated sediments and their implications for the stress state of the Nankai and Barbados subduction thrusts, *Mar. Geol., 202,* 193-210.

Kwon, O., A.K. Kronenberg, A.F. Gangi, B. Johnson, and B.E. Herbert (2004), Permeability of illite-bearing shale: 1. Anisotropy and effects of clay content and loading, *J. Geophys. Res., 109*, B10205, doi:10.209/2004JB003052.

Lachenbruch, A.H., and J.H. Sass (1980), Heat flow and energetics of the San Andreas fault zone, *J. Geophys. Res., 85*, 6185-6222.

Lambe, T.W., and R.V. Whitman (1969), Soil Mechanics, Wiley, New York, NY.

Le Pichon, X., P. Henry, and S. Lallemant (1993), Accretion and erosion in subduction zones: The role of fluids, *Annu. Rev. Earth Planet. Sci., 21*, 307-331.

Linde, A.T., M.T. Gladwin, M.J.S. Johnston, R.L. Gwyther, and R.G. Bilham, (1996), A slow earthquake sequence on the San Andreas fault, *Nature, 383*, 65-68.

Linker, M.F. and J.H. Dieterich (1992), Effects of variable normal stress on rock friction: Observations and constitutive equations, *J. Geophys. Res., 97,* 4923-4940.

Liu, Y. and J.R. Rice (2005), Aseismic slip transients emerge spontaneously in three-dimensional rate and state modeling of subduction earthquake sequences, *J. Geophys. Res., 110,* B08397, doi:10.1029/2004JB003424.

Lockner, D., J. Solum, and N. Davatzes (2006), The effect of brine composition and concentration on strength of expandable clays, *Eos Trans. AGU, 87* (52), Fall Meet. Suppl., Abstract T31F-03.

Logan, J.M., C.A. Dengo, N.G. Higgs, and Z.Z. Wang (1992), Fabrics of experimental fault zones: Their development and relationship to mechanical behavior, in *Fault Mechanics and Transport Properties of Rocks*, edited by B. Evans and T.-F. Wong, pp. 33-67, Academic Press, Ltd., San Diego, CA.

Logan, J.M. and K.A. Rauenzahn (1987), Frictional dependence of gouge mixtures of quartz and montmorillonite on velocity, composition, and fabric, *Tectonophysics*, *144*, 87-108.

Mair, K. and C. Marone (1999), Friction of simulated fault gouge for a wide range of velocities and normal stresses, *J. Geophys. Res., 104*, 28,899-28,914.

Mandl, G., L.N.J. de Jong, and A. Maltha (1977), Shear zones in granular material, *Rock Mech., 9*, 95-144.

Mares, V.M. and A.K. Kronenberg (1993), Experimental deformation of muscovite, *J. Struct. Geol., 15,* 1061-1075.

Marone, C. (1998), Laboratory-derived friction laws and their application to seismic faulting, *Annu. Rev. Earth Planet. Sci., 26*, 643-696.

Marone, C. and D.M. Saffer (2007), Fault friction and the upper transition from seismic to aseismic faulting, *in* The seismogenic zone of subduction thrust faults, T.H. Dixon and J.C. Moore (eds.), Columbia University Press, NY.

Marone, C. and S.J.D. Cox (1994), Scaling of rock friction constitutive parameters: The effects of surface roughness and cumulative offset on friction of gabbro, *Pure Appl. Geophys., 143,* 359-385.

Marone, C. and B. Kilgore (1993), Scaling of the critical slip distance for seismic faulting with shear strain in fault zones, *Nature, 362,* 618-621.

Marone, C., B.E. Hobbs, and A. Ord (1992), Coulomb constitutive laws for friction: Contrasts in frictional behavior for distributed and localized shear, *Pure Appl. Geophys., 139*, 195-214.

Marone, C.J., C.H. Scholz, and R. Bilham (1991), On the mechanics of earthquake afterslip, *J. Geophys. Res., 96,* 8441-8452.

Marone, C., C.B. Raleigh, and C.H. Scholz (1990), Frictional behavior and constitutive modeling of simulated fault gouge, *J. Geophys. Res., 95,* 7007-7025.

Marone, C. and C.H. Scholz (1988), The depth of seismic faulting and the upper transition from stable to unstable slip regimes, *Geophys. Res. Lett., 15,* 621-624.

Mazzotti, S., X. Le Pichon, and P. Henry (2000), Full interseismic locking of the Nankai and Japan-West Kurile subduction zones: An analysis of uniform elastic strain accumulation in Japan constrained by permanent GPS, *J. Geophys. Res., 105,* 13,159-13,177.

McKiernan, A., D. Lockner, and D.M. Saffer (2005), Frictional behavior of natural clay-rich fault gouges from ODP Leg 190, Nankai Trough, offshore Japan, *Eos Trans. AGU, 86*(52), Fall Meet. Suppl., Abstract.

Means, W.D. (1995), Shear zones and rock history, *Tectonophys., 247*, 157-160.

Menéndez, B., W. Zhu, and T.-F. Wong (1996), Micromechanics of brittle faulting and cataclastic flow in Berea sandstone, *J. Struct. Geol., 18*, 1-16.

Miller, S.A., A. Nur, and D.L. Olgaard (1996), Earthquakes as a coupled shear stress – high pore pressure dynamical system, *Geophys. Res. Lett., 23,* 197-200.

Moore, D.E. and D.A. Lockner (2008), Talc friction in the temperature range 25°C-400°C: Relevance for fault zone weakening, *Tectonophys., 449*, 120-132.

Moore, D.E., and D.A. Lockner (2007), Friction of the smectite clay montmorillonite: a review and interpretation of data, in *The Seismogenic Zone of Subduction Thrust Faults,* edited by T. Dixon et al., Columbia Univ. Press.

Moore, D.E. and D.A. Lockner (2004), Crystallographic controls on the frictional behavior of dry and water-saturated sheet structure minerals, *J. Geophys. Res., 109,* B03401, doi10.1029/2003JB002582.

Moore, G.F., and 14 others (2009), Structural and seismic framework of the NanTroSEIZE Stage 1 transect, *in* Kinoshita, M., H. Tobin, J. Ashi, G. Kimura, S. Lallemant, E.J. Screaton, D. Curewitz, H. Masago, K.T. Moe, and the Expedition 314/315/316 Scientists, *Proc. IODP,* 314/315/316: Washington, D.C. (Integrated Ocean Drilling Program Management International, Inc.), doi:10.2204/iodp.proc.314315316.102.2009.

Moore, G.F., N.L. Bangs, A. Taira, S. Kuramoto, E. Pangborn, and H.J. Tobin (2007), Three-dimensional splay fault geometry and implications for tsunami generation, *Science, 318,* 1128-1131.

Moore, G.F., and 25 others (2001), New insights into deformation and fluid flow processes in the Nankai Trough accretionary prism: Results of Ocean Drilling Program Leg 190, *Geochem. Geophys. Geosyst., 2,* doi:10.129/2001GC00166.

Moore, J.C., C. Rowe, and F. Meneghini (2007), How accretionary prisms elucidate seismogenesis in subduction zones, in *The Seismogenic Zone of Subduction Thrust Faults,* T.H. Dixon and J.C. Moore (eds.), Columbia University Press, NY.

Moore, J.C. and D.M. Saffer (2001), Updip limit of the seismogenic zone beneath the accrectionary prism of Southwest Japan: An effect of diagenetic to low-grade metamorphic processes and increasing effective stress, *Geology, 29,* 183-186.

Morrow, C.A., D.E. Moore and D.A. Lockner (2000), The effect of mineral bond strength and adsorbed water on fault gouge frictional strength, *Geophys. Res. Lett., 27,* 815-818.

Morrow, C., B. Radney and J. Byerlee (1992), Frictional strength and the effective pressure law of montmorillonite and illite clays, in *Fault Mechanics and Transport Properties of Rocks*, B. Evans and T.-F. Wong (eds.), 69-88.

Morrow, C.A., L.Q. Shi, and J.D. Byerlee (1984), Permeability of fault gouge under confining pressure and shear stress, *J. Geophys. Res., 89*, 3193-3200.

Niemeijer, A.R., C. Marone, and D. Elsworth (2010), Fabric induced weakness of tectonic faults, *Geophys. Res. Lett., 37,* L03304, doi:10.1029/2009GL041689.

Niemeijer, A.R., and C.J. Spiers (2006), Velocity dependence of strength and healing behavior in simulated phyllosilicate-bearing fault gouge, *Tectonophys., 427,* 231-253.

Niemeijer, A.R. and C.J. Spiers (2005), Influence of phyllosilicates on fault strength in the brittle-ductile transition: insights from rock analogue experiments, in High-strain zones: Structure and physical properties, D. Bruhn and L. Burlini (eds.), *Geol. Soc. London Spec. Pub., 245,* 303-327.

Noda, H. and T. Shimamoto (2005), Thermal pressurization and slip-weakening distance of a fault: An example of the Hanaore fault, southwest Japan, *Bull. Seis. Soc. Am., 95,* 1224-1233, doi: 10.1785/0120040089.

Numelin, T., C. Marone and E. Kirby (2007) Frictional properties of natural fault gouge from a low-angle normal fault, Panamint Valley, California, *Tectonics, 26,* TC2004, doi:10.1029/2005TC001916.

Park, J.-O., T. Tsuru, S. Kodaira, P.R. Cummins, and Y. Kaneda (2002), Splay fault branching along the Nankai subduction zone, *Science, 297,* 1157-1160.

Park, J.-O., T. Tsuru, S. Kodaira, A. Nakanishi, S. Miura, Y. Kaneda, and Y. Kono (2000), Out-of-sequence thrust faults developed in the coseismic slip zone of the 1946 Nankai earthquake (Mw=8.2) off Shikoku, southwest Japan, *Geophys. Res. Lett., 27,* 1033-1036.

Perfettini, H. and J.-P. Ampuero (2008), Dynamics of a velocity strengthening fault region: Implications for slow earthquakes and postseismic slip, *J. Geophys. Res., 113,* B09411, doi:10.1029/2007JB005398.

Perfettini, H. and J.-P. Avouac (2004), Postseismic relaxation driven by brittle creep: A possible mechanism to reconcile geodetic measurements and the decay rate of aftershocks, application to the Chi-Chi earthquake, Taiwan, *J. Geophys. Res., 109,* B02304, doi:10.1029/2003JB002488.

Pytte, A.M. and R.C. Reynolds (1989), The thermal transition of smectite to illite, in *Thermal history of sedimentary basins: Methods and case studies*, edited by N.D. Naeser and T.H. McCulloch, Springer-Verlag, New York, NY, 33-40.

Reinen, L.A. and J.D. Weeks (1993), Determination of rock friction constitutive parameters using an iterative least-squares inversion method, *J. Geophys. Res., 98*, 15937-15950.

Reinen, L.A., Weeks, J.D. and T.E. Tullis (1991), The frictional behavior of serpentinite: Implications for aseismic creep on shallow crustal faults, *Geophys. Res. Lett., 18,* 1921-1924.

Richardson, E. and C. Marone (1999), Effects of normal stress vibrations on frictional healing, *J. Geophys. Res., 104,* 28,859-28,878.

Rice, J.R. (2006), Heating and weakening of faults during earthquake slip, *J. Geophys. Res., 111*, B05311, doi:10.1029/2005JB004006.

Rice, J.R. (1992), Fault stress states, pore pressure distributions, and the weakness of the San Andreas Fault, in *Fault Mechanics and Transport Properties of Rocks*, B. Evans and T.-F. Wong (eds.), 475-503.

Rubin, A.M. (2008), Episodic slow slip events and rate-and-state friction, *J. Geophys. Res., 113*, B11414, doi:10.1029/2008JB005642.

Ruff, L. and H. Kanamori (1983), Seismic coupling and uncoupling at subduction zones, *Tectonophys., 99*, 99-117.

Sagy, A., E.E. Brodsky, and G.J. Axen (2007), Evolution of fault-surface roughness with slip, *Geology, 35,* 283-286, doi:10.1130/G23235A.1.

Saffer, D.M. and B.A. Bekins (2006), An evaluation of factors influencing pore pressure in accretionary complexes: Implications for taper angle and wedge mechanics, *J. Geophys. Res., 111,* B4101, doi:10.1029/2005JB003990.

Saffer, D.M. and B.A. Bekins (1998), Episodic fluid flow in the Nankai accretionary complex: timescale, geochemistry, flow rates, and fluid budget, *J. Geophys. Res., 103*, No. B12, 30,351-30,370.

Saffer, D.M. and C. Marone (2003), Comparison of smectite- and illite-rich gouge frictional properties: Application to the updidp limit of the seismogenic zone along subduction megathrusts, *Earth Planet. Sci. Lett., 215*, 219-235.

Saffer, D.M., K.M. Frye, C. Marone, and K. Mair (2001), Laboratory results indicating complex and potentially unstable frictional behavior of smectite clay, *Geophys. Res. Lett., 28,* 2297-2300.

Sagiya, T. and W. Thatcher (1999), Coseismic slip resolution along a plate boundary megathrust: The Nankai Trough, southwest Japan, *J. Geophys. Res., 104,* 1111-1129.

Samuelson, J., D. Elsworth, and C. Marone (2009), Shear-induced dilatancy of fluid-saturated faults: Experiment and theory, *J. Geophys. Res., 114,* B12404, doi:10.1029/2008JB006273.

Samuelson, J., C. Marone and D. Elsworth (2007), Hydro-mechanical processes in faulting: an experimental analysis of the variability of dilatancy in simulated fault gouge, *Eos Trans. AGU, 88* (52), Fall Meet. Suppl., Abstract T42-C-07.

Samuelson, J., C. Marone and D. Elsworth (2006), The effect of dilatancy and compaction on the stability and permeability of a fluid-infiltrated fault, *Eos Trans. AGU, 87* (52), Fall Meet. Suppl., Abstract S33A-0218.

Savage, H.M. and C. Marone (2008), Potential for earthquake triggering from transient deformations, *J. Geophys. Res., 113*, B05302, doi:10.1029/2007JB005277.

Savage, J.C. and J. Langbein (2008), Postearthquake relaxation after the 2004 *M*6 Parkfield, California, earthquake and rate-and-state friction, *J. Geophys. Res., 113,* B10407, doi:10.1029/2008JB005723.

Schleicher, A.M., B.A. van der Pluijm, and L.N. Warr (2010), Nanocoatings of clay and creep of the San Andreas fault at Parkfield, California, *Geology, 38,* 667-670, doi:10.1130/G31091.1.

Schleicher, A.M., S.N. Tourscher, B.A. van der Pluijm, and L.N. Warr (2009), Constraints on mineralization, fluid-rock interaction, and mass transfer during faulting at 2-3 km depth from the SAFOD drill hole, *J. Geophys. Res., 114,* B04202, doi:10.1029/2008JB006092.

Scholl, D.W., R. von Huene, T.L. Vallier, and D.G. Howell (1980), Sedimentary masses and concepts about tectonic processes at underthrust ocean margins, *Geology, 8,* 564-568.

Scholz, C.H. (2002), The mechanics of earthquakes and faulting, 2nd ed., Cambridge Press, New York, NY.

Scholz, C.H. (1998), Earthquakes and friction laws, *Nature*, 391, 38-42.

Scholz, C.H. (1992), Paradigms or small changes in earthquake mechanics, in *Fault Mechanics and Transport Properties of Rocks*, B. Evans and T.-F. Wong (eds.), 505-517.

Scholz, C.H. (1987), Wear and gouge formation in brittle faulting, *Geology, 15*, 493-495.

Scott, D.R., C.J. Marone, and C.G. Sammis (1994), The apparent friction of granular fault gouge in sheared layers, *J. Geophys. Res., 99*, 7231-7246.

Scruggs, V.J. and T.E. Tullis (1998), Correlation between velocity dependence of friction and strain localization in large displacement experiments on feldspar, muscovite and biotite gouge, *Tectonophysics*, 295, 15-40.

Segall, P. and J.R. Rice (2006), Does shear heating of pore fluid contribute to earthquake nucleation? *J. Geophys. Res., 111,* B09316, doi:10.1029/2005JB004129.

Segall, P. and J.R. Rice (1995), Dilatancy, compaction, and slip instability of a fluid-infiltrated fault, *J. Geophys. Res., 100,* 22,155-22,171.

Sekiguchi, H., K. Irikura, and T. Iwata (2000), Fault geometry at the rupture termination of the 1995 Hyogo-ken Nanbu earthquake, *Bull. Seis. Soc. Am., 90,* 117-133.

Shea, W.T. and A.K. Kronenberg (1993), Strength and anisotropy of foliated rocks with varied mica contents, *J. Struct. Geol., 15,* 1097-112.

Shimamoto, T. and J.M. Logan (1986), Velocity-dependent frictional behavior of simulated halite shear zones: An analog for silicates, *in* Earthquake source mechanics, *Geophys. Monogr. Ser., 37,* S. Das et al. (eds.), AGU, Washington, DC, 49-64,

Shimamoto, T. (1985), The origin of large or great thrust-type earthquakes along subducting plate boundaries, *Tectonophys., 295*, 1-14.

Shimamoto, T. and J.M. Logan (1981a), Effects of simulated clay gouges on the sliding behavior of Tennessee sandstone, *Tectonophys., 75*, 243-255.

Shimamoto, T. and J.M. Logan (1981b), Effects of simulated fault gouge on the sliding behavior of Tennessee sandstone: Nonclay gouges, *J. Geophys. Res., 86,* 2902-2914.

Shipboard Scientific Party (2001a), Leg 190 Summary, *in* Moore, G.F., A. Taira, A. Klaus, et al., *Proc. ODP, Init. Repts., 190*: College Station, TX, 1-149, doi:10.2973/odp.proc.ir.190.101.2001.

Shipboard Scientific Party (2001b), Site 1174, *in* Moore, G.F., A. Taira, A. Klaus, et al., *Proc. ODP, Init. Repts., 190*: College Station, TX, 1-149, doi:10.2973/odp.proc.ir.190.105.2001.

Sibson, R.H. (1986a), Earthquakes and rock deformation in crustal fault zones, *Ann. Rev. Earth Planet. Sci., 14*, 149-175.

Sibson, R.H. (1986b), Brecciation processes in fault zones: Inferences from earthquake rupturing, *Pure Appl. Geophys., 124*, 159-175.

Sibson, R.H. (1984), Roughness at the base of the seismogenic zone: Contributing factors, *J. Geophys. Res., 89*, 5791-5799.

Sleep, N.H. and M.L. Blanpied (1992), Creep, compaction and the weak rheology of major faults, *Nature, 359*, 687-692.

Smith, S.A.F., and D.R. Faulkner (2010), Laboratory measurements of the frictional properties of the Zuccale low-angle normal fault, Elba Island, Italy, *J. Geophys. Res., 115*, B02407, doi.10.1029/2008JB006274.

Solum, J.G., B.A. van der Pluijm, D.R. Peacor, and L.N. Warr (2003), Influence of phyllosilicate mineral assemblages, fabrics, and fluids on the behavior of the Punchbowl fault, southern California, *J. Geophys. Res., 108*, 2233, doi:10.1029/2002JB001858.

Takahashi, M., K. Mizoguchi, K. Kitamura, and K. Masuda (2007), Effects of clay content on the frictional strength and fluid transport property of faults, *J. Geophys. Res., 112,* B08206, doi:10.1029/2006JB004678.

Tanioka, Y., and K. Satake (2001), Detailed coseismic slip distribution of the 1944 Tonankai earthquake estimated from tsunami waveforms, *Geophys. Res. Lett., 28,* 1075-1078.

Tembe, S., D.A. Lockner, and T.-F. Wong (2010), Effect of clay content and mineralogy on frictional sliding behavior of simulated gouges: Binary and ternary mixtures of quartz, illite, and montmorillonite, *J. Geophys. Res., 115,* B03416, doi:10.1029/2009JB006383.

Thatcher, W. (1984), The earthquake deformation cycle at the Nankai Trough, southwest Japan, *J. Geophys. Res., 89,* 3087-3101.

Tichelaar, B.W. and L.J. Ruff (1993), Depth of seismic coupling along subduction zones, *J. Geophys. Res., 98*, 2017-2037.

Tullis, T.E. (1988), Rock friction constitutive behavior from laboratory experiments and its implications for an earthquake prediction field monitoring program, *Pure Appl. Geophys., 126,* 555-588.

Tullis, T.E. and J.D. Weeks (1986), Constitutive behavior and stability of frictional sliding of granite, *Pure Appl. Geophys., 124,* 383-414.

Underwood, M.B. (2007), Sediment inputs to subduction zones: Why lithostratigraphy and clay mineralogy matter, in *The Seismogenic Zone of Subduction Thrust Faults,* T.H. Dixon and J.C. Moore (eds.), Columbia Univ. Press, New York.

Vrolijk, P. and B.A. van der Pluijm (1999), Clay gouge, *J. Struct. Geol.*, *21*, 1039-1048.

Vrolijk, P. (1990), On the mechanical role of smectite, *Geology*, *18*, 703-707.

Wang, C.-Y. and N.-H. Mao (1979), Shearing of saturated clays in rock joints at high confining pressures, *Geophys. Res. Lett., 6,* 825-828.

Wang, K. and Y. Hu (2006), Accretionary prisms in subduction earthquake cycles: The theory of dynamic Coulomb wedge, *J. Geophys. Res., 111,* B06410, doi:10.1029/2005JB004094.

Wang, K. and J. He (1999), Mechanics of low-stress forearcs: Nankai and Cascadia, *J. Geophys. Res., 104,* 15,191-15,205.

Warr, L.N. and S. Cox (2001), Clay mineral transformations and weakening mechanisms along the Alpine Fault, New Zealand, *in* The nature and tectonic significance of fault zone weakening, R.E. Holdsworth et al. (eds.), *Geol. Soc. London Spec. Pub., 186,* 85-101.

Wesnousky, S.G. (1988), Seismological and structural evolution of strike-slip faults, *Nature, 335,* 340-343.

Wibberley, C.A.J. and T. Shimamoto (2005), Earthquake slip weakening and asperities explained by thermal pressurization, *Nature, 436,* 689-692, doi:10.1038/nature03901.

Wiersberg, T. and J. Erzinger (2008), Origin and spatial distribution of gas at seismogenic depths of the San Andreas fault from drill-mud gas analysis, *Appl. Geochem., 23,* 1675-1690.

Wiersberg, T. and J. Erzinger (2007), A helium isotope cross-section study through the San Andreas fault at seismogenic depths, *Geochem. Geophys. Geosyst., 8,* Q01002, doi:10.1029/2006GC001388.

Wintsch, R.P., R. Christoffersen, and A.K. Kronenberg (1995), Fluid-rock reaction weakening of fault zones, *J. Geophys. Res., 100*, 13,021-13,032.

Wu, F.T., L. Blatter, and H. Roberson (1975), Clay gouges in the San Andreas fault system and their possible implications, *Pure Appl. Geophys., 113,* 87-95.

Yang, Y. and A. Aplin (2007), Permeability and petrophysical properties of 30 natural mudstones, *J. Geophys. Res., 112,* B03206, doi:10.1029/2005JB004243.

Zhang, S., T.E. Tullis, and V.J. Scruggs (2001), Implications of permeability and its anisotropy in a mica gouge for pore pressures in fault zones, *Tectonophysics, 335,* 37-50.

Zhang, S., T.E. Tullis, and V.J. Scruggs (1999), Permeability anisotropy and pressure dependency of permeability in experimentally sheared gouge materials, *J. Struct. Geol.,* 21, 795-806.

Zhang, S. and S.F. Cox (2000), Enhancement of fluid permeability during shear deformation of a synthetic mud, *J. Struct. Geol., 22,* 1385-1393.

CURRICULUM VITA

Matt J. Ikari

Rock and Sediment Mechanics Laboratory
Department of Geoscience
522 Deike Building
The Pennsylvania State University
University Park, PA 16802
mji127@psu.edu

Education:

2010 Ph. D., Geoscience, The Pennsylvania State University
Advisors: Chris Marone, Demian M. Saffer
2002 M.S., Geologic Science, University of Rochester
Advisor : Carmala N. Garzione
2001 B.S., Geomechanics, University of Rochester

Funding Awards:

Consortium for Ocean Leadership Post-Expedition Activity Award, IODP Expedition 322 (2009)
ConocoPhillips Graduate Student Fellowship (2010)
P.D. Krynine Memorial Fund (PSU) (2005-2009)

Other :

IODP Expedition 322 Shipboard Scientific Party (2009)
Laboratory section intstructor for GEOSC 040, The Sea Around Us (introductory oceanography)